ABSTRACT

Title of dissertation: Dispersion of ion gyrocenters
in models of anisotropic plasma turbulence

Kyle Gustafson, Doctor of Philosophy, 2010

Dissertation directed by: Professor William Dorland
Department of Physics

Turbulent dispersion of ion gyrocenters in a magnetized plasma is studied in the context of a stochastic Hamiltonian transport model and nonlinear, self-consistent gyrokinetic simulations. The Hamiltonian model consists of a superposition of drift waves derived from the linearized Hasegawa-Mima equation and a zonal shear flow perpendicular to the density gradient. Finite Larmor radius (FLR) effects are included. Because there is no particle transport in the direction of the density gradient, the focus is on transport parallel to the shear flow. The prescribed flow produces strongly asymmetric non-Gaussian probability distribution functions (PDFs) of particle displacements, as was previously known. For $k_\perp \rho_{th} = 0$, where $k_\perp$ is the characteristic wavelength of the flow and ρ_{th} is the thermal Larmor radius, a transition is observed in the scaling of the second moment of particle displacements, $\sigma^2 \sim t^\gamma$. The transition separates nearly ballistic superdiffusive motion, $\gamma \approx 1.9$, at intermediate times from weaker superdiffusion, $\gamma \sim 1.6$, at later times. This change of scaling is accompanied by the transition of the probability density

function (PDF) of particle displacements from algebraic decay to exponential decay. However, FLR effects eliminate this transition. In all cases, the Lagrangian velocity autocorrelation function exhibits algebraic decay, $\mathcal{C} \sim \tau^{-\zeta}$, with $\zeta = 2 - \gamma$ to a good approximation. The PDFs of trapping and flight events show clear evidence of algebraic scaling with decay exponents depending on the value of $k_\perp \rho_{th}$. Important features of the PDFs of particle displacements are reproduced accurately with a fractional diffusion model. The gyroaveraged $\mathbf{E} \times \mathbf{B}$ drift dispersion of a sample of tracer ions is also examined in a two-dimensional, nonlinear, self-consistent δf gyrokinetic particle-in-cell (PIC) simulation. Turbulence in the simulation is driven by a density gradient and magnetic curvature, resulting in the unstable ρ_i-scale kinetic entropy mode. The dependence of dispersion in both the axial and radial directions is characterized by displacement and velocity increment distributions. The strength of the density gradient is varied, using the local approximation, in three separate trials. A filtering procedure is used to separate trajectories according to whether they were caught in an eddy during a set observation time. Axial displacements are compared to the results from the simplified Hasegawa-Mima model. Superdiffusion and ballistic transport is found, depending on the filtering and the strength of the gradient. The radial dispersion of particles, as measured by the variance, $\sigma_x^2(t)$, of tracer displacements, is diffusive. The dependence of the running diffusion coefficient, $D(t) = \sigma_x^2(t)/t$, on ρ_i for each value of the density gradient is considered.

Dispersion of ion gyrocenters in models of anisotropic plasma turbulence

by

Kyle Bergin Gustafson

Dissertation submitted to the Faculty of the Graduate School of the
University of Maryland, College Park in partial fulfillment
of the requirements for the degree of
Doctor of Philosophy
2010

Advisory Committee:
Professor William Dorland, Chair
Professor Thomas Antonsen
Professor James Drake
Professor Richard Ellis
Professor Manuel Tiglio
Professor Alan Sussman, Dean's Representative

Dedication

For my grandfather, Fridolin Stallbaumer, whose generous and curious spirit survives in multiplicity.

Acknowledgments

Before I committed to this journey, I knew the unconditional love of my parents and family followed me. Kate's expressions of this love are beyond explanation and gratitude.

My time of study at Maryland was marked by wonderful interactions with my fellow students and teachers. More than an advisor, Bill Dorland is my mentor, friend and inspiration. I thank him for opening to me his vast reservoirs of patience and optimism.

A special recognition belongs to Diego del Castillo Negrete, who directed the work in Chapter 3. Thanks to the staff and scientists at Oak Ridge National Lab for generously accommodating me on several occasions. While at Oak Ridge, I benefited from discussions with Iván Calvo and Raul Sánchez, both of whom also provided exceptional hospitality.

I am in debt to Ingmar Broemstrup for the use of his code and I owe so much of my understanding of gyrokinetics to Michael Barnes. Along with Kate Despain and Anjor Kanekar, we formed a supportive group of curious students at Maryland.

Readers and improvers of this thesis include Gabriel Plunk, Michael Barnes, Kate Despain, Jon Hillesheim and Ryan Behunin. I am especially grateful to Gabe, Michael and Felix Parra Diaz for thinking carefully through my ideas and statements, leading me towards important corrections and insights.

Jane Hessing, Linda O'Hara, Agi Alipio, Jean LaFonta, Mohini Kaul, Ed Condon, Bill Burns, and many others have enabled this work through their special talents.

I was supported by the Fannie and John Hertz Foundation during the academic year. The extended Hertz family fortified me intellectually with exposure to a variety of experts at symposiums and retreats. I appreciate the education in entrepreneurship and new friendships with extraordinary people facilitated by the Foundation. Thanks to Hertz representatives Lowell Wood and Greg Canavan for believing in me and offering candid advice. Linda Kubiak is an indispensable part of the Foundation and a great reliever of stress.

Financial support also came from the Department of Energy through the Center for Multiscale Plasma Dynamics, which created a persistent community of students, post-docs and faculty at the intersection of fusion and astrophysics. The annual Winter School at UCLA, in conjunction with the Center for Magnetic Self-Organization, will be remembered especially fondly.

This research primarily used resources of the National Energy Research Scientific Computing Center, which is supported by the Office of Science of the U.S. Department of Energy under Contract No. DE-AC02-05CH11231. This research also used resources of the National Center for Computational Sciences at Oak Ridge National Laboratory, which is supported by the Office of Science of the U.S. Department of Energy under Contract No. DE-AC05-00OR22725.

Table of Contents

List of Tables

List of Figures

Chapter 1

Introduction

Magnetized plasmas provide physicists with a variety of complex, nonlinear phenomena for study in terrestrial experiments, astrophysical observations and simulations of fluid or kinetic equations. A sufficient physical understanding of heated, confined plasmas could provide society with a solution to the limited supply of fossil fuels. One community with this goal is the international effort to design a magnetic confinement reactor for nuclear fusion. The imminent construction of ITER, planned as the largest tokamak to date, will increase global investment in fusion energy and require new ideas for managing and sustaining a burning plasma. At the same time, existing tokamaks, innovative confinement concepts, and basic plasma experiments contribute to the development of models and reactor design.

Understanding and controlling the level of heat and particle transport from the hot $(5-20\text{keV})$ core to the cold $(0-0.1\text{keV})$ edge of a magnetic confinement device is crucial to the design of a successful and economical fusion reactor. The behavior of these nonlinear, nonequilibrium systems is better understood today, compared to twenty years ago, largely because of focused efforts in gyrokinetic theory and simulation [3, 4, 5, 6, 7, 8] and thousands of experimental data points [9]. However, agreement between the best simulation predictions for transport levels and real data continues to be imprecise. While there are many reasons for discrepancies, one

problem may be the assumption that turbulent transport follows the same diffusive rules as collisional transport. In particular, the nature of particle transport in some turbulent situations may require a theory of nonlocal or nondiffusive transport, which generalizes the usual diffusive assumptions [10, 11, 12, 13, 14].

This thesis contributes to answering the fundamental question of how ion gyrocenter tracers disperse in a turbulent plasma near the ρ_i scale, where $\rho_i = \frac{v_{\perp,i}}{\Omega_i}$ is the Larmor radius of the ions, $v_{\perp,i}$ is the phase space velocity perpendicular to the magnetic field and $\Omega_i = \frac{q_i B}{m_i c}$ is the Larmor frequency. Understanding dispersion of tracers is one way to determine whether diffusive models are sufficient for describing particle transport in fusion plasmas. Our methods are based on tracking of gyrocenter trajectories following an $\mathbf{E} \times \mathbf{B}$ drift velocity field. We confine our study to examine statistics of tracer dispersion in two examples of particle m drift motion. One of these examples is a stochastic Hamiltonian model based on the Hasegawa-Mima equation for drift wave turbulence. The second example uses self-consistent, nonlinear gyrokinetic simulations in a two-dimensional geometry.

Gyrokinetic theory offers a widely applicable framework for understanding kinetic instabilities in magnetized plasmas with multiple interacting species (see Section 2.1). It was first derived in the linear regime by Antonsen and Lane [15] and then extended with nonlinear terms in Frieman and Chen [16]. Recent efforts have clarified the foundation of the theory and begun to apply it to astrophysical problems [17, 18]. In the linear approximation, the gyrokinetic dispersion relation can be solved analytically to identify several modes of instability with particular growth rates and frequencies. Linear instabilities are characterized by a range of

growing modes. When nonlinear terms are included in the equation, exchange of energy between several modes can cause competition and saturation of perturbation amplitudes. The saturated state may be turbulent, and steady-state turbulent heat and particle fluxes can then be measured in simulations. Innovations such as field-line following coordinates [19], highly accurate spectral methods and massively parallel computing platforms have enabled a number of research groups to attempt gyrokinetic simulations of tokamaks and compare the results with experimental diagnostics [20, 21].

In this thesis, we consider two simplifications of the fully electromagnetic gyrokinetic-Poisson system. First we examine gyrocenter $\mathbf{E} \times \mathbf{B}$-drift dispersion of a set of tracer ions in a prescribed velocity field based on the Hasegawa-Mima equation. The Hasegawa-Mima equation describes the nonlinear evolution of the electrostatic potential under the influence of a density gradient. Formally, it does not account for gyromotion of charged particles, so we introduce this effect externally through tracer particles following the $\mathbf{E} \times \mathbf{B}$-drift specified by $\phi(x, y, t)$, the electrostatic potential. The form of the $\mathbf{E} \times \mathbf{B}$-drift causes ϕ to be identified as a Hamiltonian. This model will therefore be referred to as a stochastic Hamiltonian model.

The interaction of a static shear flow with a time-dependent vortex chain in the stochastic Hamiltonian causes truncated Lèvy flight-type motion, which leads to superdiffusion in the direction of the flow. Lèvy flights are jumps that come from the long, non-Gaussian tail of a Lèvy distribution, and truncation is a physical upper limit to the jump sizes. Here we find that a subset of nonballistic gyrocenter tracers

disperse superdiffusively ($\sigma_y^2(t) = t^\gamma$, $\gamma > 1$) in a direction parallel to a shear flow, exhibiting a time-dependent transition from $\gamma = 1.6 \rightarrow \gamma = 1.9$. We vary the thermal gyroradius (Larmor radius) of the tracers as drawn from a Maxwellian distribution. This transition behavior ceases when the average Larmor radius reaches the size of the vortices. Moreover, the propagation of particles along this prescribed flow is found to agree with an analytical solution of a fractional diffusion equation. The fractional diffusion equation describes a generalization of Brownian motion when the underlying jump sizes and waiting times are given by power laws.

We then move to a study of gyrocenter $\mathbf{E} \times \mathbf{B}$ dispersion in self- consistent gyrokinetic turbulence with zonal flows in the nonlinear phase of a density gradient-driven instability. Using a recently benchmarked particle-in-cell code called GSP, we carefully examine the gyrocenter transport in both the radial and axial directions in a cylindrical slab. For three values of the strength of the density gradient, we find that tracer dispersion in the axial direction, parallel to the shear flow, is superdiffusive. We identify a filtering technique based on axial velocity reversal that splits the population of tracers into "flights" and "non-flights." We find that for three values of the density gradient, spanning three orders of magnitude in the saturated value of the particle flux, the dispersion of tracer particles is diffusive. This diffusive behavior is in agreement with some published work and in disagreement with others (as discussed in Chapter 5). The test-particle diffusion coefficient, D_{part}, s consistently lower than the Fick's law estimate of the diffusion coefficient, D_{flux}, from the saturated flux for each value of the gradient, with a scaling factor of order unity between D_{part} and D_{flux}. We also identify an attenuation of radial dispersion with

increasing gyroradius, regardless of the strength of the density gradient, consistent with the smoothing effect of the gyroaverage operator, and comparable to other published results.

The remainder of this introductory chapter introduces key concepts in nondiffusive transport, tracer tracking methods and a generalized description of particle dispersion. Our goal here is to provide a context for the results presented in Chapters 3 and 4.

1.1 Nondiffusive turbulent transport in fusion devices

In the presence of a density or temperature gradient, respectively, particles or heat may be transported by two basic mechanisms. Collisions (described by a Fokker-Planck term in a kinetic equation [22]) induce diffusion of particles or heat from high concentration to low concentration. This is the mechanism of the collisional transport channel, which includes the regimes of classical and neoclassical transport in tokamaks. If the gradient triggers an instability in the plasma or fluid medium, a state of turbulence may be induced. If the turbulence level is significant, it may open the corresponding channel of turbulent transport. One could describe both types of transport by microscopic dispersion, characterized by the spread of a scalar quantity,

$$\sigma^2(t) = D_{coll}t + \sigma^2(t)_{turb} \tag{1.1}$$

where $\sigma^2(t)$ is the variance of the concentration of an initially localized peak. The first term on the right-hand side of Equation 1.1 is the collisional term, assumed to

be diffusive and characterized by a diffusion coefficient (or diffusivity) D_{coll}. The second term is the dispersion due to a turbulent velocity field, which could obey a nondiffusive law: $\sigma^2(t) = D_{part}t^\gamma$. This will provide our basic definition of non-diffusive dispersion: $\gamma \neq 1$. When the turbulence has a well-defined correlation length, l_c, and well-defined correlation time, t_c, a mixing length [23] estimate for the turbulent transport will give an estimate for the scaling of the diffusion coefficient, $D_{part} = D_0 l_c^2/t_c$, where D_0 is a dimensionless scale factor.

The space-averaged (indicated by $\langle\cdot\rangle$, radial, ion flux in a turbulent plasma, ignoring collisions and using the second moment of the kinetic equation, is [24]

$$\langle n\mathbf{u}\rangle \cdot \hat{r} = \frac{1}{\Omega_{0,i}} \left\langle n\left(\hat{b} \times ((\mathbf{u}\cdot\nabla)\mathbf{u})\right) + \frac{1}{m_i}\left(\hat{b}\times\nabla\cdot\pi\right)\right\rangle \cdot \hat{r} + \langle n\mathbf{v}_{\mathbf{E}\times\mathbf{B}}\rangle \cdot \hat{r} \qquad (1.2)$$

where particle density $n = \int f d^3\mathbf{v}$, $\mathbf{u} = \frac{1}{n}\int d^3v f\mathbf{v}$, $\Omega_{0,i}$ is the cyclotron frequency, m_i is the mass, $\hat{b}$ is the magnetic field direction, $\mathbf{B}$ is the magnetic field vector and π is the off-diagonal part of the pressure tensor. This can be written as $\langle\Gamma_p\rangle = \langle\Gamma_p\rangle_s + \langle\Gamma_p\rangle_E$, where the first term on the right-hand side is the Reynolds stress generated flux and the second term is the flux due to phase matching between the density and the $\mathbf{v}_{\mathbf{E}\times\mathbf{B}} = \frac{c\mathbf{E}\times\hat{b}}{B}$ velocity. The turbulent flux can be split into a diffusive and convective part: $\langle\Gamma_p\rangle_s = -D\frac{\partial n}{\partial r} + V_p n$. The three parts of the particle flux (two turbulent parts and $\mathbf{E}\times\mathbf{B}$) are sometimes combined into a single $D_{flux}\frac{\partial n}{\partial r}$ and D_{flux} is treated as a transport coefficient, sometimes with a space and time dependence. This is a macroscopically averaged view of transport that incorporates the turbulence through phase matching between velocity and density fluctuations. We will present, in Chapter 3, an alternative framework for understanding transport

from a microscopic perspective that includes nondiffusive effects through the use of integro- differential operators.

A common way to derive a diffusion equation is to consider the equations of conservation of mass and Fick's law relating the flux to the gradient for a one-dimensional concentration density $F(x,t)$:

$$\begin{aligned}\frac{\partial F}{\partial t}+\frac{\partial \Gamma}{\partial x} =& 0\\ \Gamma =& -D_{flux}(x,t)\frac{\partial F}{\partial x} \Rightarrow\\ \partial_t F =& \frac{\partial}{\partial x}\left(D_{flux}(x,t)\frac{\partial F}{\partial x}\right)\end{aligned}$$

It is not clear whether D_{flux} and D_{part} should ever be equivalent. For Hasegawa-Wakatani turbulence, it has been shown theoretically and numerically that the two quantities are comparable [25].

Einstein's 1905 explanation of Brownian motion [26] gives the classical, neutral-fluid, diffusion coefficient $D_{sphere}=\frac{k_B T}{6\pi\eta_v\sigma_s}$ for a sphere of cross-section σ_s subject to viscosity η_v at temperature T, where k_B is Boltzmann's constant. Much of the work in explaining certain anomalous measurements for transport in plasmas has focused on finding an analogous result for the proper parameterization of the collisional and turbulent diffusion coefficients. In general, the details of a transport process should depend on the details of the turbulent structures in a flow. Simple descriptions such as the mixing length characterization of a turbulent process in terms of a typical eddy size ignore the details of the eddy shapes and the broad distribution of length scales that may be relevant.

Turbulent plasmas, both in astrophysical and laboratory contexts, may not be

consistent with these assumptions because the turbulence-induced part of the transport may be anisotropic and dependent on multiple scales. It is therefore necessary to investigate whether diffusive models for plasma heat and particle transport are sufficient for the spatial and temporal scales of interest. Early work in turbulent diffusion in plasmas concluded [27] that the electron transport in a stochastic magnetic field could be described by subdiffusion ($\langle\langle(\Delta r)^2\rangle = D\sqrt{\chi_\parallel t}$) when there are no trajectory deviations from magnetic field lines and by diffusion when particles can break free from field lines. These results were derived by examining destroyed magnetic flux surfaces, rather than the stochastic $\mathbf{E}\times\mathbf{B}$ drift dispersion studied in this thesis.

Nondiffusive transport may also be manifest in intermittent phenomena, such as sawteeth disruptions or edge-localized modes [28]. Bursts of transport on top of a fairly quiescent baseline often give a distribution of flux events with long, non-Gaussian tails. This is one reason for the use of the term "non-Gaussian" to describe intermittent events. Attempts have been made by Diamond and Hahm [29] and Carreras *et al* [10] to apply the ideas of self-organized criticality and avalanche theory to explain these phenomena. These attempts have been met with skepticism by Krommes [30]. Another area in which a generalization of the diffusive model has been examined is in the stochastic magnetic field of a reversed-field pinch [31, 32]. This computational work used a collisional tracer particle code in a magnetohydrodynamic (MHD) simulation of the Reversed-Field Experiment (RFX) plasma. The results show that long waiting times between flights of the untrapped particles lead to subdiffusive behavior for that fraction of particles. This analysis prompted a con-

sideration of continuous-time random walk models as a complementary alternative to fractional diffusion equations. The stochastic behavior considered in this thesis is due to the turbulent structures present in the $\mathbf{E} \times \mathbf{B}$ drift patterns. We examine situations where this turbulence leads to superdiffusive or ballistic transport parallel to a shear flow and diffusive transport perpendicular to the shear flow.

1.2 Lagrangian tracers for tracking gyrocenter displacements

Instead of examining only the box-averaged ($\langle\cdot\rangle$) flux $\langle\Gamma_p(x,t)\rangle = \langle n(x,t)v(x,t)\rangle$ of density transport, we seek to understand the dispersion of an ensemble of tracer particles subject to a gyroaveraged $\mathbf{E} \times \mathbf{B}$ drift. This is similar to passive scalar or passive tracer transport that is a common technique in fluid turbulence simulations and experiments. Studies of tracer and passive scalar tracking in fluids and plasmas include twisted pipe flow [33], temporally irregular flows [34] and Kolmogorov-Arnold-Moser (KAM) island chains [35, 36]. Diffusion coefficients in plasmas have been studied in lower hybrid waves [37] and propagating electrostatic waves [38]. The perspective of these works helps inform the study of gyrocenter transport in the stochastic Hamiltonian (analogous to KAM chains) and gyrokinetic turbulence in this thesis.

As we study the dispersion of particles, we are focusing on the spread of a clump from a localized starting position. This is much different than measuring the average flux of particles or heat through a relatively large region of the plasma. This sort of analysis is relevant to the dispersion of impurities or the ablation of an

injected pellet [39]. A straightforward technique is to use an ensemble of Lagrangian marker particles that follow the instantaneous velocities given by the equations of the flow. The displacements, $\delta x = x(t) - x(0)$, of these particles along the x-axis are measured at regular intervals and sorted into a histogram which contains information about the effect of the flow. This histogram, once normalized, is called the probability distribution function (PDF), $P(\delta x)$, for displacements. The moments of the PDF can be used to determine the average position of an ensemble of tracers, $\mu(t) \equiv \langle \delta x(t) \rangle$, the variance of a distribution of an ensemble of tracers, $\sigma^2(t) \equiv \langle (\delta x(t) - \langle \delta x(t) \rangle)^2 \rangle$, and higher-order moments such as the skew and kurtosis (defined in Chapter 4).

Tracers in the Hasegawa-Mima [40] and Hasegawa-Wakatani [41] equations have been used extensively to study nondiffusive transport [42, 43, 44, 45, 46, 47] in two-dimensional plasmas with finite Larmor radius (FLR) effects. Useful analogies have been drawn with geophysical flows [42] governed by the Charney equation, which is mathematically identical to the Hasegawa-Mima equation, but with the Coriolis force taking the place of a plasma density gradient. Hasegawa-Mima equation studies of tracer spreading perpendicular to the density gradient and the magnetic field found that interplay between the linear and nonlinear terms of the equation can affect γ, such that $\sigma^2(t) \sim t^\gamma$ [48]. The most anisotropic cases, those with the largest density gradient, showed persistent superdiffusive behavior. It was also shown that increasing the Larmor radius to the scale of the turbulent eddies will decrease the value of the effective diffusion coefficient. Hasegawa-Wakatani tracer studies showed that superdiffusive transport can arise, but will turn over to diffusive

transport after the characteristic particle trapping time [46].

Tracer particles, interpreted as energetic ions, have also been used to study transport in two-dimensional and three-dimensional fields obtained from continuum (pseudo-spectral) gyrokinetic simulations [49, 13, 50, 51]. These recent studies have found a temporary regime of subdiffusive radial transport of tracers in ion temperature gradient turbulence (as measured by $\sigma^2(t) \sim t^\gamma$, $\gamma < 1$). The variance converges to diffusive after $\sim 10L_\perp/c_s$ where $L_\perp$ is the scale length of the temperature profile and $c_s = \sqrt{(}T_e/m_i)$ is the ion acoustic velocity [49]. Other tokamak tracer ion studies include a gyrokinetic core ion-temperature gradient simulation with marker particles in a particle-in-cell (PIC) code [14] and an "L-mode" simulation with a two-fluid code at a timescale between the Alfvén time and the resistive time [52]. The PIC and two-fluid studies have focused on finding the exponents to characterize the nondiffusive process.

1.3 Generalization of diffusion equation for particle dispersion

Dispersion of tracer particles, e.g. in the $\hat{r}$ radial direction, is characterized by the variance $\sigma_r^2(t) = \langle(\delta r(t) - \langle\delta r(t)\rangle)^2\rangle$ of tracer displacements $\delta r(t) = r(t) - r(t_0)$. For diffusive transport, by definition, the distribution of step sizes for the random walk is given by a Gaussian distribution, and the waiting times between steps are given by a Poisson distribution. This leads to a linear scaling in the variance, such that $\sigma^2 \sim t$. If transport is nondiffusive, the distributions of step sizes and waiting times are not given by the Gaussian and Poisson distributions. If the jump

length and waiting time random variables are given by power laws, the scaling in the variance is $\sigma^2(t) \sim t^\gamma$, where $\gamma < 1$ indicates subdiffusive transport and $\gamma > 1$ indicates superdiffusive transport. For the study in this thesis of dispersion of gyrocenters in a sheared-velocity flow, one expects to have superdiffusive transport along the shear direction and subdiffusive transport perpendicular to the shear. Determining the details of how nondiffusive tracer transport depends on the details of the inhomogeneous turbulence and the finite Larmor radius effects is the principal content of the results presented here.

Much of the work in the recent wave of interest in "non-local" plasma transport in fusion physics may have been inspired by experiments with cold pulses [53, 54]. These experiments showed that a cold region at the edge of a tokamak propagates inward much faster than expected by a diffusion equation. Several theories have been developed to explain these observations [55]. One framework comes from the mathematics of fractional calculus applied to transport equations, often called fractional diffusion equations (FDE). Fractional calculus has been used to study many problems in physics [56, 57, 58]. In plasma turbulence, it has been used to study tracer transport statistics in a fluid model of a pressure-gradient driven instability [12]. Also, cold pulse experiments have been duplicated at JET recently [59], and these results have been modeled with fractional diffusion equations [60]. These models may distinguish between local, critical-gradient transport models and the non-local phenomenology of the fractional diffusion equation, which can be derived from a continuous-time random walk.

A continuous-time random walk is a framework for describing a general trans-

port process in which the dynamics are specified by probability distributions of jump lengths and waiting times. When the process is purely collisional, the one-dimensional jump length distribution, $\eta(x)$, after an appropriate equilibration/relaxation time is given by a Gaussian distribution, $\eta(x) \sim \exp(x^2/\sigma^2)$. This gives the flight lengths a typical scale, σ, and reduces the probability of jumps larger than three σ to less than one percent. The distribution of waiting times in a collisional process is given by a Poisson distribution, $\psi(t) \sim \exp(-\mu t)$, where μ is the inverse of a characteristic waiting time.

The Gaussian jump lengths and Poisson waiting times lead directly to a diffusion equation when these distributions are inserted into the appropriate general equation, as described in Chapter 2. If instead the flight lengths and waiting times are given by power law distributions (with no characteristic scale), the generalized equation leads to a fractional diffusion equation, written in compact notation (described in Chapter 2) as $\frac{d^\beta}{dt^\beta}P(x,t) = D_f \frac{d^\alpha}{dx^\alpha}P(x,t)$. Here, α and β are characteristic exponents of the FDE which are related to the exponents of the power laws determining jump lengths and waiting times of particles. Also, $P(x,t)$ is a probability distribution function, dependent on time, and D_f is an effective "diffusion coefficient." In the case where $\alpha = 2$ and $\beta = 1$, we recover the familiar diffusion equation.

For other α and β, the transport is either superdiffusive or subdiffusive, since long flights and short waiting times will lead to faster spreading, and short flights with long waiting times will lead to slower spreading of particles. Any transport not described by the diffusion equation is often called "anomalous transport" or

"strange kinetics" in the literature of stochastic processes [61, 58, 62]. Anomalous transport in plasmas, however, refers to the anomalously fast transport of heat observed in experiments as compared to the expectations of neoclassical theory. Therefore, we will use the terms nondiffusive or non-Gaussian, where nondiffusive means $\sigma^2(t) \sim t^\gamma : \gamma \neq 1$, and non-Gaussian means that the distribution of jump lengths and waiting times are not Gaussian and Poisson.

1.4 Outline

The remainder of this thesis comprises four more chapters. Chapter 2 defines and derives the necessary plasma turbulence models, the continuous time random walk framework, and the simulation tools. Chapter 3 is a self-contained and previously published study of gyrocenter drift tracer dispersion in a prescribed flow. Chapter 4 contains new results from ion gyrocenter dispersion in self-consistent gyrokinetic turbulence. Chapter 5 summarizes the results of the thesis and compares them with recently published work from other sources.

Chapter 2

Theory and simulation tools for the statistics of gyrocenter dispersion

A wide variety of flow models have been used to study ensembles of Lagrangian trajectories in time-dependent velocity fields. Here we are considering the use of $\phi(x, y, z, t)$, an electrostatic potential, as the input for the $\mathbf{E} \times \mathbf{B}$ drift equations of motion of gyrocenters, where

$$\langle v_{\mathbf{E}\times\mathbf{B}} \rangle_R = \hat{z} \times c\nabla \langle \phi \rangle / B \tag{2.1}$$

is the gyroaveraged drift velocity and c is speed of light. The gyroaveraging operator is described in Section 2.1.5. More generally, one may track particles in a three-dimensional velocity field, possibly using the full equation of motion from the Lorentz force law, explicitly including the gyration about the magnetic field lines. When the magnetic field lines are curved and have spatial dependence orthogonal to the direction of the magnetic field, the curvature and $\nabla\mathbf{B}$ drift velocities may be included by adding these drift velocities explicitly, as will be described below.

The electrostatic potential can be determined in two ways for the purposes of this thesis. First, it might be constructed from a known functional form. This construction may be a spectrum of sinusoidal oscillations approximating turbulence [38, 63, 49], or a simplification of a fluid or kinetic equation. When studying a specific feature of a velocity field, such as a shear flow or a collection of vortices, the feature can be inserted into the model, as in Chapter 2 of this thesis. Alternatively,

the potential may be constructed by solving a self-consistent system of differential equations, such as the Vlasov-Poisson system for fully kinetic dynamics. A self-consistent technique has the advantage of being more realistic, but is typically more computationally expensive and more difficult to characterize, given the presence of multiple competing effects on particle transport.

The procedure for particle pushing is the following. A turbulent (self-consistent) or quasi-turbulent (prescribed) velocity field is defined at successive times for all points in space or on a spatial grid. Probe particles are introduced into this Eulerian velocity field and moved from initial positions, $\mathbf{r}(t_0)$, according to the drift velocity. Particle positions, $\mathbf{r}(t)$, are computed and stored for statistical analysis. The drift velocity may be gyroaveraged, which means that the trajectories are those of gyrocenters. The details of the gyroaveraging operation will be described in this chapter and in Chapter 3. Here, let us note the distinction between using tracer particles versus using self-consistent particles. Tracer particles are displaced by the flow, but are unable to affect the structure of the flow. This situation may arise when the particles have negligible density. Such tracers are widely used in both experiment and simulation to characterize complex flows. In a kinetic simulation of turbulence it may be more convenient to use self-consistent kinetic particles as Lagrangian probes of the flow. The trajectories of self-consistent probes should be indistinguishable from tracers.

A study of turbulent transport would be uninteresting if the turbulent flow were purely isotropic and homogenous. With no preferred direction and a quickly decaying correlation time, dispersion should become diffusive after a short ballis-

tic transient. More interesting scenarios involve a preferred direction induced by a gradient in the system, which could create instabilities associated with wavelike structures or intermittent blob-like structures. These structures might persist, introducing longer correlation times and the possibility of nondiffusive transport. A detailed discussion of nondiffusive transport in this sense may be found in Chapter 3. For now, let us define nondiffusive transport as the dispersion of an ensemble of tracer particles with a variance (second moment of the distribution) that is not linearly dependent on time.

When choosing a flow model for testing whether nondiffusive transport is significant, it is necessary to balance tractability with realism. In the context of confined fusion plasmas, we are interested in the behavior of particle transport near transport barriers [64]. Transport barriers likely have strongly sheared flows like zonal flows observed in gyrokinetic simulations [65, 66, 67]. In this work, we select two models for sheared velocity flows. The first is a simplification of the Hasegawa-Mima equation in which the shear flow is specifically chosen as the background velocity field. Within this model we study the transport of tracer particles parallel to the direction of the shear flow, perpendicular to the density gradient. For a more realistic model, we use a numerical simulation of the gyrokinetic equations for a entropy mode turbulence in a strongly magnetized plasma Z-pinch plasma with $k_{\|} = 0$ [1].

The hierarchy of models for Lagrangian tracer probing of plasma and/or neutral fluid turbulence, from most complex to the simplest is summarized in the following chart.

Vlasov-Fokker-Planck ⇒ 3D gyrokinetic ⇒ 2D gyrokinetic ⇒ Hasegawa-Wakatani ⇒ Hasegawa-Mima ⇒ neutral modes of Hasegawa-Mima ⇒ random phase sinusoids

Qualitative similarities exist between many of these models. The modes of the Hasegawa-Mima equation may be chosen to mimic shear flows that exist in turbulence simulations. A full Fokker-Planck simulation is rarely necessary for simulating tokamak microturbulence because the gyrofrequency is much faster than the turbulent dynamics. For a given study, it is important to choose the simplest model necessary to understand the effect in question.

In this thesis, we will start from the Vlasov-Fokker-Planck equations for a multispecies plasma which, upon coupling with Maxwell's equations, constitute a complete model for the plasma dynamics. Assuming $\beta \ll 1$, and using the ordering parameter $\epsilon = \omega/\Omega_0 \sim \rho_i/L \ll 1$, where ω is the frequency of the turbulence, Ω_0 is the ion cyclotron frequency, ρ_i is the ion Larmor radius and L is the outer scale, or system size, we will use the fact that the gyration frequency of particles around the magnetic field is very fast compared to the frequencies of the turbulence in which we are interested. This yields the gyrokinetic equation. We will derive the gyrokinetic equation in a form appropriate for the application in this thesis. Finally, we will see how the gyrokinetic equation can be simplified to the Hasegawa-Mima equation, which can then be used to create streamfunctions with the proper mix of structures (free-streaming and trapping regions) to produce nondiffusive transport.

2.1 Fokker-Planck to gyrokinetic equation

The Klimontovich equation is an elementary description of the evolution of the density of a set of linearly superimposed points in phase space under the influence of a force [68]. If the force law depends on the positions and velocities of the particles, the equation is nontrivially self-consistent and may exhibit interesting nonlinear effects. In itself, this description is exactly appropriate for studying the character, whether diffusive or nondiffusive, of dispersion caused by a particular applied force. However, the full Klimontovich description, including all particle couplings and physics at all scales of space and time is intractable and hopefully unnecessary for understanding many phenomena. When the governing force is electromagnetic and particle discreteness can be ignored (small plasma parameter $\Lambda = 4\pi n\lambda_D^3$ where n is the plasma density and λ_D^3 is the Debye length), the Boltzmann equation can be derived as a limit of the Klimontovich equation. A simplification of the Boltzmann equation, for use when the dynamics of interest occur on a timescale much larger than the gyroperiod is called the gyrokinetic equation.

The starting point for this derivation is the Vlasov-Fokker-Planck or Boltzmann equation describing the evolution of a phase-space distribution function $f(\mathbf{r}, \mathbf{v})$ for each plasma species. Equations for ions and electrons can be derived using the small mass ratio m_e/m_i as a subsidiary ordering. Here, the focus will be on the ion species; therefore, species indices will be dropped in the following:

$$\frac{\partial f}{\partial t} + \mathbf{v} \cdot \frac{\partial f}{\partial \mathbf{r}} + \frac{q}{m}\left(\mathbf{E} + \frac{(\mathbf{v} \times \mathbf{B})}{c}\right) \cdot \frac{\partial f}{\partial \mathbf{v}} = C(f, f). \tag{2.2}$$

The phase space coordinates and velocities are given by $\mathbf{r}$ and $\mathbf{v}$, charge by q, mass

by m, electric and magnetic fields by $\mathbf{E}$ and $\mathbf{B}$. A collision operator $C(f, f)$ is included for completeness.

2.1.1 Separation of scales and ordering assumptions

In principle, one could simply perform a direct numerical simulation of the full ion distribution function in six-dimensional phase space, subject to the full velocity space collision operator and coupled into Maxwell's equations for $\mathbf{E}$ and $\mathbf{B}$. This technique would be prohibitively expensive for obtaining the dynamics of a realistically-sized system for an experimentally relevant timescale. Instead, the standard practice is to capitalize on natural separations of scales that arise from various processes in this equation. For a magnetized plasma, one such technique exploits the smallness of the ρ-scale turbulence compared to the size of the system being studied (L) such that:

$$\frac{\rho}{L} \equiv \epsilon \ll 1. \tag{2.3}$$

We will use ϵ as the small parameter for ordering Equation 2.2 in the following. This derivation of the slab gyrokinetic equation closely follows recent expositions [17, 18] and the detailed notes contained in [69, 70, 71, 72], The first complete derivation of the linear equation is found in Antonsen and Lane [15]. The nonlinear equations were first derived by Frieman and Chen [16]. Fundamental to the gyrokinetic approach is the requirement that the ion cyclotron frequency, $\Omega_{0,i} = \frac{q_i B}{m_i c}$, is large compared to the frequency of the turbulence, ω, such that:

$$\omega \sim \frac{v_{th}}{L} \sim \mathcal{O}(\epsilon \Omega_{0,i}). \tag{2.4}$$

Here, $v_{th} = \sqrt{T/m}$ where T is the temperature in units of Boltzmann's constant. This first order turbulent frequency is taken to be fast again compared to the slower transport time scale, $1/\tau$ over which the background may evolve:

$$\frac{1}{\tau} \sim \mathcal{O}(\epsilon^2 \omega). \tag{2.5}$$

The expansions are thus:

$$f = F_0 + \epsilon F_0 + \cdots = F_0 + \delta f_1 + \delta f_2 + \cdots$$

$$\mathbf{B} = \mathbf{B}_0 + \epsilon \mathbf{B} + \cdots = \mathbf{B}_0 + \delta \mathbf{B_1} + \cdots$$

$$\mathbf{E} = \mathbf{E}_0 + \delta \mathbf{E}.$$

Here, $\mathbf{E}_0 = 0$, and the $\mathbf{E} \times \mathbf{B}$ velocity is then small compared to v_{th}:

$$\frac{c|\delta \mathbf{E}|}{|B|} \sim \mathcal{O}(\epsilon) v_{th}. \tag{2.6}$$

The equation required for our results is electrostatic, so we will assume $\frac{\partial \mathbf{A}}{\partial t} \equiv 0$ in the following. We can write the fields in the potential formulation, for the electrostatic case, simply as:

$$\mathbf{E} = -\nabla \phi; \quad \mathbf{B_0} = \nabla \times \mathbf{A_0}. \tag{2.7}$$

The usual gyrokinetic theory also uses the ϵ parameter to separate parallel and perpendicular directions. The background quantities are allowed to vary slowly in space:

$$\nabla [F_0, B_0] \sim \mathcal{O}(1/L)[F_0, B_0]. \tag{2.8}$$

For perturbed quantities, parallel wavelengths are on the order of the system size:

$$\nabla_{\parallel} [\delta f_1, \delta B, \delta E] \sim \mathcal{O}(1/L)[\delta f_1, \delta B, \delta E] \tag{2.9}$$

and perpendicular wavelengths are on the order of the Larmor radius:

$$\nabla_\perp[\delta f_1, \delta B, \delta E] \sim \mathcal{O}(1/\rho)[\delta f_1, \delta B, \delta E]. \tag{2.10}$$

The cross-field inhomogeneity implies:

$$\frac{k_\parallel}{k_\perp} \sim \frac{\rho_i}{L} \sim \mathcal{O}(\epsilon). \tag{2.11}$$

Also note that the velocity space derivatives are on the order of the thermal velocity:

$$\frac{\partial f}{\partial v} \sim \mathcal{O}(v_{th}^{-1}). \tag{2.12}$$

Expanding the Fokker-Planck equation in ϵ for the electrostatic limit gives

$$\begin{aligned}
&\frac{\partial F_0}{\partial t} + \frac{\partial \delta f_1}{\partial t} + \mathbf{v} \cdot \frac{\partial F_0}{\partial \mathbf{r}} + \mathbf{v}_\perp \cdot \frac{\partial \delta f_1}{\partial \mathbf{r}} + \mathbf{v}_\parallel \cdot \frac{\partial \delta f_1}{\partial \mathbf{r}} \\
&+ \frac{q}{m}\delta\mathbf{E} \cdot \frac{\partial F_0}{\partial \mathbf{v}} + \frac{q}{mc}(\mathbf{v} \times \mathbf{B_0}) \cdot \frac{\partial F_0}{\partial \mathbf{v}} + \frac{q}{mc}(\mathbf{v} \times \delta\mathbf{B}) \cdot \frac{\partial F_0}{\partial \mathbf{v}} \\
&+ \frac{q}{m}\delta\mathbf{E} \cdot \frac{\partial \delta f_1}{\partial \mathbf{v}} + \frac{q}{mc}(\mathbf{v} \times \mathbf{B_0}) \cdot \frac{\partial \delta f_1}{\partial \mathbf{v}} + \frac{q}{mc}(\mathbf{v} \times \delta\mathbf{B}) \cdot \frac{\partial \delta f_1}{\partial \mathbf{v}} \\
&= C(F_0, F_0) + C(F_0, \delta f_1) + C(\delta f_1, F_0) + C(\delta f_1, \delta f_1).
\end{aligned}$$

After applying the ordering assumptions for the space and time derivatives on the equilibrium and perturbed quantities, we can multiply the equation by $L/v_{th}F_0$ to make the ordering more explicit. Also note that $\delta\mathbf{E} \sim \mathcal{O}(\epsilon B_0)$, and $\Omega_0 \equiv \frac{qB_0}{mc}$. Finally, note that the collision operator contributes a factor of order $\nu \sim \mathcal{O}(\omega)$. The following equation shows the ordering assumptions for each term of the gyrokinetic equation.

$$\underbrace{\frac{F_0}{\tau}}_{\epsilon^2} + \underbrace{\delta f_1 \omega}_{\epsilon} + \underbrace{\frac{v_{th} F_0}{L}}_{1} + \underbrace{\frac{v_{th} \delta f_1}{\rho}}_{1} + \underbrace{\frac{v_{th} \delta f_1}{L}}_{\epsilon}$$

$$+ \underbrace{\epsilon \Omega_0 F_0}_{1} + \underbrace{\Omega_0 F_0}_{\epsilon^{-1}} + \underbrace{\epsilon \Omega_0 F_0}_{1} +$$

$$+ \underbrace{\epsilon \Omega_0 \delta f_1}_{\epsilon} + \underbrace{\Omega_0 \delta f_1}_{1} + \underbrace{\epsilon \Omega_0 \delta f_1}_{\epsilon}$$

$$= \underbrace{C(F_0, F_0)}_{1} + \underbrace{C(F_0, \delta f_1)}_{\epsilon} + \underbrace{C(\delta f_1, F_0)}_{\epsilon} + \underbrace{C(\delta f_1, \delta f_1)}_{\epsilon^2}. \tag{2.13}$$

2.1.2 F_0 is independent of the angle of Larmor rotation

The lowest order term in the Fokker-Planck ϵ ordering is

$$\frac{q}{mc} \mathbf{v} \times \mathbf{B}_0 \cdot \frac{\partial F_0}{\partial \mathbf{v}}. \tag{2.14}$$

Let us take $\mathbf{B}_0 = B_0 \hat{z}$, and then work from cylindrical coordinates in velocity space as shown in Figure 2.1

Now we can use the cylindrical coordinates:

$$\begin{aligned}
\frac{q}{mc} \mathbf{v} \times \mathbf{B}_0 \cdot \frac{\partial F_0}{\partial \mathbf{v}} &= \frac{q}{mc} \begin{vmatrix} \widehat{x} & \widehat{y} & \widehat{z} \\ v_\perp \cos(\theta) & v_\perp \sin(\theta) & v_\parallel \\ 0 & 0 & B_0 \end{vmatrix} \cdot \frac{\partial F_0}{\partial \mathbf{v}} \\
&= \frac{q B_0}{mc} v_\perp (\cos(\theta) \widehat{x} - \sin(\theta) \widehat{y}) \cdot \frac{\partial F_0}{\partial \mathbf{v}} \\
&= \frac{q B_0}{mc} v_\perp \widehat{\theta} \cdot \frac{\partial F_0}{\partial \mathbf{v}} \\
&= -\Omega_0 v_\perp \frac{\partial F_0}{\partial \theta} = 0.
\end{aligned}$$

We see that $F_0 = F_0(\mathbf{r}, v_\parallel, v_\perp, t)$ must be independent of θ for $v_\perp \neq 0$.

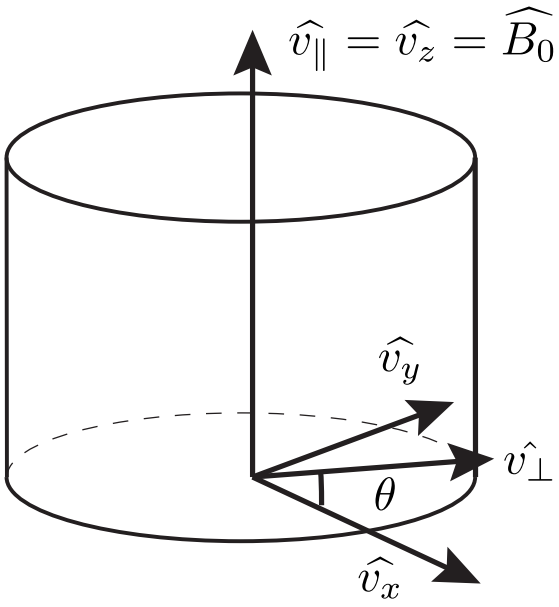

Figure 2.1: Coordinates for cylindrical velocity space, with the magnetic field aligned on the axis.

2.1.3 F_0 is a Maxwellian in velocity space

Taking the terms of Equation 2.13 at $\mathcal{O}(1)$, we have

$$\mathbf{v}\cdot\frac{\partial F_0}{\partial \mathbf{r}}+\mathbf{v}_\perp\cdot\frac{\partial \delta f_1}{\partial \mathbf{r}}+\frac{q}{m}\left(\delta\mathbf{E}+\frac{(\mathbf{v}\times\mathbf{B_0})}{c}\cdot\frac{\partial F_0}{\partial \mathbf{v}}+\frac{(\mathbf{v}\times\mathbf{B_0})}{c}\cdot\frac{\partial \delta f_1}{\partial \mathbf{v}}\right)=C(F_0,F_0)$$
$$\mathbf{v}\cdot\frac{\partial F_0}{\partial \mathbf{r}}+\mathbf{v}_\perp\cdot\frac{\partial \delta f_1}{\partial \mathbf{r}}+\frac{q}{m}\left(\delta\mathbf{E}+\frac{(\mathbf{v}\times\delta\mathbf{B})}{c}\right)\cdot\frac{\partial F_0}{\partial \mathbf{v}}-\Omega_0\frac{\partial \delta f_1}{\partial\theta}=C(F_0,F_0). \tag{2.15}$$

Before obtaining an equation for δf_1, it can be shown that F_0 is a Maxwellian. To show this, first integrate the entire equation over $\int\int\int dxdydz$ and assume periodic boundary conditions. Upon integrating by parts and noting that $\delta\mathbf{E}+\frac{(\mathbf{v}\times\delta\mathbf{B})}{c}$ is divergence free in velocity space, one can reduce the equation to:

$$\mathbf{v}\cdot\frac{\partial F_0}{\partial \mathbf{r}}-\Omega_0\frac{\partial \delta f_1}{\partial\theta}=C(F_0,F_0). \tag{2.16}$$

This equation can then be multiplied by $(1+\ln F_0)$ and integrated over velocity space. The only surviving term, assuming $\hat{b}\cdot\nabla F_0=0$ is

$$\int d^3r\int d^3v C(F_0,F_0)\ln F_0=0, \tag{2.17}$$

which implies, through the use of Boltzmann's H-theorem, that entropy is conserved and F_0 is therefore a Maxwellian:

$$F_0=F_M=\frac{n_0(\mathbf{r})}{\pi^{3/2}v_{th}^3}\exp(-v^2/2v_{th}^2) \tag{2.18}$$

where n_0 is the background density.

2.1.4 Homogeneous and particular solutions for δf_1

Using the Maxwellian form for F_0, which eliminates the collision operator, the $\mathcal{O}(1)$ equation may be rewritten as

$$\mathbf{v}_\perp \cdot \nabla_\perp \delta f_1 - \Omega_0 \frac{\partial \delta f_1}{\partial \theta} = -\mathbf{v}_\perp \cdot \nabla_\perp \left(\frac{q\phi}{T}\right) F_0 - \mathbf{v} \cdot \nabla F_0 \tag{2.19}$$

where T is the temperature from the Maxwellian and the parallel dependence of ϕ is neglected at this order. Now it is useful to change coordinates using the so-called Catto transformation to the frame of the gyrocenter position:

$$\mathbf{R} = \mathbf{r} + \frac{\mathbf{v} \times \hat{B}_0}{\Omega_0} = \mathbf{r} + \frac{v_\perp}{\Omega_c} \left(\hat{x} \sin(\Omega_c t) + \hat{y} \cos(\Omega_c t)\right) \tag{2.20}$$

with gyroradius vector $\vec{\rho} = \widehat{B_0} \times \mathbf{v}/\Omega_0$. This change of variables with respect to the locally circular gyroradius (see Figure 2.2) implies that

$$\left(\frac{\partial}{\partial \theta}\right)_{\mathbf{r}} = \left(\frac{\partial}{\partial \theta}\right)_{\mathbf{R}} + \left(\frac{\partial \mathbf{R}}{\partial \theta}\right)_{\mathbf{r}} \cdot \left(\frac{\partial}{\partial \mathbf{R}}\right)_{\theta} = \left(\frac{\partial}{\partial \theta}\right)_{\mathbf{R}} + \frac{\mathbf{v}_\perp}{\Omega_0} \cdot \frac{\partial}{\partial \mathbf{r}}. \tag{2.21}$$

The gyroangle, or phase angle of the Larmor rotation, is θ. Now one may rewrite Equation 2.19 as

$$\mathbf{v} \cdot \nabla F_0 + \mathbf{v}_\perp \cdot \nabla_\perp (\frac{q\phi}{T}) F_0 = \Omega_0 \left(\frac{\partial \delta f_1}{\partial \theta}\right)_R. \tag{2.22}$$

Solutions of this differential equation for δf_1 have homogeneous and particular parts. The homogenous part of the equation is

$$\left(\frac{\partial h}{\partial \theta}\right)_R = 0 \Rightarrow h = h(\mathbf{R}, v_\parallel, v_\perp, t), \tag{2.23}$$

so that this part does not depend on gyroangle, and describes the perturbed part of the distribution function measured at the gyrocenter coordinate.

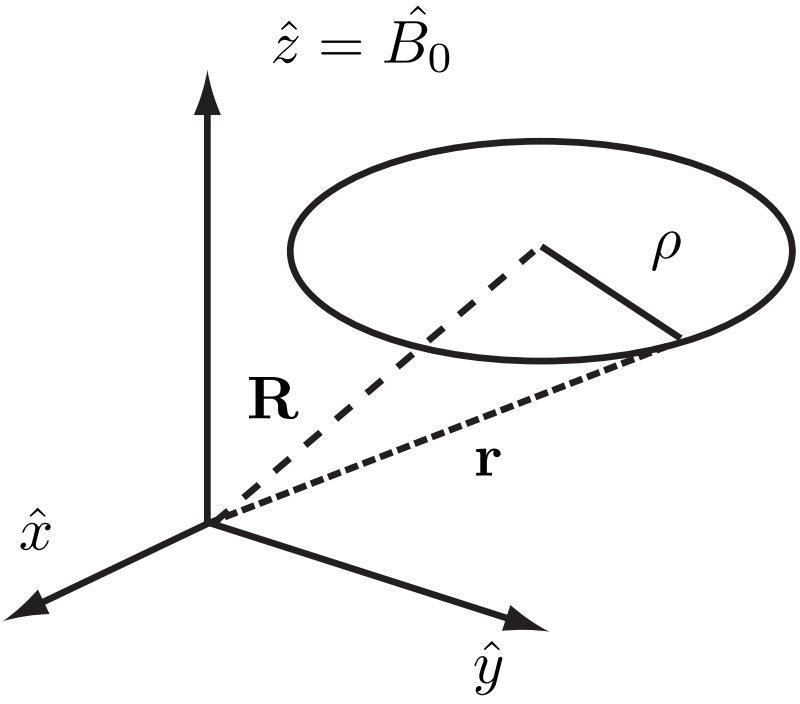

Figure 2.2: Illustration of the Catto transformation, showing the particle position vector $\mathbf{r}$ and the gyrocenter position vector $\mathbf{R}$ relative to the gyroradius vector ρ. The gyroorbit is assumed to be circular, which is exactly accurate when there are no perturbed electric or magnetic fields.

The particular solution comes from separating perpendicular and parallel components of the velocity derivatives in Equation 2.22, and recalling that the Maxwellian is gyrophase independent when applying the Catto transformation:

$$\mathbf{v}_\perp \cdot \nabla_\perp \left(F_0(1 + \frac{q\phi}{T}) \right) + v_\parallel \hat{b} \cdot \nabla F_0 = \Omega_0 \left(\frac{\partial \delta f_1}{\partial \theta} \right)_R$$
$$-\Omega_0 \left(\frac{\partial}{\partial \theta} \right)_R \left(F_0(1 + \frac{q\phi}{T}) \right) + v_\parallel \hat{b} \cdot \nabla F_0 = \Omega_0 \left(\frac{\partial \delta f_1}{\partial \theta} \right)_R .$$

Gyroaveraging this equation shows that $\hat{b} \cdot \nabla F_0 = 0$, so that F_0 is a flux function, constant on a magnetic flux surface.

This result removes the $\nabla_\parallel F_0$ term in Equation 2.22, giving

$$\mathbf{v}_\perp \cdot \nabla_\perp F_0 + \mathbf{v}_\perp \cdot \nabla_\perp (\frac{q\phi}{T}) F_0 = \Omega_0 \left(\frac{\partial \delta f_1}{\partial \theta} \right)_R .$$

This has the particular solution $\delta f_1^p = -\frac{q\phi}{T} F_0$, which can be confirmed by substitution. This piece of the distribution function may be absorbed into the definition of F_0 in gyrocenter coordinates so that

$$F_0(\mathbf{R}) = F_M(\mathbf{R}) \exp(-\frac{q\phi}{T_0}). \tag{2.24}$$

Here, we have used $\exp(-q\phi/T) \sim 1 - q\phi/T$, where $q\phi/T \ll 1$. One may also write the full distribution function as

$$F = F_M - \frac{q\phi}{T} F_M + h(\mathbf{R}) + \delta f_2 + \cdots \tag{2.25}$$

which implies that $\delta f_1 = h - \frac{q\phi}{T} F_M$, and $\langle \delta f_1 \rangle_R = h - \frac{q}{T} \langle \phi \rangle_R F_M$. The gyrokinetic equation in the end can be written in terms of either $\langle \delta f_1 \rangle_R$ or h. Our simulation will be in terms of $\langle \delta f_1 \rangle$.

2.1.5 Convenient gyrokinetic variables and their gyroaverages

Now it is useful to rewrite the Boltzmann equation in terms of the so-called gyrokinetic variables,

$$\mathbf{R} = \mathbf{r} - \frac{\hat{b} \times \mathbf{v}}{\Omega_0}; \quad \mathcal{E} = mv^2/2 + q\phi; \quad \mu = mv_\perp^2/2B_0; \quad \theta; \quad t, \tag{2.26}$$

respectively, the guiding center position, particle energy in the electrostatic field, magnetic moment, gyroangle, time. It is necessary to find the gyroaverage of the time derivatives of these variables for use in the ordered Vlasov-Fokker-Planck equation in the next section.

The gyroaveraging operators are given by two expressions. The first is for a gyroaverage at constant gyrocenter position:

$$\langle \mathcal{A}(\mathbf{r}, \mathbf{v}, t) \rangle_R = \frac{1}{2\pi} \int_0^{2\pi} \mathcal{A}\left(\mathbf{R} - \frac{\hat{b} \times \mathbf{v}}{\Omega_0}, \mathbf{v}, t\right) d\theta \tag{2.27}$$

where θ is the gyroangle. The second gyroaverage is at constant particle position:

$$\langle \mathcal{A}(\mathbf{R}, \mathbf{v}, t) \rangle_r = \frac{1}{2\pi} \int \mathcal{A}\left(\mathbf{r} + \frac{\hat{b} \times \mathbf{v}}{\Omega_0}, \mathbf{v}, t\right) d\theta. \tag{2.28}$$

Now the gyroaverages of the time derivatives of gyrokinetics variables will be examined.

The magnetic moment is conserved to $\mathcal{O}(\epsilon)$:

$$\left\langle \frac{d\mu}{dt} \right\rangle_R = 0 \Rightarrow mv_\perp^2/2B_0 = \text{constant}. \tag{2.29}$$

The time derivative of the gyro-angle is the Larmor frequency, at $\mathcal{O}(\epsilon)$, which is shown by comparing the time derivative of the velocity with the Lorentz force:

$$\left\langle \frac{d\theta}{dt} \right\rangle_R = -\Omega_0 = -\frac{qB_0}{mc}. \tag{2.30}$$

For the Z-pinch geometry, with a curved magnetic field that falls off as $1/r$ pointing out from the axis, the rate of change of the position of gyrocenters, or the gyroaveraged drifts, can be produced (see Appendix B) as:

$$\left\langle \frac{d\mathbf{R}}{dt} \right\rangle_R = \left\langle v_\parallel \hat{b} \right\rangle_R + \frac{q}{m} \left\langle (\delta\mathbf{E} + \frac{\mathbf{v} \times \delta\mathbf{B})}{c} \times \frac{\hat{b}}{\Omega_0} \right\rangle_R + \left\langle \mathbf{v} \times (\mathbf{v} \cdot \nabla(\frac{\hat{b}}{\Omega_0})) \right\rangle_R$$

$$\left\langle \frac{d\mathbf{R}}{dt} \right\rangle_R = \left\langle v_\parallel \hat{b} \right\rangle_R - \nabla_\perp \langle \phi \rangle_R \times \frac{\hat{b}}{B_0} + v_\parallel^2 \frac{\hat{b}}{\Omega_0} \times (\hat{b} \cdot \nabla \hat{b}) + \frac{v_\perp^2}{2} \frac{\hat{b} \times \nabla B_0}{\Omega_O B_0}$$

where the form of the ∇B and curvature drifts are joined in the $\hat{z}$ direction for a Z-pinch, such that

$$\mathbf{v}_B^{tot} = \frac{v_\parallel^2 + v_\perp^2/2}{\Omega_0 R_c} \hat{z} \tag{2.31}$$

in the geometry of the Z-pinch with R_c the radius of curvature. Therefore, the form of the gyrocenter position needed for the electrostatic Z-pinch is:

$$\left\langle \frac{d\mathbf{R}}{dt} \right\rangle_R = v_\parallel \hat{b} - \nabla_\perp \langle \phi \rangle_R \times \frac{\hat{b}}{B_0} + \frac{2v_\parallel^2 + v_\perp^2}{2\Omega_0 R_c} \hat{z}. \tag{2.32}$$

Finally, the energy variable is conveniently reducible after time differentiation and gyroaveraging:

$$\left\langle \frac{d\mathcal{E}}{dt} \right\rangle_R = \left\langle m\mathbf{v} \cdot \left(\frac{q}{m} \left(-\nabla\phi - \frac{1}{c} \frac{\partial \mathbf{A}}{\partial t} \right) + \frac{\mathbf{v} \times \mathbf{B}}{c} \right) + q \frac{\partial \phi}{\partial t} + q\mathbf{v} \cdot \nabla\phi \right\rangle$$

$$\left\langle \frac{d\mathcal{E}}{dt} \right\rangle_R = q \frac{d}{dt} \left(\phi - \mathbf{v} \cdot \mathbf{A} + q\mathbf{v} \cdot (\mathbf{v} \times \mathbf{B}) \right)$$

$$\left\langle \frac{d\mathcal{E}}{dt} \right\rangle_R = q \left(\frac{\partial}{\partial t} \langle \phi \rangle_R \right).$$

Note again that the gyrokinetic turbulence results presented in the following are electrostatic.

2.1.6 The gyrokinetic equation at $\mathcal{O}(\epsilon)$

Rephrasing the Vlasov-Fokker-Planck equation in terms of the gyrokinetic variables will yield the gyrokinetic equation. First, expand the total derivative:

$$\frac{\partial f}{\partial t}+\frac{\partial \mathbf{R}}{\partial t}\cdot\frac{\partial f}{\partial \mathbf{R}}+\frac{\partial \mathcal{E}}{\partial t}\frac{\partial f}{\partial \mathcal{E}}+\frac{\partial \mu}{\partial t}\frac{\partial f}{\partial \mu}+\frac{\partial \theta}{\partial t}\frac{\partial f}{\partial \theta}=\sum_s C(f,f_s). \tag{2.33}$$

The proper ordering of this equation at the turbulent time and space scale, keeping terms of $\mathcal{O}(\epsilon)$ is

$$\frac{\partial h}{\partial t}+\frac{d\mathbf{R}}{dt}\cdot\frac{\partial}{\partial \mathbf{R}}(h+F_0)+\frac{d\mu}{dt}(\frac{\partial h}{\partial \mu})+\frac{\partial \mathcal{E}}{\partial t}(\frac{\partial h}{\partial \mathcal{E}})-C(h)=\Omega_0\frac{\partial \delta f_2}{\partial \Theta}+\frac{1}{T_0}\frac{d\mathcal{E}}{dt}F_0. \tag{2.34}$$

Gyroaveraging this equation gives

$$\frac{\partial h}{\partial t}+\left\langle\frac{d\mathbf{R}}{dt}\right\rangle_R\cdot\frac{\partial}{\partial \mathbf{R}}(h+F_0)+\frac{d\mu}{dt}(\frac{\partial h}{\partial \mu})+\frac{\partial \mathcal{E}}{\partial t}(\frac{\partial h}{\partial \mathcal{E}})=$$
$$\langle C(h)\rangle_R\left\langle\Omega_0\frac{\partial \delta f_2}{\partial \Theta}\right\rangle_R+\frac{1}{T_0}\left\langle\frac{d\mathcal{E}}{dt}\right\rangle_R F_0,$$

which annihilates the δf_2 term, while the constancy of μ removes the third term on the left-hand side. Inserting the useful expressions from the previous subsection gives

$$\frac{\partial h}{\partial t}+\left(v_\parallel\hat{b}-\nabla_\perp\langle\phi\rangle_R\times\frac{\hat{b}}{B_0}+\mathbf{v}_B^{tot}\right)\cdot\frac{\partial}{\partial \mathbf{R}}(h+F_0)=$$
$$\langle C(h)\rangle_R+\frac{q}{T_0}\left(\frac{\partial}{\partial t}\langle\phi\rangle_R\right)F_0\Rightarrow$$
$$\frac{\partial h}{\partial t}+v_\parallel\hat{b}\cdot\nabla h+\left(-\nabla_\perp\langle\phi\rangle_R\times\frac{\hat{b}}{B_0}+\mathbf{v}_B^{tot}\right)\cdot\frac{\partial}{\partial \mathbf{R}}(h+F_0)=$$
$$\langle C(h)\rangle_R+\frac{q}{T_0}\left(\frac{\partial}{\partial t}\langle\phi\rangle_R\right)F_0.$$

The electrostatic h form of the gyrokinetic equation with a Z-pinch magnetic field is:

$$\frac{\partial h}{\partial t} + \left(v_{\parallel} \hat{b} + \langle v_{\mathbf{E}\times\mathbf{B}} \rangle_R + \mathbf{v}_B^{tot} \right) \cdot \nabla h + \mathbf{v}_B^{tot} \cdot \nabla F_0 = \frac{qF_0}{T} \frac{\partial \langle \phi \rangle_R}{\partial t} - \langle v_{\mathbf{E}\times\mathbf{B}} \rangle_R \cdot \nabla F_0 + \langle C(h) \rangle_R . \tag{2.35}$$

The $\delta f = \delta f_1 = h - \frac{q\phi}{T} F_0$ form of the GKE, using $\langle \delta f \rangle_R = h - \frac{q\langle\phi\rangle_R}{T} F_0$ is:

$$\frac{\partial \langle \delta f \rangle_R}{\partial t} + \left(v_{\parallel} \hat{b}_0 + \langle v_{\mathbf{E}\times\mathbf{B}} \rangle_R + \mathbf{v}_B^{tot} \right) \cdot \nabla \langle \delta f \rangle_R = - \langle v_{\mathbf{E}\times\mathbf{B}} \rangle_R \cdot \nabla F_0 - v_{\parallel} \frac{qF_0}{T} (\hat{b} \cdot \nabla \langle \phi \rangle_R) - \mathbf{v}_B^{tot} \cdot \nabla \left(\frac{q \langle \phi \rangle_R}{T} F_0 \right) + \langle C(h) \rangle_R . \tag{2.36}$$

2.1.7 Maxwell's equations to close the system

In general, it is necessary to compute the gyrokinetic limits of (1) Poisson's equation, (2) the parallel part of Ampère's Law and (3) the perpendicular part of Ampère's law. For this application, we will only need Poisson's equation, so the details of the derivation will be presented carefully now. Neglecting the Debye-scale fluctuations in the electrostatic field, we can arrive at quasineutrality, such that:

$$0 = \nabla^2 \phi = \sum_s q_s n_s \tag{2.37}$$

which is a good assumption when studying variations of plasma density on scales much larger than the Debye scale. This can be seen as follows.

In the process of computing the time evolution of the first order perturbation, δf_1, it is necessary to solve for the electrostatic potential, $\phi(\mathbf{x})$, so that the drift

velocities can be computed self-consistently. The Poisson equation for a hydrogenic plasma,

$$-\nabla^2\phi = 4\pi\rho_c = 4\pi(e\delta n_i - e\delta n_e), \tag{2.38}$$

simplifies to $\delta n_e = \delta n_i$ when quasineutrality is valid. The first-order perturbed density $\delta n_{1,s}$ for species s will be called δn_s, and the species index will be hidden unless needed. Here, ρ_c is the total charge density, $\delta n_{e,i}$ are the first-order perturbed electron and ion number densities and e is the unit charge. When δ_f or δ_n are written without specifying the order in ϵ, the quantity should be assumed first order. Quasineutrality is essentially the assumption that the interesting spatial variations in ϕ are larger than the Debye scale. This is seen in the following sequence of steps: $\frac{T_e}{4\pi n_e e^2}\nabla^2(e\phi/T_e) = (\delta n_e - \delta n_i)/n_e$ where temperature is in units of k_B, Boltzmann's constant. Now, it is clear that when $k^2\lambda_D^2 \ll 1$ the left-hand side of the Poisson equation will be negligible, at least to first order. In this case, we take $\delta n_e = \delta n_i$ to be the fundamental relationship for computing ϕ. As shown in the following paragraphs, this gyrokinetic Poisson equation contains ϕ since $\delta n_e = \int d^3v\delta f_e = \int d^3v\delta f_i = \delta n_i$ generally, and δf_s can be expressed in terms of ϕ, as we will see shortly.

Using several assumptions, it is possible to further simplify this equation by using a Boltzmann, or adiabatic, response for the electrons: $\delta n_e = n_e e\phi/T$. Let us examine the assumptions behind the adiabatic response. Starting from the first moment of the collisionless, sourceless electron Vlasov equation for small β (neglecting $\frac{\partial A}{\partial t}$) we may write the parallel component of the electron fluid linear force-balance

as

$$m_e \frac{\partial n_e V_e}{\partial t} + \nabla_\parallel \cdot p_e - e n_e E_\parallel = 0. \tag{2.39}$$

The ∂_t can be neglected if the electron mass is considered small. A more careful analysis shows that $m_e \omega n_e V_{\parallel,e} \ll k_\parallel n_e T_e = k_\parallel n_e m_e v_{th,e}^2 \Rightarrow \omega \ll k_\parallel v_{th,e}$ is the condition needed to eliminate the electron inertia term.

Now, if the electrons can be taken to be isothermal in the parallel direction (true when there are no collisions; see [73]), so that $n_e \nabla_\parallel T_e \ll T_e \nabla_\parallel n_e$, the parallel pressure gradient can be written as $\nabla_\parallel p_e = T_e \nabla_\parallel n_e$. This leads to the following assertion concerning the electron response:

$$\begin{aligned} e n_e E_\parallel + T_e \nabla_\parallel n_e &= 0 \\ e n_e \nabla_\parallel \phi &= T_e \nabla_\parallel n_e \\ e n_e \exp(-e\phi/T_e) \nabla_\parallel \phi &= T_e \exp(-e\phi/T_e) \nabla_\parallel n_e \\ \nabla_\parallel (n_e \exp(-e\phi/T_e)) &= 0 \end{aligned}$$

When $e\phi/T_e$ is small, we can expand the exponential in a Taylor series and put an arbitrary flux function on the right hand side after integrating. Splitting the electron density into mean and perturbed parts, $n_e = n_{0,e} + \delta n_e$ we find that

$$\delta n_e = n_{0,e} e\phi/T_e - n_{0,e} e \left\langle \phi \right\rangle_{fsa} / T_e \tag{2.40}$$

where the flux surface averaged quantity $\left\langle \phi \right\rangle_{fsa}$ varies only in the radial direction.

This simplification for δn_e still requires an expression for the ion density in the gyrokinetic Poisson equation (GKPE). One may express $\delta n_s(\mathbf{R})$, where s is a

species index, with the following:

$$\delta f_s(\mathbf{R}) = h - \frac{q_s\phi}{T_s}F_0 \tag{2.41}$$

$$\langle \delta f_s \rangle_R = h - \frac{q_s \langle \phi \rangle_R}{T_s}F_0 \tag{2.42}$$

so that

$$\delta f_s = \langle \delta f_s \rangle_R + \frac{q_s F_M}{T_s}\left(\langle \phi \rangle_R - \phi\right) \tag{2.43}$$

The details of the calculation for the ion density are presented here in k-space:

$$\delta n_i = \int \left(\langle \langle \delta f_i \rangle_R \rangle_r + \frac{Z_i|e|}{T_i} \left\langle J_0\left(\frac{k_\perp v_{\perp,i}}{\Omega_i}\right)\phi \right\rangle_r F_0 - \frac{Z_i|e|}{T_i}\phi F_0 \right) d^3v$$

$$\delta n_i = \int J_0\left(\frac{k_\perp v_{\perp,i}}{\Omega_i}\right)\langle \delta f_i \rangle_R d^3v + \frac{Z_i|e|}{T_i}\left(\int J_0^2\left(\frac{k_\perp v_{\perp,i}}{\Omega_i}\right) F_0 d^3v - \int F_0\phi d^3v \right)$$

$$\delta n_i = \int J_0\left(\frac{k_\perp v_{\perp,i}}{\Omega_i}\right)\langle \delta f_i \rangle_R d^3v + \frac{n_{0,i}Z_i|e|\phi}{T_i}\Gamma_0\left[\left(\frac{k_\perp v_{\perp,i}}{\Omega_i}\right)^2\right] - \frac{n_{0,i}Z_i|e|\phi}{T_i}$$

$$\delta n_i = \int J_0\left(\frac{k_\perp v_{\perp,i}}{\Omega_i}\right)\langle \delta f_i \rangle_R d^3v + \frac{n_{0,i}Z_i|e|\phi}{T_i}\left(\Gamma_0\left[\left(\frac{k_\perp v_{\perp,i}}{\Omega_i}\right)^2\right] - 1\right)$$

Now we have ϕ in the quasineutrality (Poisson) equation, and we have used the gyroaveraging identities in k-space:

$$\frac{1}{v_{th}^2}\int_0^\infty \exp(-v_\perp^2/2v_{th}^2) J_0^2(k_\perp v_\perp/\Omega) v_\perp dv_\perp F_0 \equiv n_0\Gamma_0(k_\perp^2 v_\perp^2/\Omega^2)$$

$$\langle \delta f \rangle = J_0(k_\perp v_\perp/\Omega)\delta f_k \tag{2.44}$$

where J_0 is the first order Bessel function $\Gamma_0(b) = I_0(b)\exp(-b)$, and I_0 is the modified first order Bessel function.

Therefore, when the gyrokinetic Poisson equation is used for adiabatic elec-

trons and hydrogenic ions:

$$\frac{en_{0,e}}{T_e}\left(\phi - \langle\phi\rangle_{fsa}\right) = \int J_0\left(\frac{k_\perp v_{\perp,i}}{\Omega_i}\right)\langle\delta f_i\rangle_R\, d^3v + \frac{en_{0,i}\phi}{T_i}\left(\Gamma_0\left[\left(\frac{k_\perp v_{\perp,i}}{\Omega_i}\right)^2\right] - 1\right) \Rightarrow$$

$$\phi(k_x, k_y, k_z) = \frac{\int J_0(\frac{k_\perp v_{\perp,i}}{\Omega_i})\langle\delta f_i\rangle_R\, d^3v}{\frac{en_{0,e}}{T_e} + \frac{en_{0,i}}{T_i}\left(1 - \Gamma_0\left[(\frac{k_\perp v_{\perp,i}}{\Omega_i})^2\right]\right)}. \tag{2.45}$$

where we have neglected the flux-surface averaged part of the electron response. If the electrons are not adiabatic, the electron term in the denominator of this ϕ equation may be replaced with a term analogous to the ion term, and an extra electron term is added to the numerator so that the final result for the self-consistent ϕ at position $\mathbf{r}$ at any given time (specified by the state of the distribution function) is

$$\phi(\mathbf{r}) = \sum_k \phi_{\mathbf{k}} \exp(i\mathbf{k}\cdot\mathbf{r})$$

$$\phi_{\mathbf{k}} = \frac{\int v_\perp dv_\perp dv_\parallel \left(Z_i J_0(k_\perp v_\perp/\Omega_i)\langle\delta f_i\rangle_R - J_0(k_\perp v_\perp/\Omega_e)\langle\delta f_e\rangle_R\right)}{e\left(\frac{Z_i n_{0,i}}{T_i}\left(1 - \Gamma_0(k_\perp^2 v_\perp^2/\Omega_i)\right) + \frac{n_{0,e}}{T_e}\left(1 - \Gamma_0(k_\perp^2 v_\perp^2/\Omega_e)\right)\right)}. \tag{2.46}$$

2.2 Hasegawa-Mima as a limit of the gyrokinetic-Poisson system

The Hasegawa-Mima equation was originally derived from the Navier-Stokes equation as a limit accounting for drift waves in a quasineutral plasma with cold ions [40]. It is a single field equation for the electrostatic potential, ϕ. The Hasegawa-Mima equation is perhaps the most basic model for drift waves in a magnetized plasma with an adiabatic electron response. The equation is structurally identical to the Charney equation [74] for oscillations in a planetary atmosphere or any rotating fluid, where the asymmetric term is obtained from the Coriolis force. Many authors have analyzed the nonlinear turbulence produced from direct numerical simulations

of the this equation, including the spectrum of fluctuations and the dual cascade associated with the length scale, $\rho_s = \sqrt{T_e/m_i}$, of the dynamics (c.f.[75, 36]).

It is also possible to obtain the HM equation from the gyrokinetic equation with the appropriate assumptions [76, 16, 77, 71]. Although it was originally derived with adiabatic electrons from a fluid perspective, it is more sensible to find the HM equation with adiabatic ions at the $k_\perp \rho_i \gg 1$, $k_\perp \rho_e \ll 1$ limit. First, the derivation requiring adiabatic electrons will be shown, and the problem with this derivation will be identified. Then the derivation requiring adiabatic ions will be shown.

Start from the gyrokinetic equation for ions

$$\frac{\partial \langle \delta f_i \rangle_R}{\partial t} + v_\parallel \hat{b} \cdot \nabla \langle \delta f_i \rangle_R + \frac{q}{m_i c} \langle E_\parallel \rangle_R \frac{\partial F_M}{\partial v_\parallel} + \langle \mathbf{v}_E \rangle_R \cdot \nabla \left(F_M + \langle \delta f_i \rangle_R + \frac{q}{T_i}((\langle \phi \rangle_R - \phi) F_M) \right) = 0$$

then integrate over velocity space to find an equation for $n_{i,R} = \int d^3v \langle \delta f_1 \rangle_R$

$$\frac{\partial n_{i,R}}{\partial t} + \nabla_\parallel (u_\parallel n_{i,R}) + \langle \mathbf{v}_E \rangle_R \cdot \nabla (n_0 + n_{i,R}) = 0 \tag{2.47}$$

where n_0 is the background Maxwellian density and $u_\parallel$ is a fluid velocity.

Using the same procedure as in Equation 2.46 for transforming back to the $\mathbf{r}$ coordinate, one finds that the density $n_{i,r}$ is

$$n_{i,r} = \int d^3v \langle \langle \delta f_1 \rangle_R \rangle_r + \frac{q\phi}{T}(\Gamma_0((k_\perp v_\perp/\Omega)^2) - 1) n_0 \tag{2.48}$$

In the cold ion limit $\Gamma_0 - 1 \sim (k_\perp v_\perp/\Omega)^2$ and $\int d^3v \langle \langle \delta f_1 \rangle_R \rangle_r \sim n_{i,R}$. Making the adiabaticity assumption for the electrons, $n_{e,r} = \frac{q\phi}{T_e}$ and setting the electron and

perturbed densities in the **r** coordinate equal due to quasineutrality,

$$\begin{aligned} n_{e,r} &= n_{i,r} \\ \frac{q\phi}{T_e} n_0 &= n_{i,R} + \frac{c}{B} k_\perp^2 \phi \frac{n_0}{\Omega_i} \\ n_{i,R} &= \frac{q\phi}{T_e} n_0 - \frac{c}{B} \nabla_\perp^2 \phi \frac{n_0}{\Omega_i} \\ n_{i,R} &= n_0 \left(\frac{q\phi}{T_e} - \frac{c}{B} \nabla_\perp^2 \phi \frac{1}{\Omega_i} \right). \end{aligned}$$

This expression for $n_{i,R}$ can be inserted into the collisionless gyrokinetic equation to obtain, with $\hat{b} = \hat{z}$ and $k_z = 0$:

$$\begin{aligned} \frac{\partial}{\partial t} \left(n_0 \left(\frac{q\phi}{T_e} - \frac{c}{B} \frac{1}{\Omega_i} \nabla^2 \phi \right) \right) + \nabla_\parallel \left(u_\parallel n_0 \left(\frac{q\phi}{T_e} - \frac{c}{B} \frac{1}{\Omega_i} \nabla^2 \phi \right) \right) + \\ \frac{qB}{m_i c} (\hat{z} \times \nabla \phi) \cdot \nabla \left(\frac{q\phi}{T_e} n_0 - \frac{c}{B} \frac{n_0}{\Omega_i} \nabla^2 \phi + n_0 \right) = 0, \end{aligned} \tag{2.49}$$

which implies:

$$\frac{1}{\Omega_i} \frac{\partial}{\partial t} \left(\frac{c}{B} \frac{1}{\Omega_i} \nabla^2 \phi - \frac{q\phi}{T_e} \right) + \frac{1}{n_0} (\hat{z} \times \nabla \phi) \cdot \nabla \left(\frac{c}{B} \frac{n_0}{\Omega_i} \nabla^2 \phi - \frac{q\phi}{T_e} n_0 + n_0 \right) = 0. \tag{2.50}$$

This can also be written as

$$\begin{aligned} \frac{1}{\Omega_{0,i}} \frac{\partial}{\partial t} \left(\frac{c}{B} \frac{1}{\Omega_i} \nabla^2 \phi - \frac{q\phi}{T_e} \right) + (\hat{z} \times \nabla \phi) \cdot \nabla (\ln(n_0)) + \\ \frac{1}{n_0} n_0 (\hat{z} \times \nabla \phi) \cdot \nabla \left(\frac{c}{B} \frac{1}{\Omega_i} \nabla^2 \phi - \frac{q\phi}{T_e} \right) - \left(\frac{c}{B} \frac{1}{\Omega_i} \nabla^2 \phi - \frac{q\phi}{T_e} \right) (\hat{z} \times \nabla \phi) \cdot \nabla (\ln(n_0)) = 0, \end{aligned} \tag{2.51}$$

or

$$\frac{1}{\Omega_i} \frac{\partial}{\partial t} \left(\frac{c}{B} \frac{1}{\Omega_i} \nabla^2 \phi - \frac{q\phi}{T_e} \right) + (\hat{z} \times \nabla \phi) \cdot \nabla \left(\ln(n_0) + \frac{c}{B} \frac{1}{\Omega_i} \nabla^2 \phi - \frac{q\phi}{T_e} \right) = 0. \tag{2.52}$$

The normalization for the this cold ion HM equation is $\phi \to \frac{q\phi}{T_e}$, $\nabla \to \rho_s \nabla$, where $\rho_s = \sqrt{T_e/m_i}$ and $\partial_t \to \frac{1}{\Omega_i} \partial_t$, which is easily seen when one realizes that $c/B\Omega_i = \frac{q}{T_e}/\rho_s^2$.

One problem with this derivation for cold ions is with the approximation of adiabatic electrons. It should be noted that this approximation is not valid for describing ion-temperature gradient turbulence at $k_\perp \rho_i \ll 1$ ([78]. To see this, take the $\mathcal{O}(1)$ terms from the δf_1 electron gyrokinetic equation:

$$\begin{aligned} v_\parallel \nabla_\parallel \left(\langle \delta f_1 \rangle - \frac{q \langle \phi \rangle}{T_e} F_M \right) = 0 \Rightarrow \\ \delta f_1 = \frac{q\phi}{T_e} F_M + G(x,y) \Rightarrow \\ G(x,y) = -\frac{q}{T_e} F_M \langle \phi \rangle_{fsa} \Rightarrow \\ \delta f_1 = \frac{q}{T_e} F_M \left(\phi - \langle \phi \rangle_{fsa} \right) \end{aligned}$$

where $\langle \cdot \rangle_{fsa}$ is a flux surface average operator, working as a spatial average over a magnetic flux surface, introduced already in Equation 2.40. The conventional assumption for adiabatic electrons is only obtained if the one assumes $\langle \phi \rangle_{fsa} = 0$.

An alternative derivation of the Hasegawa-Mima equation for $k_\perp \rho_e \ll 1$ and $k_\perp \rho_i \gg 1$ arrives at adiabatic ions by using:

$$n_i(r) = \int d^3v (\langle \delta f_i \rangle_R + \frac{q}{T_i} \langle \phi \rangle_R F_M) - \int d^3v \frac{q\phi}{T_i} F_M$$

and noting that the first two terms on the left-hand side are negligible since the gyroaverage translates as a J_0, which is small for large values of the argument $k_\perp \rho_i$. The equation is found in the same form as before but with the new normalizations: $\Omega_i \to \Omega_e$, $\rho_s \to \rho_{s,e} = \sqrt{T_i/m_e}/\Omega_e$ and $q/T_i \to q/T_e$.

A shorthand notation for the Hasegawa-Mima equation is

$$\left[\partial_t + (\mathbf{z} \times \nabla\phi) \cdot \nabla \right] \left(\nabla^2 \phi - \phi - \beta x \right) = 0 \,, \tag{2.53}$$

where the x coordinate corresponds to the direction of the density gradient driving the drift-wave instability, and y corresponds to the direction of propagation of the drift-waves. In toroidal geometry, x is analogous to a normalized coordinate along the minor radius, and y is a poloidal-like coordinate. Here we assume a slab approximation and treat (x, y) as Cartesian coordinates. The parameter $\beta = n_0(x)'/n_0(x)$ measures the scale length of the density gradient, and not the ratio of plasma and magnetic pressure.

Many simulations of this equation have been performed, including many studies of the transport of Lagrangian tracer particles and gyrocenters [48, 45, 79, 43, 44]. One may perform a direct numerical simulation for freely decaying turubulence, with an artificial viscosity term added. One may also apply a forcing to the system, which can drive an inverse cascade. When the β term is strong enough compared to the nonlinear term, saturated states of the HM equation turbulence appear as zonal flows [44]. If the nonlinear term is relatively strong compared to the asymmetry, a saturated state consisting of two large vortices, the so called modon solution, will appear [80]. This solution is also obtainable from analysis [75]. A dipole state is natural for the HM equation because the turbulent cascade of energy in this quasi-two dimensional geometry is inverse compared to the standard three dimensional Kolmogorov direct cascade of energy to small scales. Another interesting result with a strong similarity to a solution of the HM equation comes from electron temperature gradient turbulence in a continuum gyrokinetic code [81].

2.3 Overview of continuous-time random walks and fractional calculus

We are interested in the drift dispersion of particles or gyrocenters in flows where a coherent component is combined with an incoherent component. Perhaps a narrow band of relatively large amplitude, anisotropic waves coexists with smaller amplitude, randomly phased Fourier components. For the limit of a purely coherent flow with no time dependence, the motion of particles will be completely predictable on a particle-by-particle basis. In a simple shear flow without any stochastic region, particles are completely trapped in the direction perpendicular to the flow and free-streaming parallel to the flow. For the opposing limit of a purely random flow, such as isotropic and homogeneous turbulence, each particle trajectory will be unpredictable, but the overall dispersion will be given by a diffusion equation.

This conclusion follows from the Markovian (short memory) nature of homogeneous turbulence, such that the autocorrelation function for velocities is given by an exponential decay:

$$C(\tau) = \frac{\langle u(t)u(t+\tau)\rangle}{\langle u^2\rangle} = \exp(-\tau/\tau_c) \tag{2.54}$$

where τ_c is a typical decay time. This timescale can be interpreted as the time for which memory, or history, is not relevant for trajectories or dispersion on average. Taylor's theorem [82] (which is an example of a Green-Kubo relation) relates the integral of the velocity correlation function to the dispersion of particles:

$$\frac{d\sigma^2(t)}{dt} = \int_0^t \langle v(0)v(\tau)\rangle \, d\tau \tag{2.55}$$

which implies

$$\sigma^2(t) = 2\bar{v^2} \int_0^t (t-\tau)C(\tau)d\tau \tag{2.56}$$

as shown quite clearly in [83]. Here, $\bar{v^2}$ is the average initial velocity. Equation 2.56 implies that

$$\sigma^2(t) = \bar{v^2}t^2 + \mathcal{O}(t^4) \tag{2.57}$$

as $\tau \to 0$ if $C(\tau) \to 1$. Also,

$$\sigma^2(t) = 2\bar{v^2}t_0(t - t_1) \tag{2.58}$$

as $\tau \to \infty$ assuming that the integral of the correlation function converges, where t_0 is the zeroth moment of the correlation function and t_1 is the first moment. This is the functional form predicted by the classical diffusion equation.

For the intermediate scenarios we are confronting here, inhomogeneities and persistent structures in a flow extend the effects of memory and influence the underlying random walk process so that the result of the process may not be diffusive, perhaps for some significant amount of time. A foundation for understanding and quantifying these nondiffusive processes comes from the so-called continuous-time random walk (CTRW) theory based on a generalized master equation for the space and time dependence of the probability function for locating a single particle.

Nondiffusive transport, e.g. in the $\hat{r}$ radial direction, is characterized in this thesis by the moments of the particle displacement distribution function, including the mean $M(t) = \langle \delta r(t) \rangle$ (if there is advection) and the variance $\sigma_r^2(t) = \langle (\delta r(t) - \langle \delta r(t) \rangle)^2 \rangle$ of particle displacements $\delta r(t) = r(t) - r(0)$. For diffusive transport, the distribution of step sizes for the random walk is given by a Gaussian

distribution and the waiting times between steps are given by a Poisson distribution. This leads to a linear scaling in the variance and the mean, such that $M(t) \sim t$ for normal advection and $\sigma^2 \sim t$ for normal diffusion. If transport is nondiffusive, the variance scales as $\sigma^2(t) \sim t^\gamma$, where $\gamma < 1$ indicates subdiffusive transport and $\gamma > 1$ indicates superdiffusive transport by definition [84]. If power law distributions are assumed or detected for the microscopic dynamics of the particle trajectories, the value of γ can be related to the exponents of those power laws, as we will see in this Section and in Chapter 3.

The particle propagator for the probability of finding the particle at a future time and place, given the probability at a starting time and place is given by

$$P(\mathbf{x}, t|\mathbf{x}', t') \equiv P(\mathbf{x}, t) \tag{2.59}$$

where the equivalency here indicates our notation shortcut. In the remainder of this section, the notation will also only include one dimension: $\mathbf{x} \rightarrow x$. Computing the evolution of this propagator is the fundamental tool of this work. We obtain numerical approximations to the propagator by pushing a large number of individual particles and examining the distribution of their displacements.

Predictions for the particle propagator can be derived from the foundation of the continuous-time random walk (CTRW) formalism [85, 58]. The CTRW method supposes that the information content of a random walk is contained in $\Psi(x, t)$, a probability density function called the kernel of particle propagation or the jump PDF. The probability of jump length is given by

$$\eta(x) = \int_{-\infty}^{\infty} \Psi(x, t) dt \tag{2.60}$$

and the probability of a waiting time is given by

$$\psi(t) = \int_{-\infty}^{\infty} \Psi(x,t)dx. \tag{2.61}$$

Note carefully the difference between $\Psi(x,t)$ and $\psi(t)$. Often, the assumption of separability is made for the transport kernel, so that $\Psi(x,t) = \eta(x)\psi(t)$. Let us now see how a master equation for the propagator, under the influence of $\Psi(x,t)$ can lead to both a diffusion equation and a fractional diffusion equation. Following [58], define the probability of just having arrived at (x,t) from (x',t'), with initial condition starting from $t = 0$, $x = 0$ as:

$$J(x,t) = \int_{-\infty}^{\infty} dx' \int_0^t dt' J(x',t')\Psi(x-x',t-t') + \delta(x)\delta(t) \tag{2.62}$$

so that the cumulative probability of being at (x,t) is given by another integration

$$P(x,t) = \int_0^t J(x,t')k(t-t')dt' \tag{2.63}$$

where

$$k(t) = 1 - \int_0^t \psi(t')dt' \tag{2.64}$$

is called the survival probability [85]. Putting it all together:

$$\begin{aligned} P(x,t) &= \int_0^t J(x,t')k(t-t')dt' \\ &= \int_0^t dt' \left[\int_{-\infty}^{\infty} dx' \int_0^{t'} J(x',t'')\Psi(x-x',t-t'')dt'' + \delta(x)\delta(t') \right] k(t-t') \\ &= k(t)\delta(x) + \int_0^t dt' \int_{-\infty}^{\infty} dx' \int_0^{t'} dt'' J(x',t'')\Psi(x-x',t-t'')k(t-t'), \end{aligned}$$

and so,

$$P(x,t) = k(t)\delta(x) + \int_0^t dt' \int_{-\infty}^{\infty} dx' \Psi(x-x',t-t')P(x',t') \tag{2.65}$$

This type of relationship between a particle propagator and a kernel is called a master equation [86], since it contains all of the information necessary to predict where a particle will be at any point in space and time, assuming the kernel is perfectly accurate.

Fourier and Laplace transforms are defined in one dimension as:

$$\mathcal{F}\left[f(x)\right] = \hat{f}(k) = \int_{-\infty}^{\infty} f(x)e^{-ikx}dx \tag{2.66}$$

and

$$\mathcal{L}\left[f(t)\right] = \tilde{f}(s) = \int_{0}^{\infty} e^{-st}f(t)dt. \tag{2.67}$$

We will often omit the $\widehat{\cdot}$ and $\widetilde{\cdot}$ for brevity, while explicitly stating the argument for clarity.

Next note that the Laplace transform of $k(t)$ is given by

$$k(s) = \frac{1-\psi(s)}{s} \tag{2.68}$$

With this, the transform of Equation 2.65 follows from a convolution theorem

$$P(k,s) = \frac{1-\psi(s)}{s}\frac{1}{1-\Psi(k,s)}. \tag{2.69}$$

Equation 2.69 is identified with the Montroll-Weiss equation [87, 86] which becomes, in the separable limit,

$$P(k,s) = \frac{1-\psi(s)}{s}\frac{1}{1-\eta(k)\psi(s)}. \tag{2.70}$$

Recent versions of this derivation can be found in [12, 88] and references therein.

2.3.1 Gauss and Poisson ⇒ diffusion equation

The standard diffusion equation follows when the distribution of step sizes is given by a Gaussian

$$\eta(x) = \frac{1}{\sqrt{2\pi\sigma^2}} \exp(-x^2/2\sigma^2)$$
$$\eta(k) = \frac{1}{2} \exp(-k^2\sigma^2/2) = \frac{1}{2}(1 - (k\sigma)^2/2 + \mathcal{O}(k^4)). \tag{2.71}$$

The distribution of waiting times is given by a Poisson distribution, which is equivalent to a Markov (memory-free) process

$$\psi(t) = \mu \exp(-\mu t)$$
$$\psi(s) = \frac{\mu}{s+\mu} = 1 - \frac{s}{\mu} + \mathcal{O}(s^2). \tag{2.72}$$

In the small s and small k limits, the master equation becomes

$$P(k,s) \sim \frac{1}{s + k^2 D} \Rightarrow \frac{\partial P}{\partial t} = D\frac{\partial^2 P}{\partial x^2} \tag{2.73}$$

Transforming back to x and t gives the diffusion equation with diffusion coefficient $D = \sigma^2\mu$ given by the characteristic step size and waiting times. Note that this result is valid in the limit of long times and long wavelengths. This means that the diffusion equation may not describe a Gauss-Markov process at scales comparable to the characteristic waiting time $1/\mu$ or the characteristic jump length σ. This is usually manifested as a period of ballistic motion before asymptotic diffusion.

2.3.2 Power laws ⇒ fractional diffusion equation

Another special case of the CTRW model is the fractional diffusion equation. Start from two power laws for the step sizes and waiting times,

$$\eta(x) = A|x|^{-(\alpha+1)}$$

$$\psi(t) = Bt^{-(\beta+1)}$$

In Fourier and Laplace space, these power laws have the asymptotic forms

$$\eta(x) \sim 1 - |k|^{\alpha}$$

$$\psi(t) \sim 1 - s^{\beta}$$

These algebraically decaying tails are characteristic of stable Lèvy distributions with a stability index α less than 2 [89, 86, 88]. Let us quickly define Lèvy distributions for future reference. The symmetrical Lèvy stable distribution with stability index $0 < \alpha_L \leq 2$ and scale factor $\gamma_L > 0$ is [90]:

$$L(x) = \frac{1}{\pi} \int_0^{\infty} \exp\left(-\gamma_L q^{\alpha_L}\right) \cos(qx) dq. \tag{2.74}$$

For $1 < \alpha < 2$, $L(x)$ has a series representation with power law tails [90].

Again, in the small s, small k limit, the master equation can be simplified and rearranged

$$P(k,s) = \frac{s^{\beta}}{s} \frac{1}{c_1 s^{\beta} + c_2 |k|^{\alpha}}$$

$$s^{\beta} P(k,s) - s^{\beta-1} = -D_f |k|^{\alpha} P(k,s) \tag{2.75}$$

where $D_f = c_2/c_1$ is an effective diffusion coefficient with dimensions x^{α}/t^{β}. Inverse

transforming gives, by definition, the fractional diffusion equation:

$$ {}_0^C D_t^\beta P(x,t) = D_f D_x^\alpha P(x,t) \tag{2.76} $$

where the fractional integro-differential operators can be defined in several ways [57]. There is some ambiguity to their definition, since several forms can give the same result. Regularizations are sometimes necessary to obtain sensible physical interpretations. The operator must be equivalent with the Fourier-Laplace transform in Eq uation 2.75.

Another way to see the origin of the fractional operator is to take the Cauchy formula for repeated integration and generalize it to non-integer order. The Cauchy formula

$$ \mathcal{I}^n \left(f(x) \right) = \frac{1}{\Gamma(n)} \int_{x_1}^{x_2} (x-u)^{n-1} f(u) dt \tag{2.77} $$

where $\Gamma(n)$ is the factorial function for integers. This well-known result can be proven inductively or by using the binomial theorem and integration by parts. While Equation 2.77 is derived assuming $n \in \mathbf{N}$, it is easy to simply assert that $n \to \nu$, with $\nu \in \mathbf{R}$, and therefore define a fractional integral. A fractional derivative is then defined by applying an integer-order derivative to fractional integral. (The term fractional is misleading, since this generalization is not confined to rational numbers.)

The most common definition of the spatial fractional derivative operator, called the Riemann-Liouville (RL) fractional derivative appears as :

$$ {}_x D_b^\alpha P = \frac{1}{\Gamma(m-\alpha)} \frac{\partial^m}{\partial x^m} \int_x^b \frac{P(y,t)}{(y-x)^{\alpha+1-m}} dy. \tag{2.78} $$

More specifically, this is the right-hand RL operator. The left-hand operator is

$$ {}_bD_x^\alpha P = \frac{1}{\Gamma(m-\alpha)} \frac{\partial^m}{\partial x^m} \int_b^x \frac{P(y,t)}{(x-y)^{\alpha+1-m}} dy. \tag{2.79} $$

Here, $m-1 \leq \alpha < m$ is an integer and $\Gamma(m-\alpha)$ is the gamma function (compare to Equation 2.77). The temporal operator, which is "regularized in the time origin" [91] is called the Caputo fractional derivative and appears (for $0 < \beta < 1$) as

$$ {}_0^C D_t^\beta P = \frac{1}{\Gamma(1-\beta)} \int_0^t \frac{\partial_{t'} P(t')}{(t-t')^\beta} dt' \tag{2.80} $$

This form of the fractional operator satisfies the Laplace transform in Equation 2.75 and requires the initial value of the function as a boundary condition, rather than the initial value of the fractional derivation as in other definitions [12]. Interpretation of the fractional diffusion equation as a description of a probability density is limited to $[0 < \alpha \leq 2] \cap [0 < \beta \leq 1]$ or $1 < \beta \leq \alpha \leq 2$ [91].

2.3.3 Premise for deducing a CTRW from a flow

Power laws are found in many different contexts to describe many types of behavior. As we have seen, if a random walk is governed by step sizes and waiting times drawn from pure power laws, a fractional diffusion equation is the result. The solution of the fractional diffusion equation takes a well-defined form, and attempts have been made to identify the probability distribution of particles with fractional diffusion solutions, including the work in Chapter 3 of this thesis, and [12]. In scenarios where the random walk is not dictated by pure power laws, which includes any realistic example where infinite step sizes are impossible, other forms of the

kernel $\Psi(x,t) = \eta(x)\psi(t)$ must be identified. Truncated power laws from truncated Lévy flights [90] provide one way of obtaining a realistic non-Gaussian random walk. Another technique, which introduces the complication of coupling between $\eta(x)$ and $\psi(t)$ is the Lèvy walk [85], in which "long steps are penalized by required more time to be performed."

More generally, it would be useful to obtain a kernel from the structure of a particular flow. In the context of magnetic stochastic transport on RFX, speculation on this possibility has been made [32]. Plainly, one would like to construct $\eta(x)$ and $\psi(t)$ from some average values of Eulerian quantities, such as velocity, density and vorticity. This kernel could then be used to simulate a continuous time random walk and determine whether nondiffusive transport is important without performing explicit Lagrangian probe simulations of the flow. Lagrangian studies might be especially difficult for experimental situations where highly time-resolved data is not available. Obtaining the kernel from direct observation of the flow would also eliminate the expense of integrating a statistically significant number of tracers through interpolation and ODE solving. The simulation of the kernel as a random walk would only require a Monte Carlo-style sampling of the transport kernel. In some sense, such a method shifts the responsibility for capturing the details of the flow from the computation of single particle trajectories to the determination of an accurate kernel from Eulerian data. It remains to be seen whether this technique can be useful in the context of the results of this thesis.

Next, a framework will be described for translating a set of flow data into a kernel for a random walk. The question is to determine both the step size and

waiting time distributions. In general, these may be coupled, so that the step size depends on the waiting time (or vice versa) for some range of values [85].

The step size distribution is easier to define. Let the step size for a particle in an eddy of scale k be given by

$$\Lambda(k) = \mathcal{S}\Lambda_0(k) = \mathcal{S}\frac{2\pi}{k} \tag{2.81}$$

where $\mathcal{S}$ is a scale factor correcting for the possibility that particle escape might occur before the structure is crossed. This scale factor might be drawn from a random distribution. Then the probability of step size x is given by

$$\eta(x,t) = \frac{\sum_k 2S\pi/kF_k(t)}{\sum_k F_k(t)} \tag{2.82}$$

where time (not waiting time) dependence has been introduced in the frequency, F_k, of occurrence of eddies with scale k in the bounded system of interest.

The waiting time distribution is a bit harder to define since the scaling is not as obvious as the inverse wavelength was for the scale of the steps. Let the Lagrangian persistence time of an eddy be given by

$$\Phi(k) = \mathcal{P}\Phi_0(k) = \mathcal{P}\tau_k^{to} \tag{2.83}$$

where $\mathcal{P}$ is a (possibly randomized) scale factor and τ_k^{to} is the eddy turnover time at scale k. Then the probability of waiting time τ is

$$\psi(\tau,t) = \frac{\sum_k \mathcal{P}\tau_k^{to}F_k(t)}{\sum_k F_k(t)}. \tag{2.84}$$

The complexity of the problem has now been isolated into two unknown quantities, plus two scale factors. First is the lifetime of an eddy, which is related to

the eddy turnover time, but is likely a complicated object to measure. Second is the frequency of occurrence for an eddy of scale k. From a brute force point of view, this quantity could be measured using a manual or automated counting routine. A possibly more reliable and more general technique would be to look at the wavenumber spectrum for a flow and observe which wavenumbers are present. Then the frequency of occurrence for the eddy of scale k will be comparable to the product of the scale length and the size of the bounded domain: $\frac{kL}{2\pi}$. Once the turbulence reaches a steady state, the frequency of occurrence should be a fairly time-independent function, but it may be necessary to have some oscillatory time dependence included.

Once $\psi(\tau, t)$ and $\eta(x, t)$ have been estimated by examining the Eulerian flow data appropriately, these distributions could be used to numerically solve for the particle propagator $P(x, t)$. The goal of such an effort would be to predict whether particle dispersion in a given streamfunction is non-Gaussian based on the particular structure of an experimental flow. This technique could avoid the more expensive tracer tracking simulations by replacing interpolation and ODE solving with a time-dependent random selection of jump and waiting times from realistic distributions, rather than power law or Gaussian approximations.

2.4 Implementation of the gyrokinetic equation

Many numerical implementations of the gyrokinetic formalism are in use by the fusion, and recently, the space physics [17] communities. While the wide vari-

ety of gyrokinetic codes can cause confusion, cooperative efforts such as the Cyclone initiative for ion-temperature gradient turbulence [65] have identified points of agreement. Gyrokinetic codes can be classified in several ways. Here, we stay within the δf_1 form of the gyrokinetic equation and describe the significant differences between continuum/Eulerian and particle/Lagrangian methods.

2.4.1 Continuum gyrokinetic solvers

One technique for solving the gyrokinetic PDE is to employ a pseudospectral description of the distribution function and fields, combined with a finite difference scheme for the nonperiodic dimensions. This technique is generally referred to as a continuum method, since the distribution function is represented smoothly in a given domain, in the spirit of the Vlasov equation. A spectral solver, such as in GS2 [92, 3], GYRO [93] or GENE [94] transforms the δf or $h = \delta f - q\phi/T$ into Fourier space in the directions perpendicular to the magnetic field: $\delta f(x_{\perp,1}, x_{\perp,2}, x_\parallel, v_\parallel, v_\perp) \Rightarrow \delta f(k_{x,1}, k_{x,2}, x_\parallel, v_\parallel, v_\perp)$. Since the fast Fourier transform FFTW [95] is a very quick parallel algorithm, it allows derivatives in the periodic directions to be found quickly with high accuracy. It also allows the gyroaveraging operator to be applied to the fields using the exact Bessel function multiplier: $J_0(k_\perp v_\perp/\Omega)$.

For the nonperiodic directions, continuum codes use finite differencing schemes on grids in phase space. Timestepping of the PDE is accomplished typically with a Runge-Kutta method. Realistic collision operators can be implemented with continuum codes since the derivatives in pitch-angle or energy can be taken directly on

the smoothly defined distribution function. These collision operators are important for removing the fine-scale (grid-scale) structure in velocity space that should be physically damped [96, 97].

2.4.2 Particle-in-cell simulation technique

A competing framework for solving the δf gyrokinetic equation for the $k_\perp \rho \sim 1$ scale turbulence is the particle-in-cell (PIC) type of algorithm, first implemented by [98] and [99], then used extensively by many authors, e.g [100, 101]. In the spirit of the Klimontovich equation for the evolution of individual points (Dirac δ-functions) in phase space, which represent a distribution function in aggregate, a PIC simulation uses the method of characteristics to convert the gyrokinetic PDE into a set of ODEs to be solved for many initial conditions. The solution on each characteristic is interpreted as a marker particle which follows a phase space trajectory specified by the gyrokinetic equation. Each marker with index i carries a weight, $w_i = \delta f_i / F_0$, which represents the perturbation of the distribution function at the location of the marker.

When necessary, the marker weights can be interpolated onto a phase space grid to give the perturbed distribution function. This function is used to solve for the electromagnetic fields, in general, so that such self-consistent fields can be used to find the marker weights and positions at the next time step. PIC codes may be parallelized quite trivially by partitioning the ensemble of markers onto a large number of processors, so that the only interprocessor communication is during a

field solve. This is the technique chosen for GSP, but it is not common.

For the gyroaveraging operation, PIC codes often use a four or eight-point stencil on the ring, though GSP uses a spectral method as described below. Collision operators with pitch-angle or other phase space derivatives can be difficult or expensive to implement in PIC codes since the discrete differencing operation requires another interpolation, which is one of the slowest parts of the PIC algorithm. We will show here that artificial fine scale structure on the PIC grid must be controlled. The inaccuracies from this structure, which should be damped by a physical mechanism, can overwhelm the signal even when the number of particles per cell is very high. In this thesis, we use a Krook collision operator, as explained in Section 4.2.2.

In recent history, δf gyrokinetic PIC codes for magnetic confinement fusion applications have had trouble with discrete particle noise [102], part of which is the $1/\sqrt{N}$ noise inherent in Monte Carlo sampling of an integral (where N is the number of marker particles). Nevertheless, it is possible to obtain results with PIC codes that benchmark favorably with continuum codes. PIC codes are quite attractive because of the relative simplicity of the fundamental algorithm and ease of parallelization. For the main point of this thesis, a PIC code is a natural way of tracking the dispersion of an ensemble of particles since a subset of the marker particles used to sample the distribution function can be used directly as the Lagrangian probes for the turbulent flow.

2.5 Our implementation of particle-in-cell

The gyrokinetic simulations used for the results of Chapter 4 are based on a code originally written by Broemstrup for his doctoral thesis. Preliminary results from this code, dubbed GSP, showed that it was capable of reproducing some results from GS2 in ion-temperature-gradient and entropy mode turbulence. The unique features of GSP include its ability to study plasma behavior at $k_\perp \rho > 1$ due to the implementation of the gyroaveraging operator in k-space with the Bessel function. The contributions to the code for this thesis include the marker particle tracking algorithm and associated diagnostics, which are described in Section 4.3. The results in this thesis are obtained at higher spatial resolution than used in the original work, and the basic diagnostics for the code have been refined. Explicit spatial filtering during the field solve is implemented, and original convergence tests have been performed, with details in Sections 4.2.1 and 4.2.2.

2.5.1 Method of characteristics

The foundation for the PIC algorithm is the method of characteristics, which is a standard technique used to split an N variable partial differential equation into $N + 1$ ordinary differential equations. The general form of a first order PDE in N variables with source term $\mathcal{S}$ can be written as:

$$\sum_i^N \mathcal{C}_i \frac{\partial \mathcal{F}}{\partial x_i} = \mathcal{S}. \tag{2.85}$$

The main idea is to parameterize the terms of this equation such that $x_i = x_i(t)$, where we will identify t as time in the gyrokinetic equation. Thus,

$$\frac{dx_i}{dt} = \mathcal{C}_i \forall i \tag{2.86}$$

and

$$\frac{d\mathcal{F}}{dt} = \mathcal{S} \tag{2.87}$$

is the value of the function along the N characteristics parameterized by t. Now we will see how this method applies to our example.

The coordinates used here will be the same as in Figure 4.1, but as stated again in Chapter 4, results will be reported with notation consistent with Chapter 3. Starting from the gyrokinetic equation for the Z-pinch, Equation 2.36,

$$\begin{aligned} &\frac{\partial \langle \delta f \rangle_R}{\partial t} + (v_\parallel \mathbf{B}_0 + \langle \mathbf{v}_{\mathbf{E}\times\mathbf{B}} \rangle_R + \mathbf{v}_D^{tot}) \cdot \nabla \langle \delta f \rangle_R \\ &= - \langle v_{\mathbf{E}\times\mathbf{B}} \rangle_R \cdot \nabla F_0 - v_\parallel \frac{qF_0}{T} (\hat{\mathbf{B}}_0 \cdot \nabla \langle \phi \rangle_R) - \mathbf{v}_D^{tot} \cdot \nabla \left(\frac{q \langle \phi \rangle_R}{T} F_0 \right), \end{aligned}$$

and comparing with the expansion Equations 2.86 and 2.87 to find the coefficients $\mathcal{C}_i$,

$$\frac{dr}{dt} = \langle \mathbf{v}_{\mathbf{E}\times\mathbf{B}} \rangle_R \cdot \hat{r} \tag{2.88}$$

$$\frac{dz}{dt} = \langle \mathbf{v}_{\mathbf{E}\times\mathbf{B}} \rangle_R \cdot \hat{z} + v_D^{tot} \tag{2.89}$$

$$\frac{d\varphi}{dt} = v_\parallel \tag{2.90}$$

$$\frac{d\mathbf{v}_\perp}{dt} = 0 \tag{2.91}$$

$$\frac{d\mathbf{v}_\parallel}{dt} = 0 \tag{2.92}$$

$$\frac{d \langle \delta f \rangle_R}{dt} = - \langle \mathbf{v}_{\mathbf{E}\times\mathbf{B}} \rangle_R \cdot \nabla F_0 - v_\parallel \frac{qF_0}{T} (\hat{\mathbf{B}}_0 \cdot \nabla \langle \phi \rangle_R) - \mathbf{v}_D^{tot} \cdot \nabla \left(\frac{q \langle \phi \rangle_R}{T} F_0 \right). \tag{2.93}$$

Since the Maxwellian background distribution function is $\mathcal{O}(\epsilon^{-1})$ larger than δf, one typically chooses to decrease the Monte Carlo noise in the simulation by using the relative weight $w_i = \langle \delta f \rangle_R / F_0$ as the evolved quantity in the simulation. This is equivalent to importance sampling as described in [103]. Importance sampling requires separation of scales between a relatively large and stationary background (preferably known analytically) and a perturbation on the background. Solving for the integral of the background using a closed form (such as the Maxwellian in gyrokinetics) relegates sampling error to the estimate of the perturbed part. This sampling error is therefore smaller by the order of the scale separation, which in this case is $\epsilon = \rho/L$.

Now we show how to convert Equation 2.93 into an equation for w_i. The form of the Maxwellian (with species index suppressed) is given by

$$\begin{aligned} F_0 &= \frac{n_0(\mathbf{r})}{\pi^{3/2} v_{th}^3} \exp(-v^2/2v_{th}^2) \\ &= \frac{n_0(\mathbf{r}) T_0(\mathbf{r})^{-3/2}}{(\pi/m)^{3/2}} \exp\left(-\frac{m}{2} v^2 T_0^{-1}(\mathbf{r})\right) \end{aligned}$$

so that the ∇F_0 terms may use

$$\begin{aligned} \nabla F_0 &= \frac{\exp(-\frac{m}{2} v^2 T_0^{-1}(\mathbf{r}))}{(\pi/m)^{3/2}} \left(n_0' T_0^{-3/2} - n_0 \frac{3}{2} T_0^{-5/2} T_0' + \frac{m}{2} v^2 n_0 T_0^{-7/2} T_0' \right) \\ \Rightarrow \nabla F_0 / F_0 &= \frac{n_0'}{n_0} - \frac{3}{2}\frac{T_0'}{T_0} + \frac{m v^2 T_0'}{2T_0^2} = \frac{n_0'}{n_0} - \frac{3}{2}\frac{T_0'}{T_0} + \frac{v^2 T_0'}{2 T_0 v_{th}^2} = \frac{-1}{L_n} + \frac{3}{2L_T} - \frac{v^2}{2 L_T v_{th}^2} \end{aligned}$$

Since F_0 is static on the timescale of the derivative on $\langle \delta f \rangle_R$,

$$\begin{aligned} \frac{\partial \langle \delta f \rangle_R / F_0}{\partial t} = \frac{\partial \langle w \rangle_R}{\partial t} = & - \langle \mathbf{v}_{\mathbf{E}\times\mathbf{B}} \rangle_R \cdot \hat{r} \left(-\frac{1}{L_n} + \frac{3}{2L_T} - \frac{v^2}{2 L_T v_{th}^2} \right) \\ & + v_\parallel \frac{q}{T_0} E_\varphi - v_D^{tot} \frac{q}{T_0} E_z. \end{aligned}$$

This equation for the evolution of the weight will apply to each trajectory, each having a unique input for $\langle \mathbf{v}_{\mathbf{E}\times\mathbf{B}} \rangle_R$, $v_\parallel$ and v_D^{tot}. Each characteristic with the associated solution of $d_t w$ represents a realization of the perturbed distribution function for a particular initial condition. By taking many thousands or millions of these sample solutions and following them for a certain amount of time, one finds an accurate Monte Carlo estimate of the distribution function.

There are many reasons for inaccuracy in any sort of numerical simulation, relative both to analytic limits of the model and the natural processes meant to be reproduced by the model. In a PIC simulation, the inaccuracies relative to the model are often referred to as discrete particle noise. There are at least four obvious sources of discrete particle noise:

- Grid resolution

- Interpolation accuracy

- Finite timestep size

- Number of particles or Monte Carlo sampling

The finite number of particles in a PIC simulation leads to Monte Carlo sampling error as noted by [103, 102] The sampling error is the only error specific to a particle code - continuum codes will also be susceptible to error from the other listed sources. Sampling error is slowly converging with particle number, as $\sqrt{1/N}$, and in a collisionless simulation, the weights will always grow no matter how many particles are used per grid cell for interpolation [104].

2.5.2 Normalization: code units

We define several reference quantities to be used in the normalization of the three nontrivial characteristic equations. A reference gyroradius ρ_r is given by a reference thermal velocity $v_{th,r} \equiv \sqrt{T_r/m_r}$ and a reference Larmor frequency, $\Omega_r \equiv Z_r|e|B/m_r c$. Two length scales are present, so two normalizations for length are needed. Perpendicular lengths are normalized by ρ_r. Parallel lengths are normalized by the system size a. Time is normalized by $t \Rightarrow tv_{th,r}/a$ and $\phi \Rightarrow \frac{Z_r|e|\phi}{T_r}\frac{a}{\rho_r}$. This factor of $\frac{a}{\rho_r}$ is present in order to make the perturbed quantities $\mathcal{O}(1)$.

Normalization of the curvature and ∇B terms into dimensionless code units goes as follows:

$$
\begin{aligned}
w &= \cdots - \Delta t \frac{\partial}{\partial z} \langle \phi \rangle_R \frac{c}{B} \frac{Z|e|}{T} \frac{v_\parallel^2 + \frac{1}{2}v_\perp^2}{\Omega R_c} \\
\frac{\rho}{a} w_N &= \cdots - \frac{a}{v_{th}} \Delta t_N \frac{1}{\rho} \frac{\partial}{\partial z_N} \frac{\rho T}{Z|e|a} \langle \phi_N \rangle_R \frac{c}{B} \frac{Z|e|}{T} \frac{v_{th}^2}{a} \frac{v_{\parallel N}^2 + \frac{1}{2}v_{\perp N}^2}{\Omega R_{cN}} \\
w_N &= \cdots - \Delta t_N \frac{c}{B} \frac{v_{\parallel N}^2 + \frac{1}{2}v_{\perp N}^2}{R_{cN}} \frac{\partial}{\partial z_N} \langle \phi_N \rangle_R
\end{aligned}
$$

2.5.3 Initialization details

Our particle loading scheme for the Z-pinch gives random and uniform positions in r, z, and $v_\parallel$. For $v_\perp$, the markers are loaded on a regularly spaced grid. This is to facilitate the gyroaveraging procedure that will be described below. Initial weights are also chosen uniformly random with a small initial amplitude. This amplitude is chosen so that the primary instability is excited promptly, but able to

grow at the rate specified by the linear dispersion relation.

2.5.4 Parallelization

GSP utilizes multiple processors by splitting the population of marker particles equally onto each computing core. When solving the field equations, the entire population is required to resolve the integral of the distribution function, which is require to calculate ϕ. Message Passing Interface (MPI) routines are used to combine the marker information on the grid and share with each processor. After receiving the field solve result, each processor pushes its allocation of markers independently again. Consolidation of information from each processor is also necessary when computing an integrated diagnostic quantity, such as the particle flux averaged over the entire box. The spatial domain is not parallelized in GSP.

2.5.5 Numerical integration of the characteristic ODEs

A predictor-corrector method is used to advance the ODEs for marker position and weight. It is equivalent to the explicit so-called midpoint method, which is a version of Runge-Kutta order 2 (error at each time step is $\mathcal{O}(\delta t^3)$). This method computes the solution of each ODE at half of the specified time step, and uses this prediction to find the estimated value of the function at the full time step. Thus, the following are computed for each equation $dA/dt = f(t, A)$:

$$A_1 = A_0 + \frac{\Delta t}{2} f(t_0, A_0)$$

$$A_2 = A_0 + \Delta t f(t_0, A_1) \qquad ()$$

Here A_2 is the final result of the timestepping technique. These value of the position, velocity and weight for each particle from the ODE solver is then used to find the fields for the next time step. We recall that in our application, the phase space velocities are constant.

2.5.6 Interpolation techniques in GSP

The marker particles in GSP are pushed by Equations 2.88-2.93 without reference to a finite grid of positions in the gyrocenter coordinate, $\mathbf{R} = (\widehat{X}, \widehat{Y}, \widehat{Z})$. Markers carry information about their positions and δf weights. When a field solve is required, it is necessary to resolve information from the markers onto a grid for solving the Poisson equation and, separately, for computing the gyroaveraged $\mathbf{E} \times \mathbf{B}$ velocities.

This second grid, for $v_\perp$, is designed to use the exact Bessel function for computing gyroaverages (see Figure 3.2 in Section 3.3 for details on the accuracy of this computation). This is a unique feature of GSP compared to many other gyrokinetic PIC codes which use a four point stencil for the gyroaverage. The velocity space grid in the code is chosen at regular values of $v_\perp$ for efficient computation of the gyroaverage operator in spectral space. The values of $v_{\parallel,i}$ are chosen at random, and scaled to a maximum value set such that $v_{\perp,i}^2 + v_{\parallel,i}^2$ is constant (see Figure 2.3.

Interpolation for finding the gyroaveraged $\mathbf{E} \times \mathbf{B}$ drift velocity is done with the nearest neighbor technique. A higher order bilinear method is used for the solution of the Poisson equation. This is also referred to as a "cloud-in-cell" technique [105]

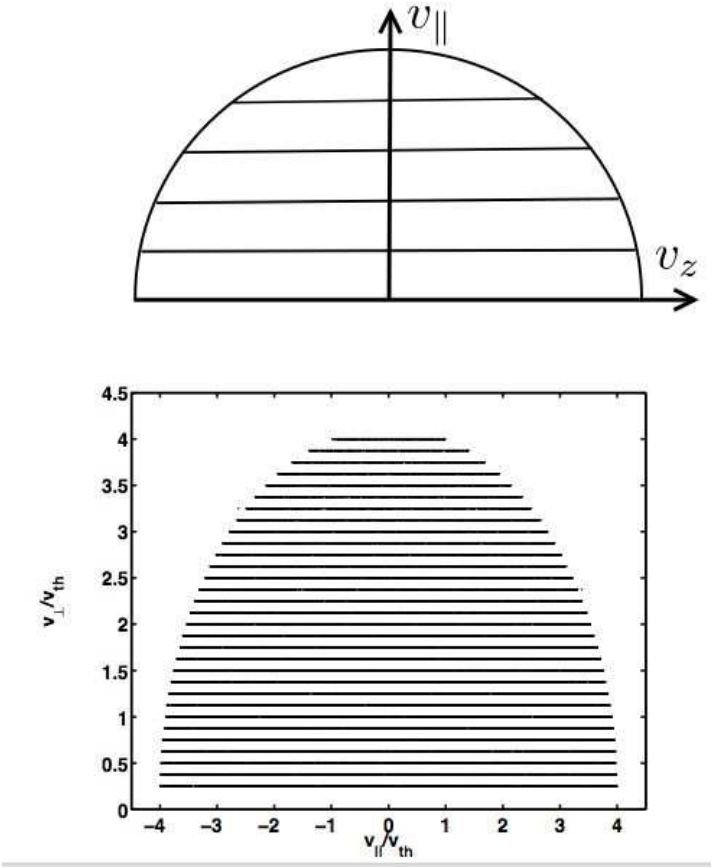

Figure 2.3: Top: idealized gridding scheme for $v_\perp$ to facilitate spectrally accurate gyroaveraging. Bottom: actual grid points used in a GSP simulation.

since it effectively gives the point particle a (triangular) shape with respect to the grid. It is second order accurate [106].

2.5.7 Essential steps in the algorithm

In GSP, the following sequence of events occurs. Before the first timestep, marker positions and weights are either initialized according to Section 2.5.3 or from a restart file. Then the initial potential ϕ_k is computed in Fourier space. The gyroaveraged electric field and associated drift velocities are then computed, and the characteristic equations 2.88 - 2.93 are found for a half timestep as described in Section 2.5.5. The next positions are found from:

$$x_{i,j+1} = modulo(x_{i,j} + v_{E\times B,x} * \delta t/2, L_x)$$

$$y_{i,j+1} = modulo(y_{i,j} + v_{E\times B,y} * \delta t/2, L_y)$$

where L_x and L_y are the dimensions of the periodic box. Quasineutrality is used to find ϕ again, and the procedure is repeated, using the field at the half timestep to solve the characteristics agin, completing the full δt timestep.

At the end of the timestep, trajectory positions are found by computing the displacement without using the modulo function. This allows tracers to be tracked outside of the periodic box. These "outside the box" positions are kept in memory throughout a run of the code. The positions, weights and velocities of the markers on a small number of processors are saved at regular intervals to produce an ASCII file of reasonable size. If the simulation is restarted, these tracer positions are forgotten, and the tracking begins again with the positions modulo the box dimensions. The

magnetic drift term v_B^{tot} is used to find the tracer positions, but the displacement due to this term can be subtracted from the total displacement to focus on the $\mathbf{E}\times\mathbf{B}$ drift, as is done in Chapter 4.

Chapter 3

Superdiffusive gyrocenter drift transport parallel to a shear flow with persistent vortices

3.1 Introduction

Simulations of self-consistent turbulent transport involve nonlinear interactions at disparate scales, which often makes numerical computations expensive and analytic methods intractable. As an alternative, one may consider models of intermediate complexity that incorporate important aspects of transport within a relatively simple reduced description. This approach can reduce confusion and direct the course of more comprehensive studies. In this chapter we accept a reduced model and present a numerical study of the role of finite Larmor radius (FLR) effects on non-diffusive poloidal transport in zonal shear flows using a $\mathbf{E} \times \mathbf{B}$ Hamiltonian test particle transport model.

Following Ref. [42], we model the flow as a superposition of a shear flow and drift waves obtained from the linearized Hasegawa-Mima (HM) equation [40]. Test particle characteristics in this flow are generally not integrable and exhibit chaotic

advection, also known as Lagrangian turbulence, which reproduces key ingredients of particle transport in more complex flows. High frequency FLR effects are incorporated by solving the test particle equations of motion for the gyroaveraged $\mathbf{E} \times \mathbf{B}$ velocity. As demonstrated by Ref. [107], we compute the gyroaverage using a discrete N-polygon approximation.

We adopt a statistical approach and apply non-diffusive transport diagnostics to large ensembles of particles. One of the simplest diagnostics is the scaling of the second moment of particle displacements, $\sigma^2(t) = \langle[\delta y - \langle\delta y\rangle]^2\rangle$, where $\delta y = \delta y(t)$ denotes the particle's displacement and $\langle\,\rangle$ denotes the ensemble average. In the standard diffusion case, $\sigma^2(t) \sim t$, linear scaling allows the definition of an effective diffusivity as the ratio $D_{eff} = \sigma^2(t)/(2t)$ in the limit of large t. However, in the case of non-diffusive transport, $\sigma^2(t) \sim t^\gamma$ with $\gamma \neq 1$. When $0 < \gamma < 1$, the growth of the variance is slower than diffusion and transport is sub-diffusive. When $1 < \gamma < 2$ transport is super- diffusive, which means the spreading is faster than diffusion, and the displacements may be Lévy flights [58]. In both super- and sub-diffusion, characterization of transport as a diffusive process with an"effective diffusivity" D_{eff} breaks down because $D_{eff} \to 0$ when $0 < \gamma < 1$, and $D_{eff} \to \infty$ when $1 < \gamma < 2$. Other measures of non-diffusive transport, which will be discussed in detail later, include non-Gaussianity of the probability distribution of displacements (propagator), slow decay of the Lagrangian velocity autocorrelation function, the presence of long jumps (Lévy flights) and long waiting times, and the non-local (*i.e.*, non-Fickian) dependence of fluxes on gradients. A general review of non-diffusive transport can be found in Ref. [108], and discussions focusing on plasmas

can be found in Ref. [109, 110].

Test particle transport in HM flows, as in Fig. 3.1(a), has been studied in Refs. [111, 48, 45, 112, 43, 42, 44]. In Ref. [42], which did not include FLR effects, it was shown that zonal flows give rise to Lévy flights and strongly asymmetric non-Gaussian PDFs of particle displacements. References [48, 45] addressed the role of FLR effects but restricted attention to diffusive transport. More recently, Ref. [44] considered FLR effects in non-diffusive transport in HM turbulence and concluded that the exponent γ does not change appreciably with the Larmor radius but that the effective diffusion coefficient is reduced. There is a very close connection between drift waves as described by the HM equation and Rossby waves as described by the quasigeostrophic equation, see for example Ref. [75]. Therefore, statistical test particle studies in fluid mechanics, such as Refs. [36, 113], are in principle applicable to drift wave transport.

The main new results presented here, which to our knowledge have not been reported in the literature before, include: (i) a transition from algebraic to exponential decay in the tails of PDFs of particle displacements accompanied by a transition from ballistic ($\gamma \approx 2$) to super- diffusive ($1 < \gamma < 2$) transport; (ii) a numerical study of the role of FLR on the Lagrangian velocity autocorrelation function and on the particle trapping and particle flight PDFs; (iii) the construction of a effective fractional diffusion model that reproduces the shape and the spatio-temporal anomalous self-similar scaling of the PDF of particle displacements. In recent years, fractional diffusion models have been applied to describe non-diffusive plasma transport, *e.g.* Refs. [114, 12, 115, 116, 60, 117]. Although the present

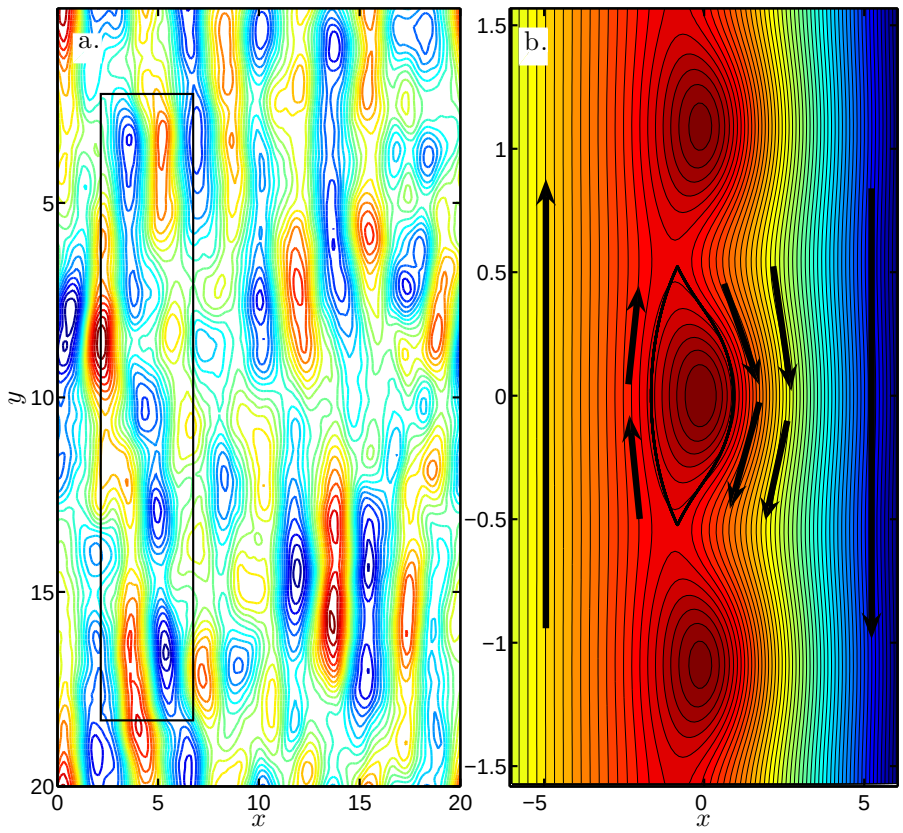

Figure 3.1: Contour plots of electrostatic potential ϕ. Panel (a) shows a snapshot of the potential obtained from a direct numerical simulation of the Hasegawa-Mima equation (3.5). Panel (b) shows ϕ at a fixed time according to the chaotic Hamiltonian transport model in Eq. (3.9). The thick line limiting the central vortex in (b) is the separatrix. Particles inside the separatrix are trapped, and, as the arrows show, particles outside the separatrix are transported by the zonal flow. The Hamiltonian model in (b) provides a reduced description of $\mathbf{E} \times \mathbf{B}$ transport dominated by vortices and zonal flows as highlighted by the rectangle in (a).

work focuses on a prototypical model of transport, the diagnostics used and the non-diffusive phenomenology discussed here might be of relevance to the study of transport in more general flows dominated by coherent structures like zonal flows and eddies. Despite the fact that these coherent structures are ubiquitous in simulations and experiments [75, 118, 119], their influence on non-diffusive transport is not well understood. In this regard, Ref. [50] showed evidence of non-diffusive transport in gyrokinetic turbulence for "intermediate" simulation times.

The rest of the chapter is organized as follows. In Sec. 3.2 the $\mathbf{E}\times\mathbf{B}$ transport model with and without FLR effects is explained. Section 3.3 shows a benchmark of the numerical method against an exact solution for the particle propagator in a parallel flow. Section 3.4 presents a summary of Lagrangian diagnostics to study non-diffusive transport. The main numerical results are presented in Sec. 3.5. Section 3.6 describes the anomalous self-similarity properties of the PDF of particle displacements and presents an effective fractional diffusion model. Section 3.7 contains the conclusions.

3.2 Transport model

We follow a Lagrangian approach to study transport and consider large ensembles of discrete particles moving in a prescribed flow. We limit attention to test particles, neglecting self-consistency effects and assuming that the particles are transported by the flow without modifying it. When finite Larmor radius (FLR) effects can also be neglected, the dynamics are determined by a drift equation which,

in the $\mathbf{E} \times \mathbf{B}$ approximation, is

$$\frac{d\mathbf{r}}{dt} = \frac{\mathbf{E} \times \mathbf{B}}{B^2}\,, \tag{3.1}$$

where $\mathbf{r} = (x, y)$ denotes the particle position, $\mathbf{E}$ is the electrostatic field, and $\mathbf{B}$ is the magnetic field. Writing $\mathbf{B} = B_0\hat{\mathbf{z}}$, and $\mathbf{E} = -\nabla\phi(x, y, t)$, Eq. (3.1) can be equivalently written as the Hamiltonian dynamical system

$$\frac{dx}{dt} = -\frac{\partial\phi}{\partial y}\,, \qquad \frac{dy}{dt} = \frac{\partial\phi}{\partial x}\,, \tag{3.2}$$

where the electrostatic potential is analogous to the Hamiltonian, and the spatial coordinates are the canonical conjugate phase space variables.

For relatively high energy particles or for a flow varying relatively rapidly in space, the zero Larmor radius approximation fails and it is necessary to incorporate FLR effects. A simple, natural way of doing this is to substitute the $\mathbf{E} \times \mathbf{B}$ flow on the right hand side of Eq. (3.2), which is evaluated at the location of the guiding center, by its value averaged over a ring of radius ρ, where ρ is the Larmor radius [107]. Formally, the procedure is given by

$$\frac{dx}{dt} = -\left\langle \frac{\partial\phi}{\partial y} \right\rangle_\theta\,, \qquad \frac{dy}{dt} = \left\langle \frac{\partial\phi}{\partial x} \right\rangle_\theta \tag{3.3}$$

where the gyroaverage, $\langle\,\rangle_\theta$, is defined as

$$\langle\Psi\rangle_\theta \equiv \frac{1}{2\pi}\int_0^{2\pi} \Psi\left(x + \rho\cos\theta, y + \rho\sin\theta\right) d\theta\,. \tag{3.4}$$

This is a good approximation provided the gyrofrequency is greater than other frequencies in the system.

In the HM model for drift waves the electrostatic potential is determined from [40]

$$[\partial_t + (\mathbf{z} \times \nabla\phi) \cdot \nabla] \left(\nabla^2\phi - \phi - \beta x\right) = 0\,, \tag{3.5}$$

where the x coordinate corresponds to the direction of the density gradient driving the drift-wave instability, and y corresponds to the direction of propagation of the drift-waves. In toroidal geometry, x is analogous to a normalized coordinate along the minor radius, and y is a poloidal-like coordinate. Here we assume a slab approximation and treat (x, y) as Cartesian coordinates. The parameter $\beta = n_0(x)'/n_0(x)$ measures the scale length of the density gradient. We model the electrostatic potential (test particle Hamiltonian) as a superposition of an equilibrium zonal shear flow, $\varphi_0(x)$, and the corresponding eigenmodes of Eq. (3.5), $\varphi_j(x)$, with perpendicular wave numbers, $k_{\perp j}$, and frequencies, $c_j k_{\perp j}$,

$$\phi = \varphi_0(x) + \sum_{j=1}^{N} \varepsilon_j\, \varphi_j(x)\, \cos k_{\perp j}(y - c_j t)\ . \tag{3.6}$$

We consider a monotonic zonal flow of the form

$$v_{y,0}(x) = \tanh(x)\,. \tag{3.7}$$

In this case, depending on the parameter values, there is a band of unstable modes bounded by two regular neutral modes with eigenfunctions [42]

$$\varphi_j = [1 + \tanh x]^{\frac{1-c_j}{2}}\, [1 - \tanh x]^{\frac{1+c_j}{2}}\ . \tag{3.8}$$

Since these modes are neutral, c_1 and c_2 are real and the corresponding values of $k_{\perp j}$ are obtained from the linear dispersion relation. Neutral modes are important

because they describe dynamics near marginal stability. Following Ref. [42], we consider a traveling wave perturbation of the first neutral mode. The electrostatic potential in the co-moving reference frame of the neutral mode takes the form

$$\phi = \ln(\cosh x) + \varphi_1(x)\,[\varepsilon_1 \cos k_{\perp 1} y + \varepsilon_2 \cos(k_{\perp 2} y - \omega t)] - c_1 x. \tag{3.9}$$

The first term on the right hand side of Eq. (3.9) is the potential of the shear flow in Eq. (3.7), and ω is the frequency of the perturbation. The wavenumbers perpendicular to the uniform magnetic field, $k_{\perp 1}$ and $k_{\perp 2}$, characterize the size of $\mathbf{E}\times\mathbf{B}$ eddies, while ε_1 and ε_2 give the amplitudes of the waves. When computing $k_\perp \rho_{th}$ to compare the scale length of the eddies in this flow to the thermal gyroradius, we use the mean value $k_\perp = (k_{\perp 1} + k_{\perp 2})/2$.

When $\varepsilon_2 = 0$ the Hamiltonian in Eq. (3.9) is time independent, and the test particles follow contours of constant ϕ shown in Fig. 3.1(b). In this case, particles inside the separatrix remain trapped and those outside the separatrix are always untrapped with $\dot{y} > 0$ left of the vortices and $\dot{y} < 0$ right of the vortices. However, when there is a time dependent perturbation, *i.e.* when $\varepsilon_2 \neq 0$ in Eq. (3.9), the $\mathbf{E}\times\mathbf{B}$ particle trajectories are in general not integrable. In this case, the separatrix breaks and forms a stochastic layer where test particles alternate chaotically between being untrapped in the zonal flow and being trapped inside the vortices. This is the phenomenon of chaotic transport that has been studied in both plasmas and fluid systems, see for example Refs. [111, 120, 121, 36] and references therein. As Fig. 3.1(a) illustrates, the simple Hamiltonian model in Eq. (3.9) provides a reduced

description of $\mathbf{E}\times\mathbf{B}$ eddies embedded in a background zonal flow in HM turbulence.

3.3 Numerical method

The zero Larmor radius calculations are based on the Hamitonian-like equations of Eq. (3.2). For the numerical integration of these equations we used the second-order symplectic predictor-corrector scheme of Ref. [122] with a fixed time step of 0.05 and 8 iterations in the predictor-corrector loop. These parameters were chosen based on numerical convergence studies and by monitoring the accuracy of energy conservation. For the model parameters we used $\varepsilon_1 = 0.5$, $\varepsilon_2 = 0.2$, $c_1 = 0.4$, $k_{\perp 1} = 6.0$, $k_{\perp 2} = 5.0$ and $\omega = 6.0$. This choice is motivated by Refs. [36, 42] where it was shown that, for this set of parameters, test particles exhibit strongly asymmetric, non-Gaussian statistics. As such, these parameters are a good starting point to study the role of FLR effects on non-diffusive transport. For the initial conditions we used an ensemble of particles located in the vicinity of the hyperbolic fixed point of the Hamiltonian at $(x_0, y_0) \sim (-1, -0.5)$. This localization guarantees that a large fraction of the particles will stay in the stochastic layer and undergo chaotic transport. Other choices of initial positions can lead to integrable motion with particles permanently either inside the eddies, circling, or outside, following the zonal flow.

The only difference between the zero and finite Larmor radius calculations is in the evaluation of the velocity of the test particle. Assuming fast gyration in a strong $\mathbf{B}$ field, the gyroaverage of the $\mathbf{E}\times\mathbf{B}$ velocity is computed over a circle of

radius ρ, where ρ is the Larmor radius of the particle. Throughout this chapter we will assume a Maxwellian equilibrium distribution for the Larmor radii of the test particles of the form

$$H(\rho) = \frac{2}{\rho_{th}^2} e^{-\rho^2/\rho_{th}^2} , \tag{3.10}$$

normalized according to $\int_0^\infty H(\rho)\rho d\rho = 1$. For the numerical computation of the gyroaverage we approximate the circle with an inscribed polygon with N_g-sides and approximate the integral over the circle as the average over the vertices of the polygon. This method, widely used in kinetic particle codes (*e.g.* [107]), simply samples the field on the gyration arc at a small number of equally spaced points. For example, the 8-point (octagon) approximation evaluates the gyroaverage by considering $N_g = 8$ points distributed around the circle in equal increments, *i.e.*, at $\theta = \{2\pi/8, 2\pi/7, \ldots 2\pi\}$. If the mean gyroradius, $\langle\rho\rangle = (\sqrt{\pi}/2)\rho_{th}$, becomes large relative to the typical scale length, $\sim 1/k_\perp$, of the flow, *i.e.*, if $k_\perp\rho_{th} \gg 1$, the number of points used to compute the gyroaverage must be increased to maintain the same level of accuracy.

The error involved in the approximation of the gyroaverage on N_g for a given value of $k_\perp\rho_{th}$ and, therefore, a benchmark for the accuracy of the numerical scheme can be studied by considering the following parallel flow in arbitrary geometry

$$\phi = \phi_0 \cos(k_\perp x) . \tag{3.11}$$

The main object of interest is the probability distribution function of particle displacements, or propagator, $P = P(y, t|y', t')$, which gives the probability for a particle to be at y' at time t' if it was at y at time t. Since $v_x = 0$ for this choice of ϕ,

we restrict study to the y direction. The function P depends on $k_\perp \rho_{th}$ and the goal is to study the error in the numerical evaluation of P as function of $k_\perp \rho_{th}$ and the value of N_g used in the approximation of the gyroaverage. As discussed in Appendix A, the exact propagator for Eq. (3.11) is given by

$$P(y,t|y',t') = \frac{1}{U_0(t-t')}\,\mathcal{G}(\zeta)\,, \qquad \zeta = \frac{1}{U_0}\frac{(y-y')}{(t-t')}\,, \tag{3.12}$$

with

$$\mathcal{G}(\zeta) = \frac{2}{(k_\perp \rho_{th})^2}\sum_{i=1}^{N_z}\frac{z_i\, e^{-(z_i/k_\perp\rho_{th})^2}}{|J_1(z_i)|}\,, \tag{3.13}$$

where $z_i = z_i(\zeta)$ denotes the i-th zero of the equation $J_0(z_i) - \zeta = 0$. Here, J_0 is the order zero Bessel function of the first kind. For a given ζ, the number of zeros of this equation is N_z which goes to ∞ as ζ goes to zero. Note also that because the minimum and maximum values of J_0 are -0.4025 and 1, respectively, no zero exists for $\zeta < -0.4025$ or $\zeta > 1$. Therefore, P identically vanishes outside the interval $\zeta \in (-0.4025, 1)$. Despite its apparent complexity, this analytical result provides a valuable benchmark to assess the accuracy of the gyroaverage computation.

Figure 3.2 compares the exact propagator in Eq. (3.12) with the propagator obtained from direct numerical integration of the gyroaverage equations of motion in Eq. (3.3) for different values of $k_\perp \rho_{th}$ and N_g. The FLR effects significantly change the $k_\perp \rho_{th} = 0$ propagator, which is a δ-function centered at $\zeta = 1$: $P(y,t|y',t') = (1/U_0(t-t'))\delta(\zeta - 1)$. It is observed that for $k_\perp \rho_{th} = 3.0$, $N_g = 8$ produces relatively good results, although it misses the small spike in P around $\delta y/U_0 t \sim 0.25$. Other $N_g = 8$ cases with $k_\perp \rho_{th} \leq 3.0$ (not shown) give nearly exact agreement. However, for $k_\perp \rho_{th} = 5.0$, the $N_g = 8$ average departs significantly from the exact result. This

failure means that choosing $N_g > 8$, such as $N_g = 16$, is necessary. One is led to conclude that the $N_g = 8$ method should not be used for values of $k_\perp \rho_{th} \gtrsim 3.0$.

This statement is further supported by an assessment of accuracy when representing $J_0(\iota)$ as a finite sum based on the integral

$$J_0(\iota) = \frac{1}{2\pi} \int_0^{2\pi} \cos(\iota \sin \tau) d\tau \,. \tag{3.14}$$

The Bessel function is used in spectral simulations of the gyrokinetic equation, which gives the spectral technique an advantage that we cannot use here. The Bessel integral representation may be discretized and evaluated using different numbers of terms in the sum. Additional terms in the sum reduce the error of discretization just as increasing N_g reduces the error of discrete gyroaveraging. When the integral is approximated with 8 or 16 equally spaced points between 0 and 2π, the result agrees to 0.1% with the value of $J_0(\iota)$ up to $\iota = 3.0$ or $\iota = 9.0$, respectively. For higher values of ι, the approximation diverges quickly, just as the discrete gyroaverage method diverges from the analytic result for increasing $k_\perp \rho_{th}$. Based on this, care must be taken in selecting N_g for large values of $k_\perp \rho_{th}$. In this chapter we restrict attention to $k_\perp \rho_{th} \leq 3.0$ and use an adaptive N_g technique based on Ref. [123].

3.4 Diagnostics for non-diffusive transport

In this section we review several Lagrangian diagnostics for transport study. After defining each diagnostic, we recall expected behavior for both diffusive and non-diffusive transport. These diagnostics have been successfully used in transport experiments, models, and simulations in both fluids and plasmas. For examples

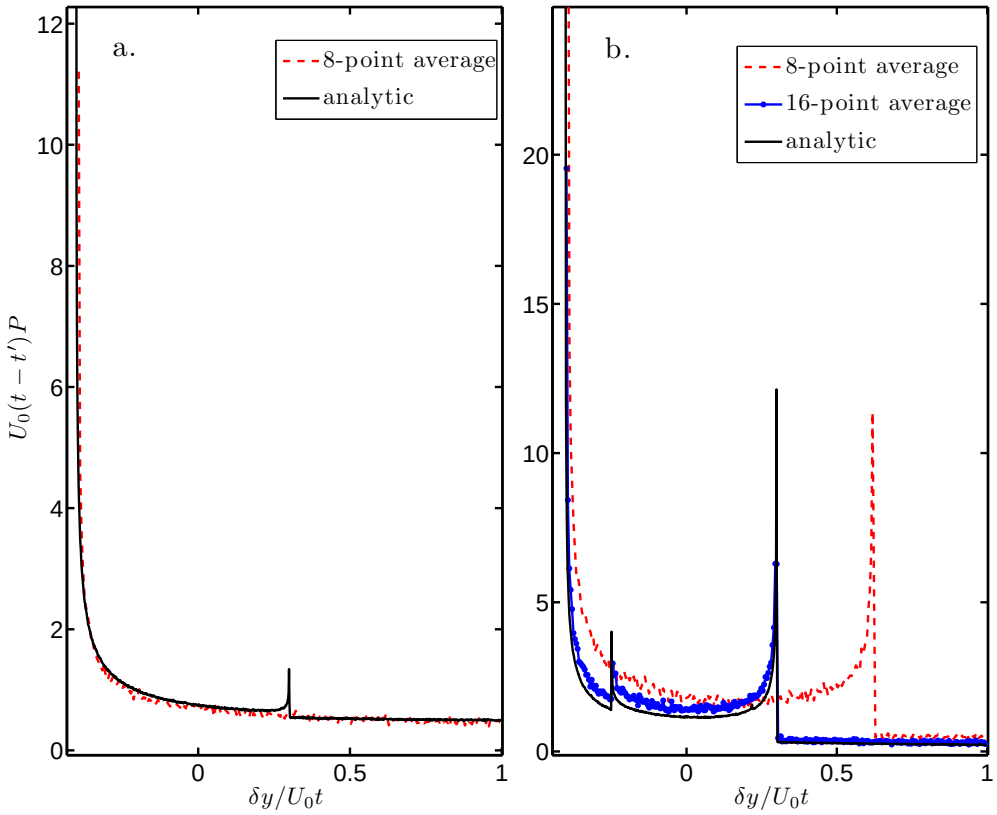

Figure 3.2: Particle propagator for finite Larmor radius transport in the parallel shear flow of Eq. (3.11). Panel (a) corresponds to $k_\perp \rho_{th} = 3.0$ and (b) corresponds to $k_\perp \rho_{th} = 5.0$. The solid line denotes the exact analytical result in Eq. (3.12), the dashed line and the marked line (shown only in (b)) denote the 8-point and the 16-point average numerical results, respectively.

see Refs. [121, 36, 12] and references therein. To simplify the discussion we limit attention to one-dimensional transport, *i.e.* transport in the poloidal-like direction y. In the specific transport problem considered in this chapter, y is in the direction of the propagation of the zonal flow and the drift waves, and is orthogonal to both the density gradient and the magnetic field. Generalization of the diagnostics to higher dimensions is straightforward.

3.4.1 Statistical moments of particle displacements

The basic particle data consists of the ensemble $\{y_i(t)\}$, with $i = 1, 2, \ldots N_p$, containing the time evolution of the y-coordinate of the N_p test particles in the simulation. From here we define the ensemble of particle displacements, $\{\delta y_i(t)\}$, where $\delta y_i(t) = y_i(t) - y_i(0)$. The statistical moments of the particle displacements provide one of the simplest and most natural characterizations of Lagrangian transport. Of particular interest are the mean $M(t) = \langle \delta y \rangle$ and the variance $\sigma^2(t) = \langle [\delta y - \langle \delta y \rangle]^2 \rangle$ where $\langle\ \rangle$ denotes ensemble average. In the case of diffusive transport (*e.g.*, a Brownian random walk), the moments exhibit asymptotic linear scaling in time, which allows the definition of an effective transport velocity (pinch) V_{eff} and an effective diffusivity D_{eff} according to $V_{eff} = \lim_{t\to\infty} M(t)/t$ and $D_{eff} = \lim_{t\to\infty} \sigma^2(t)/2t$.

However, in the case of nondiffusive transport, the moments display anomalous scaling of the form

$$M \sim t^{\chi}\,, \qquad \sigma^2 \sim t^{\gamma}\,, \tag{3.15}$$

with $\chi \neq 1$ and $\gamma \neq 1$. If $0 < \gamma < 1$ the spreading is slower than in the diffusive

case and transport is called sub-diffusive. If $1 < \gamma < 2$, the spreading is faster than diffusion and transport is super-diffusive. A similar classification applies for sub-advection ($0 < \chi < 1$) and super-advection ($1 < \chi < 2$). In the presence of anomalous scaling, the introduction of an effective transport velocity or an effective diffusivity is meaningless since these transport coefficients are either zero (in the sub-advection/sub-diffusion case) or infinite (in the super-advection/super-diffusion case). The diagnostics based on the statistical moments are straightforward to implement. The key is to look for a scaling region in a log-log plot of the moments as functions of time, after transients have passed. However, as with the data analyzed below, it is possible for the moments to follow different scaling regimes for different time intervals.

3.4.2 Particle displacement PDFs: spatial scaling

The probability distribution function (PDF) of particle displacements, $P(\delta y, t|\delta y', t')$, contains all of the statistical information from displacements beyond the first and second moments. By definition, $P(\delta y, t|\delta y', t' = t) = \delta(y)$. Numerically, P is constructed from the normalized histogram of particle positions at a given time. Formally, $P(\delta y, t|\delta y', t')$ corresponds to the Green's function determining the distribution of the test particles in terms of the initial particle distribution. For a Brownian random walk, the central limit theorem implies that P asymptotically approaches a Gaussian distribution, P_G, that satisfies diffusive scaling, $P_G = t^{-1/2}G(Y/t^{1/2})$, where G is a Gaussian and $Y = \delta y - \langle \delta y \rangle$. However, a non-diffusive propagator can

exhibit the more general (anomalous) self-similar scaling

$$P = t^{-\gamma/2} L(Y/t^{\gamma/2}) \,, \tag{3.16}$$

where $0 < \gamma < 2$ and L is a non-Gaussian function. Note that, by construction, the propagator has zero mean, and the scaling exponent γ in Eq. (3.16) is the same as the exponent in Eq. (3.15). From Eq. (3.16) it follows that $P(Y,t) = \lambda^{\gamma/2} P(\lambda^{\gamma/2} Y, \lambda t)$ where λ is a real number. Therefore, if the propagator is self-similar, P is invariant with respect to the space-time renormalization transformation $(Y,t) \rightarrow (\lambda^{\gamma/2} Y, \lambda t)$, up to a scale factor.

Equation (3.16) provides a useful diagnostic to reveal non-diffusive transport and, in particular, the existence of anomalous self- similar scaling. This diagnostic is implemented by plotting the propagator at different times in rescaled coordinates, *i.e.* $t^{\gamma/2} P$ versus $Y/t^{\gamma/2}$. With self-similar non-diffusive transport, the plots at different times rescale and collapse into a single function L. One of the most important departures from Gaussianity is algebraic decaying, "fat" tails in the propagator for large δy at fixed t,

$$P \sim \delta y^{-\zeta} \,. \tag{3.17}$$

When this behavior is found, the value of the scaling exponent ζ is a useful diagnostic that characterizes the intermittency of the transport process.

3.4.3 Trapping and flight probability distribution functions

Diffusive transport can be interpreted as a coarse-grained (macroscopic) description of a fine-grained (microscopic) Brownian random walk. In a similar way,

non-diffusive transport can sometimes be viewed as the result of a non-Brownian random walk with a non-Gaussian and/or non-Markovian [84] underlying stochastic process. Trapping and flight probability distribution functions are two useful diagnostics for the characterization of non-Brownian random walks. Given a particle trajectory, $y_i(t)$, a trapping event is defined a portion of the trajectory during which the particle stays on an eddy. Flight events are portions that are not trapping events. Thus, each particle orbit in the ensemble of initial conditions may be decomposed as a sequence of trapping and flight events.

Numerically, the events are detected by tracking reversals in the Lagrangian acceleration of particles. From the histograms of trapping and flight events one may construct the probability distribution functions of trapping events, $\psi(t)$, and flight events, $\lambda(y)$. Indications of non-diffusive transport can be explored by studying the departures of $\lambda(y)$ and $\psi(t)$ from the Gaussian and exponential dependencies characteristic of Brownian random walks. Of particular interest is the presence of asymptotic algebraic scaling of the form,

$$\psi \sim t^{-\nu}\,, \qquad \lambda \sim y^{-\mu}\,. \tag{3.18}$$

When $\mu < 1$ the mean waiting time, $\int t\psi dt$, is infinite and no characteristic temporal scale exists. In the Lévy flight regime $\mu < 3$, and therefore the second moment, $\int y^2\lambda dy$, diverges and no characteristic spatial scale exists. The PDFs of flight and trapping events are in principle interesting because of their connection to the continuous time random walk (CTRW) model, which, in the fluid continuum limit, can be described using fractional diffusion equations [87, 124, 58].

3.4.4 Lagrangian velocity autocorrelation function

Further insights into non-diffusive transport can be gained by looking at the Lagrangian velocity autocorrelation function $C(\tau) = \langle v_y(\tau)v_y(0)\rangle$ where v_y is the Lagrangian velocity of a particle. The Green-Kubo relation, $d\sigma^2/dt = 2\int_0^t C(\tau)d\tau$, relates the velocity autocorrelation function to the variance of displacements. When C decays fast enough so that the integral converges, this relation can be used to define an effective diffusivity according to $D_{eff} = \int_0^\infty C(\tau)d\tau$. However, when C has algebraic decay of the form

$$C(\tau) \sim \tau^{-\kappa}\,, \tag{3.19}$$

with $\kappa < 1$, the integral diverges and the concept of effective diffusivity loses meaning. For super-diffusive transport, $\sigma^2 \sim t^\gamma$ implies $\gamma = 2 - \kappa$.

3.5 Numerical results

For the Lagrangian statistics we consider ensembles of $N = 8 \times 10^4$ test particles, and integrate the equations of motion, with and without FLR effects, up to $t = 5.2 \times 10^3$. The zero Larmor radius results were obtained from the numerical integration of the guiding center equations in Eq. (3.3) with the Hamiltonian in Eq. (3.9) with $\varepsilon_1 = 0.5$, $\varepsilon_2 = 0.2$, $c_1 = 0.4$, $k_{\perp 1} = 6.0$, $k_{\perp 2} = 5.0$, $\omega = 6.0$. The same Hamiltonian and parameter values were used in the FLR ($0 < k_\perp \rho_{th} < 3$) calculations based on an N_g adaptive gyroaverage.

The Poincaré plots in Fig. 3.3 show the dependence of the degree of stochasticity on the value of $k_\perp \rho$. Figure 3.3(a) corresponds to $k_\perp \rho = 0$. The degree of stochas-

ticity is relatively large and, consistent with the results reported in Refs. [36, 42], the stochastic layer is strongly asymmetric. In particular, the region of stochasticity left of the unperturbed separatrix (shown with the bold line) is very small. As will be discussed below, this asymmetry manifests directly in the skewness of the tail of the test particle propagator, which decays strongly for $\delta y > 0$ due to the very low probability of having sticky-flight particles jumping in the $y > 0$ direction. It may be interesting to compare ρ_{th} to the thickness of the lower branch of the stochastic region, Δ_s. For example, when $k_\perp \rho_{th} = \{1.2, 2\}$, $\rho_{th}/\Delta_s = \{0.44, 1.8\}$. This trend is mainly due to the rapid shrinkage of the stochastic layer as a function of ρ_{th}. When $k_\perp \rho_{th} = 3$, the value of Δ_s is very difficult to determine because the stochastic layer has almost completely disappeared.

In the FLR calculations the test particles have a Maxwellian distribution of Larmor radii characterized by a mean value, ρ_{th}. Thus, depending on its specific value of ρ, each particle "sees" a different Hamiltonian, which in general will be stochastic to a lesser degree as ρ increases. Figures 3.3(b)-(d) illustrate this with Poincaré plots corresponding to (b) $k_\perp \rho = 1.2$, (c) $k_\perp \rho = 2.0$ and (d) $k_\perp \rho = 3.0$. Each one of these Poincaré sections was computed by assigning the *same* value of $k_\perp \rho$, to all the initial conditions. It is observed that the value of $k_\perp \rho$ has a direct non-trivial influence on the degree of stochasticity. In general, a Poincaré plot corresponding to an ensemble of particles with a Maxwellian distribution of gyroradii will be a mixture of $k_\perp \rho$ Poincaré plots, as seen in Fig. 3.4. The crossings of curves in the Poincaré plots indicates the presence of multiple Hamiltonian systems indexed by values of $k_\perp \rho$.

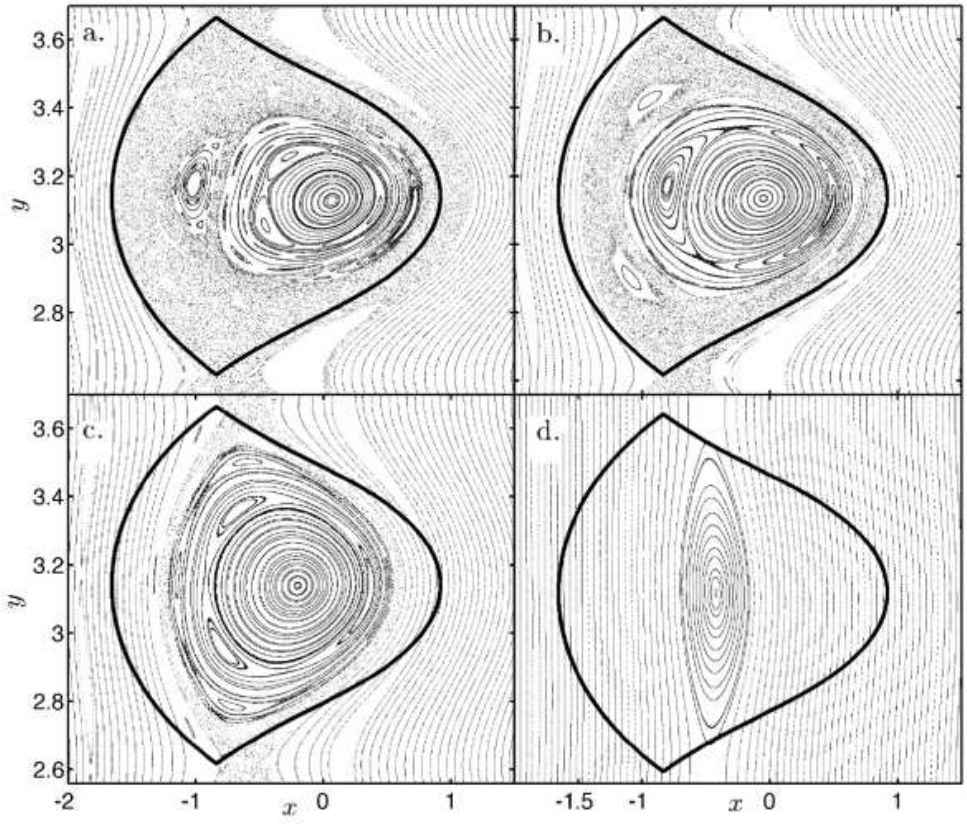

Figure 3.3: Dependence of phase space topology and stochasticity on Larmor radius for the Hamiltonian model in Eq. (3.9). The panels show Poincaré maps for a ensemble of particles with gyroradius distribution of the form $H = \delta(k_\perp \rho - k_\perp \rho_{th})$ with (a) $k_\perp \rho_{th} = 0$, (b) $k_\perp \rho_{th} = 1.2$, (c) $k_\perp \rho_{th} = 2.0$ and (d) $k_\perp \rho_{th} = 3.0$. The bold, solid curve indicates the unperturbed separatrix for $k_\perp \rho_{th} = 0$.

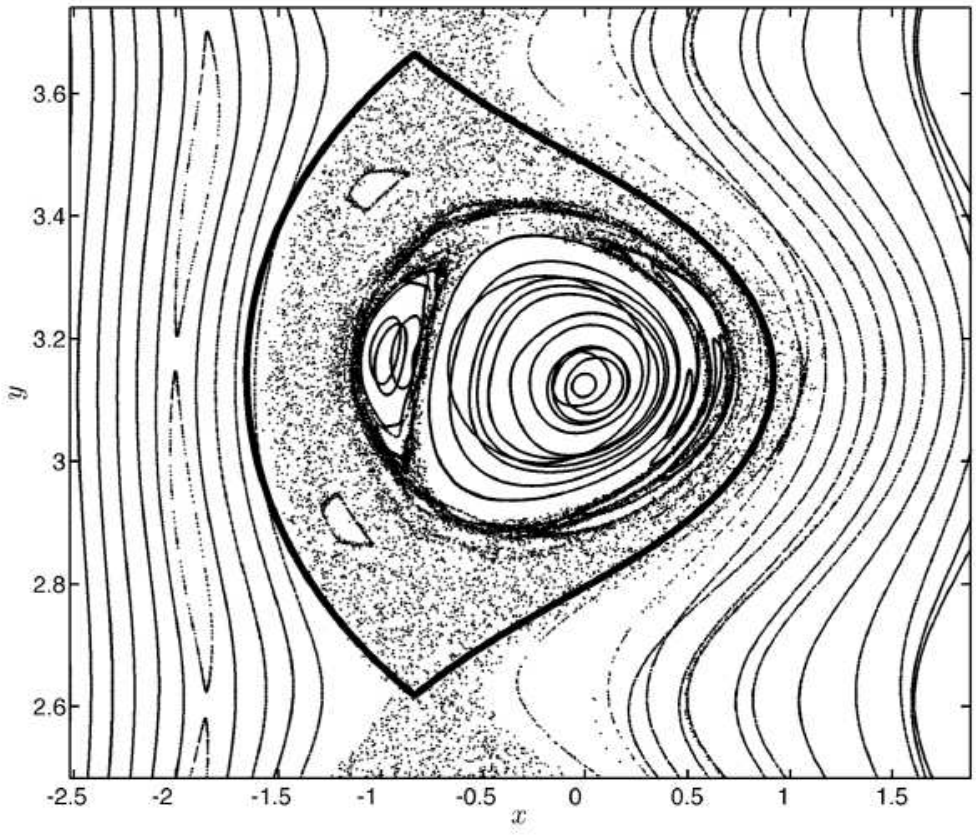

Figure 3.4: Poincaré plot for multiple gyroradii values from the Maxwellian distribution with $k_\perp \rho_{th} = 0.6$. Crossings of curves indicate the presence of multiple Hamiltonian systems, one for each value of ρ.

To compute the Lagrangian diagnostics of non-diffusive transport, we considered groups of particles located in the vicinity of a hyperbolic equilibrium point of the Hamiltonian. The resulting trajectories can be divided into three categories: (a) passing trajectories that follow the zonal flow and never enter an $\mathbf{E} \times \mathbf{B}$ eddy (vortex), (b) stagnant trajectories which never leave an eddy and (c) sticky-flight trajectories which, as shown in Fig. 3.5, alternate between the eddies and the zonal flow. Since the statistics of the passing and the stagnant trajectories are trivial, these particles will be ignored during the data analysis.

Several techniques for isolating sticky-flight trajectories can be devised. Our trajectory filter works by examining all trajectories during their entire history, and discarding those that never encircle a vortex (passing) and those that do not move more than one vortex width from ther original positions (stagnant). We have also tested a filter in Fourier-velocity space that discards horizontal velocity time series without a broadband spectrum. Depending on the threshold for defining "broadband," the Fourier filter gives practically the same results as the trajectory filter. Analysis of sticky-flights in more realistic velocity fields would be served better by a Fourier-velocity filter. The proper threshold for defining a "broadband" spectrum can be found from asymptotic considerations.

Figure 3.6 shows the effect of the trajectory filter on the histogram of Larmor radii. In the computation of the histogram we show the number of particles, N, multiplied by the appropriate metric factor ρ. The solid line denotes the histogram considering all the particles in the ensemble, *i.e.* without the filter. As expected, this histogram corresponds to a sampling of the Mawellian distribution in Eq. (3.10). It

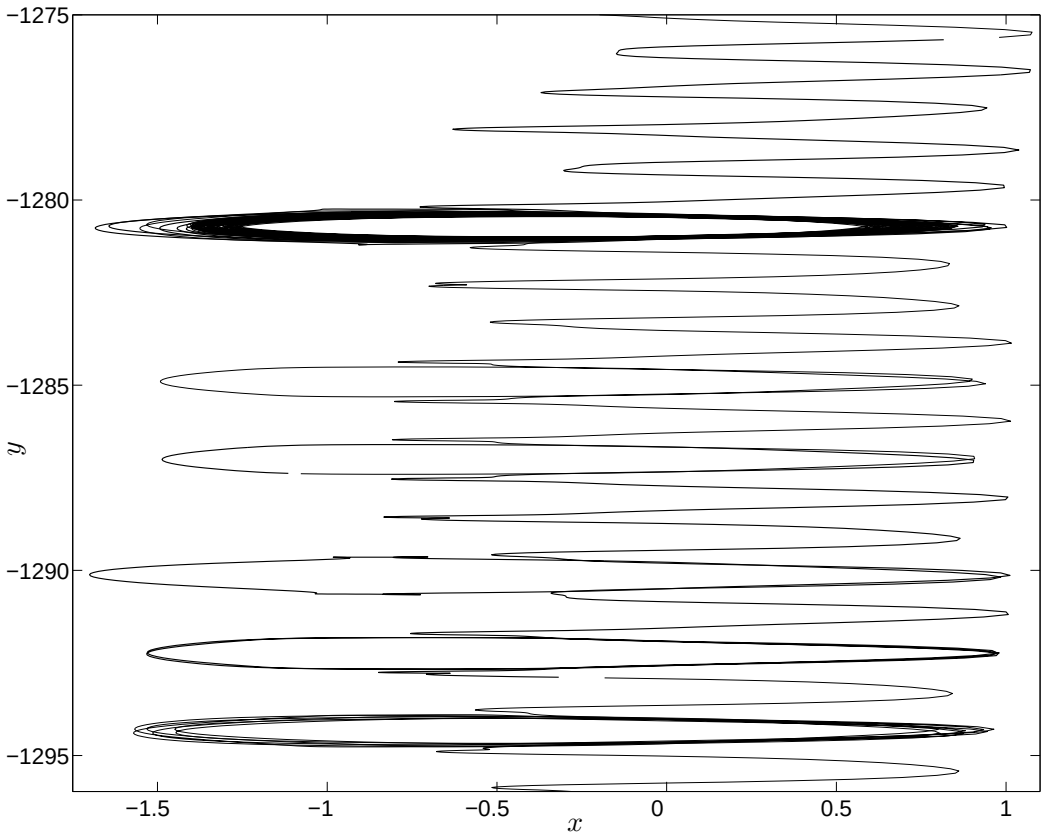

Figure 3.5: Typical sticky-flight trajectory in the Hamiltonian transport model. This particle alternates in a seemingly unpredictable way between being trapped in $\mathbf{E} \times \mathbf{B}$ eddies and being transported following the zonal shear flow. Other types of orbits, not shown, correspond to trapped orbits that never leave the original eddy, or passing orbits that move following the zonal flows without being trapped.

is observed that the filter tends to remove particles with large ρ, and, as expected, the number of particles removed decreases with t_l, the time of filter application. Since $t_l = 5200$ appears to give an asymptotic value for the number of sticky-flights, it is used as the filtering time for the following diagnostics. When scaling values are reported for $t < 5200$, the filter is still applied uniformly at $t = 5200$. The first column in Table 3.1 gives Π_s, the percentage of sticky-flights, for each tested value of $k_\perp \rho_{th}$ when the filter is applied at $t_l = 5200$.

3.5.1 Super-diffusive scaling

Before presenting the chaotic transport results, it is instructive to go back to the simple parallel flow in Eq. 3.11 to explore the role of FLR effects on particle dispersion in the context of an integrable flow for a ensemble of particles initially distributed according to $P = \delta(x - x_0)\delta(y - y_0)$. If all the particles have the *same* Larmor radius, i.e. if $H(\rho) = \delta(\rho - \rho_{th})$, then as Eq. A.3 in Appendix A shows, P maintains its delta function shape and simply drifts with the effective velocity $J_0(k\rho)U_0$, which in the limit of zero Larmor radius corresponds to the parallel flow velocity. In this case, FLR effects are irrelevant since they simply rescale the velocity. However, when the particles have different Larmor radii, as in the Maxwellian case of Eq. A.4, the effective velocity of each particle will be different and the initial delta function will spread in space as is evident in the particle propagators shown in Fig. 3.2. In this case, the first and second moments are $M = V_{eff}t$ and $\sigma^2 = At^2$, where V_{eff} and A are functions of $k_\perp \rho_{th}$ given in Appendix A. The key issue to

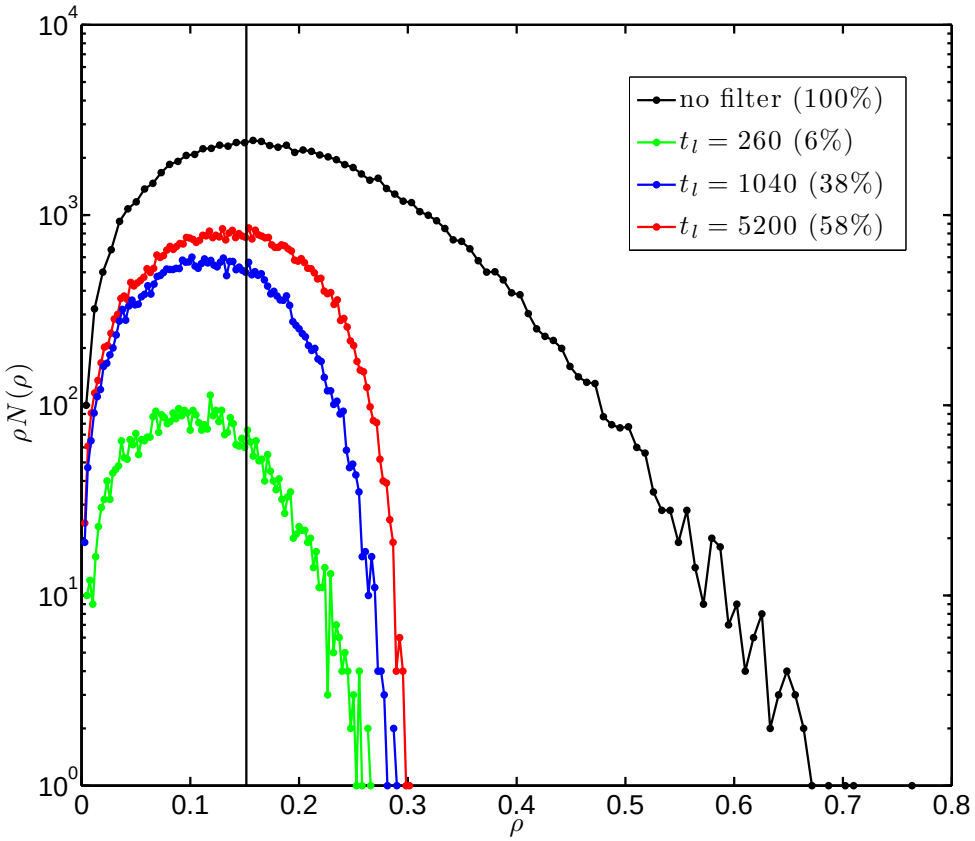

Figure 3.6: Gyroradius histogram for $k_\perp \rho_{th} = 1.2$ with sticky-flight filter applied at various times. The uppermost curve shows the unfiltered distribution obtained from the sampling of the 2-D Maxwellian distribution in Eq. (3.10). The other curves give the distribution at different times after the filter (which keeps only the sticky-flight orbits) has been applied. The vertical line marks the maximum of the unfiltered distribution.

Table 3.1: Measures of sticky trajectories and non-diffusive transport for the $v_y = \tanh(x)$ model with initial positions in a box centered on a hyperbolic fixed point. The percentage of sticky trajectories at $t = 5200$, Π_s, is shown, along with the mean and variance time power law exponents, χ and γ respectively, at early and late time. "Early" refers to a fit for $104 < t < 1040$ and "late" refers to $4700 < t < 5200$. Accuracy for these fits is similar to that observed in Fig. 3.7, and equal to ± 0.1.

$k_\perp \rho_{th}$	Π_s	χ_{early}	χ_{late}	γ_{early}	γ_{late}	$\zeta_{t=1040}$
0.0	96	1.1	1.0	1.9	1.6	2.0
0.001	96	1.1	1.0	1.9	1.6	2.0
0.01	96	1.1	1.0	1.9	1.6	2.0
0.1	98	1.1	1.1	2.0	1.8	2.2
0.2	97	1.1	1.1	2.0	1.8	2.3
0.4	96	1.1	1.1	1.9	1.9	2.3
0.6	92	1.1	1.0	1.9	1.9	2.7
0.8	83	1.1	1.1	1.9	1.9	2.7
1.2	58	0.9	1.0	1.8	1.8	2.9
1.6	36	0.8	1.0	1.8	1.8	2.9
3.0	11	0.9	0.9	1.8	1.6	3.1

observe is that the variance does not exhibit diffusive scaling, and that a distribution of Larmor radii gives rise to a ballistic spreading of the particles.

For transport in the nonintegrable flow with the zonal flow and drift waves, Fig. 3.7 shows the mean, $M(t)$, and variance, $\sigma^2(t)$, for $k_\perp \rho_{th} = 0$ and $k_\perp \rho_{th} = 0.6$. A summary of the values of the scaling exponents χ and γ for all the values of $k_\perp \rho_{th}$ studied is presented in Table 3.1. To a good approximation, the mean exhibits linear scaling, *i.e.* $\chi \approx 1$ in Eq. (3.15), indicative of regular advection, for all values of $k_\perp \rho_{th}$. The variance consistently shows clear evidence of super-diffusive transport, *i.e.* $\gamma > 1$ in Eq. (3.15). In the zero Larmor radius case, two scaling regimes are observed. Up to $t \approx 10^3$, which corresponds to the simulations in Ref. [36], the power law fitting in Fig. 3.7(b) indicates an almost ballistic scaling with $\gamma = 1.9$. However, at a later time there is a transition to $\gamma = 1.6$. As Table 3.1 shows, FLR effects seem to eliminate the distinction between early and late regimes. In particular, according to Fig. 3.7(d) where $k_\perp \rho_{th} = 0.6$, the scaling $\gamma = 1.6$ holds throughout the integration time. As a general trend, it is observed that the exponent γ decreases with increasing $k_\perp \rho_{th}$ beyond 0.1. Statistics for sticky-flights become poor for $k_\perp \rho_{th} = 3$ because the degree of stochasticity [see Fig. 3.3(d)] becomes small.

3.5.2 Asymmetric, non-Gaussian PDF of particle displacements

Motivated by the presence of two different scaling regimens in the variance, we study the PDF of particle displacements at intermediate and large times. Figure 3.8

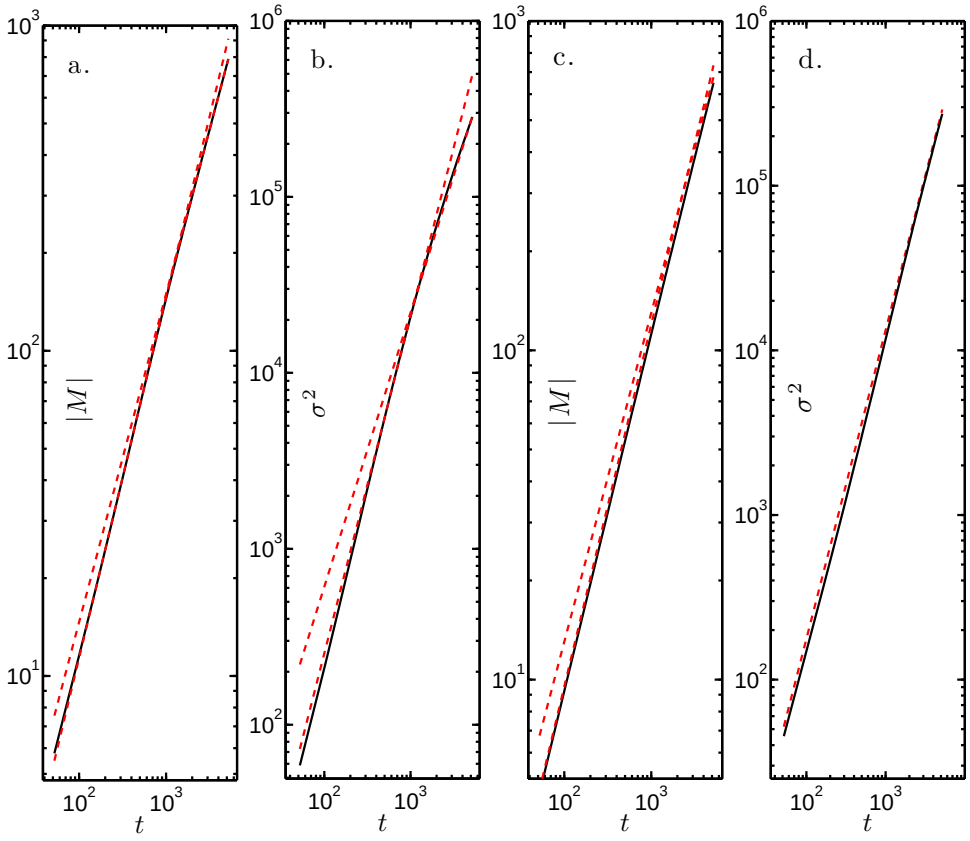

Figure 3.7: Time evolution of statistical moments of particle displacements. Panels (a) and (b) correspond to $k_\perp \rho_{th} = 0$ and panels (c) and (d) correspond to $k_\perp \rho_{th} = 0.6$. Plots (a) and (c) give the absolute value of the first moment M, and plots (b) and (d) show the second moment. The dashed lines in panels (a) and (c) have slopes corresponding to $\chi = 1.1(0.9)$ and $\chi = 1.0$ indicative of normal advection scaling, *i.e.* $|M| \sim t^\chi$ with $\chi \approx 1$. The variance shows super-diffusive scaling *i.e.* $\sigma^2 \sim t^\gamma$ with $\gamma \neq 1$. However, in the $k_\perp \rho_{th} = 0$ case, a sharp transition is observed in the anomalous diffusion exponent. The dashed lines in panels (b) have slopes corresponding to $\gamma = 1.9$ and $\gamma = 1.6$. The dashed line in panel (d) has a slope corresponding $\gamma = 1.9$ indicating a uniform scaling of the variance for $k_\perp \rho_{th} = 0.6$.

shows the PDFs at intermediate times, with 3.8(a) corresponding to $k_\perp \rho_{th} = 0$ and 3.8(b) corresponding to $k_\perp \rho_{th} = 1.2$. The solid lines denote the PDFs of the filtered data, (*i.e.* including only sticky-flight orbits) and the dashed line denotes the PDFs of the unfiltered data. The spikes for large δy in the unfiltered distributions result from the contribution of passing orbits that the filter effectively removes. The filtered PDFs are clearly non-Gaussian with strong skewness in the negative δy direction. The strong left-right asymmetry of the PDFs results from the asymmetry of the stochastic layer.

In particular, as the Poincaré plots in Fig. 3.3 show, the stochastic layer is thicker on the right side of the vortex. This asymmetry depends on the value of the perturbation frequency ω in Eq. (3.9). In fact, as discussed in Ref. [36], the relative thickness of the stochastic layers, and therefore the symmetry of tracer transport, can be controlled by changing ω. As the insets in Fig. 7 show, both PDFs decay algebraically as in Eq. (3.17). However, a strong dependence of the decay exponent on the value of the Larmor radius is observed. For $k_\perp \rho_{th} = 0$, $\zeta \approx 1.95$, and for $k_\perp \rho_{th} = 1.2$, $\zeta \approx 2.9$. As Table 3.1 indicates, the value of the decay exponent ζ increases monotonically with $k_\perp \rho_{th}$.

The particle displacement PDFs at longer times are shown in Fig. 3.9. As before, the solid lines denote the filtered distribution and the dashed lines the unfiltered distribution. A critical dependence on the Larmor radius is observed. For $k_\perp \rho_{th} = 0$ the PDF transitions to an exponential decaying distribution, whereas for $k_\perp \rho_{th} = 0.6$ the PDF maintains its algebraic decay with the same exponent as the one observed at short times, $\zeta \approx 2.9$. The robustness of the algebraic decay in the

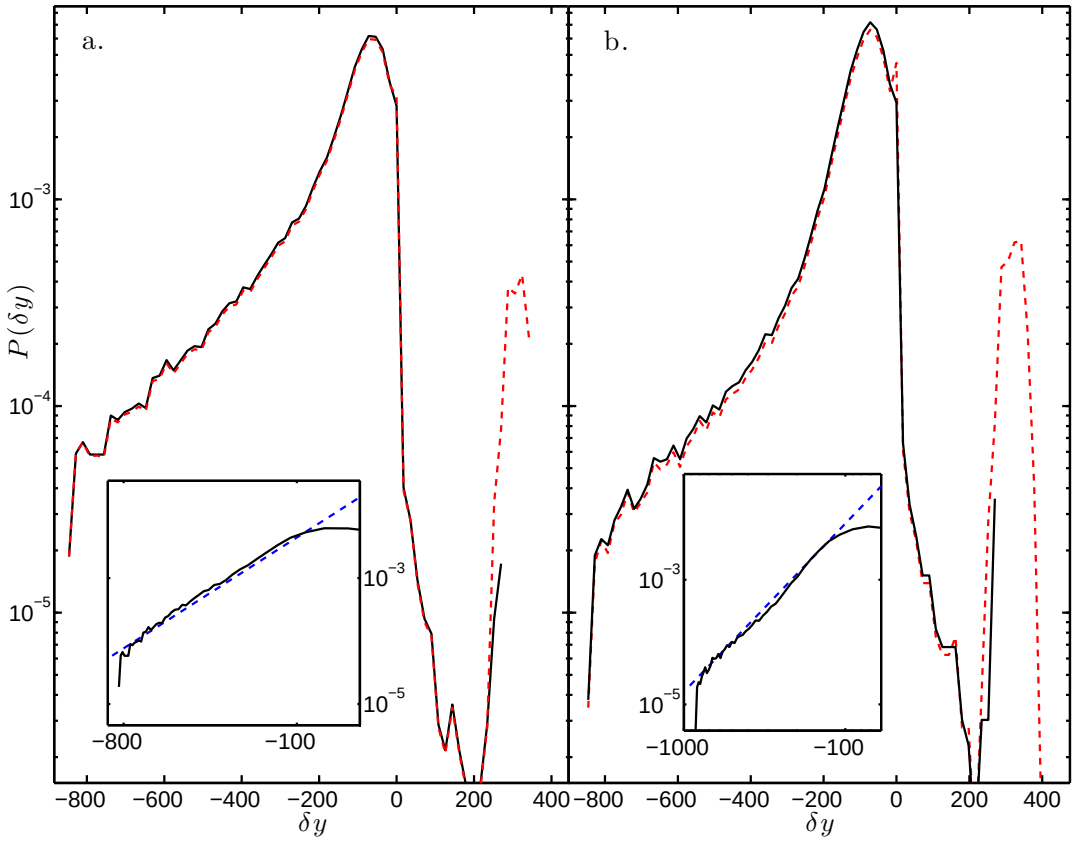

Figure 3.8: Probability distribution function of particle displacements at intermediate times, $t = 1040$. Panel (a) corresponds to $k_\perp \rho_{th} = 0$ and panel (b) corresponds to $k_\perp \rho_{th} = 1.2$. The insets in both figures show evidence of algebraic decaying tails, $P \sim \delta y^{-\zeta}$ with $\zeta = 1.95$ for $k_\perp \rho_{th} = 0$ and $\zeta = 2.9$ for $k_\perp \rho_{th} = 1.2$. In both plots, the solid line denotes the PDF of sticky-flights (*i.e.*, excluding the passing and trapped orbits), and the dashed line denotes the PDF computed using all the orbits.

finite Larmor radius case might be attributed to the persistence of large particle displacements which, due to the presence of the strong zonal flows, are enhanced by the gyroaverage. One should note that a Lévy process requires $\zeta < 3$, which means that the increase of $k_\perp \rho_{th}$ moves the process away from the Lévy type.

The transition from algebraic to exponential decay in the zero Larmor radius case is likely due to the presence of truncated Lévy flights. Exact Lévy flights produce long particle displacements that result in slowly decaying algebraic tails at all times. However, non-ideal effects such as particle decorrelation might preclude the existence of arbitrarily long displacements, resulting in a faster than algebraic decay of the tails at long times. See, for example, Refs. [90, 125, 126] for more details on truncated Lévy processes. One obvious reason for a truncated Lévy process in the present system is the finite velocity requirement, which precludes the existence of infinite jumps.

3.5.3 Lévy flights and algebraic trapping PDFs

Figure 3.10 shows the trapping time and flight length PDFs for $k_\perp \rho_{th} = 0$ in (a) and (c), and for $k_\perp \rho_{th} = 1.2$ in (b) and (d). In both cases, the trapping PDF clearly decays algebraically as in Eq. (3.18), with $\nu = 1.8$ for $k_\perp \rho_{th} = 0$, and $\nu = 2.0$ for $k_\perp \rho_{th} = 1.2$. Figures 3.10(c) and 3.10(d) show the PDFs of flight lengths. Note that, because transport in this case is asymmetric, there are actually two flight PDFs, one corresponding to positive flights (with dashed fit line) and another corresponding to negative flights (solid fit line). The PDF of negative flights decays as a power law

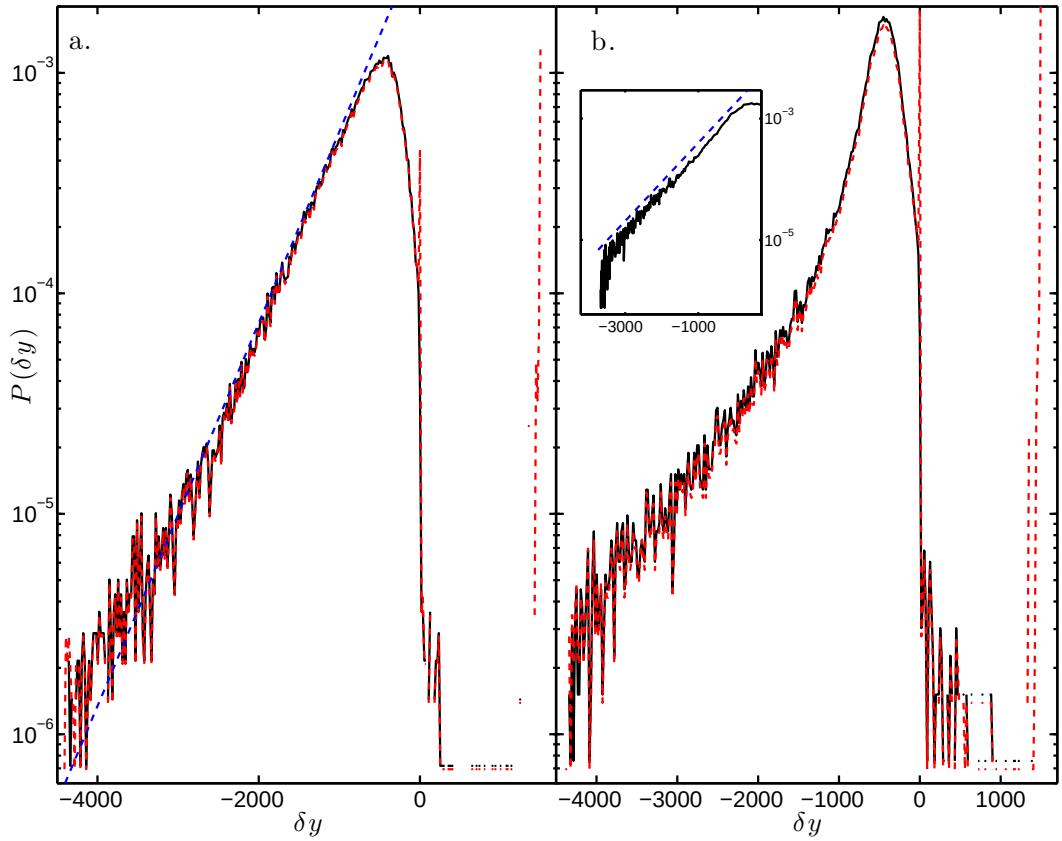

Figure 3.9: Probability distribution function of particle displacements at large times, $t = 5200$. Panel (a) corresponds to $k_\perp \rho_{th} = 0$ and panel (b) corresponds to $k_\perp \rho_{th} = 1.2$. In case (a) the PDF decays exponentially, $P \sim e^{-\lambda \delta y}$ with $\lambda \sim 0.002$. On the other hand, for $k_\perp \rho_{th} = 1.2$, the inset shows evidence of algebraic decay, $P \sim \delta y^{-\zeta}$ with $\zeta = 2.9$. In both plots, the solid line denotes the PDF of sticky-flights (*i.e.*, excluding the passing and trapped orbits), and the dashed line denotes the PDF computed using all the orbits.

with $\mu = 1.8$ for $k_\perp \rho_{th} = 0$, and $\mu = 2.7$ for $k_\perp \rho_{th} = 1.2$. Since $\mu < 3$ in both cases, these flights correspond to Lévy flights. However, the decay of the curve for positive flights is much steeper with $\mu \gtrsim 3$ regardless of the value of $k_\perp \rho_{th}$, which implies that positive displacements are not Lévy flights. The tails of the trapping and flight PDFs transition to exponential decay at $\delta y_{flight} \approx -1000$ and $t_{trapt} \approx 2000$. As discussed before, this transition is indicative of the possible presence of truncated Lévy flights.

3.5.4 Algebraic decay of Lagrangian velocity autocorrelation function

Figure 3.11 shows the Lagrangian velocity autocorrelation function for the sticky-flights with $k_\perp \rho_{th} = 0$ in Fig. 3.11(a) and with $k_\perp \rho_{th} = 1.2$ in Fig. 3.11(b). Both curves follow algebraic decay of the form $C(\tau) \sim \tau^{-\kappa}$. When $k_\perp \rho_{th} = 0$, $\kappa = 0.2$ and when $k_\perp \rho_{th} = 1.2$, $\kappa = 0.3$. Both values are consistent with the Green-Kubo relation between the decay of the velocity correlation and the scaling of the variance according to which $\kappa = 2 - \gamma$. The frequency of small scale oscillations observed in the correlation seems to increase when $k_\perp \rho_{th}$ changes from $0 \rightarrow 1.2$.

3.6 Self-similar anomalous scaling and fractional diffusion modeling

An important goal of transport modeling is to construct effective transport equations that describe the "macroscopic" coarse grained dynamics when given information at the "microscopic" kinetic level. When the microscopic dynamics in-

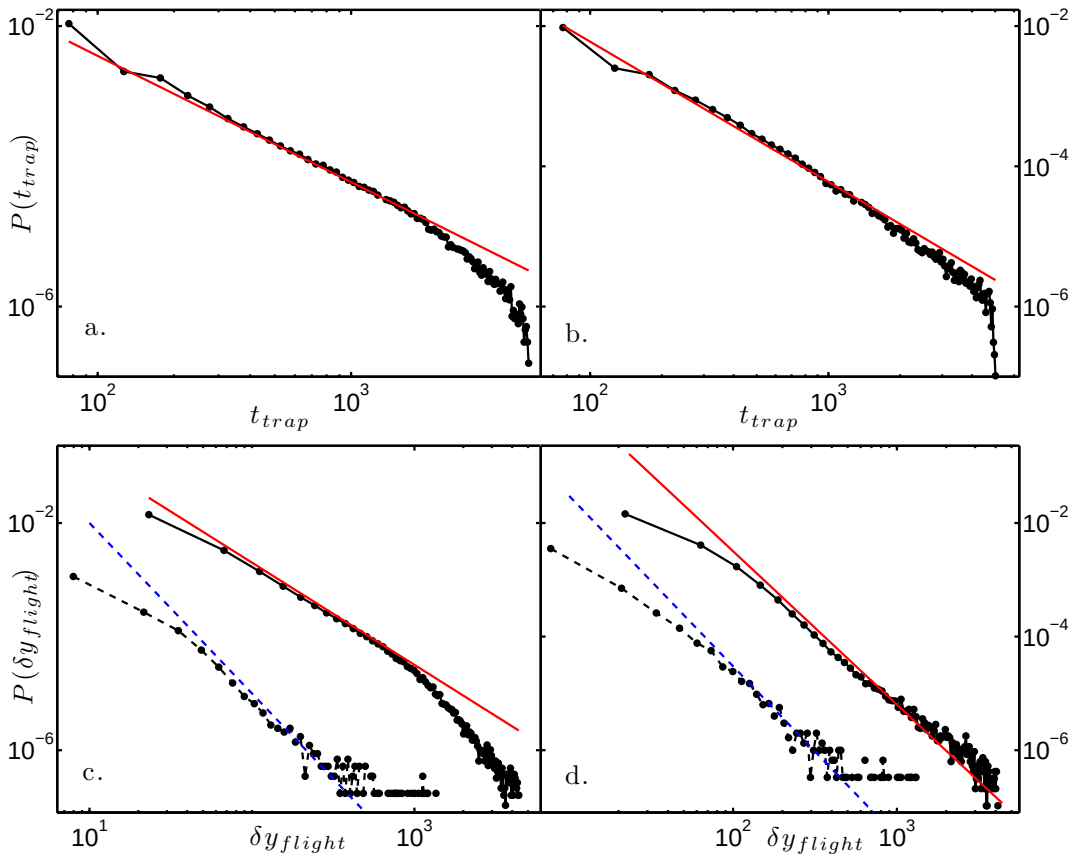

Figure 3.10: Probability distribution functions of particle trapping events and particle flight events for $k_\perp \rho_{th} = 0$ and $k_\perp \rho_{th} = 1.2$. The trapping PDFs are shown in (a) and (b), and the flight PDFs are shown in (c) and (d). Panels (a) and (c) correspond to $k_\perp \rho_{th} = 0$, and panels (b) and (d) correspond to $k_\perp \rho_{th} = 1.2$. The solid straight lines in (a) and (c) indicate that the trapping PDFs show algebraic decay, $P \sim t_{trap}^{-\nu}$, with $\nu \approx 1.8$ for $k_\perp \rho_{th} = 0$, and $\nu \approx 2.0$ for $k_\perp \rho_{th} = 1.2$. The negative flights PDF shown fit with solid lines also exhibit algebraic decay of the form $P \sim t_{flight}^{-\mu}$ with $\mu \approx 1.8$ for the case $k_\perp \rho_{th} = 0$, and $\mu \approx 2.7$ for the case $k_\perp \rho_{th} = 1.2$. The PDFs of positive flights, shown fit with dashed lines, show a faster exponential-type decay with $\mu \approx 3.0$ in both cases.

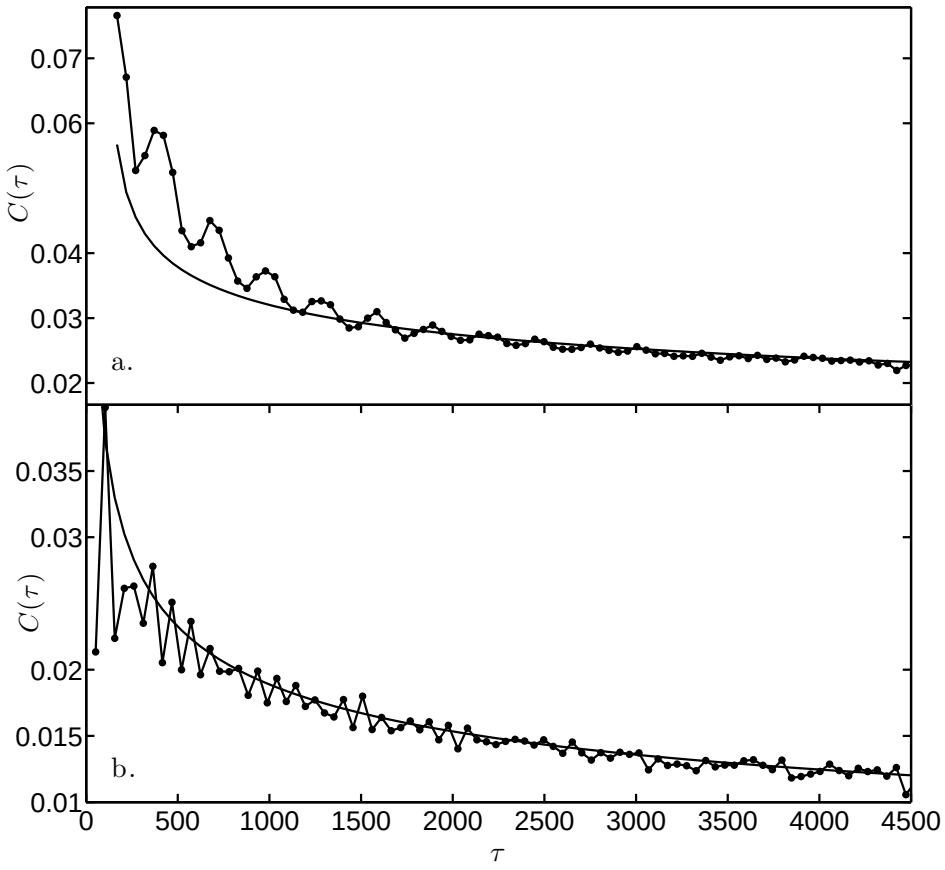

Figure 3.11: Lagrangian velocity autocorrelation function for sticky-flight trajectories. Panel (a) corresponds to $k_\perp \rho_{th} = 0$ and panel (b) corresponds to $k_\perp \rho_{th} = 1.2$. The curves with dots are the numerical results, and the solid line curves are algebraic fits of the form $\mathcal{C} \sim \tau^{-\kappa}$ with $\kappa = 0.2$ in (a) and $\kappa = 0.3$ in (b).

volves Gaussian, Markovian stochastic processes (*e.g.*, a Brownian random walk) the macroscopic dynamics can be modeled using diffusion type equations. This is the basic idea behind the use of diffusive models to describe collisional transport. However, in recent years it has been shown that the standard diffusion picture can fail when non- Gaussian and/or non-Markovian statistics are present.

In particular, experimental, numerical and analytical transport studies in fluids and plasmas (*e.g.* Refs. [112, 34, 127, 128, 36, 113, 12, 129, 130, 50] and references therein) have shown that underlying stochastic processes governing particle transport in flows with coherent structures, like zonal flows and eddies, typically involve anomalously large particle displacements induced by the zonal flows and/or anomalous particle trapping in eddies. The presence of large particle displacements can invalidate the Gaussianity of displacement distributions. Particle trapping can introduce waiting time effects that invalidate the Markovian assumption because of memory effects. The statistics of particle transport discussed in the previous section shows clear evidence of these type of phenomena. This section presents an effective macroscopic model that describes quantitatively the spatio-temporal evolution of the PDF of particle displacements.

An important piece of information needed for constructing an effective transport model is shown in Fig. 3.12. Figures 3.12(a)-(c) show the temporal evolution of the PDF of particle displacements for different values of $k_\perp \rho_{th}$. As discussed before, the PDF develops a strong "fat" tail to the left and, by conservation of probability, the peak of the distribution goes down. Figures 3.12(d)-(f) show the same data plotted using rescaled variables as in Eq. (3.16). In the horizontal axis,

$\eta = \delta y/t^{\gamma/2}$, and in the vertical axis, P has been multiplied by the factor $t^{\gamma/2}$, where γ is the anomalous diffusion exponent in Eq. (3.15). From this it follows that the PDF at a time λt is related to the PDF at time t by the scaling transformation $P(\delta y, \lambda t) = \lambda^{-\gamma/2} P(y/\lambda^{\gamma/2}, t)$. The fact that, for the problem of interest here, $\gamma \neq 1$, rules out the possibility of constructing a transport model based on the diffusion equation with an effective diffusivity because the solution of the diffusion equation scales as $P = t^{-1/2} L(\delta y/t^{1/2})$.

A natural way to built transport models that display self-similar anomalous scaling is to use fractional diffusion equations of the from

$$ {}_0^C D_t^\beta P = \chi_f [l \ {}_{-\infty} D_y^\alpha + r \ {}_y D_\infty^\alpha] P \,, \tag{3.20} $$

where $l = -\sec(\alpha\pi/2)(1-\theta)/2$, and $r = -\sec(\alpha\pi/2)(1+\theta)/2$. The operators ${}_{-\infty}D_y^\alpha$ and ${}_yD_\infty^\alpha$ are called the left and right fractional derivatives. These non-local operators are a natural generalization of the regular differential operator, ∂_y^n, of integer order n. For example, Fourier transforms of the fractional operator, $\mathcal{F}[f] = \hat{f} = \int e^{iky} f dy$, satisfy

$$ \mathcal{F}\left[{}_{-\infty}D_y^\alpha P\right] = (-ik)^\alpha \hat{P} \,, \qquad \mathcal{F}\left[{}_yD_\infty^\alpha P\right] = (ik)^\alpha \hat{P} \,, \tag{3.21} $$

for non-integer values of α. In a similar way, the operator on the left hand side of Eq. (3.20) is a natural extension of the regular time derivative, $\partial_t f$, in the sense that its Laplace transform, $\mathcal{L}[f] = \tilde{f} = \int e^{-st} f dt$, satisfies

$$ \mathcal{L}\left[{}_0^C D_t^\beta P\right] = s^\beta \tilde{P} - s^{\beta-1} P(t=0) \,, \tag{3.22} $$

for $0 < \beta < 1$. As expected, Eq. (3.20) reduces to the standard diffusion equation

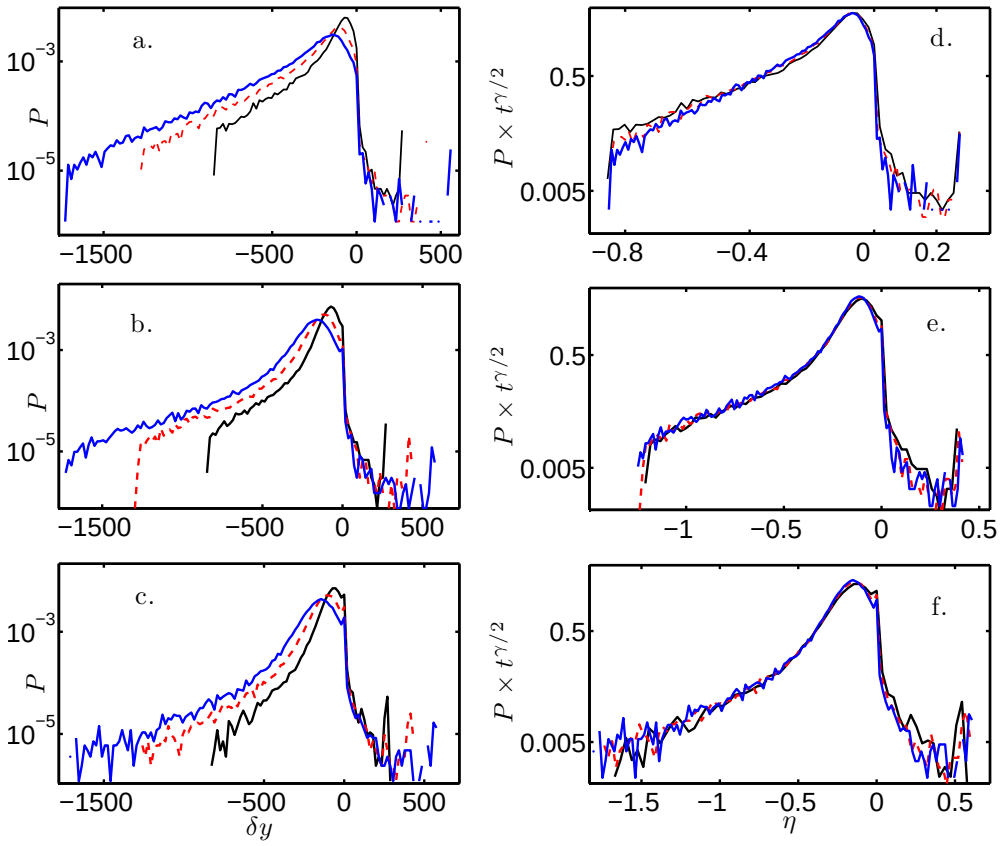

Figure 3.12: Self-similar scaling of probability distribution function of particle displacements (PDF). The curves denote the PDFs at $t = 1040$, $t = 1560$, and $t = 2080$, with later times showing more spreading in the PDF. Panels (a), (b) and (c) show the PDFs corresponding to $k_\perp \rho_{th} = 0$, $k_\perp \rho_{th} = 0.6$ and $k_\perp \rho_{th} = 1.2$, respectively. Panels (d), (e) and (f) show the collapse of the corresponding PDFs when plotted as functions of the similarity variable $\eta = \delta y / t^{\gamma/2}$ and rescaled with the factor $t^{\gamma/2}$.

when $\alpha = 2$ and $\beta = 1$. Further formal details on fractional derivatives, including their representation in the y and t domains in terms of non-local operators can be found in Refs. [56, 131]. For a discussion on the use of these operators to model non-diffusive transport in plasmas, see for example Refs. [12, 115] and references therein.

To explore the self-similarity properties of the fractional diffusion model we use Eqs. (3.21)-(3.22) and write the Fourier-Laplace transform, $\hat{\tilde{\mathcal{G}}}$, of the Green's function, $\mathcal{G}$, of Eq. (3.20) as

$$\hat{\tilde{\mathcal{G}}} = \frac{s^{\beta-1}}{s^\beta - \Lambda}\,, \qquad \Lambda = \chi_f \left[l\,(-ik)^\alpha + r\,(ik)^\alpha \right], \tag{3.23}$$

where $\alpha \neq 1$ and $\mathcal{G}(y, t = 0) = \delta(y)$. It follows directly from Eq. (3.23) that $\hat{\tilde{\mathcal{G}}}(k, s/\lambda) = \lambda \hat{\tilde{\mathcal{G}}}(\lambda^{\beta/\alpha} k, s)$ which in y-t space implies the self-similar scaling $\mathcal{G}(y, \lambda t) = \lambda^{-\beta/\alpha} \mathcal{G}(\lambda^{-\beta/\alpha} y, t)$ of the fractional diffusion propagator Eq. (3.20). Therefore, the fractional equation will exhibit the same self-similar scaling as the numerically obtained PDF provided the fractional orders of the spatial and temporal derivatives satisfy

$$\gamma = 2\beta/\alpha\,. \tag{3.24}$$

According to Table 1, to a good approximation, $\gamma \approx 2$ in the intermediate asymptotic regime. Based on this observation, and following Eq. (3.24), we will assume $\alpha = \beta$ in the fractional diffusion model. This special case, known as neutral fractional diffusion, has a Green's function that can fortunately be expressed in

closed form using elementary functions, as shown in Ref. [91]:

$$\mathcal{G}(\eta;\alpha,\hat{\theta}) = \frac{1}{\pi}\frac{\sin\left[\pi(\alpha-\hat{\theta})/2\right]\eta^{\alpha-1}}{1+2\eta^{\alpha}\cos\left[\pi(\alpha-\hat{\theta})/2\right]+\eta^{2\alpha}}\,, \qquad \text{for} \qquad \eta>0\,, \tag{3.25}$$

where $\eta = \delta y/t^{\gamma/2}$ is the similarity variable and $|\hat{\theta}| \leq \min\{\alpha, 2-\alpha\}$. The solution for $\eta < 0$ is obtained using the relation $\mathcal{G}(-\eta;\alpha,\hat{\theta}) = \mathcal{G}(\eta;\alpha,-\hat{\theta})$. The parameter $\hat{\theta}$ is related to the asymmetry parameter θ introduced before in the definition of the weighting factors l and r according to $\theta = \tan(\pi\hat{\theta}/2)/\tan(\pi\alpha/2)$. Given the Green's function, the solution of the fractional diffusion equation for an initial condition $P_0(\delta y) = P(\delta y, 0)$ is

$$P(\delta y, t) = \int_{-\infty}^{\infty} P_0(\delta y')\,\mathcal{G}(\delta y - \delta y', t)d\delta y'\,. \tag{3.26}$$

For the initial condition we assume a localized distribution of the form $P_0 = 1/A$ for $|\delta y| < A/2$ and $P_0 = 0$ elsewhere (see Ref. [12]). The use of this initial condition is necessary to account for the presence of transients in the evolution of the PDF not reproduced by the fractional diffusion equation, which describes the intermediate time regime. Figure 3.13 shows the comparison of the solution of the fractional diffusion equation in Eq. (3.20) according to Eqs. (3.26) and (3.25) and the numerically obtained PDF obtained from the histograms of particle displacements at $t = 936$ for $k_\perp\rho_{th} = 0$ in Fig. 3.13(a) and $k_\perp\rho_{th} = 0.6$ in Fig. 3.13(b). For the fractional diffusion model parameters we used $\alpha = \beta = 0.80$ and $\hat{\theta} = 0.79$ in the $k_\perp\rho_{th} = 0$ case, and $\alpha = \beta = 0.85$ and $\hat{\theta} = 0.84$ in the $k_\perp\rho_{th} = 0.6$ case. In both cases, we used $A = 60$, which is small compared to the maximum range of the PDF, $\delta y \sim -800$.

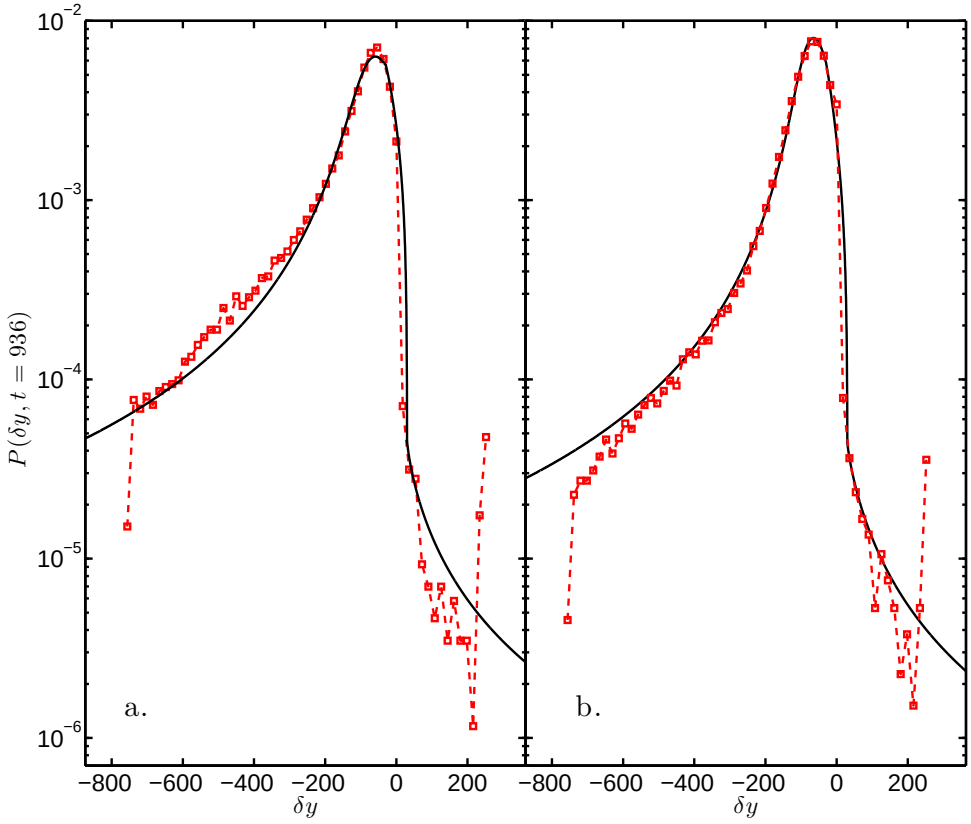

Figure 3.13: Comparison between the numerically determined PDF of particle displacements (square markers) and the solution of the effective fractional diffusion model in Eq. (3.25)(solid lines) with a localized initial condition. In panel (a), which corresponds to $k_\perp \rho_{th} = 0$, the fractional diffusion parameters are $\alpha = 0.8$, $\hat{\theta} = 0.79$, $A = 60$ and $\chi_f = 0.15$. For the case $k_\perp \rho_{th} = 0.6$, shown in panel (b), $\alpha = \beta = .85$, $\hat{\theta} = 0.84$, $A = 60$ and $\chi = 0.12$.

3.7 Summary and conclusions

In this chapter we presented a numerical study of FLR effects on non-diffusive transport of test particles in a flow dominated by a strong zonal shear flow and large scale $\mathbf{E} \times \mathbf{B}$ eddies. We modeled the flow using a Hamiltonian dynamical system consisting of a linear superposition of a strong zonal shear flow and eigenmodes of the HM equation. For the parameter values considered, the Hamiltonian causes chaotic transport. Test particles alternate stochastically between being trapped in the vortices and being transported by the zonal flow. To expose the non-diffusive properties of the system we used Lagrangian statistical diagnostics including: (i) the scaling in time of statistical moments; (ii) the PDFs of particle displacements, (iii) trapping events and (iv) flight events; and (v) the decay of the Lagrangian velocity autocorrelation function.

Finite Larmor radius effects were incorporated in the particle calculations by substituting the value of the $\mathbf{E} \times \mathbf{B}$ velocity at the location of the guiding center by its value averaged over a ring of radius ρ, where ρ is the Larmor radius. The ring average was computed using a discrete approximation. The numerical method was benchmarked using an analytical solution for a parallel zonal flow with no waves. We found that for $k_\perp \rho < 3$ an 8-point average gives accurate results, but higher order approximations must be used for for $k_\perp \rho > 3$. Contrary to previous works where all the particles were assumed to have the same value of ρ, here we considered a more realistic Maxwellian distribution of Larmor radii. Poincaré plots revealed that the Larmor radius has a direct nontrivial effect on the topology of the flow and

the degree of chaos of test particles. In particular, it was observed that the amount of chaos, measured by the width of the stochastic region, is significantly reduced as $k_\perp \rho_{th}$ increases from 0 to 3. A distribution of Larmor radii can also have a direct effect on the dispersion of particles. In particular, we have shown that, even in the case of a completely integrable flow, particles exhibit ballistic spreading, $\sigma^2 \sim t^2$, when they have different Larmor radii.

For the Lagrangian statistics we limited attention to sticky-flight orbits and ignored trapped and passing orbits. The rationale for this filter is that the trivial dynamics of passing and trapped particles give rise to outliers that artificially bias the statistics. The first moment, to a good approximation, has normal advective scaling, *i.e.* $M \sim t^\chi$, with $\chi \approx 1$, and the second moment has super-diffusive scaling, *i.e.* $\sigma^2 \sim t^\gamma$, with $\gamma > 1$. For $k_\perp \rho = 0$, a sharp transition was observed in the scaling exponent, from $\gamma = 1.9$ at intermediate times to $\gamma = 1.6$ at larger times. Similar transitions in the value of γ have been also found in other systems including temporally irregular channel flows [34], time dependent, three dimensional flows [132], and two-dimensional vortex flows [113]. For specific experimental instances, early time behavior will be more important than late time behavior if the domain crossing time is small enough. We have found that FLR effects seem to eliminate the distinction between early and late time. For the range of $k_\perp \rho_{th}$ considered, $\gamma \approx 1.8 \pm 0.1$. We refer to this regime as super-diffusive ballistic transport since the variance approaches ballistic scaling ($\gamma = 2$) but the PDF of displacements retains a super- diffusive appearance. Complementary results were obtained in Ref. [43] for nonlinear HM simulations.

We also observed that the Lagrangian velocity autocorrelation function decays algebraically, $\mathcal{C} \sim \tau^{-\zeta}$ where, in reasonable agreement with the Green-Kubo scaling, $\zeta = 2-\gamma$. The trapping and flight distributions show algebraic decay. The trapping time exponent, ν, remains the same when $k_\perp \rho_{th}$ changes. The PDFs of negative flights qualify as truncated Lévy distributions but positive flights are definitively not Lévy. The negative flight exponent for $k_\perp \rho_{th} = 1.2$ is larger than expected in the context of a CTRW.

At intermediate times, consistent with Refs. [36, 42], the PDF of particle displacements in the zero Larmor radius case is an asymmetric non-Gaussian distribution with an algebraic decaying leftward tail. However, for larger times, the tail of the PDF transitions from algebraic to exponential decay. This algebraic-exponential transition in the PDF is likely to be related to the presence of truncated Lévy flights, which, as discussed in Ref. [126], might result from particle decorrelation or the finite size of possible displacements. The robustness of the algebraic decay in the finite Larmor radius case might be attributed to the persistence of large particle displacements which, due to the presence of the strong zonal flows, are enhanced by the gyroaverage. We have also shown that the PDF of particle displacements has self-similar scaling behavior for $0 \leq k_\perp \rho_{th} \leq 3$ and $k_\perp \rho_{th} \neq 0$. Most importantly, we have shown that these distributions correspond to solutions of the neutral ($\alpha = \beta$) asymmetric fractional diffusion equation.

Future work will apply the ideas and tools developed here to turbulent flows to more realistic plasma turbulence models. In particular, we will examine self-consistent particle transport parallel to a density gradient in a gyrokinetic particle-

in-cell simulation. Transport properties of tracers and self-consistent particles should be compared.

Chapter 4

Gyrocenter dispersion in a Z-pinch using self-consistent markers

Here we expand our investigation to a cylindrical magnetic geometry with gyrokinetic ions and electrons in self-consistent turbulence. The source of free energy for the turbulence is a fixed density gradient chosen in the regime of the entropy mode. The entropy mode is the kinetic analogy to the MHD interchange mode. We vary the density gradient and characterize the dispersion of ion tracer gyrocenters across a zonal flow, parallel to the direction of the density gradient. The Z-pinch magnetic geometry is simple compared to the fully three-dimensional tokamak or other confinement device. However, the self-consistent turbulence of the entropy mode at the ρ_i scale is qualitatively similar to the zonal flows seen in gyrokinetic simulations of tokamak turbulence. Therefore, the results from this study should be helpful for developing physical intuition and elucidating the relevant parameters for dispersion of gyrocenters in a shear flow.

The entropy mode with kinetic ions and electrons can be used to study the box averaged particle transport $\langle \Gamma \rangle_p$ and tracer particle dispersion simultaneously. This is in contrast to 3D tokamak ion-temperature gradient (ITG) global PIC (UCAN [133]) gyrokinetic simulations with adiabatic electrons [14]. Our use of a PIC code is also in contrast to local continuum (GENE) gyrokinetic simulations of tracer transport in Cyclone ITG turbulence [50]. Our major contributions, complementary to

other works, are: a comparison between several values of the density gradient, a careful study of the axial and radial displacement and velocity statistics for ion gyrocenters, and quantification of the dependence of the dispersion on the size of the gyroradius (or the perpendicular velocity). As we will see, varying the density gradient qualitatively changes the dispersion properties of drifting gyrocenters. We choose three values of the density gradient in the linear instability range for the gyrokinetic entropy mode [1]: $L_n/R_c = [0.5, 0.625, 0.75]$. GS2 predicts $\langle\Gamma\rangle_p^\infty \sim [1, 0.1, 0.01]$ for the collisionless case, where $\langle\Gamma\rangle_p^\infty$ is a steady state flux during saturation of the instability. We choose these values for our most detailed analysis because we want to see how the tracer dispersion varies as the converged flux varies significantly.

Based on our vortex/shear studies described in Chapter 3, one suspects that the $\mathbf{E} \times \mathbf{B}$ dispersion associated with tracers in a shear flow may be nondiffusive. In particular, it may be subdiffusive perpendicular to the direction of the drift velocity shear (radial in the Z-pinch) and superdiffusive parallel to the shear (axial in the Z-pinch). The radial direction is more directly relevant to confinement in a fusion device, but the axial transport should well-understood also. Studying the axial transport also allows us to compare with Chapter 3, where the nature of the prescribed flow made radial transport uninteresting.

We vary the strength of the density gradient and examine several measures of the properties of the dispersion, including the displacement distribution function and its moments, the Lagrangian velocity correlation function, and the velocity increment distribution. Furthermore, the dependence of the test-particle diffusion coefficient on particle energy is considered. This dependence is relevant to the

transport of energetic ions, since gyroaveraging effects are expected to affect their transport properties [134].

4.1 Premises of the Z-pinch and entropy mode

The Z pinch, in which a straight vertical current creates a cylindrically symmetric magnetic field, is a useful intermediate step between slab and tokamak geometry. For $\beta \ll 1$, the parallel dynamics are negligible, so $k_\parallel = 0$ and we can reduce to two dimensions in configuration space. At the same time, the Z pinch includes both the $\nabla \mathbf{B}$ and curvature drifts that produce important instabilities. As shown in Figure 4.1, the Z pinch is essentially a slab wrapped around into a cylinder so that the $\mathbf{B}$ field is axisymmetric. The static magnetic field is in the azimuthal direction, $\hat{\mathbf{B}}_0 = -\hat{\varphi}$, with a radial dependence $B \sim 1/r$. A combination of $\nabla \mathbf{B}$ and curvature gives a drift that is always perpendicular to both the $\hat{r}$ and $\hat{\varphi}$ directions and depends on the sign of the charged particle. The $\mathbf{E} \times \mathbf{B}$ drift, on the other hand, is generally in both the $\hat{r}$ and $\hat{z}$ directions. The gyrokinetic equation derived in Chapter 2 is valid for the electrostatic Z-pinch since it includes the curvature and ∇B drift terms, which manifest in both the weight equation and the $\hat{z}$ position equation in the characteristic ODEs. From this point forward the axial direction in the Z-pinch will be referred to as the $\hat{y}$ and the radial direction will be $\hat{x}$ for agreement with Chapter 3. This means that the conventions used in Chapter 2 will be changed in this chapter, as such: $\hat{r} \to \hat{x}$, $\hat{z} \to \hat{y}$ and $\hat{\varphi} \to \hat{z} = \hat{b}$.

The entropy mode in the Z-pinch is a low frequency ($\omega \sim \omega_{d,i}$, the ion drift

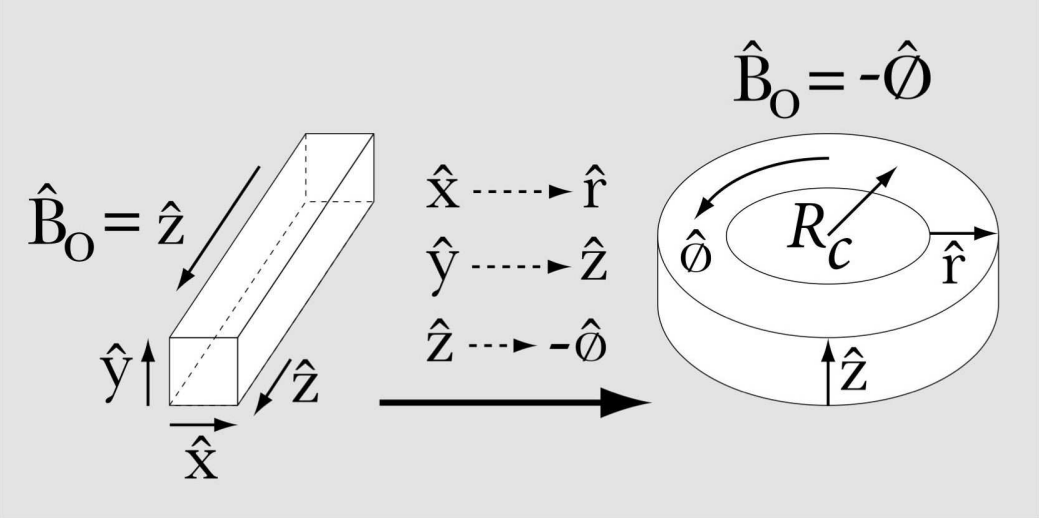

Figure 4.1: Geometry for the Z pinch is a mapping of the (x, y, z) code coordinates to the (r, z, φ) coordinates of the Z pinch. The current is in the $\hat{z}$ direction, and the **B** field in purely in the $-\hat{\varphi}$ direction in a right-handed coordinate system. (Graphic courtesy Dr. Ingmar Broemstrup and Kenton Kodner)

frequency) wave that exists when the density and (optionally) the temperature are perturbed while keeping the pressure constant. This non-ideal mode was studied in the context of classical plasma stability theory [135], and more recently for the Levitated Dipole Experiment (LDX) at MIT [136, 137]. Gyrokinetic studies at $k\rho_s \sim 1$ in both the linear and nonlinear regimes of instability have recently been added to the literature by Ricci *et al* [1, 138] using the continuum gyrokinetic code GS2 [92]. This mode exists at weaker pressure gradients than the ideal magnetohydrodynamic (MHD) interchange mode, and can have growth rates comparable to the MHD mode when the density gradient scale length, $L_n^{-1} = -n'/n$ is in the proper range: $2/7 < L_n/R_c < \pi/2$, where R_c is the radius of curvature (see Figure 4.1). For this range of linear instability, the temperature gradient is negligibly small and the

temperature ratio between electrons and ions is $\tau_{e,i} = 1$. It was shown that the entropy mode creates radial streamer-type $\mathbf{E} \times \mathbf{B}$ flows in the linear phase, which break up into zonal $\mathbf{E} \times \mathbf{B}$ drift flows in the $\hat{y}$ direction during the nonlinear phase because of a secondary Kelvin-Helmholtz instability [1].

This type of secondary instability drive for zonal flow generation is similar to that observed in tokamak geometry [66]. While the Z-pinch studied here is missing the third dimension and the effects of trapped particles due to nonuniform magnetic fields, zonal flows in tokamaks are qualitatively similar to the entropy mode zonal flows and the present results should contribute to understanding tokamak transport. The results may also be important for devices such as the LDX and perhaps simple magnetized torii, such as TORPEX [139]. In any case, there is little argument that zonal flows are an important phenomenon for confinement. The zonal flows generated self-consistently in the local approximation of the gyrokinetic Z-pinch constitute an important step for studying dispersion of tracer particles across sheared-velocity flows in more comprehensive physical models.

4.2 Structure of the inhomogeneous turbulence

For the results presented here, GSP is run with ∼12 million particles, or 786 particles per (x, y, z) grid cell for a $128 \times 128 \times 1$ run. This is a significantly larger marker particle density than is often used in the literature [140, 14]. As shown in Section 4.2.3, smaller numbers of particles per cell can give different answers for the converged particle flux even with explicit noise control. The box dimensions are

$L_x = L_y = 125.66, L_z = 6.28$ and the timestep $\delta t = 0.05$ is constant for the second-order predictor-corrector method used for solving the ODEs from the method of characteristics. See Section 2.5.2 for the normalizations used in the code. Two kinetic species are used: electrons and singly-charged ions with equal temperature, $T_i = T_e$ and realistic hydrogenic mass ratio $m_e/m_i = 5.4 \times 10^{-4}$.

Before examining the dispersion of an ensemble of particles in the gyrokinetic Z-pinch, it is useful to examine the structure of the inhomogeneous turbulence generated by our nonlinear PIC simulations. There are two benefits to starting with this perspective. First, verification of the code's ability to represent the physics of the gyrokinetic equation can be demonstrated by comparison with GS2 results. Second, an intuition for the structure of the flow is gained. We perform convergence and signal-to-noise tests in addition to benchmarking against published results from the continuum code, GS2. Such verification efforts are crucial to all numerical studies that hope to represent a physical model.

Our figure of merit for convergence tests and GS2 benchmarking is the box averaged particle flux generated by the unstable entropy mode in a stationary state of nonlinear saturation [1]. This saturated state is steady in the sense that the spectrum of excited modes has a converged time average. For this example, the secondary instability in the entropy mode has a shearing rate below the critical value for a tertiary shear instability. In the code, we define the normalized, y integrated, radial particle flux for species s as follows. To normalize a probability distribution function, its integral over all of phase space should be unity. In our scheme, this means that the integral over the entire distribution function, $f = f_0 + \delta f$ should be

unity to order ϵ. The following calculation demonstrates the proper way to compute the flux in a GSP simulation.

First, the box-averaged particle flux of the perturbed density, δn_1, must be computed, taking into account the Maxwellian factors $\delta f_1 = w_i F_0$, which give the proper weight to large velocities contributions. These factors are

$$F_0 = \exp(-v_\perp^2/2v_{th}^2)\exp(-v_\parallel^2/2v_{th}^2). \tag{4.1}$$

When integrating over velocity space, the proper Jacobian for the cylindrical $(v_\perp, v_\parallel)$ geometry gives $v_\perp dv_\perp dv_\parallel$ as the measure. Therefore, the radial $\mathbf{E}\times\mathbf{B}$ particle flux in GSP must be computed as

$$\Gamma_{p,x} = \int_{x,y,z}\int_{v_\perp,v_\parallel} w v_{\mathbf{E}\times\mathbf{B}}\cdot\hat{x} v_\perp \exp(-v_\perp^2/2v_{th}^2)\exp(-v_\parallel^2/2v_{th}^2) dv_\perp dv_\parallel. \tag{4.2}$$

When this integration is taken over marker particles, treated as δ-functions in velocity space, as in the Klimontovich representation, these δ-functions are inserted into the integrals:

$$\delta(\mathbf{x}-\mathbf{x}_i)\delta(\mathbf{v}_\perp - \mathbf{v}_{\mathbf{i},\perp})\delta(v_\parallel - v_{i,\parallel}). \tag{4.3}$$

Thus, the non-normalized particle flux computed in GSP is exactly:

$$\Gamma_{p,x} = \sum_i w_i v_{i,\mathbf{E}\times\mathbf{B}}\cdot\hat{x} v_{\perp,i}\exp(-(v_{i,\perp}^2 + v_{i,\parallel}^2)/2v_{th}^2), \tag{4.4}$$

which also includes the Monte Carlo estimate in (x, y, z) space, where the Jacobian is trivial and there are no other factors. The velocity space normalization factor,

M, necessary for finding any integrated quantity in the code is:

$$M \int_x \int_y \int_z \int_{v_x} \int_{v_y} \int_{v_z} d^3x d^3v F_0 = 1$$

$$M \int_{x,y,z} \int_{v_\perp, v_\parallel} d^3x dv_\perp dv_\parallel v_\perp \delta(\mathbf{x} - \mathbf{x}_i) \delta(\mathbf{v}_\perp - \mathbf{v}_{\mathbf{i},\perp}) \delta(v_\parallel - v_{i,\parallel}) \exp(-(v_\perp^2 + v_\parallel^2)/2v_{th}^2) = 1$$

$$M^{-1} = \sum_i v_{i,\perp} \exp(-(v_{\perp,i}^2 + v_{i,\parallel}^2)/2v_{th}^2) \tag{4.5}$$

With the correct normalization, ambipolarity is fulfilled to a high degree of accuracy in all of the simulations shown here, as expected when using quasineutrality to solve for the gyrokinetic potential. It is worth mentioning that both the GS2 and GSP runs show a systematically higher ion particle flux ($1 - 3\%$) compared to electron particle flux throughout the simulations, pointing to a phenomenon common to both codes.

Next we will examine convergence of the y-averaged radial particle flux with respect to the particle number, timestep, collisionality, and explicit spatial filtering. We will show the results of tests for determining whether the signal or the noise is producing particle transport, and we will compare the spectrum of the turbulence and the particle flux to the results from GS2.

4.2.1 Convergence test

We have been able to compute the average radial particle flux for three values of the timestep using the strongest density gradient, as shown in Figure 4.2. The flux is similar for both of the smaller timesteps tested, and is similar to the result from GS2, as discussed below. Testing smaller values of the time step becomes prohibitively

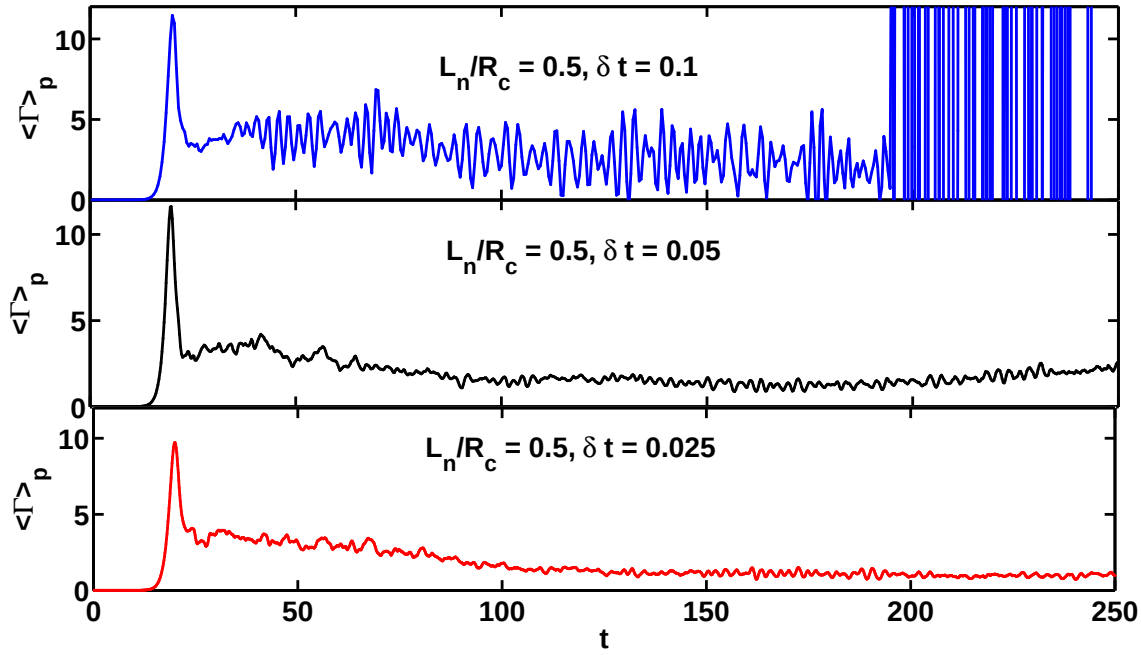

Figure 4.2: Particle flux for three different timesteps, from top to bottom, $\delta t = 0.1$, $\delta t = 0.05$ and $\delta t = 0.025$.

expensive. While the stability of the simulation is clearly better for $\delta t = 0.05$ compared to $\delta t = 0.1$, the values of the flux at $t = 250L/v_{th}$ are significantly different. Note that in Figure 4.6, the $\delta t = 0.05$ simulation is carried to $t = 1000L/v_{th}$, and the particle flux remains converged.

For our purposes, it is sufficient to use the converged result with $\delta t = 0.05$. Our study is concerned with the dispersion of tracers for three values of the density gradient for which the converged particle flux varies by 10^2. While the particle flux will depend on the dispersion of the tracers, which are markers of the flow, we are reporting a trend in a parameter scan rather than flux levels to compare quantitatively with an experiment.

Box size convergence tests have not been performed in detail at the time of

this writing because of the expense. However, the box size was chosen to give the same range of wavenumbers used in GS2 for the entropy mode study mentioned previously [1, 138].

4.2.2 Noise tests

One perspective on controlling noise due to increasing particle weights comes from the collision operator in the gyrokinetic equation. The physical motivation for including an accurate pitch-angle scattering collision operator is to control the fine-scale structures in velocity space, with a corresponding damping of fluctuations in configuration space as well [1] A collision operator can also be used to control the growth of the weights, independent of the physical content of the operator. Careful consideration of a gyroaveraged linearized Landau collision operator leads to a comprehensive collision operator that includes FLR effects, energy diffusion and resistivity while satisfying an H theorem [96, 97].

For our purposes, a simpler example of a collision operator is the Krook operator. This is a simple and coarse way to decrease the amplitude of the distribution function at all scales:

$$C(\langle \delta f \rangle_R) = -\nu_K \langle \delta f \rangle_R. \tag{4.6}$$

It can be very effective at managing weight growth for the proper choice of ν_K, but this collision frequency must not be so large that an unphysical damping of low k structure occurs.

Another method for controlling noise in a particle simulation is to employ a

low-pass spatial filter for the electrostatic potential, which eliminates high frequency structures due to the lack of dissipation at small scales and the low resolution at small scales for finite numbers of particles. This is because there are effectively fewer markers used to represent the distribution function at shorter wavelengths. The use of a low-pass filter for removing the unphysical information at large k can be very effective and perhaps essential for producing good results from a particle code.

The form of low-pass filter that we have used is a hyper-Gaussian:

$$\mathcal{F}(k) = \exp[-A_\perp (k_\perp \rho)^8] \tag{4.7}$$

where $A_\perp$ must be chosen carefully for the range of wavenumbers deemed to be physically important to the turbulence. This form of filter is chosen because it has almost no effect on low k and a smooth but fast transition to decreasing the amplitude of large k. The shape of this filter is shown in Figure 4.3.

The effect of the Krook operator, with and without the low-pass filter, is shown in Figures 4.4 and 4.5. It is apparent that both noise control techniques have some success in drawing the expected behavior from the code. Using both the Krook operator and the filter is the only method for obtaining a particle flux that is always positive and similar to GS2 results. For the production of the data for this thesis, the same forms of the Krook operator and the low-pass filter are used, and the number of particles per cell is increased to 786 to ensure a high signal to noise ratio with a reasonable amount of simulation time. This particle density is more difficult to achieve in a full three-dimensional simulation, where the same number of particles and isotropic resolution would give only 6 particles per cell. It is possible to obtain

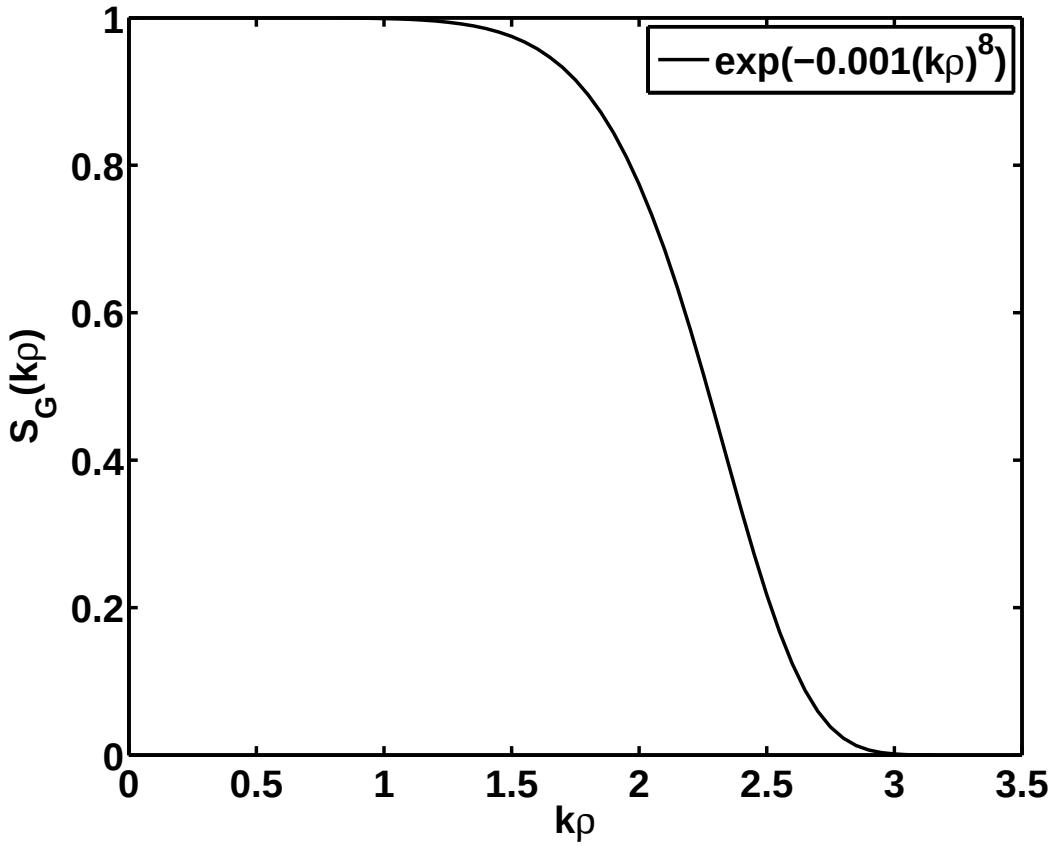

Figure 4.3: Shape of the low-pass filter used for the simulations in this chapter.

similar results for the particle flux using fewer particles, but we are choosing to be cautious, since it is expensive to perform rigorous particle number convergence tests.

4.2.3 Particle flux in PIC and continuum simulations

Besides convergence tests, which are expensive to perform comprehensively, a reasonable way to decide whether the results from a code are producing physically accurate output is to compare with a similar trusted code, such as GS2 [92]. GSP solves the same gyrokinetic equation as GS2 using the particle-in-cell technique rather than continuum/Vlasov method. Here we compare the GSP and GS2 particle flux in a stationary nonlinear state for three different density gradients in the range of entropy mode instability. The result for the strongest gradient is seen in Figure 4.6, where the mean value of the GSP flux is $\Gamma^{\infty}_{p,GSP} = 1.9$, and the mean value for GS2 is $\Gamma^{\infty}_{p,GS2} \sim 4$ in units of $(\rho_i/R)^2 n_0 v_{th,i}$. The other gradients show flux levels with similar comparisons to the reported GS2 levels, as shown in Figure 4.7. While the flux is appreciably lower for the strongest gradient case compared to the GS2 result [1], our statistical studies of displacements are hoped to be only weakly dependent on the exact flux levels. A comparison with tracers in similar GS2 turbulence has not been completed.

In addition, we perform a "scrambling test" (similar to the "Bolton-Lin noise test" discussed by Nevins *et al* [102]) to ascertain the signal to noise ratio indicated in the particle flux diagnostic. This test is implemented by restarting a run with a value of the particle flux that seems to be stationary and converged to a value comparable

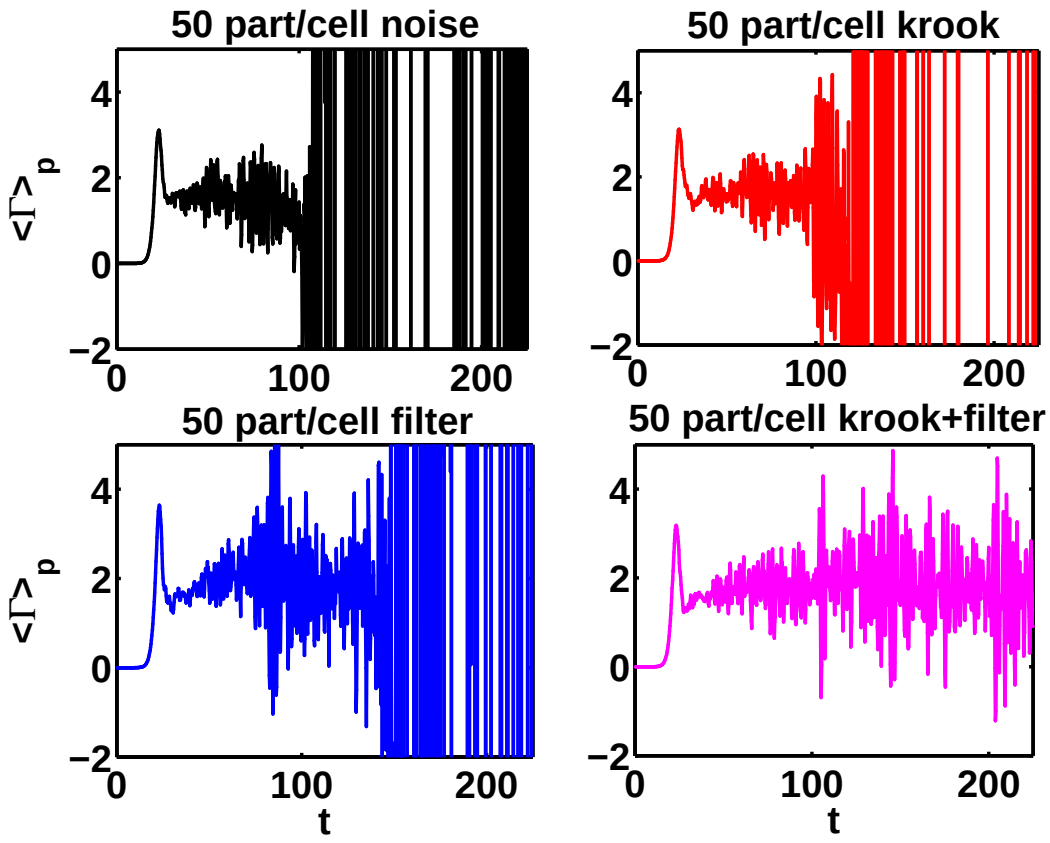

Figure 4.4: Effect of the Krook collision operator and the low-pass filter on the particle flux diagnostic for a simulation of the entropy mode with 100 particles per cell. The upper left panel has no noise control; upper right has a Krook operator with coefficient $\nu_K = 0.0055$; lower left has the low-pass filter detailed above with width $a_{v_\perp} = 0.001$; lower right has both the Krook operator and low-pass filter.

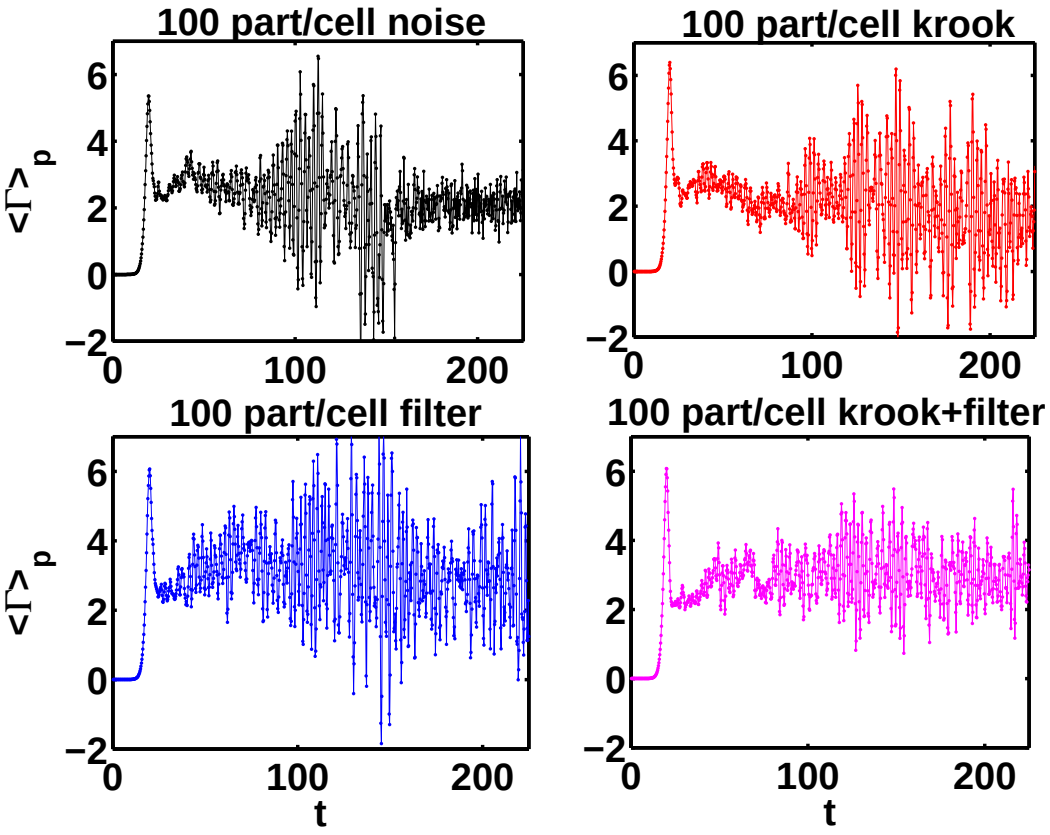

Figure 4.5: Effect of the Krook collision operator and the low-pass filter on the particle flux diagnostic for a simulation of the entropy mode with 200 particles per cell. The upper left panel has no noise control; upper right has a Krook operator with coefficient $\nu_K = 0.0055$; lower left has the low-pass filter detailed above with width $a_{v_\perp} = 0.001$; lower right has both the Krook operator and low-pass filter.

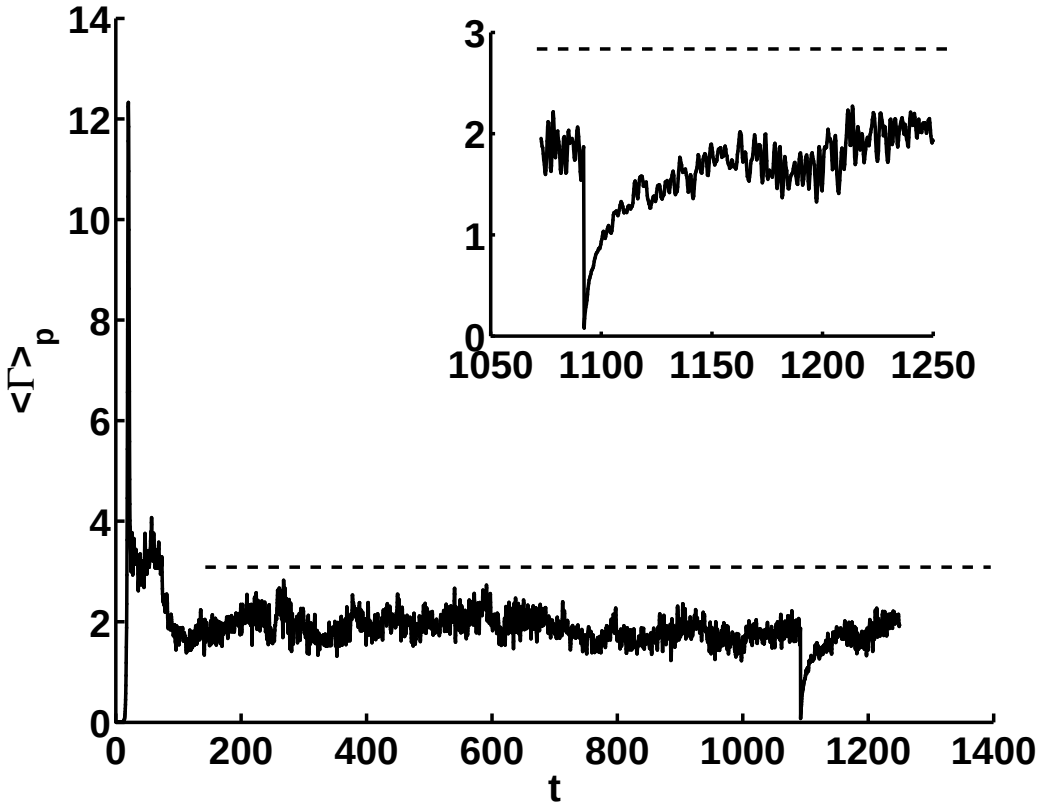

Figure 4.6: Radial ion gyrocenter flux for nonlinear entropy mode instability for $L_n/R_c = 0.5$, showing the burst of radial transport caused by the linear instability and the saturated nonlinear state. A horizontal line shows the level of transport found in a GS2 simulation [1]. After $t = 1000R/v_{th}$, a scrambling of the y positions of all the markers causes the flux to drop to zero, then recover to the previous level. This indicates that the particle flux is converged and due to a physical signal from the turbulence. No time-averaging has been applied here, so fluctuations from the mean value are smaller than in the lower right-hand plots of Figures 4.4 and 4.5.

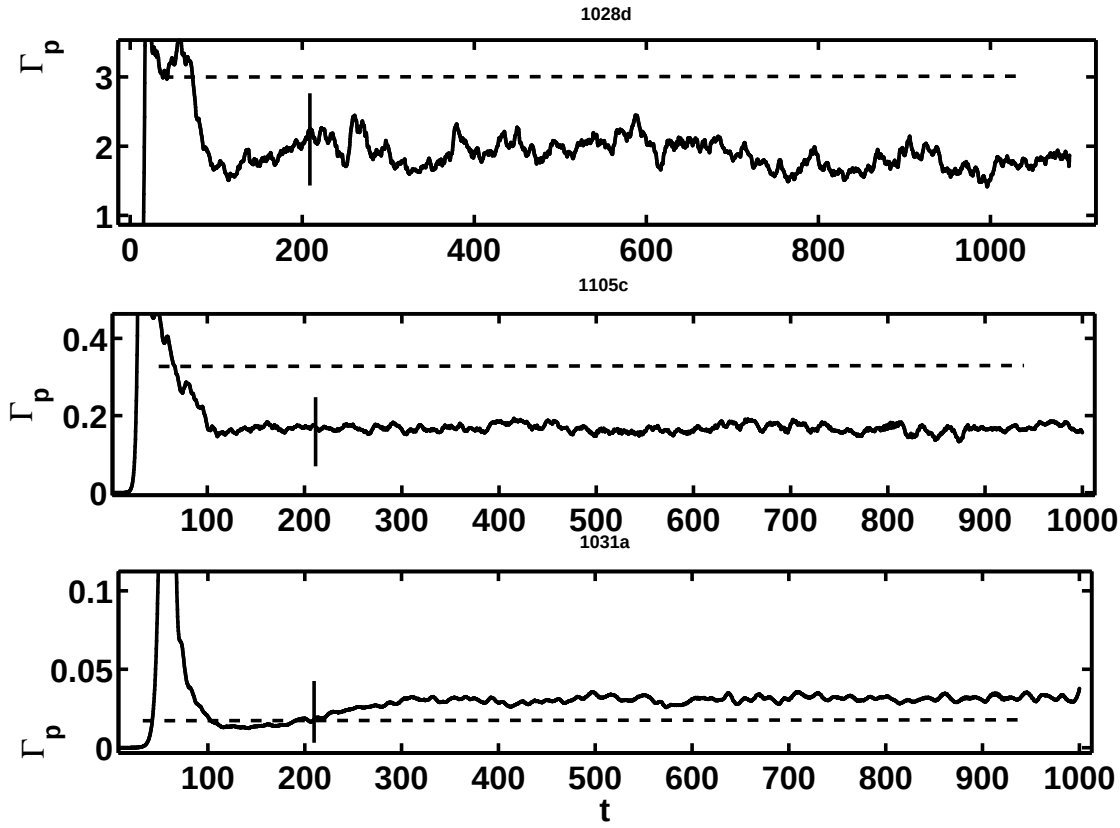

Figure 4.7: Radial ion particle flux for entropy mode instability for (top to bottom) $L_n/R_c = [0.5, 0.625, 0.75]$. The mean value of the flux after the drawn-in vertical lines for each gradient strength, respectively, is $\Gamma_p^\infty = [1.9, 0.17, 0.03]$. For comparison, the approximate value for the GS2 flux for each case is given as a dashed vertical line in each plot. These traces of numerical data have been boxcar averaged over ten time points, unlike Figure 4.6.

to the result from GS2. Upon restart, the axial (y) positions of all the marker particles are randomized while keeping the radial positions and weights the same. If the level of transport is set by noise in the simulation. the flux should remain the same upon scrambling. If the level is set by a physical signal, the scrambling should erase that signal and change the flux. If the simulation is converged to a true steady state, the transport level should return to the pre-scrambled state. The results of this scrambling test, shown in Figure 4.6 for the strongest gradient (with largest weight growth) indicate that the flux is a converged signal. The y-position scrambling test has a similar result, in terms of convergence, for all three values of the gradient tested.

Weight growth is controlled by the Krook operator, but the instability is not overdamped, as shown in Figure 4.8 and confirmed by the favorable comparison of the stationary $\left\langle \Gamma_p^\infty \right\rangle$ to GS2 results.

4.2.4 Streamfunction plots

The next few figures display the appearance of the electrostatic potential, ϕ, which is also the streamfunction for the $\mathbf{E} \times \mathbf{B}$ drift of ions and electrons. First, isosurface plots (from Matlab) of $\phi(x, y)$ are displayed in Fig. 4.9 and 4.10 from a typical snapshot during the linear growth and the nonlinear stationary state for the two extreme values of the gradient studied. These plots clearly show the inhomogeneity of the flow: first the $k_y\rho \sim 1$ streamers of the linear instability, and then the $k_x\rho_i \sim 1$ directed zonal flows of the secondary instability. In the nonlinear phase,

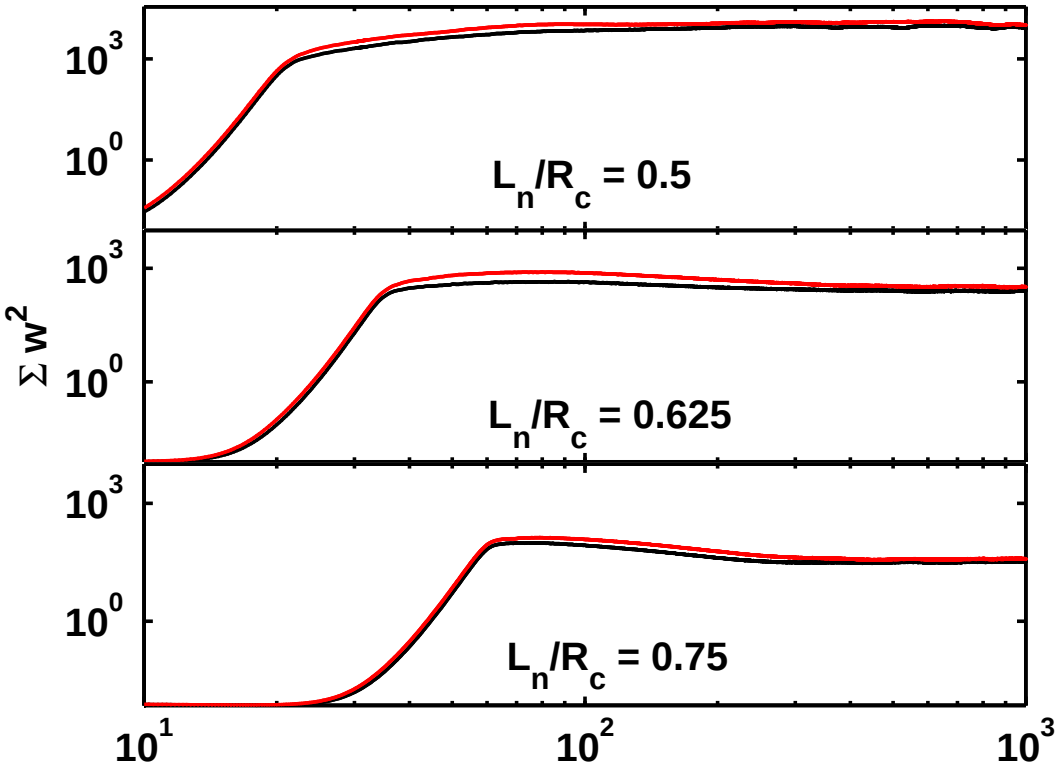

Figure 4.8: Sum of the squared weights for ions (black) and electrons (red). This computation uses $\sum_i w_i^2$ where $w_i = \delta f_1 / F_M$.

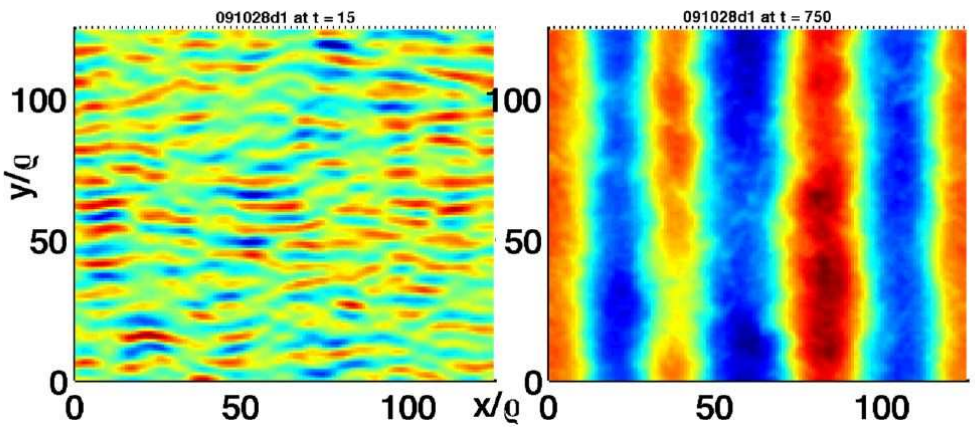

Figure 4.9: Electrostatic potential surface for the linear and nonlinear state of the entropy mode for $L_n/R_c = 0.5$.

one may also observe a long wavelength mode in the axial direction similar to the inverse box size, $k_y\rho_i \sim 1/L$. This mode is peaked at $k_x\rho_i = 0$ and represents one of the excited modes of the secondary instability.

There are structures in the turbulence with lower amplitudes than the strong zonal flow. These structures have finite k_y and are responsible for drift transport in the radial direction. A Fourier filter at to remove $k_x > 0, k_y = 0$ modes removes the zonal flows and reveals the structure underneath. This effect of this filter is shown in Figures 4.11, 4.12 and 4.13 for all three gradients studied here. These figures also show the value of ϕ, showing that the turbulence amplitude for the stronger gradient is larger, and the amplitude of the zonal flows is larger than the background turbulence.

Now it is also useful to examine the mode structure of the turbulence in k space. Figures 4.14 and 4.15 show the dependence of the $|\phi|^2$ spectra as a function of k_x and k_y with summation taken over the perpendicular direction for each data

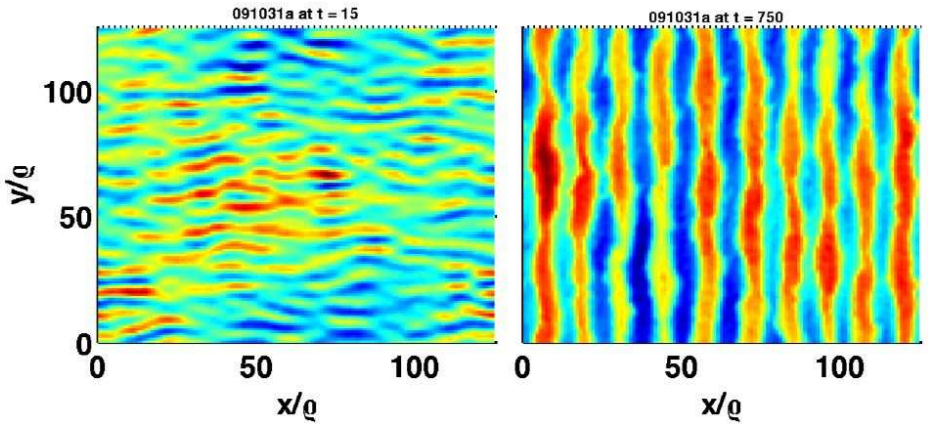

Figure 4.10: Electrostatic potential surface for the linear and nonlinear state of the entropy mode for $L_n/R_c = 0.75$.

set. These plots also show the effect of the zonal flow filtering on both k_x and k_y spectra. Wavenumbers larger than $k\rho = 2.5$ are not shown in these plots because the low-pass filter makes their amplitudes negligible. The broader spectrum of excited modes $\phi^2(k_x)$ and $\phi^2(k_y)$ is closer to parity for the stronger gradient.

4.3 Analysis of dispersion of gyrocenters

A PIC code such as GSP provides a straightforward way to extract Lagrangian particle tracking data from the simulation. The marker particles used for solving the gyrokinetic characteristics can be appropriated as the tracers for the $\mathbf{E}\times\mathbf{B}$ drift. The markers are not strictly tracers, since their positions affect the field. However, when a small number of markers is isolated and used to probe the turbulence, the statistics of the markers should give the same result as pure tracer particles when the number of probe markers is small, and thus represents a low density species. Each marker also carries a weight, which contains information about the fraction

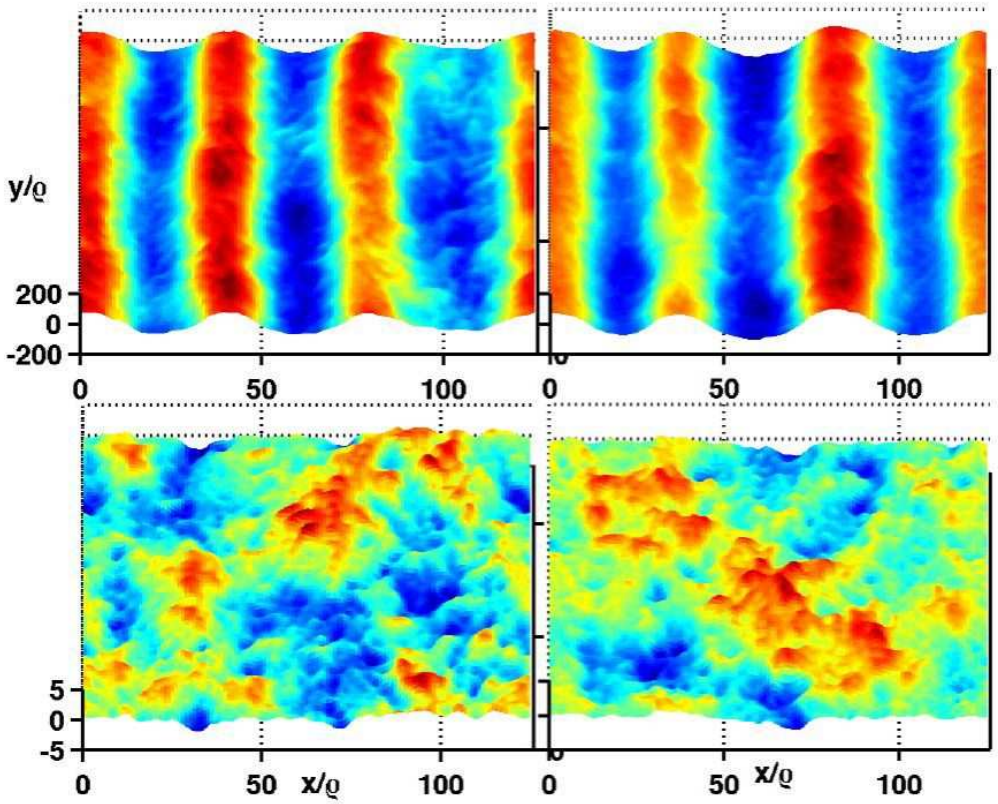

Figure 4.11: Electrostatic potential surface for two snapshots of the nonlinear state of the entropy mode for $L_n/R_c = 0.5$. The top panels are the unfiltered data, while the bottom panels have all significant k_x structure at $k_y = 0$ removed.

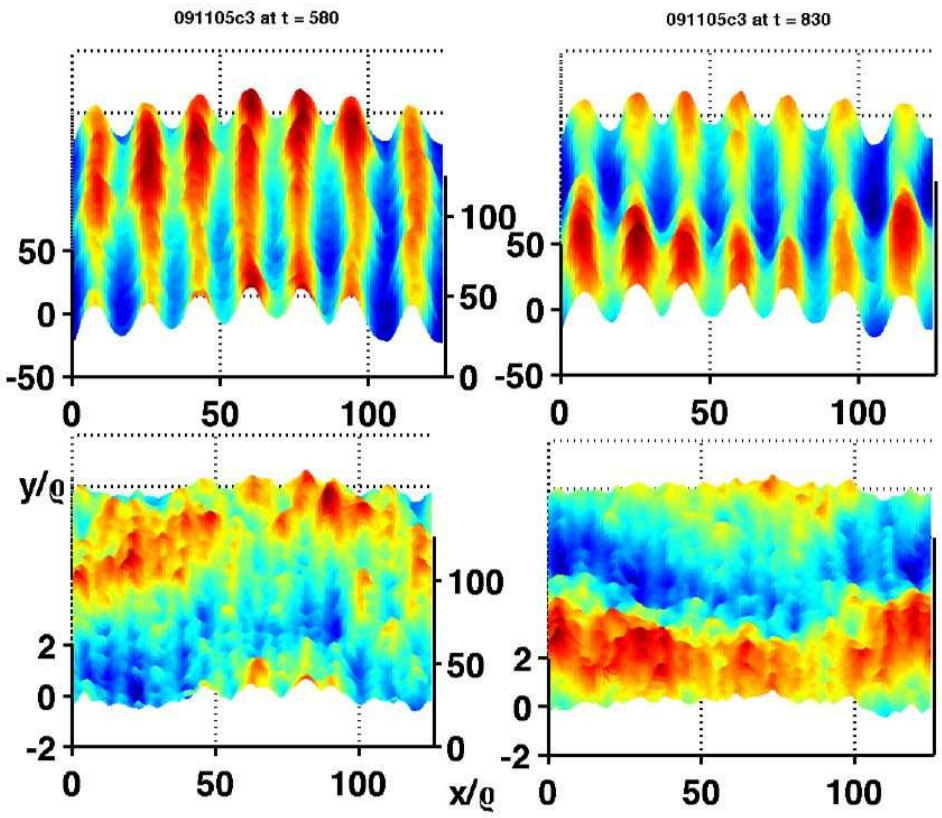

Figure 4.12: Electrostatic potential surface for two snapshots of the nonlinear state of the entropy mode for $L_n/R_c = 0.625$. The top panels are the unfiltered data, while the bottom panels have all significant k_x structure at $k_y = 0$ removed.

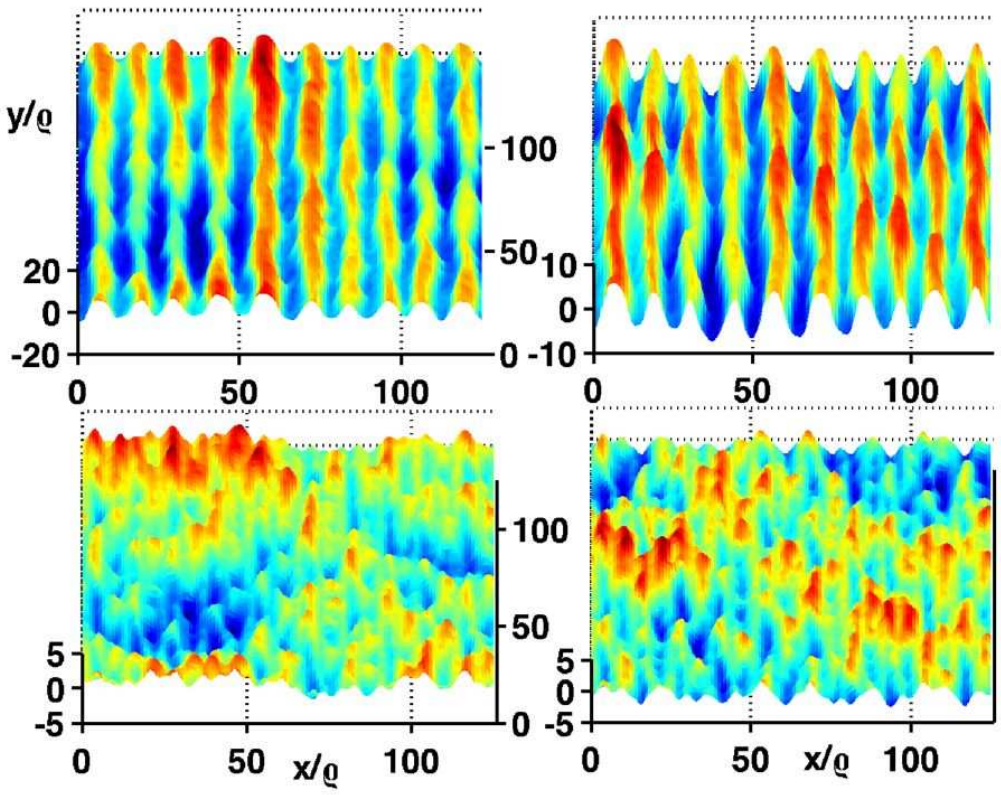

Figure 4.13: Electrostatic potential surface for two snapshots of the nonlinear state of the entropy mode for $L_n/R_c = 0.75$. The top panels are the unfiltered data, while the bottom panels have all significant k_x structure at $k_y = 0$ removed.

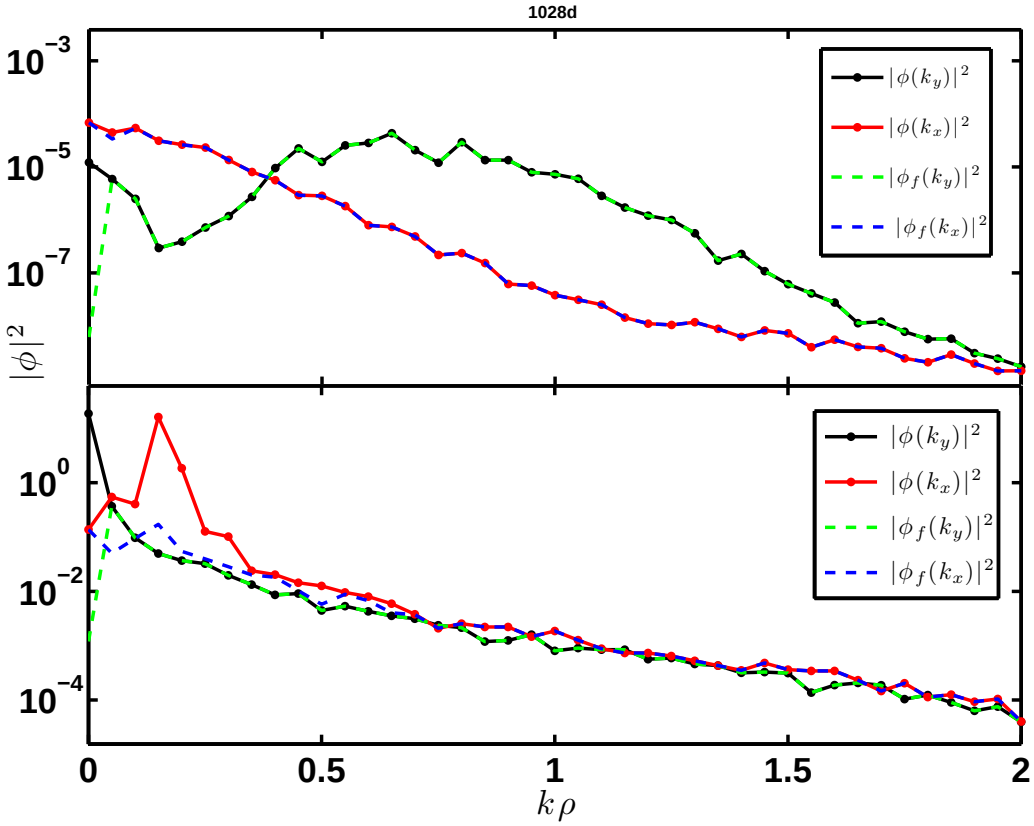

Figure 4.14: Spectra of $|\phi|^2$ for the strongest gradient $L_n/R_c = 0.5$ in the linear transient (top) and nonlinear stationary phase (bottom). The spectra $\phi(k_x)$ are integrated over all k_y and vice versa. Dashed lines show the spectra (ϕ_f) after the zonal flows ($k_x > 0, k_y = 0$) have been filtered out of the spectra.

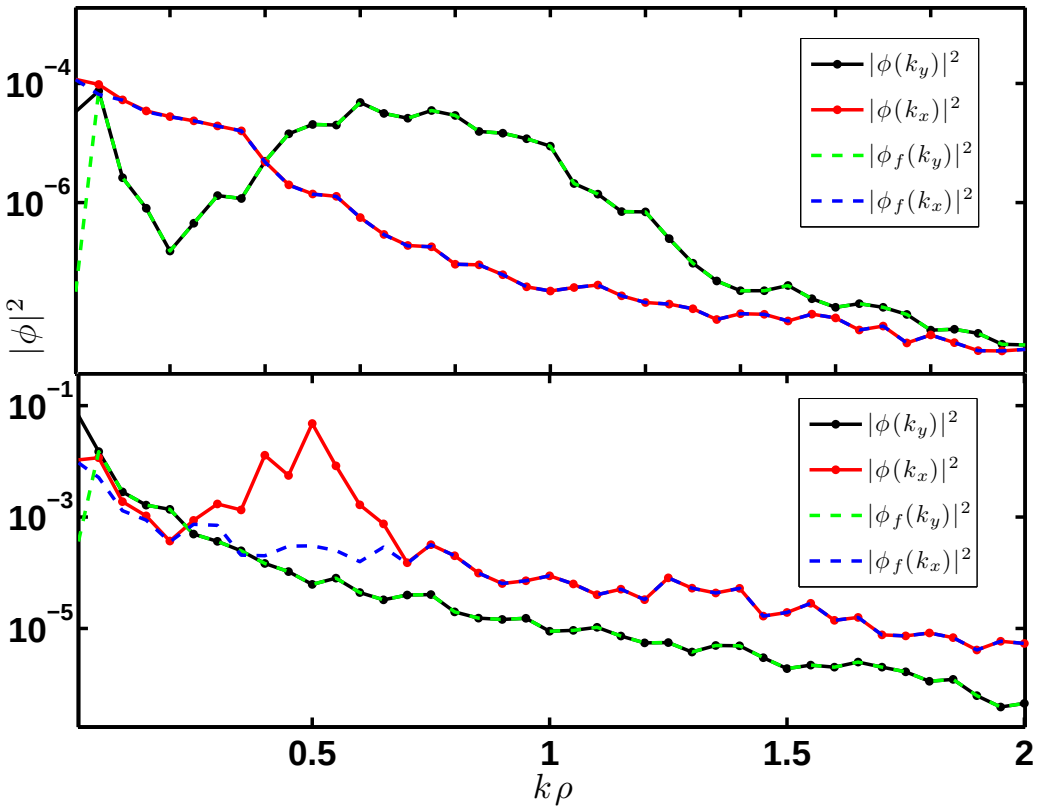

Figure 4.15: Spectra of $|\phi|^2$ for the weaker gradient $L_n/R_c = 0.75$ in the linear transient (top) and nonlinear stationary phase (bottom). The spectra $\phi(k_x)$ are integrated over all k_y and vice versa. Dashed lines show the spectra (ϕ_f) after the zonal flows ($k_x > 0, k_y = 0$) have been filtered out of the spectra.

of the perturbed distribution function represented by each marker. These weights change as the simulation proceeds, and when the weight changes, the identities of the plasma particles represented by the marker changes as well. One way to understand this is to realize that the gathering and scattering of information on and off the grid for solving the gyrokinetic Poisson equation mixes the identities of the individual particles that each marker is meant to represent. Therefore, when using particle tracking techniques, the weights should be treated carefully, and the markers can be interpreted as tracers. Each one represents the same number of massless plasma particles. Unlike the δf weights, which impart a positive or negative deviation from the background Maxwellian to each marker, the tracer interpretation gives a constant value to the weight of each tracer. The tracer weight can be assumed unity, and the variance of tracer displacements can be taken formally with this trivial weight factor.

All of the following data on marker trajectories is based on the ion gyrocenter motion for ~ 50000 tracers taken from the self-consistent ensemble. These probe are meant to be a random sample from the entire set of markers. A similar, independently random set of markers is initialized on each processor in the parallel simulation. Though the turbulence simulation has periodic boundary conditions, the subset of probe markers is allowed to follow a trajectory outside of the periodic box, where they encounter a copy of the streamfunction.

A lucid interpretation of the statistics of gyrocenter dispersion is aided by inspection of several sample drift trajectories in the flow. The following figures show sample trajectories in the $(\hat{x}, \hat{y})$ plane for various values of $v_\perp$. Figure 4.16 shows

the tracks of several gyrocenters, ignoring the initial burst of quick radial transport from the streamers. This gives an idea of the range of possible trajectory types in the flow. Most trajectories move long axial distances, some reversing direction frequently and others perhaps never reversing direction. The incremental radial and vertical $\mathbf{E} \times \mathbf{B}$ drift velocities of these tracers are quite similar, but the directed motion along the zonal flow causes much larger axial displacements. The size of the gyroradius changes the dispersion properties of gyrocenters, as expected from Chapter 3. For example, gyrocenters with the largest gyroradii are ten times less likely to undergo a radial excursion of more than $30\rho_i$ when $L_n/R_c = 0.5$. Section 4.5.4 contains more details on the ρ_i dependence of radial dispersion statistics.

4.4 Self-consistent δf marker particle axial tracer dispersion

For a comparison between the tracer statistics from Chapter 3 and the self-consistent turbulence addressed here, it is necessary to examine the axial displacements for the marker ion gyrocenters in the Z-pinch. In Chapter 3 we noted the superdiffusive behavior of the streaming of sticky-flight trajectories in this direction. The superdiffusion experienced a transition in time (for small values of ρ), from nearly ballistic ($\gamma = 1.9$) to moderately superdiffusive ($\gamma = 1.6$). Larger average gyroradii erased this transitional behavior by smoothing over the stochastic region. The number of sticky flights reduced to zero in the limit of $\rho >> \mathcal{O}(1/k)$, where k is the wavenumber of the well-defined vortices in the single shear layer of Chapter 3. Presently, with self-consistent, doubly periodic turbulence, we expect

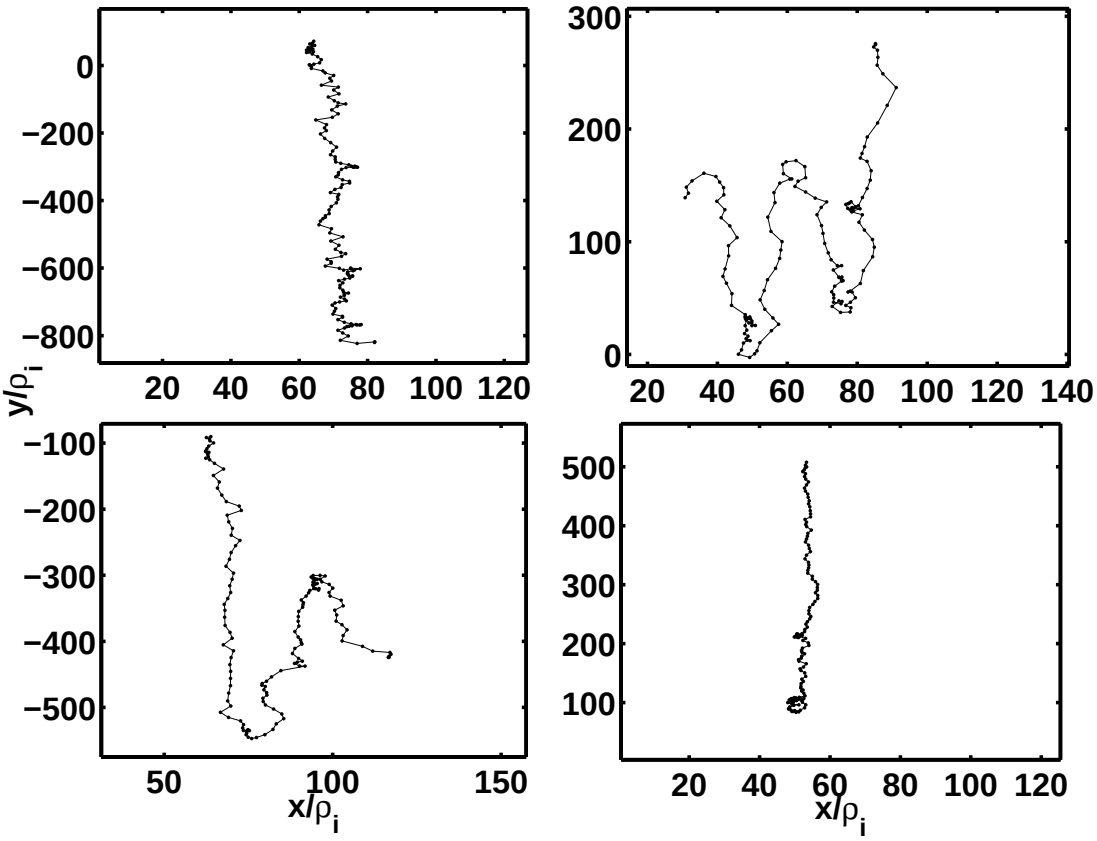

Figure 4.16: Four sample particle trajectories from the $L_n/R_c = 0.5$ case, for $100L/v_{th} < t < 250L/v_{th}$. Clockwise from upper left, the value of $v_\perp/v_{th}$ is $[0.125, 0.125, 3.0, 1.5]$. The upper right and lower left trajectories are classified as non-flights, while the other two are flights, as decided by the velocity reversal filter.

complications, since there is no longer a sharp transition between integrable and nonintegrable orbits (see Figure 3.4).

4.4.1 Filtering the ballistic trajectories

A filter was implemented in the example of the Hamiltonian flow of Chapter 3 to focus on the most interesting trajectories. This filter separated the population according to the time of first reversal in the sign of v_y. The same technique yields a meaningful separation of trajectories in the self-consistent case as well. Let the observation of $sign(v_y)$ begin at $t_{obs} = 540$. If the cutoff time t_{rev} for the first reversal is taken as $t_{rev} = 840$ after the beginning of the simulation, the population breaks into two distinct categories for each value of the gradient examined here. Let us use the term "flights" for trajectories which do not reverse velocity within $t_{obs} < t < trev$, and the term "non-flights" for other trajectories. A velocity reversal indicates that a trajectory is trapped, at least briefly, in an eddy. For gradients given by $L_n/R_c = [0.5, 0.625, 0.75]$, the ratio of number of flights to number of non-flights is $N_f/N_{nf} = [0.16,\ 1,\ 1]$. The effect of the filter can be seen for the weak gradient example in Figures 4.17 and 4.18. The distinction between final positions in both radial and axial directions is clear: flights travel further axially than non-flights, and flight travel less far radially than non-flights.

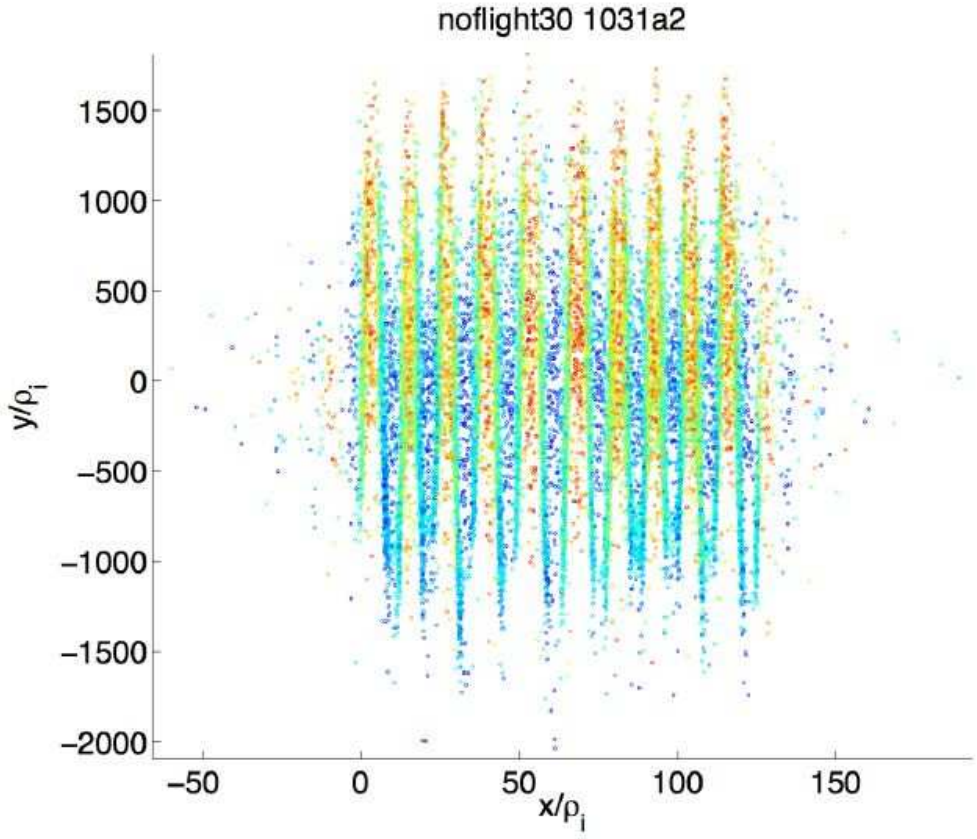

Figure 4.17: Positions of gyrocenters at the end of the simulation for the weakest gradient, $L_n/R_c = 0.75$. These are the gyrocenters categorized as non-flights. Colored according to instantaneous value of $-3.2 < \mathbf{v}_{E\times B} \cdot \hat{y} < 4.0$.

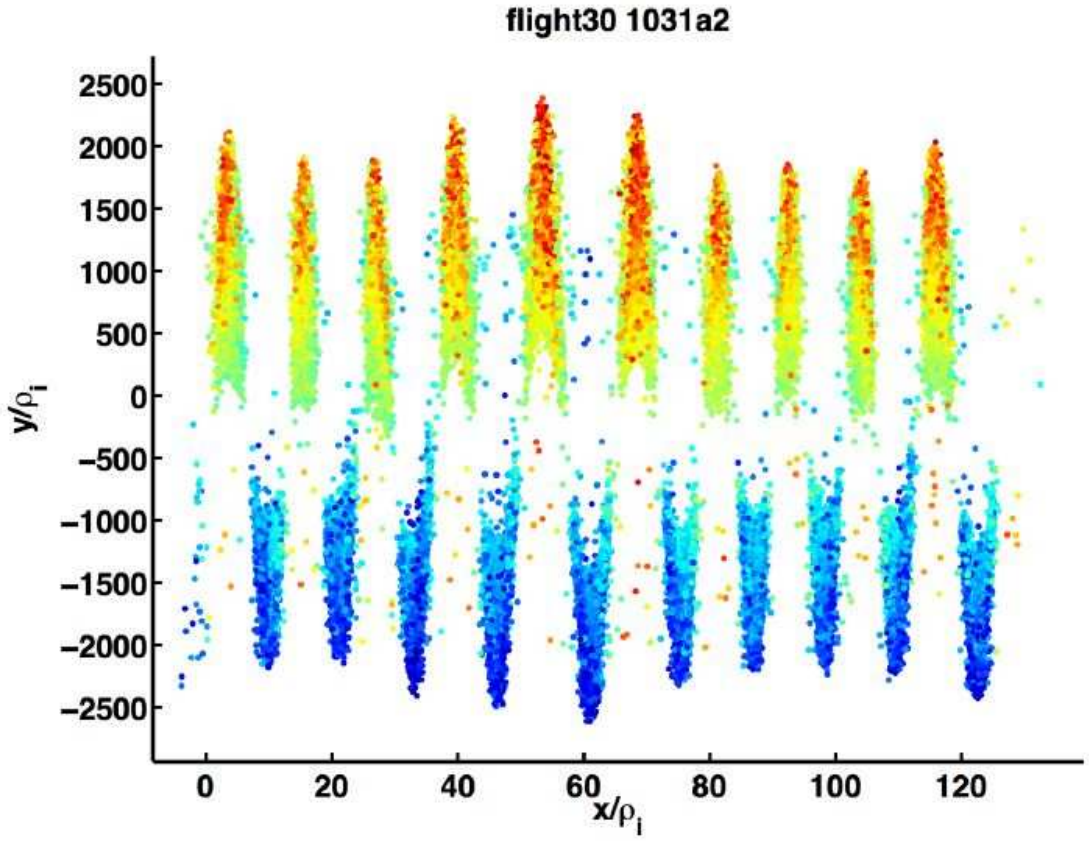

Figure 4.18: Positions of gyrocenters at the end of the simulation for the weakest gradient, $L_n/R_c = 0.75$. These are the gyrocenters categorized as flights. Colored according to instantaneous value of $-3.4\mathbf{v}_{E\times B} \cdot \hat{y} < 4.2$.

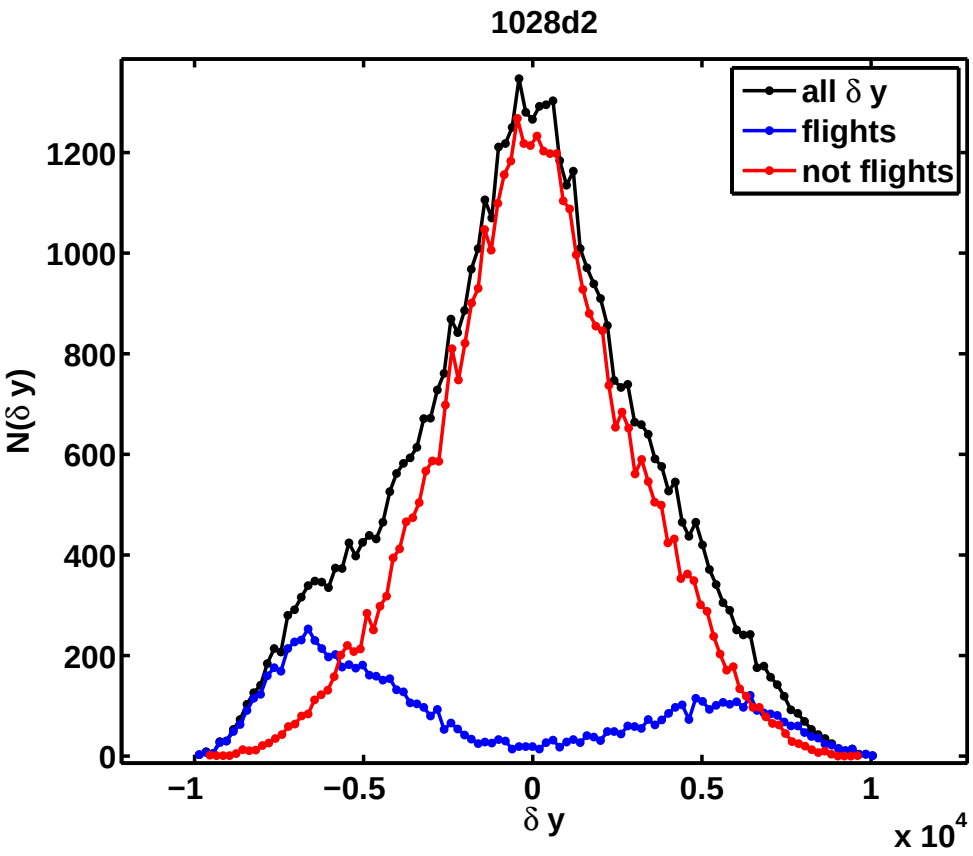

Figure 4.19: Axial displacement distribution (not normalized) for the strong gradient, $L_n/R_c = 0.5$, showing all trajectories in black, flights in blue and non-flights in red. The split between flights and non-flights is 16/84.

4.4.2 Statistics of axial gyrocenter displacements

Figure 4.19, 4.20 and 4.21 show the distribution of axial displacements for all three gradients. Notable is the trend for increasing number of flight trajectories with decreasing gradient strength. The flight trajectories have an asymmetric bimodal distribution for all values of the gradient. Non-flight trajectories have a single, slightly asymmetric peak for all values of the gradient.

From the displacement PDFs, moments can be computed numerically, giv-

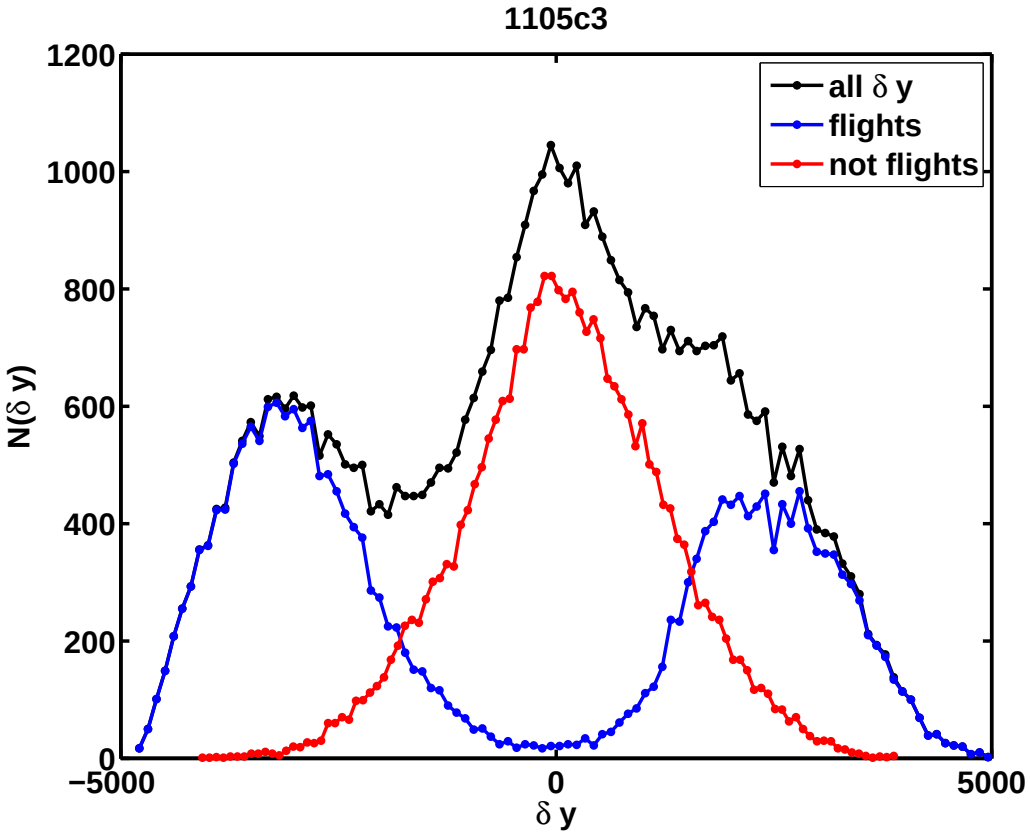

Figure 4.20: Axial displacement distribution (not normalized) for the intermediate gradient, $L_n/R_c = 0.625$, showing all trajectories in black, flights in blue and non-flights in red. The split between flights and non-flights is 47/53.

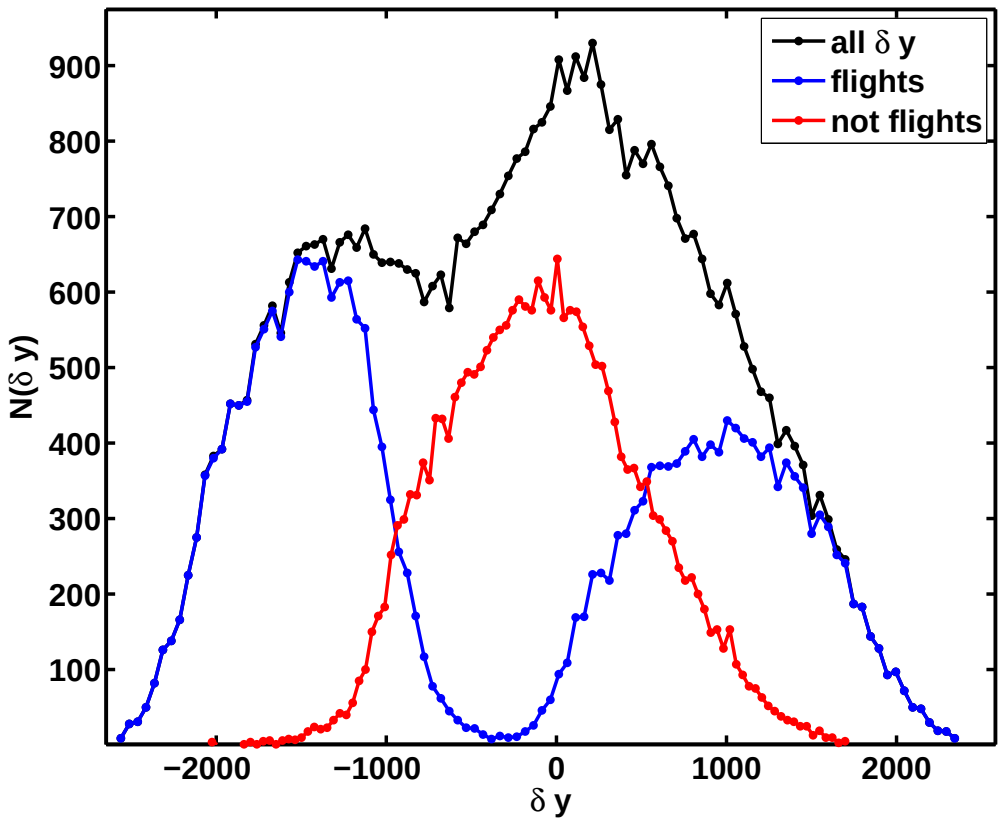

Figure 4.21: Axial displacement distribution (not normalized) for the weakest gradient, $L_n/R_c = 0.75$, showing all trajectories in black, flights in blue and non-flights in red. The split between flights and non-flights is 53/47.

ing (for the axial direction: $\hat{y}$) the mean: $M_y(t) =< \delta y(t) >$, variance: $\sigma_y^2(t) = \langle(\delta y(t) - \langle\delta y(t)\rangle)^2\rangle$, skewness: $\gamma_{1,y}(t) = \left\langle \frac{(\delta y(t) - \langle\delta y(t)\rangle)^3}{\sigma(t)^3} \right\rangle$ and kurtosis: $\beta_{1,y}(t) = \left\langle \frac{(\delta y(t) - <\delta y(t)>)^4}{\sigma(t)^4} \right\rangle$.

A running diffusion coefficient may be defined as $D_y(t) = \frac{\sigma(t)^2(t)}{2t}$, and a ballistic coefficient may be defined as $F_y(t) = \frac{\sigma(t)^2(t)}{t^2}$. With the brackets, $\langle D_y \rangle$ (or $\langle F_y \rangle$), is a mean value of the running diffusion (or ballistic) coefficient. The mean value is always taken after the transient period, which is easily identified for the radial diffusion in Section 4.5.1.

Figures 4.22, 4.23 and 4.24 show the ballistic coefficient of the axial displacement for three values of L_n/R_c, alongside the same data for both flights and non-flights. Ballistic behavior ($\sigma_y^2(t) \sim t^2$) is observed by the end of the simulation for each density gradient when considering all trajectories. An oscillation is seen for the strongest value of the gradient, including a period of $\sigma_y^2(t) \sim t^3$ dispersion. The non-flights have a period of superdiffusion before settling into a ballistic mode. As in Chapter 3, we compute the superdiffusion coefficients γ_y for each value of the gradient, placing the results into Table 4.1.

4.4.3 Statistics of axial velocity increments

Another measure of the Lagrangian statistics in a turbulent flow comes from the velocity increments. For each trajectory, the value of the radial and axial velocity is recorded at the same frequency as the position data. A histogram or normalized distribution function of these instantaneous trajectory velocities is easily con-

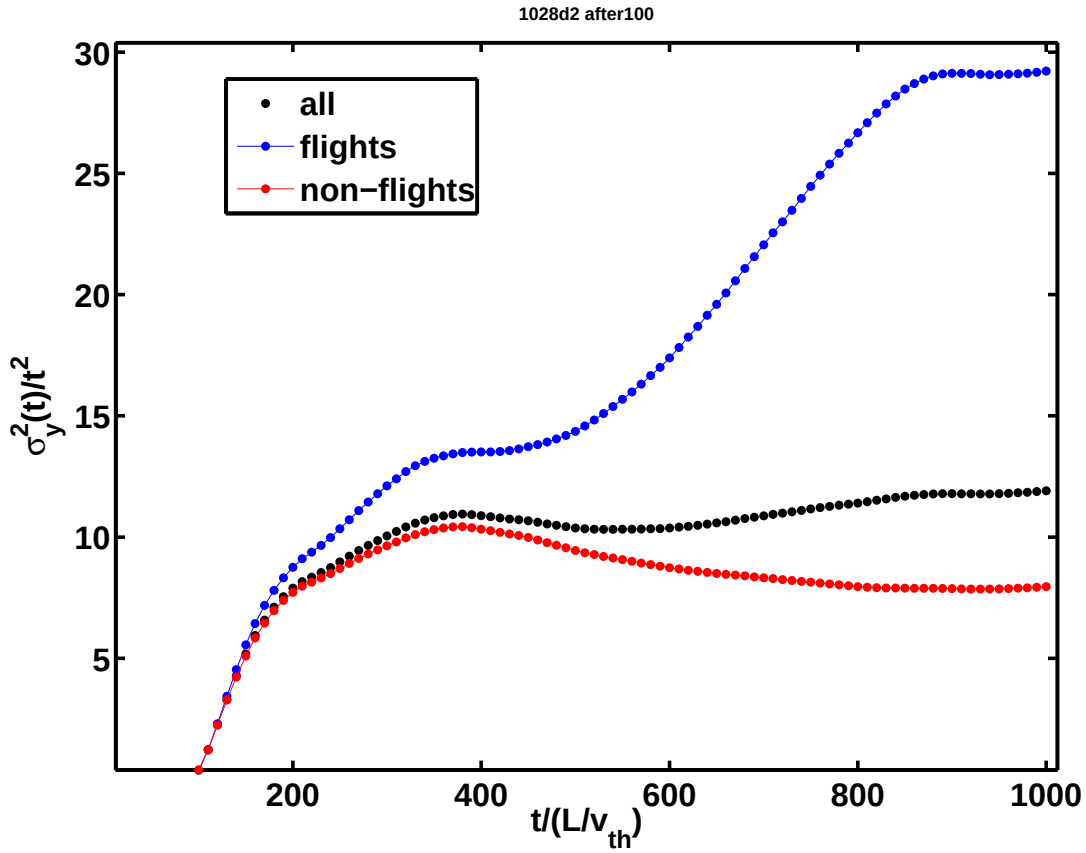

Figure 4.22: Variance of axial displacement for $L_n/R_c = 0.5$ scaled by t^2 to emphasize the ballistic nature of the motion. Flights are shown in blue, the full ensemble is shown in black and non-flights are shown in red.

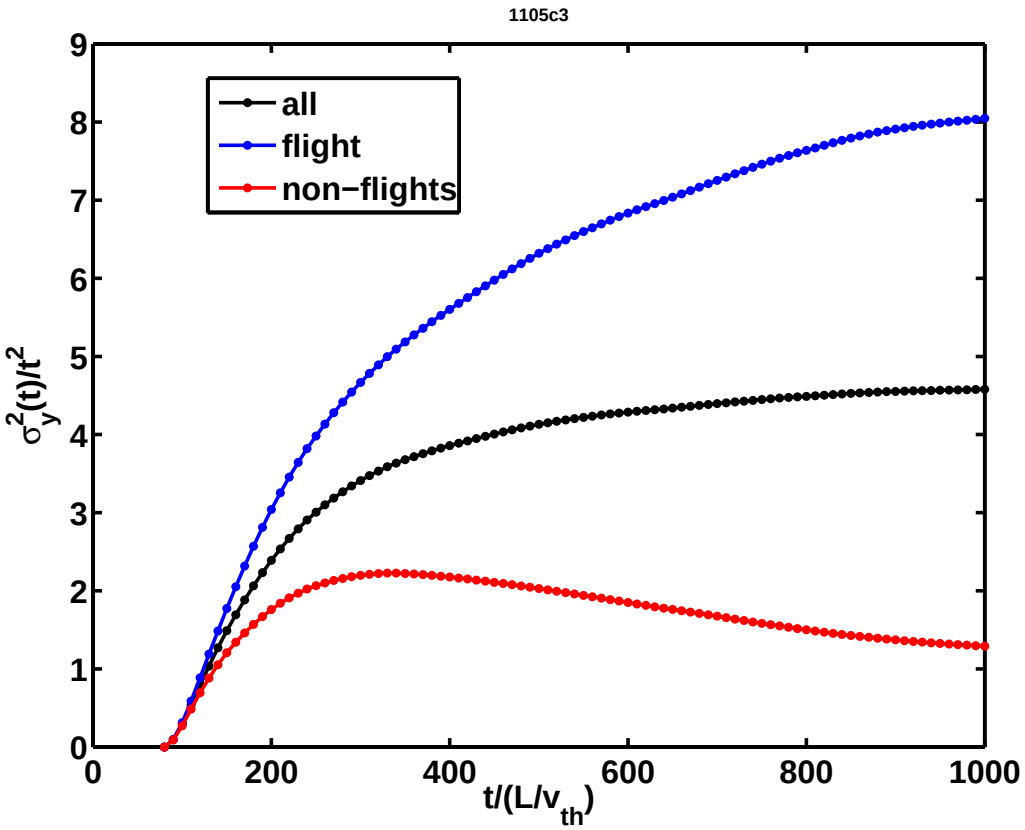

Figure 4.23: Variance of axial displacement for $L_n/R_c = 0.6255$ scaled by t^2 to emphasize the ballistic nature of the motion. Flights are shown in blue, the full ensemble is shown in black and non-flights are shown in red.

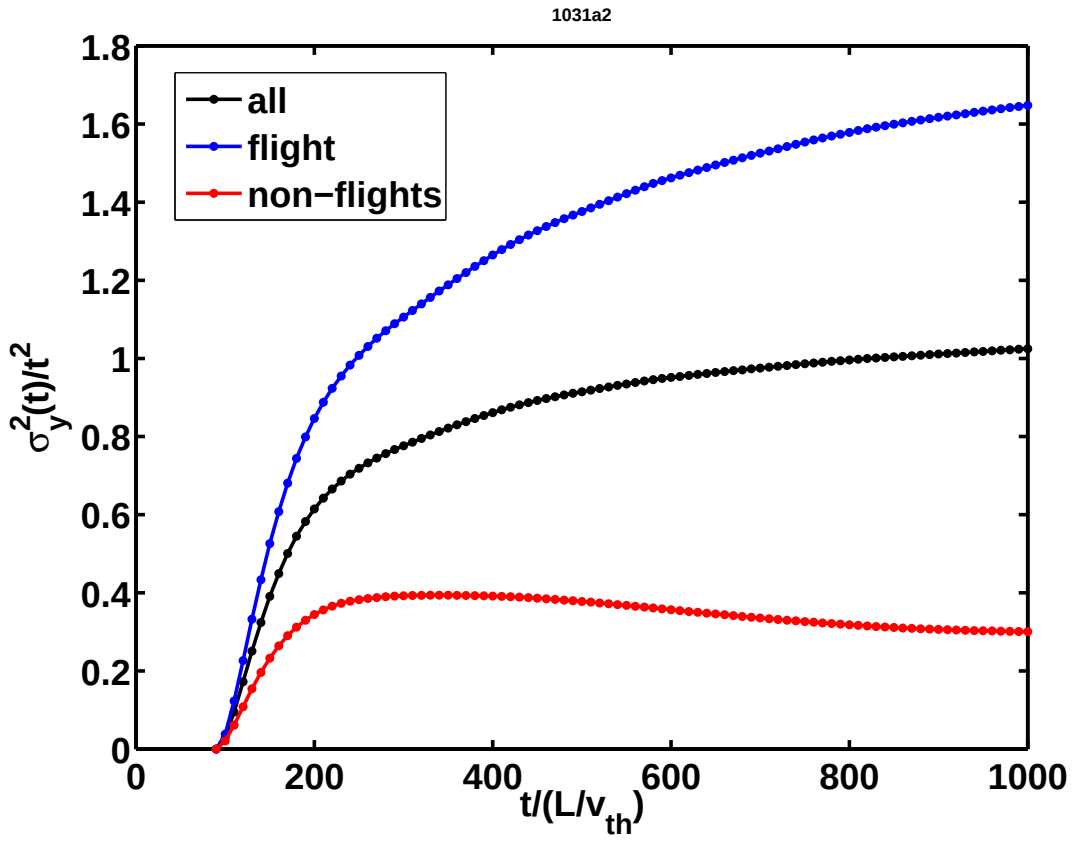

Figure 4.24: Variance of axial displacement for $L_n/R_c = 0.75$ scaled by t^2 to emphasize the ballistic nature of the motion. Flights are shown in blue, the full ensemble is shown in black and non-flights are shown in red.

Table 4.1: Superdiffusion coefficient γ_y for non-flight axial tracer displacements in the self-consistent zonal flows for three values of the density gradient. This coefficient is computed with a curve-fitting routine using only the non-flight trajectories. After the specified regime of superdiffusion, during the time frame specified in the table, the dispersion becomes ballistic, as confirmed by comparison with a t^2 curve.

L_n/R_c	γ_y	Δt
0.5	1.64	$500 < t < 800$
0.625	1.25	$600 < t < 900$
0.75	1.64	$440 < t < 920$

structed. In isotropic three-dimensional Navier-Stokes turbulence, the distribution of velocity increments is believed to undergo a transition from long tail power-law type PDFs to Gaussian-shaped PDFs [141].

Here we show the distribution of axial velocities in Figures 4.25, 4.26 and 4.27. The distributions reach a steady state by $t = 500R/v_{th}$. We note that it is possible to rescale the axial velocity PDFs for different values of the gradients so that the PDFs are self-similar, as shown in Figure 4.28. Most notable is the distinction between flights and non-flights for the weaker gradients. The flights have a bimodal distribution, showing the populations of particles moving up and down in the shear flow. The asymmetry in the heights of the peaks indicates a greater likelihood for downward flights The non-flights have a single peak with approximately zero mean

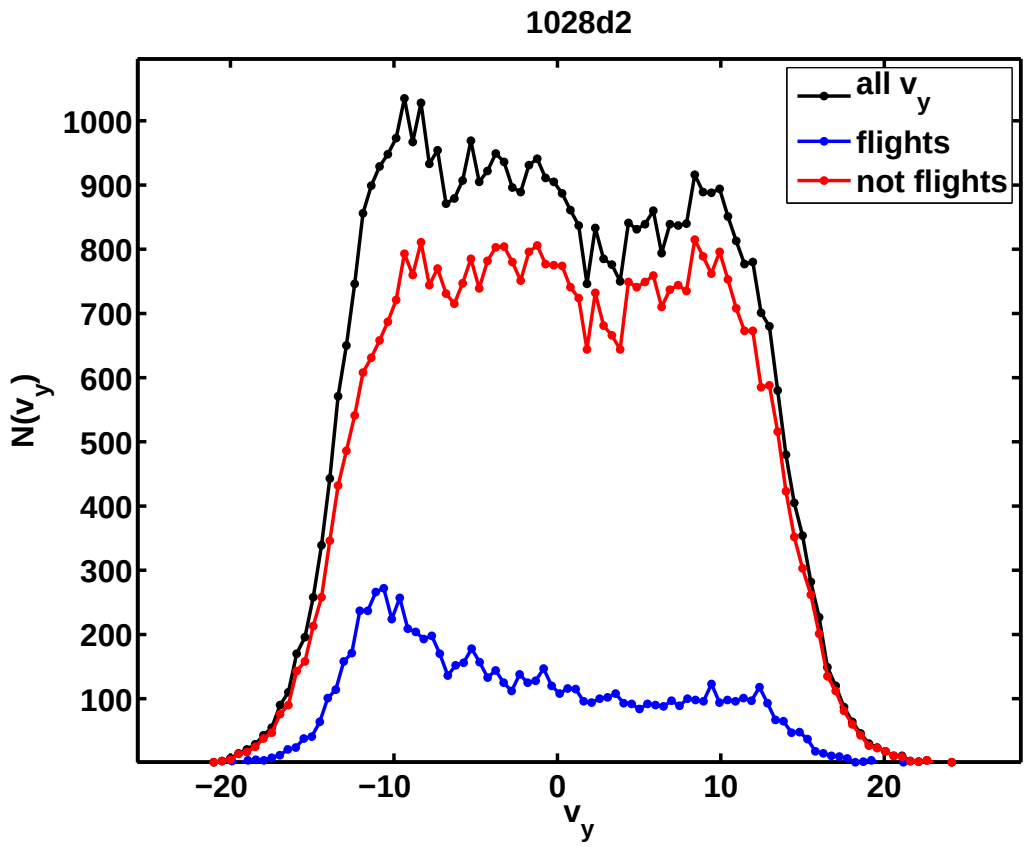

Figure 4.25: Axial velocity increment distributions for several times during the simulation for $L_n/R_c = 0.5$ showing saturation.

and long, non-Gaussian tails that cause the superdiffusion.

4.4.4 Axial velocity Lagrangian correlation function

The Lagrangian velocity correlation function is computed for the strongest and weakest gradients and compared in Figure 4.29. For the stronger gradient, the correlation drops to zero with essentially an exponential decay, $C_L(v_y) \sim \exp(-t/\tau_C)$ with $\tau_C \sim 200L/v_{th}$. The weaker gradient decays to a nonzero value, indicating that there are long-lived correlations in the axial motion. This can be explained

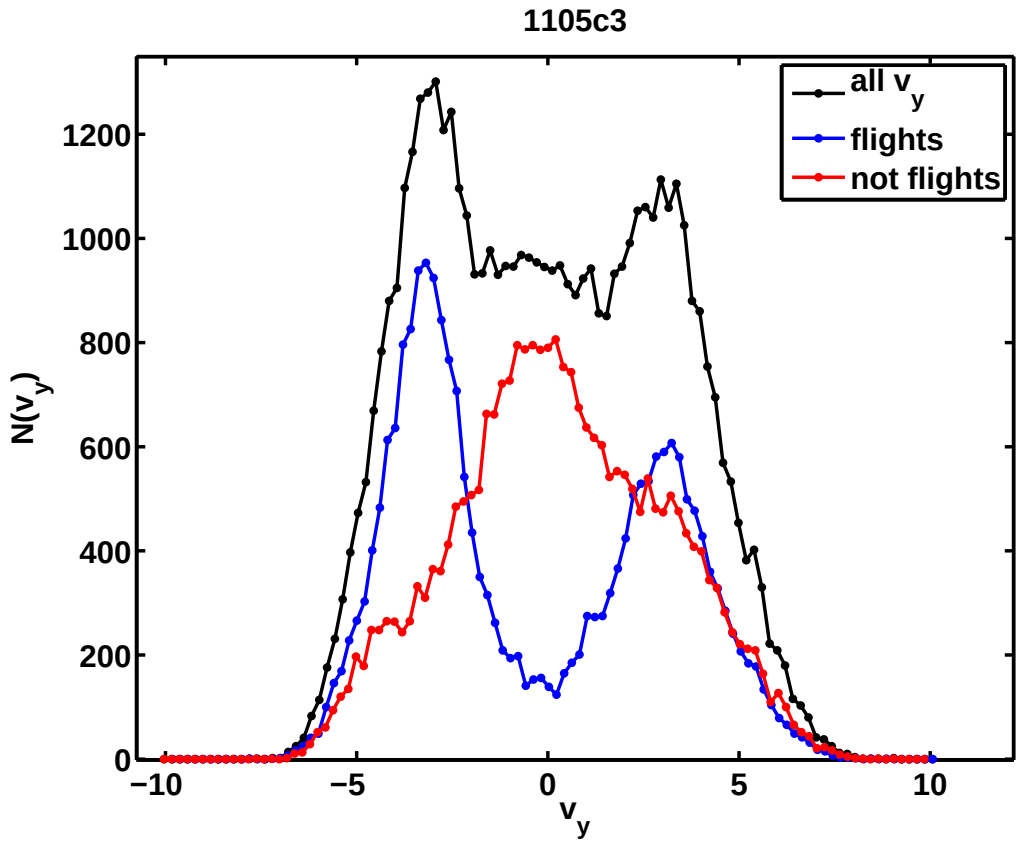

Figure 4.26: Axial velocity increment distributions for several times during the simulation for $L_n/R_c = 0.625$ showing saturation.

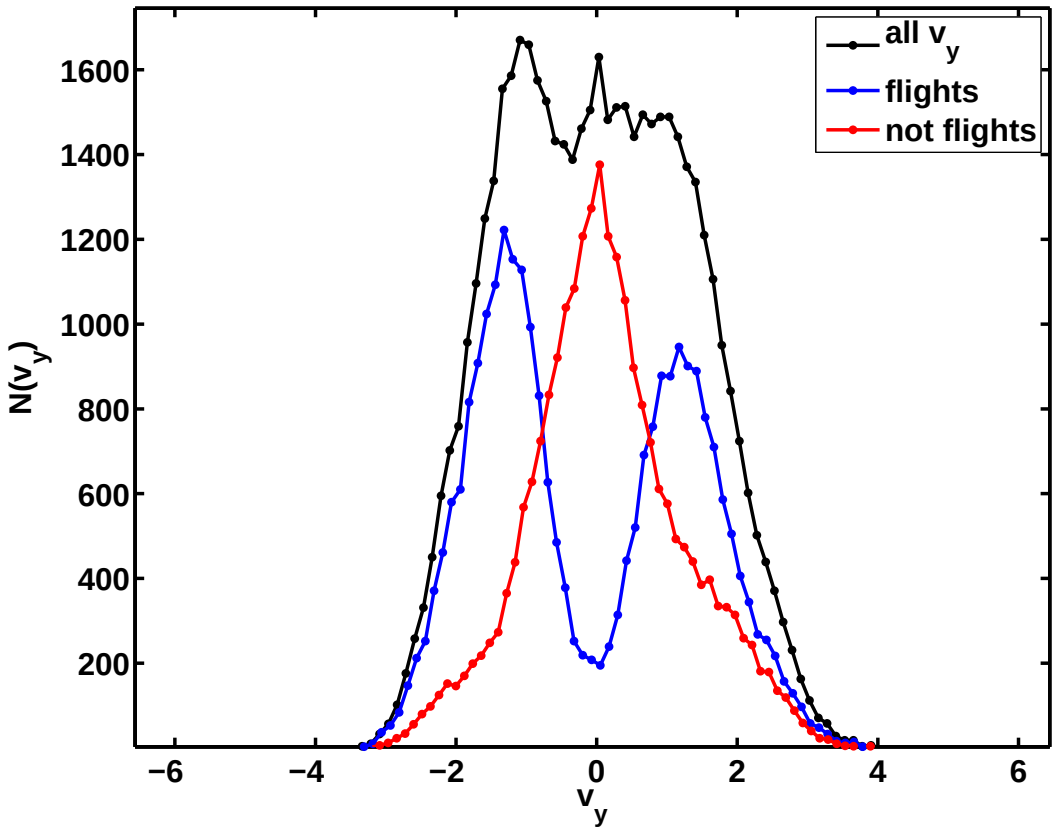

Figure 4.27: Axial velocity increment distributions for several times during the simulation for $L_n/R_c = 0.75$ showing saturation.

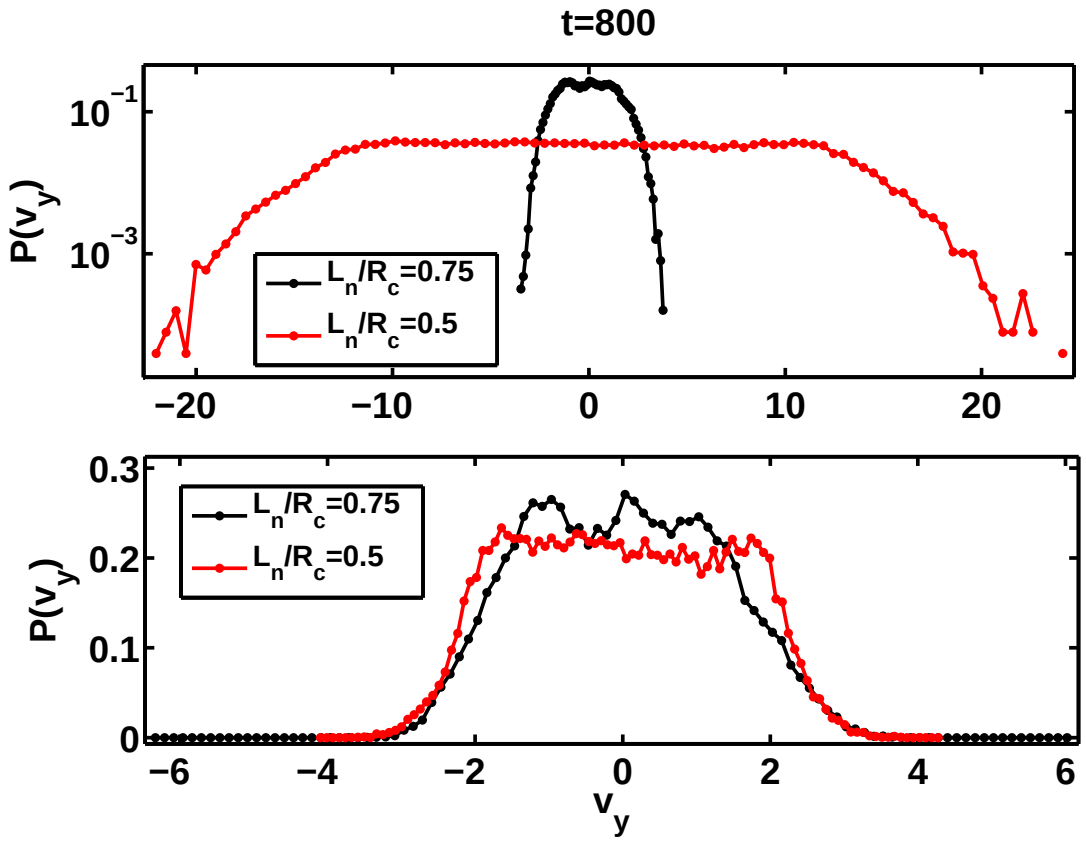

Figure 4.28: Axial velocity increment PDFs in the saturated state for $L_n/R_c = [0.5, 0.75]$ showing a mapping of the PDF for one gradient onto the other by a rescaling of both axes by a factor of 6.

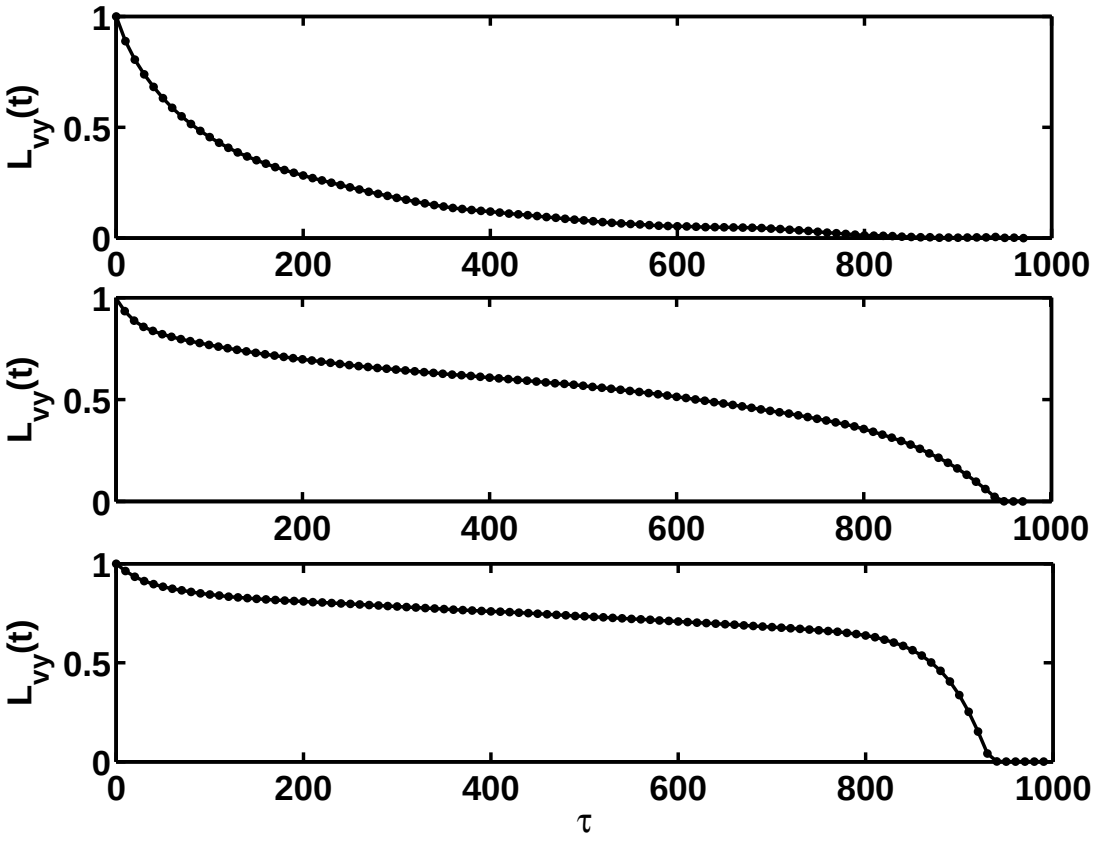

Figure 4.29: Axial Lagrangian velocity correlation for (top to bottom) $L_n/R_c = [0.5, 0.625, 0.75]$.

by noting that the zonal flows for stronger gradients have a shearing rate nearer a tertiary shear instability [66, 1]. The approach of the shearing rate to the instability boundary causes the turbulence to have higher amplitude k_y structure relative to the amplitude of the k_x structure, as seen in Figure 4.14. These relatively stronger k_y structures allow more radial dispersion, and are also the source of the larger box averaged particle flux.

4.5 Self-consistent δf marker particle radial tracer dispersion

Axial transport, as described in the previous section, can be compared with results from the Hamiltonian flow model (see Chapter 3). The $v_y = \tanh(x)$ shear flow in that model is qualitatively similar to the zonal flows in self-consistent turbulence. However, radial transport is more relevant to plasma confinement, and the aperiodicity of the $\tanh(x)$ function prohibits the study of radial transport in the stochastic Hamiltonian. Therefore, radial displacement and velocity statistics will be considered in this section without much comparison to Chapter 3. As mentioned previously, several recent studies of radial tracer transport in gyrokinetic turbulence simulations should be compared instead, from Sánchez *et al* [14], Hauff *et al* [50] and Zhang *et al* [142]. In particular, non-Gaussian statistics of radial tracer gyrocenter dispersion across a shear flow may have an effect on confinement times. This may not be true for the bulk plasma, since the tracers are not inclusive of the weights. Test-particle statistics are therefore most immediately useful to describe the motion of impurities, a species of fast ions or perhaps an ablating pellet [39]. However, as discussed by [143] and [25], there can be an equivalence between the test-particle diffusion coefficient and the diffusion coefficient derived from the Fick's Law relationship between the steady-state flux and the local gradient (see Appendix C). We will see that this equivalence is followed, up to a scaling factor of order unity, for this two-dimensional gyrokinetic simulation.

4.5.1 Statistics of radial gyrocenter displacements

In this section the various moments of the radial displacement distribution are examined and compared to a Gaussian distribution. Each of the mean, variance, skewness and kurtosis (defined in Section 4.4.2) are either plotted or described. Distributions of radial displacements for all three gradients appear in Figures 4.30, 4.31 and 4.32.

The mean (Figure 4.33, 4.34 and 4.35) and skewness fluctuate about zero for all values of L_n/R_c. This means that the direction of radial dispersion of tracers is insensitive to the direction of the density gradient. Of course, the outward $\langle\Gamma\rangle_p^\infty > 0$ is due to the cross-phase between the velocity and perturbed density. This can be seen in a scatter plot of final positions colored according to the marker weight, Figure 4.36. The marker weights are large and positive in the positive radial direction, but large and negative in the negative radial direction. This implies that the positive flux information is contained in the weights, which are not considered when computing the dispersion of a subset of probe markers.

For all gradients the distributions have longer tails than a Gaussian. This leads to a large kurtosis, as shown in Figures 4.37, 4.38 and 4.39. The only kurtosis which is nearly Gaussian is the flight kurtosis for the strongest gradient (Figure 4.37). This means that the flights in the strongest gradient did not experience as many large steps in the radial direction. The long tails of the other PDFs also have few particles, compared to the peak, but these rare radial displacements are sufficient to cause a large kurtosis relative to Gaussian.

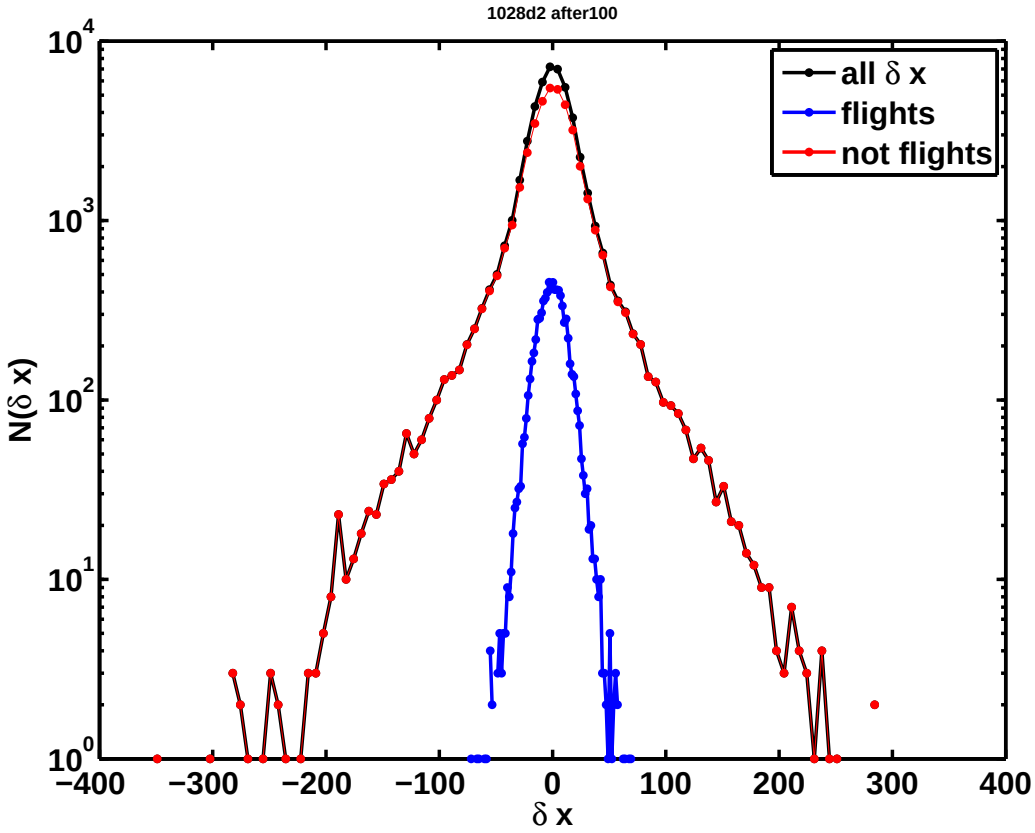

Figure 4.30: Radial displacement distribution for the strong gradient, $L_n/R_c = 0.5$, showing all trajectories in black, flights in blue and non-flights in red. The non-Gaussian tails in the non-flight PDF contrast with the Gaussian shape of the flight PDF.

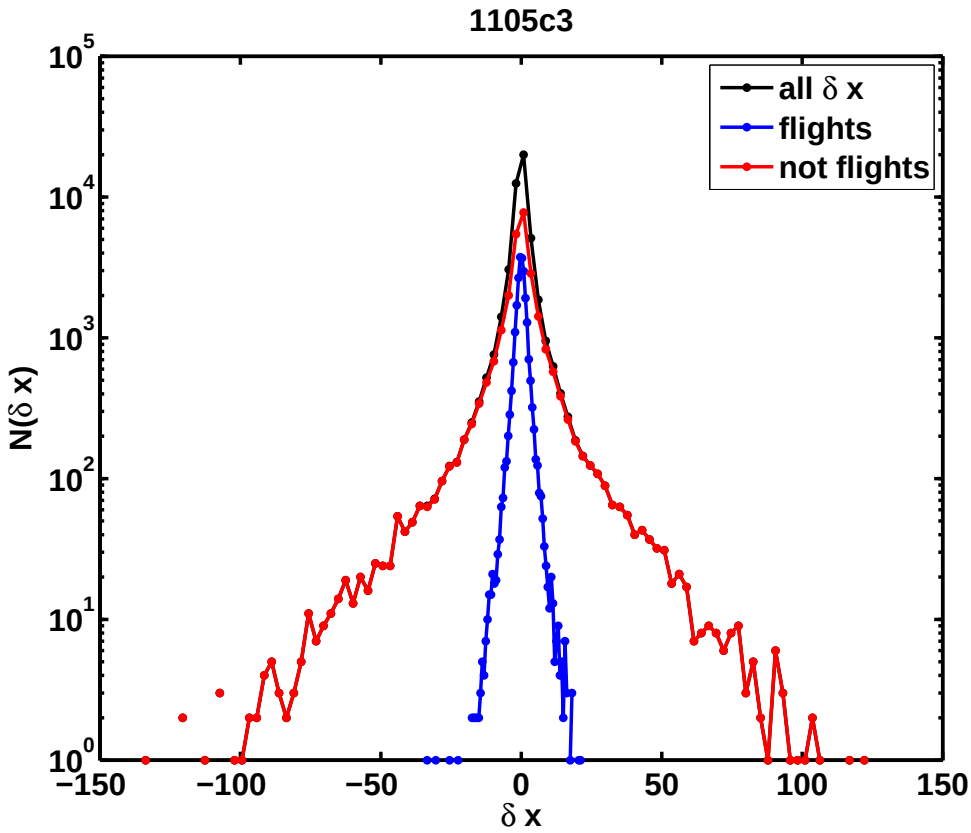

Figure 4.31: Radial displacement distribution for the intermediate gradient, $L_n/R_c = 0.625$, showing all trajectories in black, flights in blue and non-flights in red.

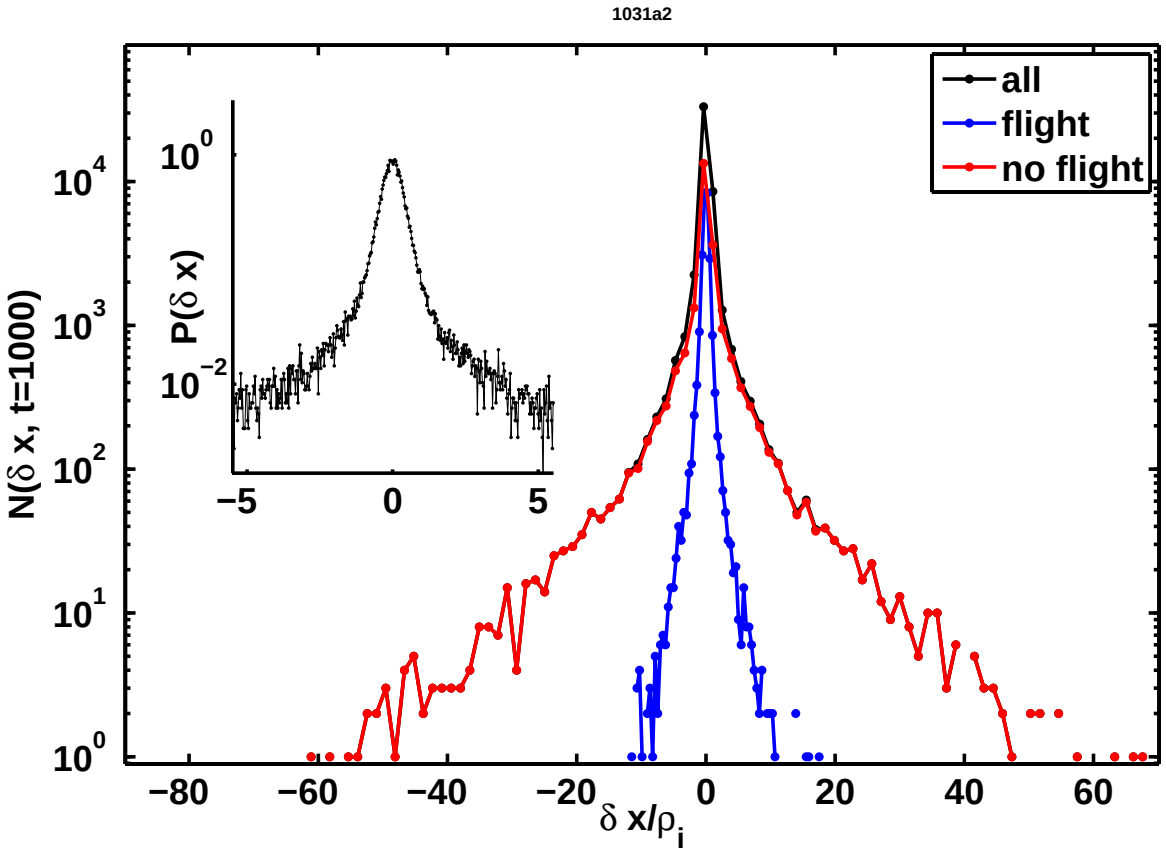

Figure 4.32: Radial displacement distribution for the weakest gradient, $L_n/R_c = 0.75$, showing all trajectories in black, flights in blue and non-flights in red.

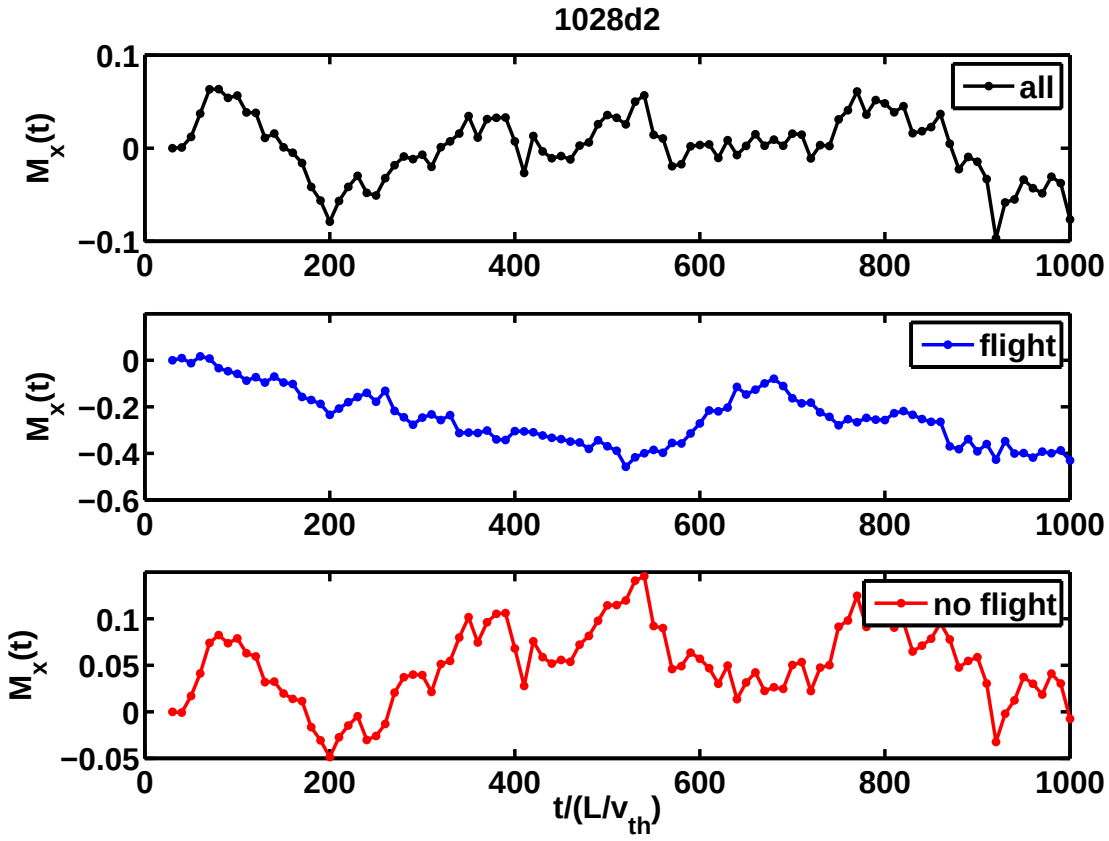

Figure 4.33: Mean of radial displacement for $L_n/R_c = 0.5$ showing the lack of advection in this flow. Flights are shown in blue, the full ensemble is shown in black and non-flights are shown in red.

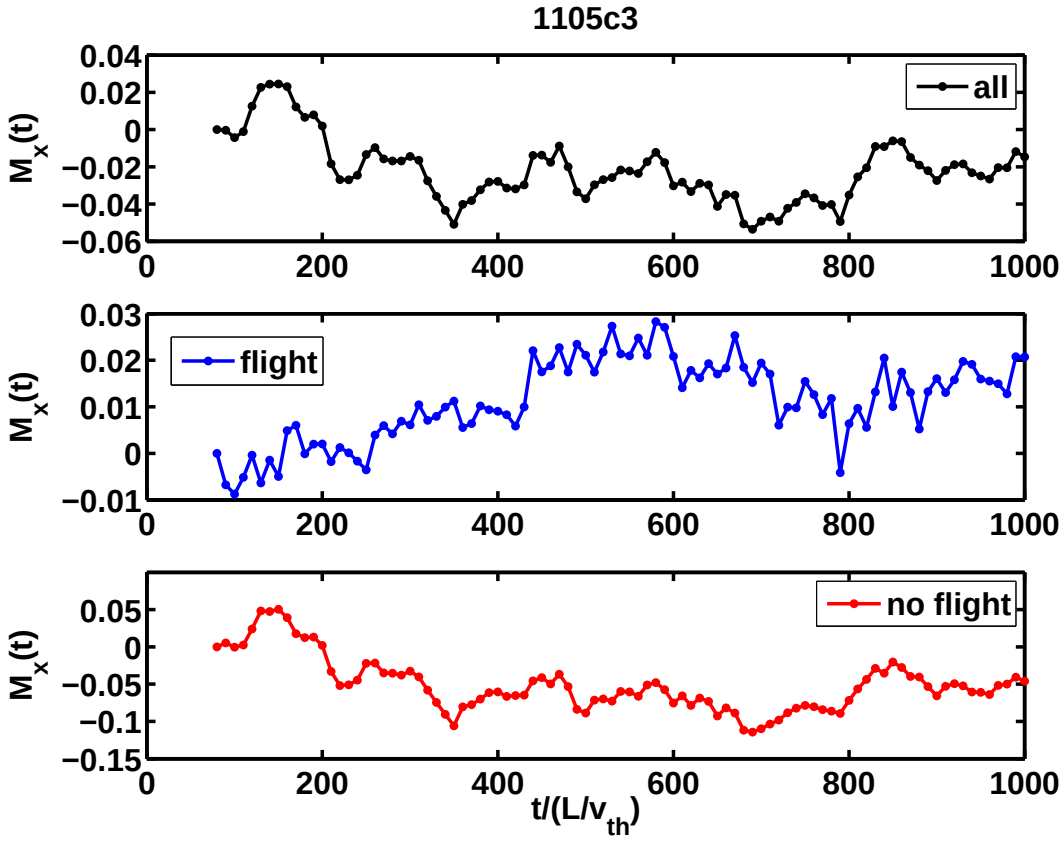

Figure 4.34: Mean of radial displacement for $L_n/R_c = 0.625$ showing the lack of advection in this flow. Flights are shown in blue, the full ensemble is shown in black and non-flights are shown in red.

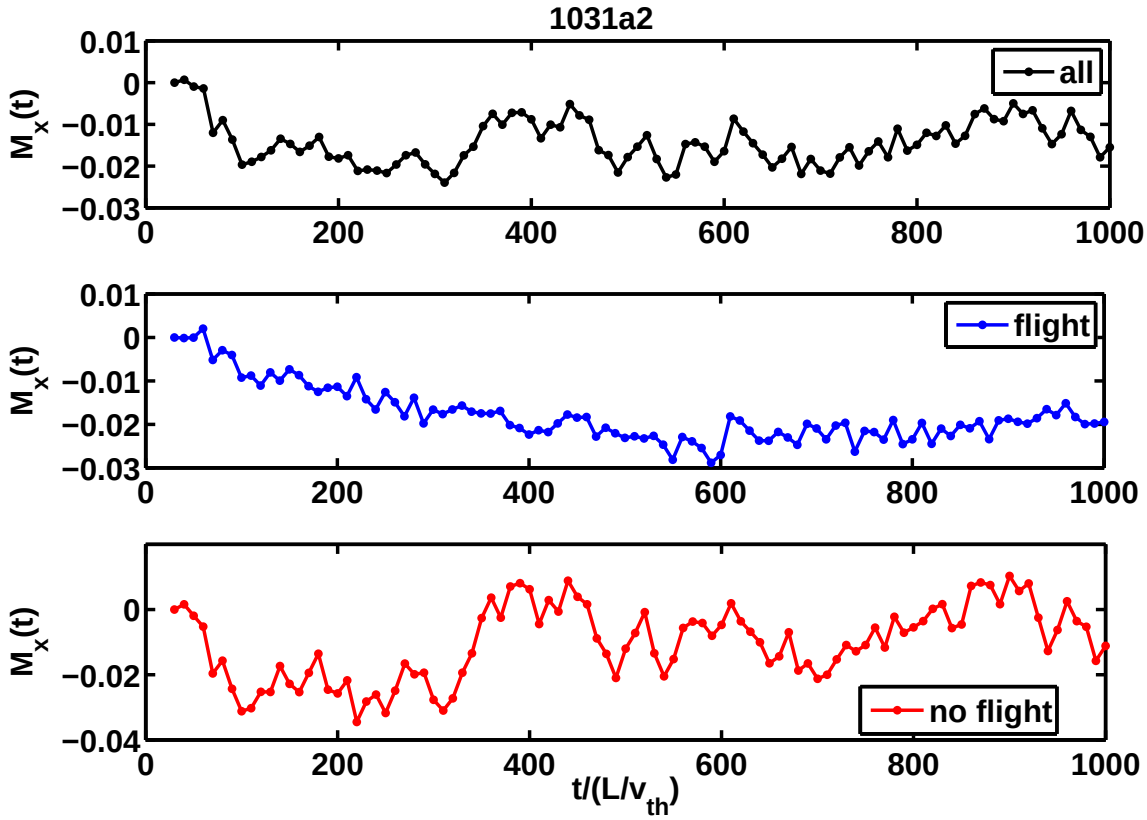

Figure 4.35: Mean of radial displacement for $L_n/R_c = 0.75$ showing the lack of advection in this flow. Flights are shown in blue, the full ensemble is shown in black and non-flights are shown in red.

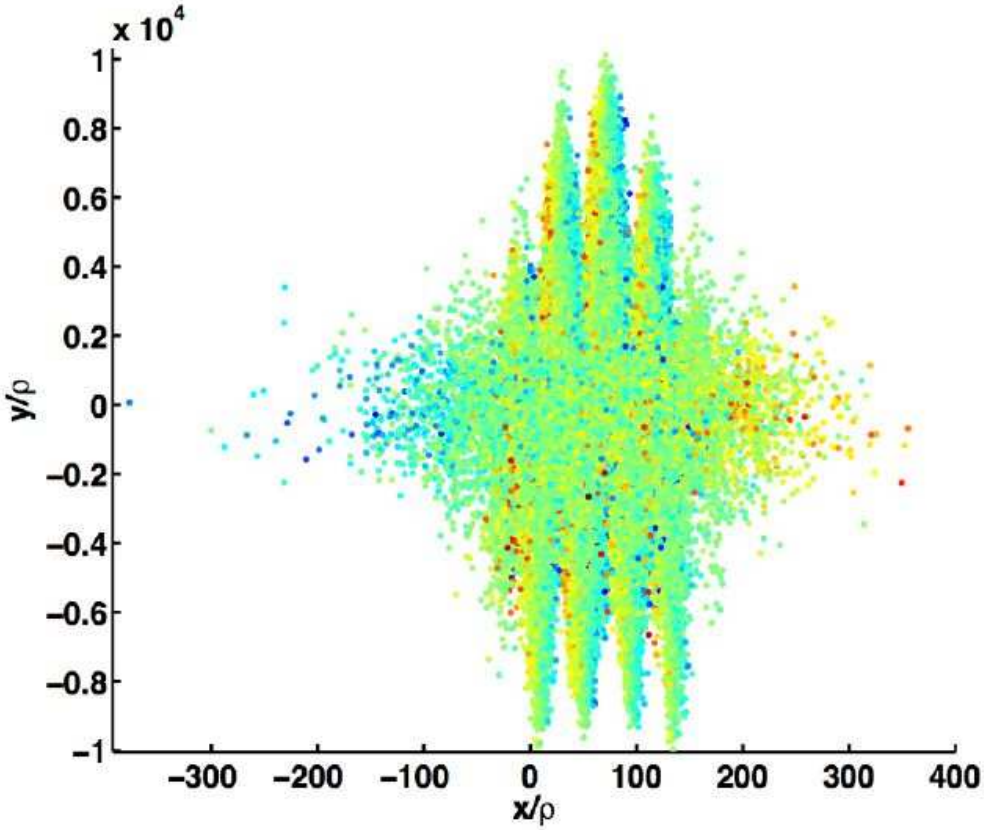

Figure 4.36: Positions of gyrocenters at the end of the simulation for the strongest gradient, $L_n/R_c = 0.5$. Colored according to $w_i = \delta f_1/F_0$, where $-215.08 < w_i < 212.78$.

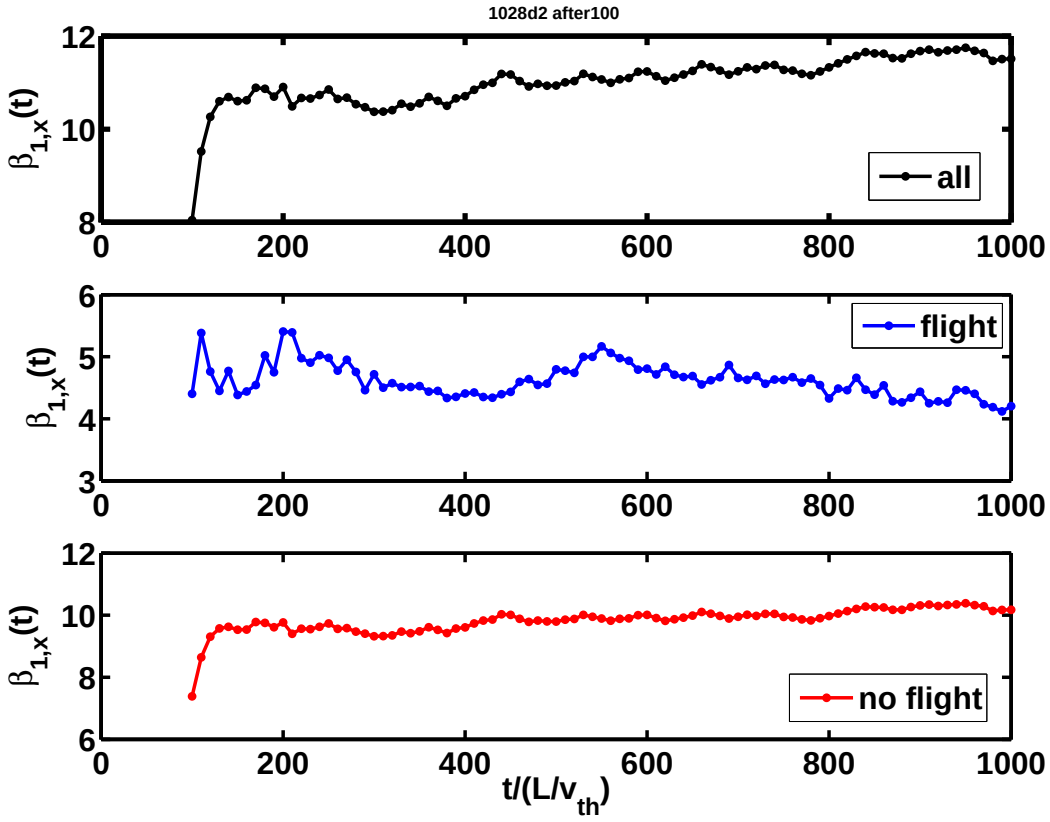

Figure 4.37: Kurtosis of radial displacement for $L_n/R_c = 0.5$ showing non-Gaussian values for non-flights and the overall distribution of trajectories. Flights are shown in blue, the full ensemble is shown in black and non-flights are shown in red.

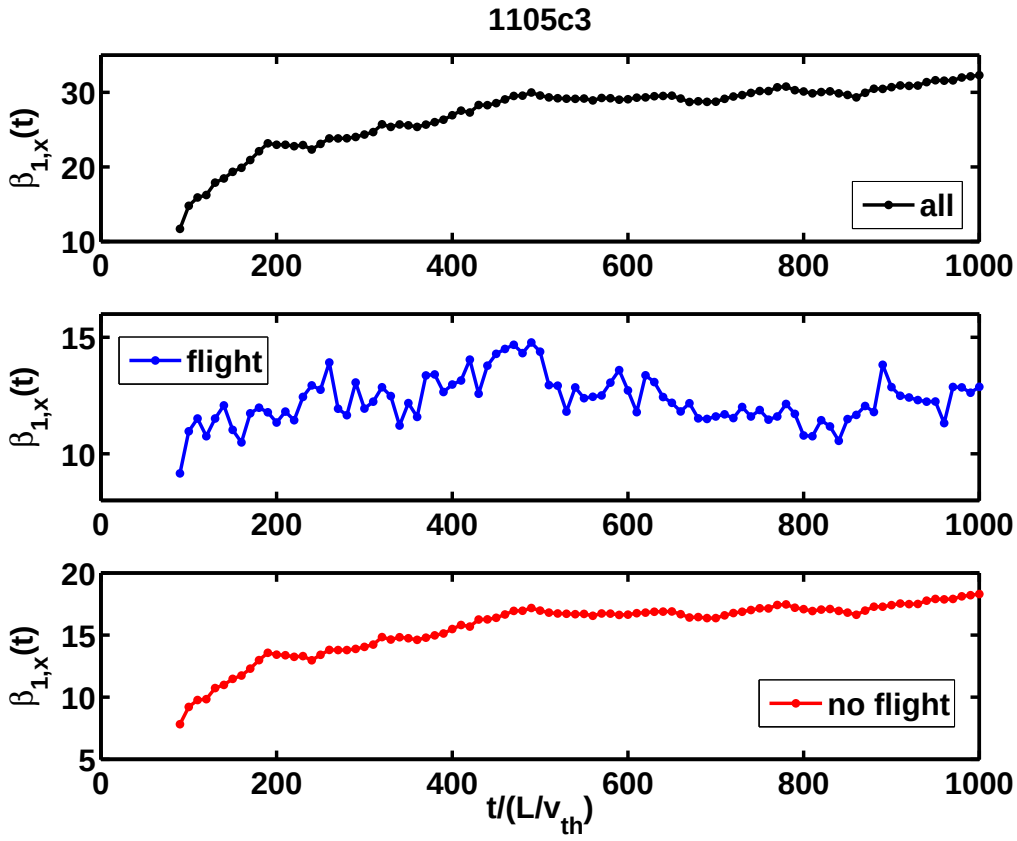

Figure 4.38: Kurtosis of radial displacement for $L_n/R_c = 0.625$ showing non-Gaussian values. Flights are shown in blue, the full ensemble is shown in black and non-flights are shown in red.

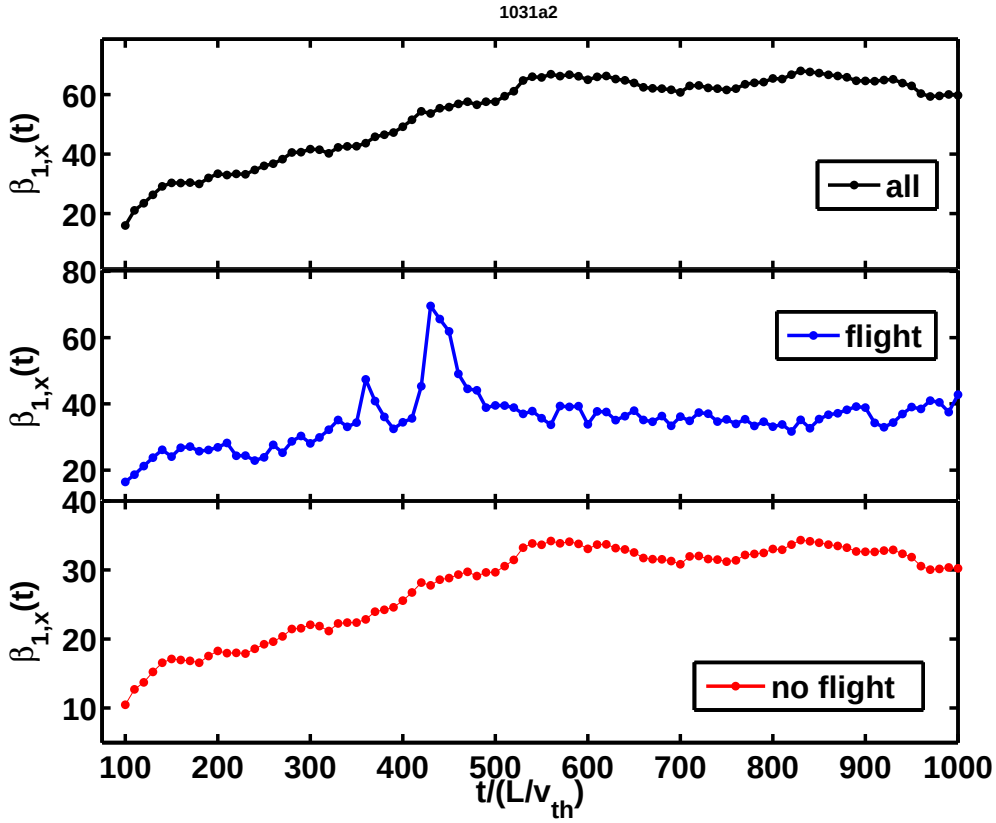

Figure 4.39: Kurtosis of radial displacement for $L_n/R_c = 0.75$ showing non-Gaussian values. Flights are shown in blue, the full ensemble is shown in black and non-flights are shown in red.

Running diffusion coefficients for all three gradients appear in Figures 4.40, 4.41 and 4.42. All three gradients show asymptotically diffusive variance after a period of superdiffusive spreading. The variance for the largest gradient is shown in Figure 4.43 with a log-log plot and the running diffusion coefficient inset. It is useful to compare both of these measurements to confirm the type of dispersion. The variance for the weakest gradient is shown in Figure 4.44 with a log-log plot and the running diffusion coefficient inset. It is very important to exclude from the variance diagnostic the fast radial spreading during the linear phase of the instability. When this transient is included, the dispersion can appear to be subdiffusive, even if only a small portion of the transient is kept (see Figures 4.40 and 4.42). If the simulation were run long enough to make the transient time negligible compared to the entire runtime, the dispersion should be asymptotically diffusive even if the transient were included. It is simply easier and less expensive to exclude the transient in order to find the asymptotic behavior. For the measurements of the variance (and therefore the test-particle diffusion coefficient) in this thesis, the starting point for the displacement is taken at $t = 100L/v_{th}$. As shown in Figure 4.6, this time is after the peak in flux caused by the linear growth phase.

We can compare the diffusivity D_{part} obtained from test-particle tracking with the ion gyrocenter diffusivity D_{flux} obtained from the flux-gradient relationship. One finds

$$D_{part} = \frac{\sigma_x^2(t)}{2t} \tag{4.8}$$

and

$$D_{flux} = \Gamma_p^{\infty} L_n \tag{4.9}$$

for the normalization used in the code, where D is in units of $\rho_i^2/(L/v_{th})$. The diffusivities found using these formulae are shown Table 4.2. The proper trend for the diffusivity is found, but the magnitudes are wrong by order unity, with $D_{flux} > D_{part}$ for each gradient studied. A recent study of tracer particles by Basu *et al* [25] in the Hasegawa-Wakatani equation found that the test-particle and flux-gradient diffusivities closely agree, as expected from conservation of potential vorticity in that equation. Some thoughts on calculating the diffusivity in the gyrokinetic equation were given by Krommes [143], and these are summarized in Appendix C. The disagreement in scaling for the two methods in our study is currently unresolved.

Table 4.2: Comparison of two methods for finding the gyrocenter diffusivity. The test-particle variance data gives D_{part} and the steady state flux gives D_{flux}.

L_n/R_c	D_{part}	D_{flux}
0.5	0.55	0.95
0.625	0.045	0.12
0.75	0.0075	0.03

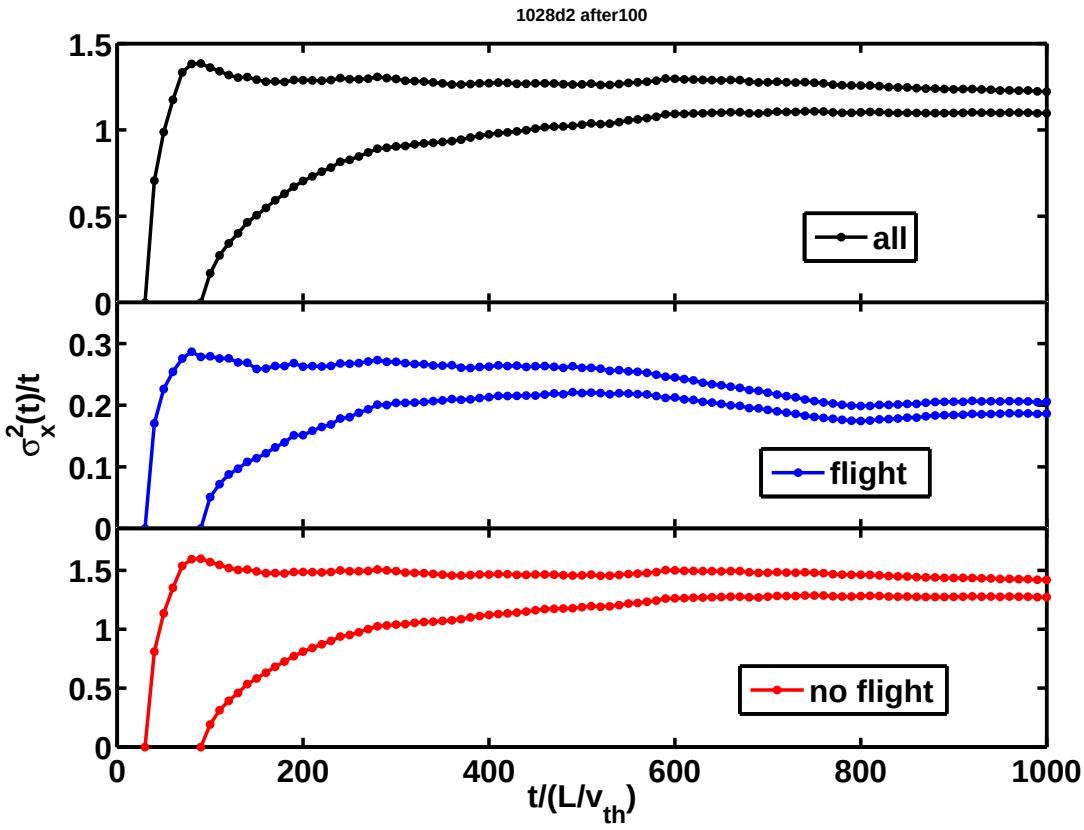

Figure 4.40: Variance of radial displacements for $L_n/R_c = 0.5$ scaled by t to emphasize the dispersion relative to diffusion. Flights are shown in blue, the full ensemble is shown in black and non-flights are shown in red, according to the velocity reversal filter. Each subplot has two data traces, showing the difference between taking the initial position of the trajectory before the end of the transient phase (upper traces, at $t = 30L/v_{th}$) or after the transient phase (lower traces, at $t = 100L/v_{th}$).

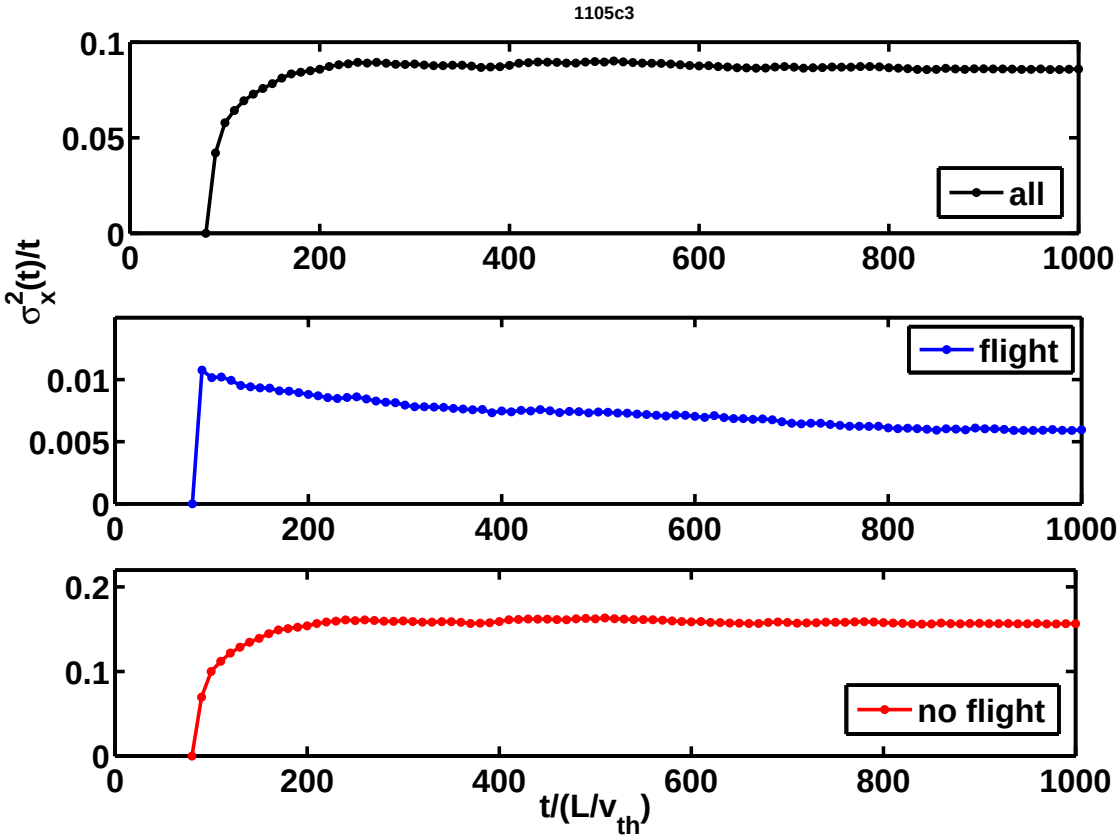

Figure 4.41: Variance of radial displacements for $L_n/R_c = 0.625$ scaled by t to emphasize dispersion relative to diffusion. Flights are shown in blue, the full ensemble is shown in black and non-flights are shown in red.

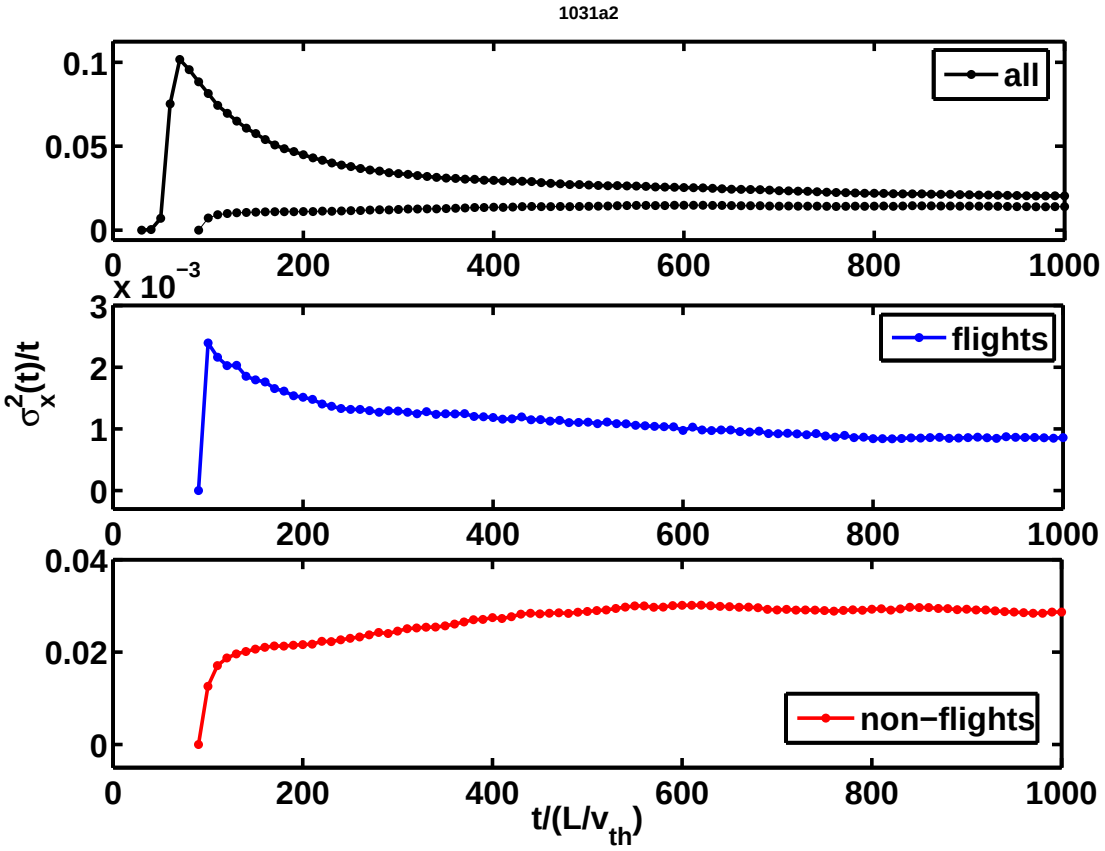

Figure 4.42: Variance of radial displacements for $L_n/R_c = 0.75$ scaled by t to emphasize dispersion relative to diffusion. Flights are shown in blue, the full ensemble is shown in black and non-flights are shown in red. The first subplot has two data traces, showing the difference between taking the initial position of the trajectory before the end of the transient phase (upper trace, starting at $t = 30L/v_{th}$) or after the transient phase (lower trace, starting at $t = 100L/v_{th}$).

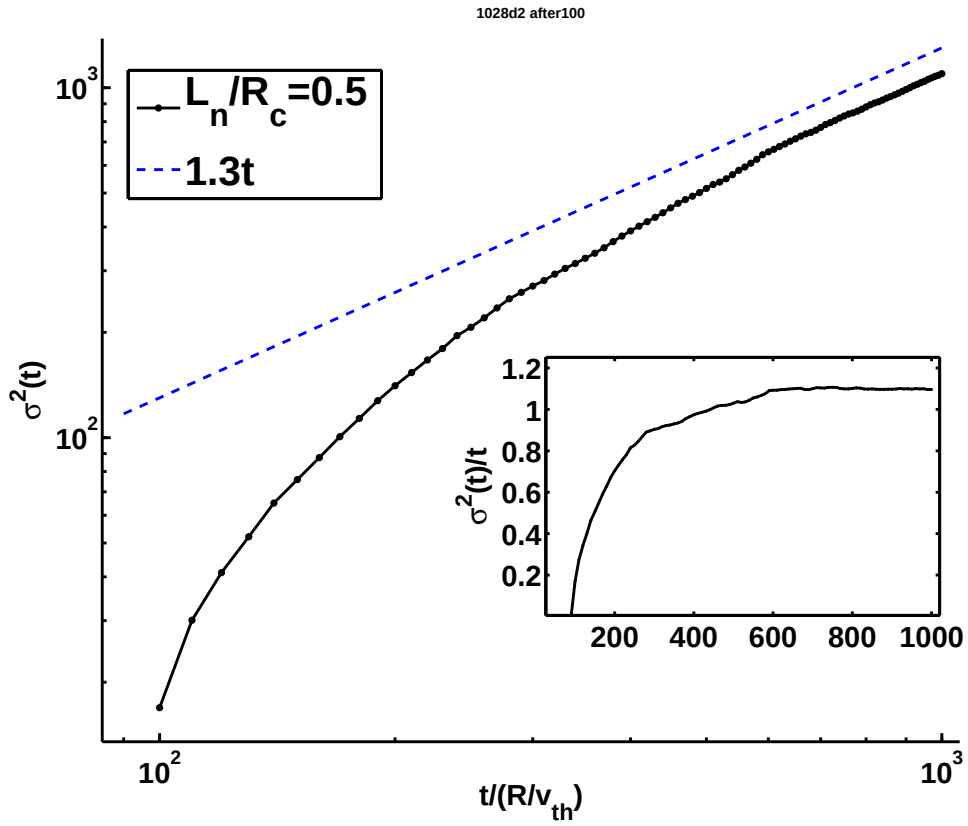

Figure 4.43: Variance and running diffusion coefficient (inset) for the strong $L_n/R_c = 0.5$ gradient, showing diffusive dispersion after a superdiffusive interval.

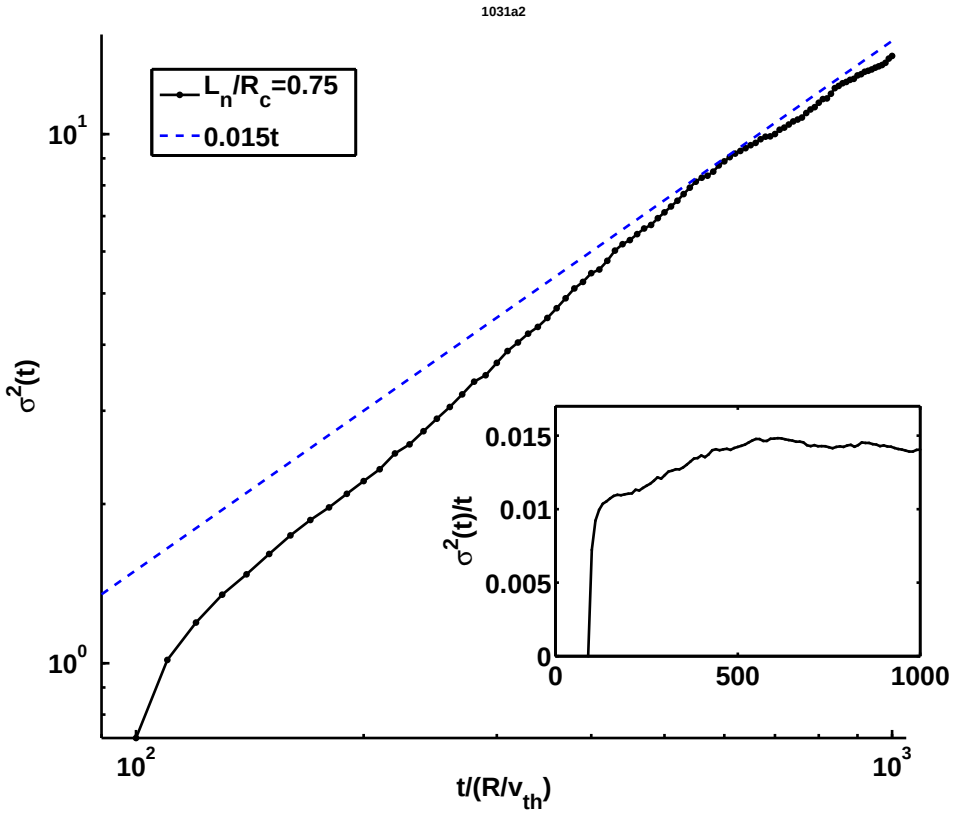

Figure 4.44: Variance and running diffusion coefficient (inset) for the weak $L_n/R_c = 0.75$ gradient, showing diffusive dispersion after a superdiffusive interval.

4.5.2 Statistics of radial velocity increments

The radial velocity increment distribution function is shown for $L_n/R_c = 0.5$ in Figure 4.45 and for $L_n/R_c = 0.75$ in Figure 4.46. These PDFs approach a steady state by $t = 300L/v_{th}$. For the stronger density gradient, the steady state seems to have fatter tails than a Gaussian. The weaker gradient has a Gaussian shape in steady state. Also, it is possible to map the radial velocity PDFs for different gradients onto each other with a simple rescaling of the axes, as shown in Figure 4.47. The radial velocity increment distribution, separated with the velocity reversal filter, is shown for all three gradients in Figure 4.48, 4.49 and 4.50. The shapes of the PDFs appear invariant to the application of the velocity reversal filter. Recall that the radial displacement PDFs have a strong dependence on the filter. This implies that the longer tails for radial displacements are not due to especially large velocities, but rather an accumulated displacement.

4.5.3 Radial velocity Lagrangian correlation function

The radial Lagrangian velocity correlation function gives a correlation time much smaller than the axial correlation time, as shown in Figure 4.51. The correlation time falls within the linear transient phase, $\tau_{vx} < 50L/v_{th}$. The correlation time is not well-resolved because of the velocity sampling time.

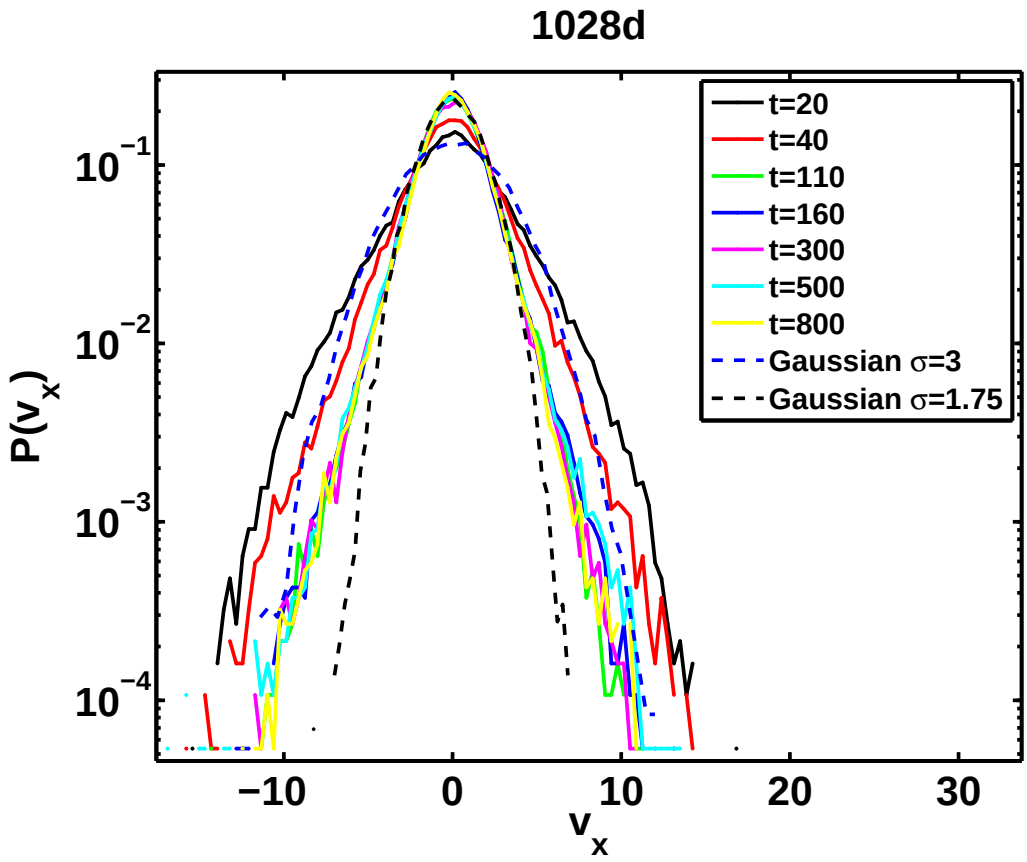

Figure 4.45: Distribution of radial velocity increments for $L_n/R_c = 0.5$ at several time points throughout the run, compared to Gaussian distributions with equivalent widths.

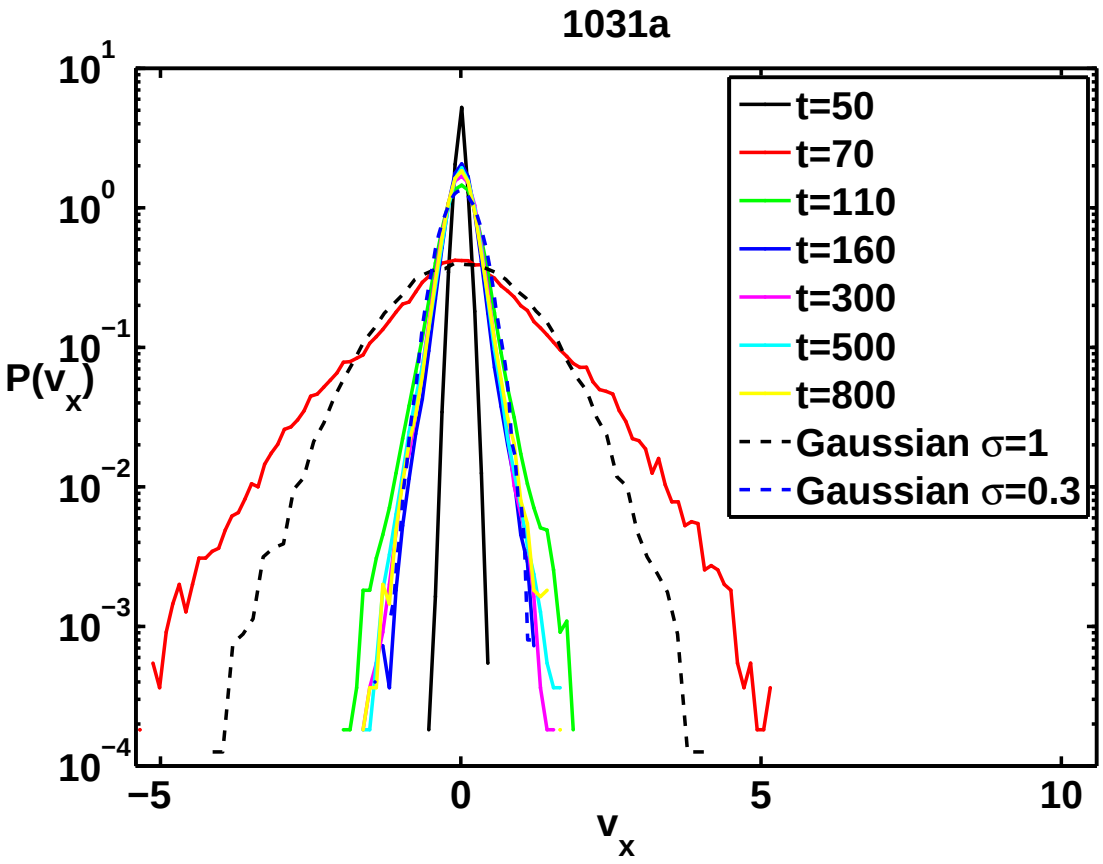

Figure 4.46: Distribution of radial velocity increments for $L_n/R_c = 0.75$, at several times throughout the run compared to Gaussian distributions with equivalent widths.

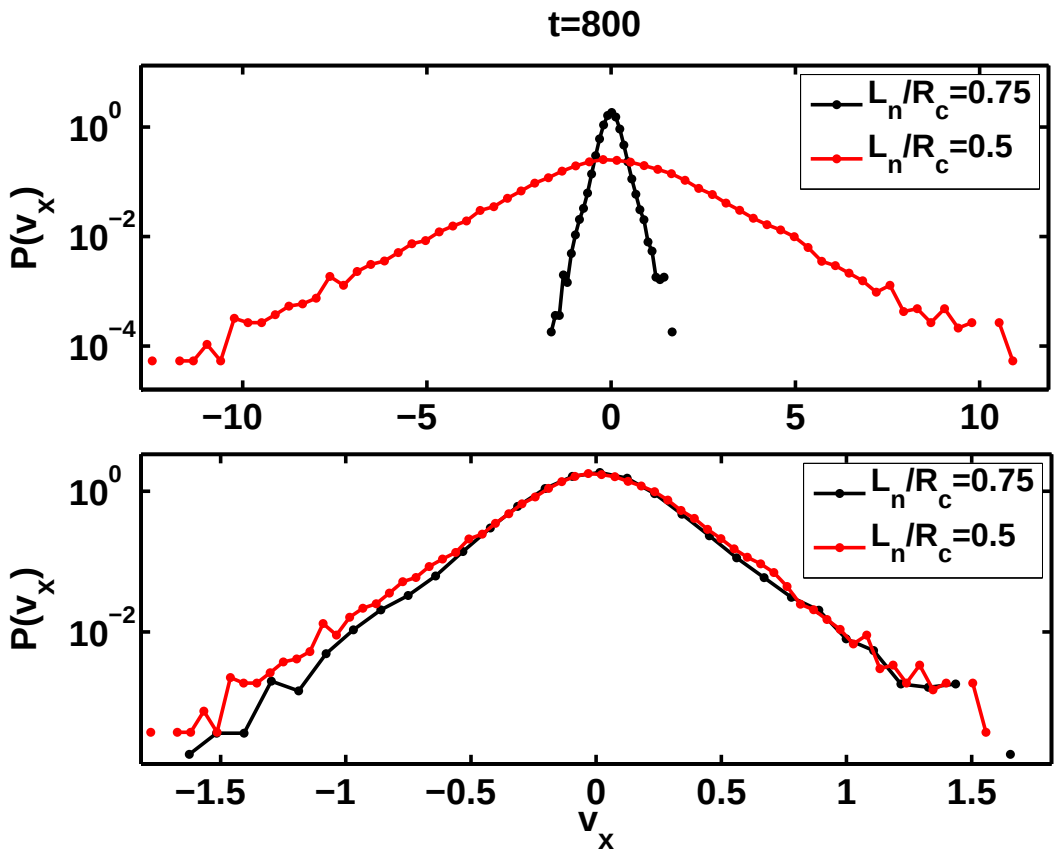

Figure 4.47: Radial velocity increment PDFs in the saturated state for $L_n/R_c = [0.5, 0.75]$ showing a mapping of the PDF for one gradient onto the other by a rescaling of both axes by a factor of 7.

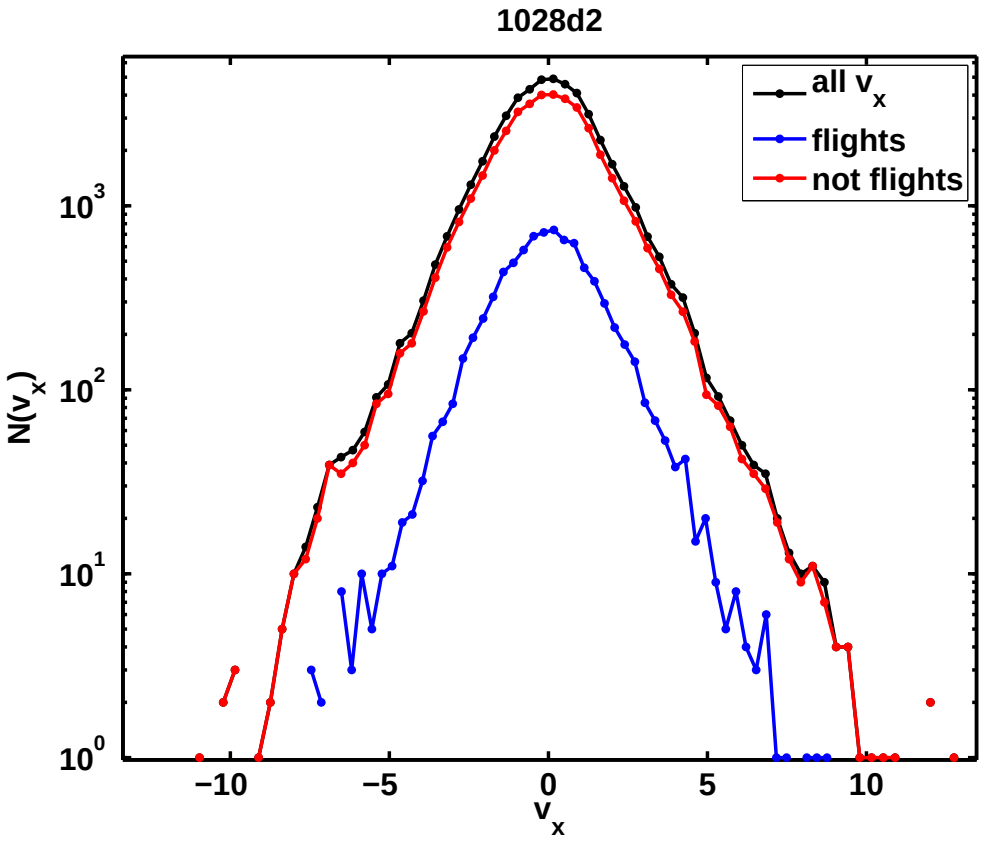

Figure 4.48: Radial velocity increment distributions at the end of the simulation for $L_n/R_c = 0.5$, separated according to the velocity reversal filter.

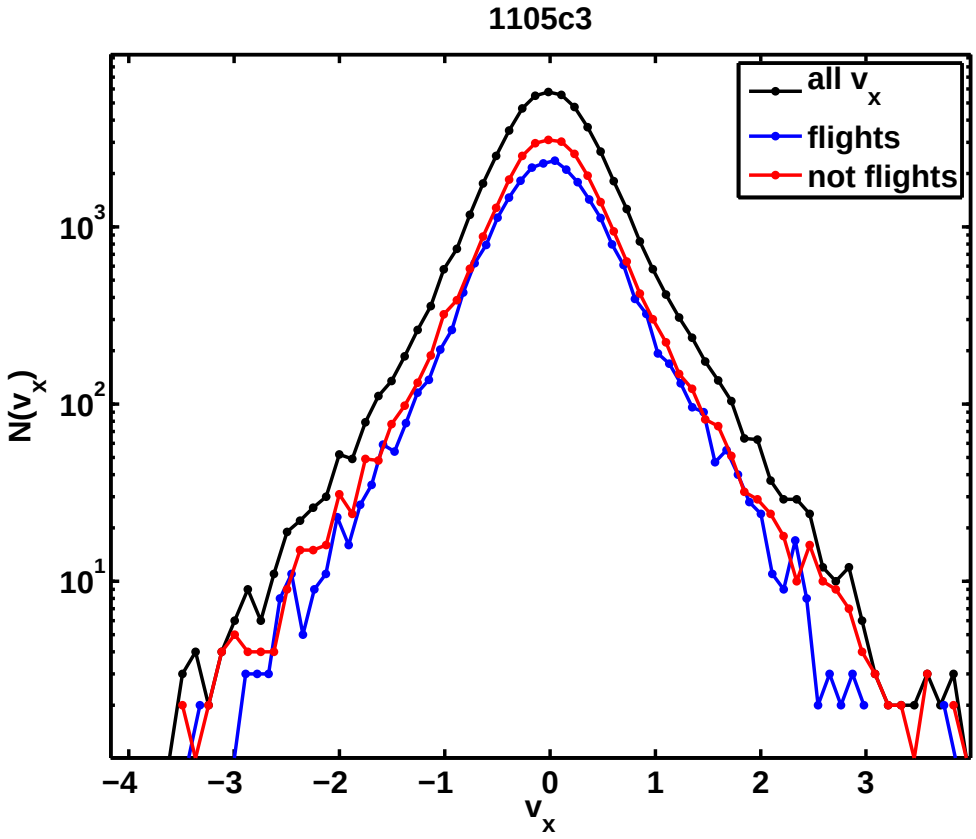

Figure 4.49: Radial velocity increment distributions at the end of the simulation for $L_n/R_c = 0.625$, separated according to the velocity reversal filter.

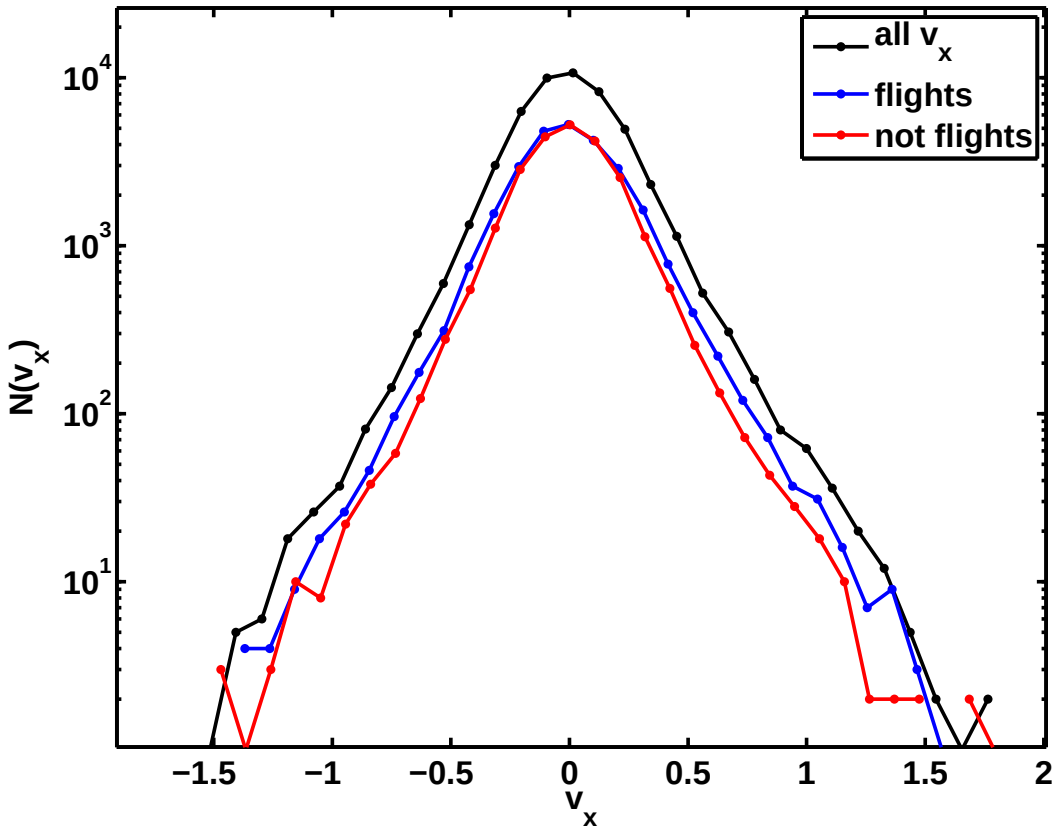

Figure 4.50: Radial velocity increment distributions at the end of the simulation for $L_n/R_c = 0.75$, separated according to the velocity reversal filter.

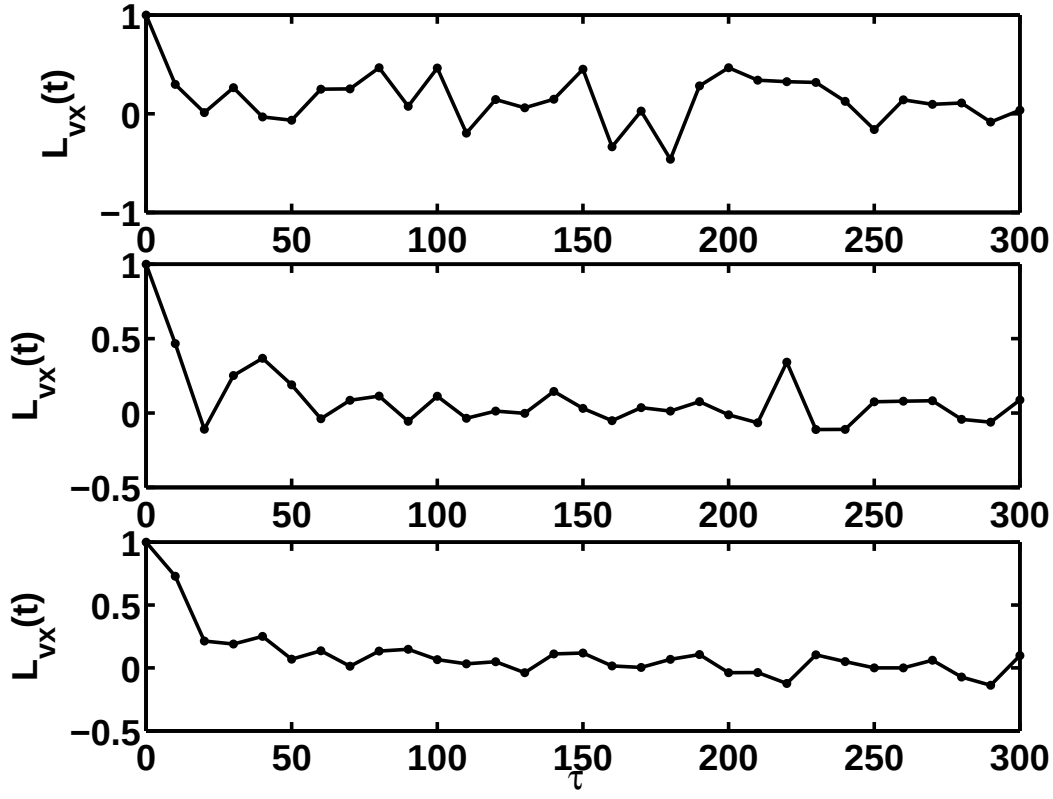

Figure 4.51: Radial Lagrangian velocity correlation for (top to bottom) $L_n/R_c = [0.5, 0.625, 0.75]$.

4.5.4 Velocity space dependence of dispersion: fast ions

In the following section, the mean value of the running radial diffusion coefficient $\langle D_x \rangle$ (where the $\langle \cdot \rangle$ average is taken over the last half of the time series) is computed while varying three separate parameters. These parameters are $v_\perp$, energy: $E = v_\perp^2 + v_\parallel^2$, and $W = v_\perp/2 + v_\parallel^2$. In these simulations, the values of $v_\perp$ range from $0.125 v_{th,ref} < v_\perp < 4.0 v_{th,ref}$ at equally spaced intervals. The values of $v_\parallel$ are chosen randomly within a range such that $v_\perp^2 + v_\parallel^2 < E_{v_\perp} = \text{constant}$.

First, we can quantify the relationship between flight and non-flight trajectories and the mean value of $v_\perp$, $\bar{v}_\perp$, for flight and non-flight trajectories. This value will be biased downwards because there are fewer particles at higher values of $v_\perp$. For $L_n/R_c = 0.5$, $\bar{v}_{\perp,flight} = 2.3$, while $\bar{v}_{\perp,non-flight} = 1.8$. We also note that the maximum and minimum values of $v_\perp$ for flights and non-flights are the same. Therefore, there is no sharp cutoff for the Larmor radius of a flight, just a better chance of being stuck in an eddy (non-flight) when the Larmor radius is small. For $L_n/R_c = 0.75$, $\bar{v}_{\perp,flight} = 1.97$ and $\bar{v}_{\perp,non-flight} = 1.73$, indicating a weaker dependence on ρ_i for the weaker gradient. For the intermediate case, $L_n/R_c = 0.625$, $\bar{v}_{\perp,flight} = 2.16$ and $\bar{v}_{\perp,non-flight} = 1.62$.

Now we examine the dependence of the running diffusion coefficient on ρ_i, combining the flight and non-flight trajectories. A clear trend in $\langle D_x(\rho_i) \rangle$ is found for all values of L_n/R_c tested. Note that $k_{\perp,N} v_{\perp,N} = k_{\perp,N} \rho_{i,N}$ for normalized units. Figure 4.52 shows this dependence for the strongest gradient, while Figure 4.53 and Figure 4.54 show the behavior for the other gradients. There are two important

features on this plot. First, in the log-log scale, there is a clear change in the trend at $k_\perp \rho \sim 1$, from a weak, or nearly constant, downward slope to a much steeper power law, at least for some subset of gyroradii. The power law has a well-defined value in the center of this parameter range. For $L_n/R_c = [0.5, 0.625, 0.75]$, the exponent is $[-1.75, -2.18, -2.47]$.

There is no trend for the mean value of the running diffusion coefficient for either E or W. This indicates that the trend detected in $\langle D(v_\perp) \rangle$ is due only to $v_\perp$, since both of the quadratic variables mix the $v_\perp$ ladder with random values of $v_\parallel$. Since there are no trapped or passing particles in the Z-pinch geometry used here, the only orbit averaging is the gyroaveraging, which reveals itself in the diffusivity dependence. We note the similarity of this result to the functional dependence of $A(k_\perp \rho)$ in Equation A.6, for the running diffusion coefficient of a Maxwellian distribution of gyrocenters in a monochromatic wave. Several authors propose scaling laws for the diffusion coefficient with energy [144, 145, 142, 146, 147]. These scaling laws all predict that the transport coefficient should decrease with gyroradius, but there is disagreement over the functional form. Further analysis is needed to compare our results with the literature.

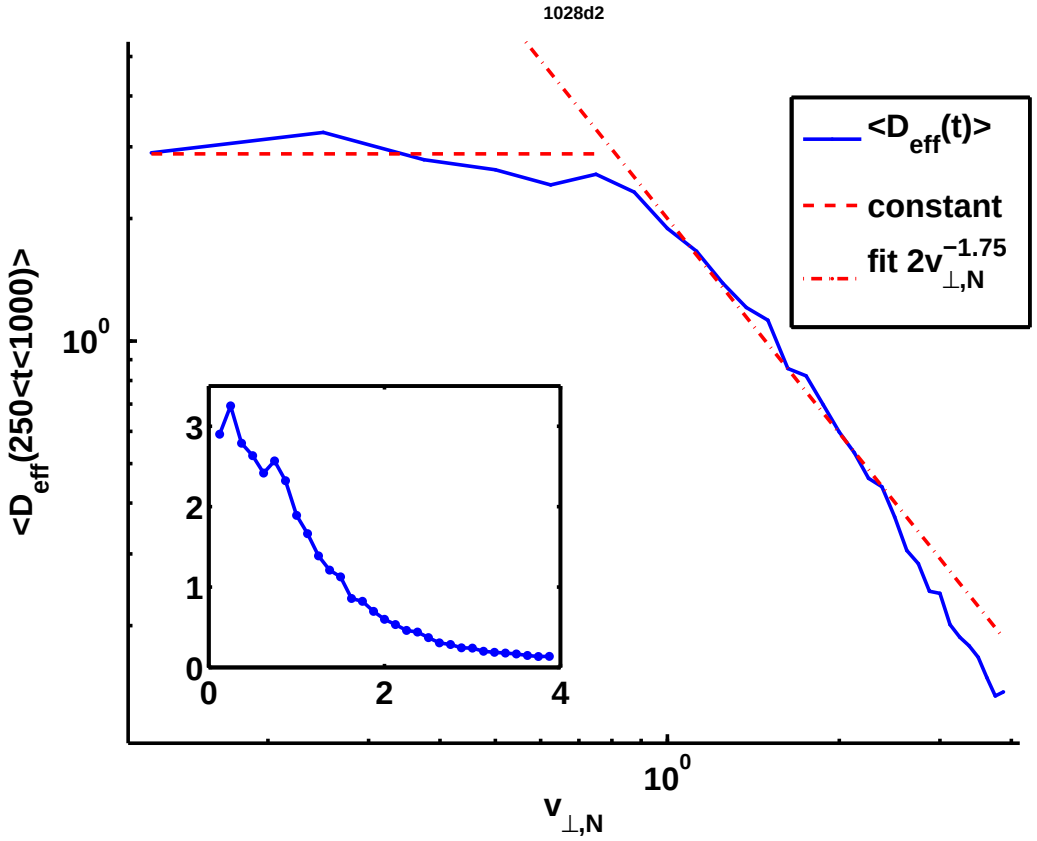

Figure 4.52: Dependence of the mean value of the running diffusion coefficient, averaged for $250 < t < 1000L/v_{th}$, on $v_\perp$ for $L_n/R_c = 0.5$. The inset shows the data on a linear plot, while the main plot uses a log-log scale, which highlights the knee in the trend at $v_{\perp,N} \sim 0.7$. The approximate power law in the central portion of the trend has an exponent of ~ 1.75 (power law fit using method provided by [2]).

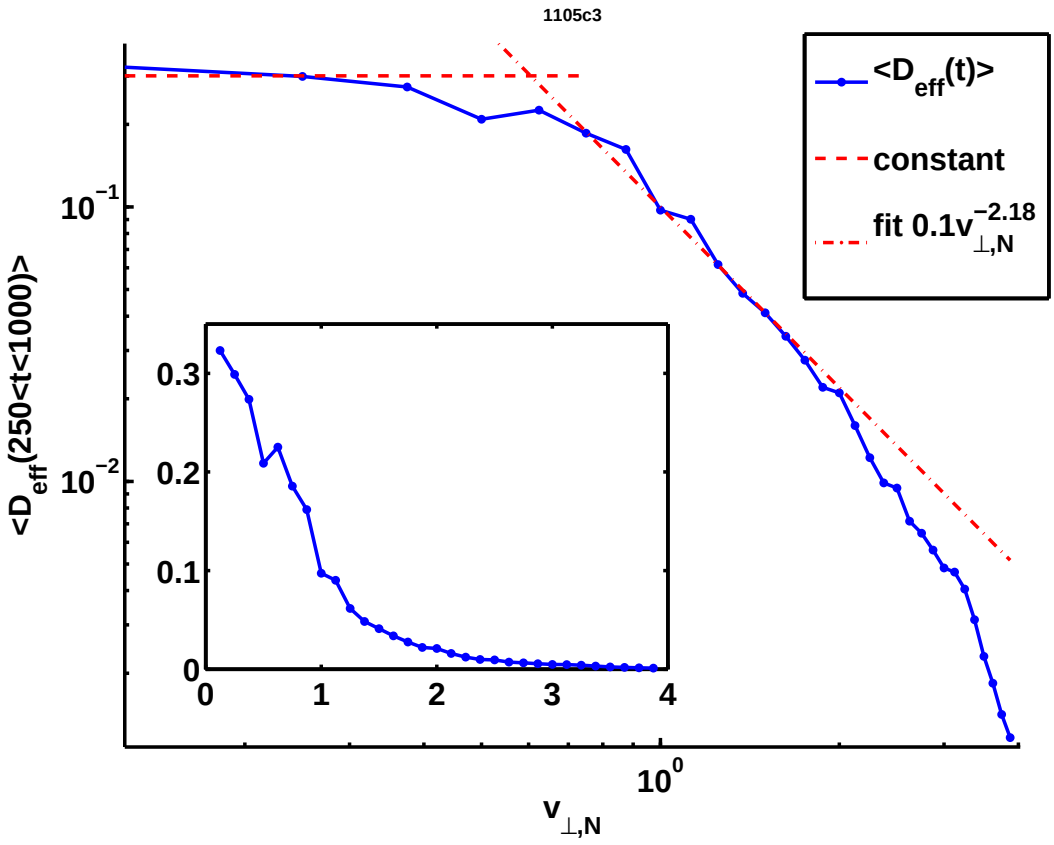

Figure 4.53: Dependence of the mean value of the running diffusion coefficient, averaged for $250 < t < 1000L/v_{th}$, on $v_\perp$ for $L_n/R_c = 0.625$. The inset shows the data on a linear plot, while the main plot uses a log-log scale, which highlights the knee in the trend at $k_\perp \rho \sim 0.7$. The approximate power law in the central portion of the trend has an exponent of ~ 2.18 (power law fit using method provided by [2]). The power law is only valid for about half of the data, after the knee.

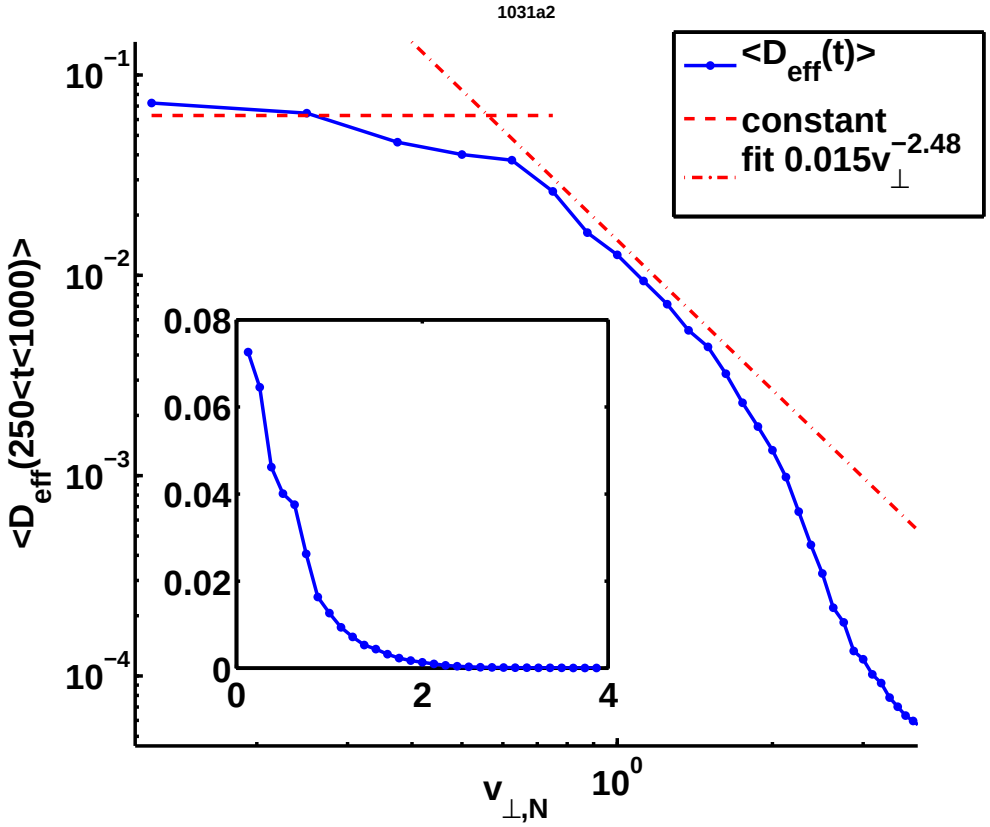

Figure 4.54: Dependence of the mean value of the running diffusion coefficient, averaged for $250 < t < 1000L/v_{th}$, on $v_\perp$ for $L_n/R_c = 0.75$. The inset shows the data on a linear plot, while the main plot uses a log-log scale, which shows that there is not a region of near-constant $\langle D(t) \rangle$. The power law in the central portion of the trend has an exponent of ~ 2.47 (power law fit using method provided by [2]). This trend is only valid for a small range, indicating the data is not described well by a power law.

Chapter 5

Conclusion and discussion

In this numerical study of ion gyrocenter dispersion in zonal flows, we have examined the statistics of dispersion in a stochastic Hamiltonian model and a density-gradient-driven turbulence model. The ion species used for this study can be considered a tracer, or low-density probe of the flow. We varied the gyroradii of the ions in both models, finding that the behavior of the dispersion changes predictably with gyroradius. In the stochastic Hamiltonian model, we found that fractional diffusion can describe the superdiffusive dispersion of a subclass of tracers parallel to a zonal flow. In the simulations of gyrokinetic turbulence, we found that the axial dispersion is superdiffusive for a similar subclass of tracers. The radial dispersion for the tracers is found to be diffusive for a wide range of turbulence amplitudes.

A subset of the gyrocenters in the stochastic Hamiltonian model, those that experience a trapping event (called sticky-flights), undergo superdiffusive dispersion ($\sigma_y^2(t) = t^\gamma$, $\gamma > 1$), parallel to the shear flow. When $\rho_{th} = 0$ there is a change in the exponent of this dispersion ($\gamma = 1.6 \rightarrow \gamma = 1.9$) between early and late time windows during the simulation. Larger ρ_{th} decreases the probability of sticking events and erases the temporal distinction between these two exponents, with their mean value being the value only value of γ observed at larger ρ_{th}. Applying the formalism of the fractional diffusion equation as a description of the dispersion, we

found it was possible to find a solution of the fractional diffusion equation matching the distribution of displacements. The parameters for this matching solution were taken from the power law tails of the distribution, cross-checked against the value of γ and the power-law tails of the trapping and flight distributions.

In self-consistent gyrokinetic turbulence modeled by a δf particle-in-cell simulation of a Z pinch entropy mode, we also find superdiffusive axial (parallel to velocity shear) dispersion for a subset of particles. This subset is selected using a velocity reversal filter, which separates trajectories that do not get trapped in eddies. The particles that do experience a trapping event follow superdiffusive dispersion before settling into ballistic dispersion. Steeper local gradients lead to faster radial dispersion of gyrocenter tracers, as the turbulence level and radial flux also increase with steeper gradient. At three values of the gradient scale length, $L_n/R_c = \{0.5, 0.625, 0.75\}$ the radial dispersion is diffusive as measured by the variance of displacements. The test-particle diffusion coefficient, D_{part}, decreases with the strength of the gradient, taking values consistently smaller than the diffusivity, D_{flux}, computed using Fick's Law and the steady-state turbulent particle flux. These two measures of the diffusivity follow the same downward trend with weakening gradient.

The kurtosis of the radial dispersion is larger than Gaussian for each case studied. This indicates a small population of tracers which experience large excursions. These non-Gaussian tails are apparently not large enough to cause non-diffusive dispersion. Note that the determination of the qualitative behavior of the dispersion is very sensitive to the exclusion of the transient radial dispersion due to the

linear instability. If the transient burst of radial motion is included in the trajectory displacement, the average dispersion appears subdiffusive. This confusion would disappear if the observation time were much larger than the duration of the transient. It is less expensive to simply exclude the transient.

There is a definite dependence of the test-particle diffusivity $D_{part}(t)$ upon gyroradius for a spectrum of gyroradii larger and smaller than the thermal gyroradius of the system. The functional form appears to have a critical value when the gyroradius approaches the thermal value, at least for stronger density gradients. The dependence of $\langle D(t) \rangle$ is not a power law across the whole range of ρ_i, but it is possible to fit a power law to the region where $\rho_i \gtrsim \rho_{th,i}$. The slope of this power law is steeper for weaker value of the density gradient, when the zonal flows are more stable. Further investigation is required to compare these observations with results from fast ion diffusivity studies.

A similar study by Sánchez *et al* [14], found subdiffusive transport of marker particles in three dimensional ion temperature- gradient turbulence. This result was reported using a global PIC simulation, rather than the local gradient approximation used in this thesis. They used artificial suppression and generation of zonal flows to compare with the self-consistent zonal flows generated by the temperature gradient. Subdiffusion was observed for external and self-consistent zonal flows, with non-Gaussian displacement distributions observed for the self-consistent zonal flows. The explanation offered by Sánchez *et al* for the subdiffusive dispersion is not dependent on a toroidal geometry. The qualitative disagreement with our results could be due to differences in the turbulence induced by a temperature versus a density gradient

or differences between global and local simulations.

Other studies found diffusive transport of marker particles for a particular value of the ion temperature gradient. Zhang *et al* used a "full-torus" PIC simulation [142] to examine test-particle dispersion in the radial direction. They found it to be diffusive for a wide range of particle energies. Another study by Hauff *et al* used a local gradient model of ion temperature-gradient driven zonal flows in a continuum simulation with external tracer particles [50]. These simulations used two-dimensional cross-sections of a toroidal geometry for the Cyclone parameters [65]. Their findings show diffusive transport in both the poloidal and radial directions, after intermediate superdiffusive and subdiffusive behavior, respectively. Further investigation of our results and comparison with the details of the other simulations is needed to resolve the differences in the results of these studies.

Appendix A

Propagator equation for gyroaveraged parallel zonal flow

The gyroaverage equations of motion for test particles in the parallel zonal flow of Eq. 3.11 are

$$\frac{dx}{dt} = 0\,, \qquad \frac{dy}{dt} = -\phi_0 k_\perp \left\langle \sin(k_\perp x) \right\rangle_\theta = -\phi_0 k_\perp J_0(k_\perp \rho) \sin(k_\perp x)\,. \tag{A.1}$$

A straightforward integration assuming an intial condition (x_0, y_0) gives

$$x = x_0\,, \qquad y = y_0 - U_0 J_0(k_\perp \rho)\, t\,, \tag{A.2}$$

where $U_0 = \phi_0 k_\perp \sin(k_\perp x_0)$. From here it follows that the two-dimensional propagator is

$$\mathcal{P}(\mathbf{r}, t|\mathbf{r}', t'; \rho) = \delta(x - x')\, \delta\left[y - y' + J_0(k_\perp \rho) U_0 t\right]\,. \tag{A.3}$$

Integrating over x and assuming a Maxwellian distribution of gyro-radii gives the one-dimensional propagator in y,

$$P(y, t|y', t'; \rho) = \frac{2}{\rho_{th}^2} \int_0^\infty \delta\left[y - y' + J_0(k_\perp \rho) U_0 t\right] \rho\, e^{-\rho^2/\rho_{th}^2}\, d\rho\,. \tag{A.4}$$

Integrating over ρ using basic properties of the delta function gives Eq. 3.12. From Eq. (A.4) it follows that the n-th moment of the gyrocenter displacement $\delta y = y - y'$ scales like t^n according to

$$\left\langle (\delta y)^n \right\rangle = (U_0 t)^n \int_0^\infty J_0^n(k_\perp \rho)\, H(\rho) d\rho\,. \tag{A.5}$$

where $H(\rho)$ is the gyro-radii distribution function. For $n = 1$ and $n = 2$ we recover the moments in Sec. 3.5(A) with

$$V_{eff} = U_0 e^{-k_\perp^2 \rho_{th}^2/4}\,, \qquad A = U_0^2 e^{-k_\perp^2 \rho_{th}^2/2} \left[I_0 \left(k_\perp^2 \rho_{th}^2/2 \right) - 1 \right] \tag{A.6}$$

in the case when H is Maxwellian, where I_0 is the modified Bessel function of zero-order. It is interesting to note that A has a maximum for $k_\perp \rho_{th} \approx 2.5$.

Appendix B

Magnetic drifts in the Z-pinch

B.1 ∇B drift

Assume that a magnetic field in the circumferential direction $\hat{\varphi}$ with some radial $\hat{r}$ dependence is present in the torus. This is the field that creates some confinement in the Z-pinch, and it can be expressed as $\mathbf{B} = B_0(r)\hat{\varphi}$. Now expand the field around the gyrocenter position coordinate to get $\mathbf{B} = \mathbf{B_0} + (\mathbf{r} \cdot \nabla)\mathbf{B_0}$. Also separate the drift velocity into a background $\mathbf{v}_\perp$ and a perturbed $\mathbf{v_D}$, so that $\mathbf{v} = \mathbf{v}_\perp + \mathbf{v}_D$. One can write an equation of motion now for v_D, using this ordering, such that when $\nabla B_0 = \frac{B_0}{R_c}\hat{r}$:

$$\frac{d\mathbf{v_D}}{dt} = \frac{q}{mc}(\mathbf{v_D} \times \mathbf{B}_0 + \mathbf{v}_\perp \times (\mathbf{r} \cdot \nabla)B_0) \tag{B.1}$$

This equation can then be gyroaveraged to eliminate the left hand side, and manipulated as follows,

$$< \mathbf{v}_D \times \mathbf{B}_0 >_R = - < \mathbf{v}_\perp \times (\mathbf{r} \cdot \nabla)\mathbf{B}_0 >_R$$

$$< \mathbf{v}_D \times \mathbf{B}_0 >_R \times \mathbf{B}_0 = - < \mathbf{v}_\perp \times (\mathbf{r} \cdot \nabla)\mathbf{B}_0 \times \mathbf{B}_0 >_R$$

$$(\mathbf{B}_0 \cdot \mathbf{v}_D)\mathbf{B_0} - (\mathbf{B}_0 \cdot \mathbf{B}_0)\mathbf{v}_D = - < \mathbf{v}_\perp \times (\mathbf{r} \cdot \nabla)\mathbf{B}_0 \times \mathbf{B}_0 >_R$$

$$-\mathbf{v}_D B_0^2 = - < \mathbf{v}_\perp \times (\mathbf{r} \cdot \nabla)\mathbf{B}_0 \times \mathbf{B}_0 >$$

$$\mathbf{v}_D = \frac{1}{B_0} v_\perp^2 < \sin^2(\Omega t) >_R (\mathbf{B}_0 \times \nabla B_0)$$

$$\mathbf{v}_D = \frac{1}{B_0} \frac{v_\perp^2}{2\Omega} (\mathbf{B}_0 \times \nabla B_0)$$

$$\mathbf{v}_D = \frac{v_\perp^2}{2\Omega R_c} (\hat{\varphi}) \times (-\hat{r})$$

$$\mathbf{v}_D = \frac{v_\perp^2}{2\Omega R_c} \hat{z}$$

B.2 Curvature drift

Finding the drift velocity associated with the curvature of the magnetic field requires writing the gyration averaged force-balance equation, where the acceleration is removed by averaging. Manipulations reveal an expression for the drift velocity,

as follows.

$$
\begin{aligned}
0 &= < \mathbf{F}_\perp + \frac{q}{c}\mathbf{v}_D \times \mathbf{B}_0 >_R \\
< \mathbf{F}_\perp >_R \times \mathbf{B}_0 &= -\frac{q}{c} < (\mathbf{v}_D \times \mathbf{B}_0) \times \mathbf{B}_0 >_R \\
< \mathbf{F}_\perp >_R \times \mathbf{B}_0 &= -\frac{q}{c} < -\mathbf{v}_D >_R B_0^2 \\
\frac{c}{qB_0^2} < \mathbf{F}_\perp >_R \times \mathbf{B}_0 &= \mathbf{v_D}
\end{aligned}
$$

Now if we take the centripetal force on particles moving on curved field lines, $\mathbf{F}_\perp = -\frac{mv_\parallel^2}{R_c}\hat{r}$, we can find $\mathbf{v}_D$ due to that force, now called the curvature drift.

$$
\begin{aligned}
\mathbf{v}_D^c &= (-\hat{r}) \times (\hat{\phi})\frac{cB_0 m v_\parallel^2}{qB_0^2 R_c} \\
\mathbf{v}_D^c &= \hat{z}\frac{v_\parallel^2}{\Omega R_c}
\end{aligned}
$$

Now the curvature and ∇B drifts can be combined into a total vertical drift:

$$
\mathbf{v}_B = \frac{v_\parallel^2 + \frac{1}{2}\mathbf{v}_\perp^2}{\Omega R_c} \tag{B.2}
$$

These drifts will enter into the $\frac{dw_i}{dt}$ weight evolution equation on the right-hand side as:

$$
\begin{aligned}
\frac{dw_i}{dt} &= \cdots - \frac{1}{F_0}(\mathbf{v}_B \cdot \nabla(\frac{q < \phi >_R}{T})F_0 - \mathbf{v}_B \frac{q < \phi >_R}{T}\nabla F_0) \\
\frac{dw_i}{dt} &= \cdots + \mathbf{v}_B \cdot \frac{q}{T} < \mathbf{E} >_R \\
\frac{dw_i}{dt} &= \cdots + \mathbf{v}_B \frac{q}{T} < E_z >_R
\end{aligned}
$$

where the F_0 background only has gradients in the radial direction.

Appendix C

Two ways to calculate diffusivity

One must consider that the diffusivity of a transport process, driven by a fixed density gradient $n'(x) = -\frac{1}{L_n}n(x)$ can be characterized either by (1) tracking the displacements, $\delta x(t) = x(t) - x(0)$, of an ensemble of particles drifting in the turbulent structures created by the gradient, or (2) by computing the average flux, $\Gamma_n(t) = \int n(t)v(t)dz$, of particles and assuming $\Gamma_n = -D_{flux}(x,t)n'(x)$. The particle-tracking technique (1) requires a computation of the variance of displacements, $\sigma^2(t) =< \delta x(t)^2 >_i = D_{part}t$. For the gyrokinetic equation in a slab geometry, these two diffusion coefficients, D_{part} and D_{flux} are defined and are equivalent if several assumptions are met. The following describes how these quantities may be found and compared, using an outline from [143].

Starting from the collisionless gyrokinetic equation for a slab, where $< \cdot >_R$ is a gyroaverage,

$$\frac{\partial}{\partial t} < \delta f >_R + v_\parallel \frac{\partial}{\partial z} < \delta f >_R + < v_{\mathbf{E}\times\mathbf{B}} >_R \cdot \nabla < \delta f >_R \; = \\ - < v_{\mathbf{E}\times\mathbf{B}} >_R \cdot \nabla F_0 - v_\parallel \frac{q}{T} F_0 \mathbf{b}_0 \cdot \nabla < \phi >_R \qquad \text{(C.1)}$$

multiply by $\delta f / F_0$, letting $\kappa = 1/L_n$ with this density gradient in the x direction

$$\frac{1}{2}\frac{\partial}{\partial t} < \delta f >_R^2 /F_0 + \frac{1}{2} v_\parallel \frac{\partial}{\partial z} < \delta f >_R^2 /F_0 \quad + \quad \nabla \cdot (< v_{\mathbf{E}\times\mathbf{B}} >_R < \delta f >_R^2 /F_0) \quad =$$

$$(< v^x_{\mathbf{E}\times\mathbf{B}} >_R \kappa \quad + \quad v_\parallel \frac{q}{T} < E_\parallel >_R) < \delta f >_R \qquad \text{(C.2)}$$

integrate over phase space ($\int(\cdot)dxdydz$) with periodic boundary conditions, letting $\mathcal{F} = V^{-1} \int \frac{1}{2}\delta f^2/F_0 dxdydz$, and neglecting the Landau damping term to arrive at

$$\frac{\partial}{\partial t}\mathcal{F} = \kappa \overline{\delta v^x_{\mathbf{E}\times\mathbf{B}} (\delta n/\bar{n})} \qquad \text{(C.3)}$$

where the overline indicates a spatial average over the parallel and perpendicular directions. Now, if we hold to Fick's Law: $\Gamma^x_n \equiv \overline{\delta v^x_{\mathbf{E}\times\mathbf{B}} (\delta n/\bar{n})} \sim -D_{flux} \frac{\partial n}{\partial x}$ and remember that $\kappa = -\frac{\partial_x n}{\bar{n}}$,

$$\frac{\partial}{\partial t}\mathcal{F} = \kappa^2 D_{flux}. \qquad \text{(C.4)}$$

Note the assumptions in the previous calculation include neglect of both collisions and Landau damping, periodic boundary conditions and, especially, Fick's Law, which neglects any nonlocal contribution of density perturbations to the flux.

Now, in a different direction, consider a calculation of the particle diffusion coefficient from the δf gyrokinetic equation using the characteristic equation for the marker weights, $w_i \equiv \frac{<\delta f_{1,i}>_R}{F_0}$. Note first the proportionality $\mathcal{F} \propto \frac{1}{2}\sum_i w_i^2(t)$ up to a factor of the background distribution, and if the sum over all marker particles can be considered an ensemble average, it may be written as $\mathcal{F} \propto \frac{1}{2} < w_i^2(t) >$. The $< \cdot >$ brackets here refer to a ensemble average, in the sense of an integration over

microstates in phase space, but in the computer simulation, it may as well be an average over all particles. Using the method of characteristics, the weight evolution equation for slab gyrokinetics can be written as

$$\frac{\partial w_i}{\partial t} =< v^x_{\mathbf{E}\times\mathbf{B},i} >_R \kappa + \frac{q}{T} v_{\parallel,i} < E_\parallel(x_i, y_i) >_R \tag{C.5}$$

If the parallel term is negligible, one may write $w_i(t) = \int_0^t < v^x_{\mathbf{E}\times\mathbf{B},i} >_R (t)\kappa dt'$ when the initial weight is small. Now,

$$< w_i(t)^2 >= \left\langle \int_0^t \int_0^{t'} dt' dt'' \kappa^2 (< v^x_{\mathbf{E}\times\mathbf{B},i} >_R (t'))(< v^x_{\mathbf{E}\times\mathbf{B},i} >_R (t'')) \right\rangle. \tag{C.6}$$

If $t \gg \tau_{autocorr}$ then the correlation product inside this integral will decay when the correlation goes as $e^{-\beta t}$, and the integral can be computed as equal to the diffusion coefficient of test particles, D_{part} multiplied by time, t, according to Taylor's theorem: $\frac{\overline{dx^2}}{dt} = 2\bar{u^2} \int_0^t R(\tau) d\tau = D_{part} t$. Then $\mathcal{F} = D_{part} \kappa^2 t$. This shows the equivalence of the two diffusion coefficients.

If a curvature+∇B term is added to the GKE, as in a Z-pinch with a cylindrically symmetric vacuum magnetic field $\mathbf{B} = -\frac{B_0 r}{R_c}\hat{r}$, there will be a new drift $\mathbf{v}^{tot}_{D,i} = \frac{2v_\parallel^2 + v_\perp^2}{2\Omega R_c}(\hat{r} \times \hat{b_0}) = \frac{2v_\parallel^2 + v_\perp^2}{2\Omega R_c}\hat{z}$. This drift introduces two terms into the δf GKE, $\mathbf{v}^{tot}_{D,i} \cdot \nabla < \delta f >_R$ on the LHS, and $-\mathbf{v}^{tot}_{D,i} \cdot \nabla(\frac{q<\Phi>_R}{T} F_0)$ on the RHS. The LHS term will disappear when integrating over the GKE to find $\mathcal{F}$, assuming periodic boundary conditions again. The RHS term will become $-\mathbf{v}^{tot}_{D,i} \cdot \nabla(\frac{q<\Phi>_R}{T})\delta f$ when the equation is multiplied by $\delta f / F_M$. Note that the Maxwellian here has no dependence on the vertical direction, since density and (possibly) temperature gradients are in the radial direction. This term will be proportional to $\frac{\partial <\Phi>_R}{\partial z}$. Interestingly,

$< v^x_{\mathbf{E}\times\mathbf{B}} >_R \propto \frac{\partial <\Phi>_R}{\partial z}$, so it seems possible to combine the radial $\mathbf{E}\times\mathbf{B}$ drift and vertical curvature/$\nabla\mathbf{B}$ drifts in the weight growth equation, so that:

$$\frac{\partial w_i}{\partial t} =< v^x_{\mathbf{E}\times\mathbf{B},i} >_R \kappa + \frac{q}{T} v^{tot}_{D,i}\hat{\mathbf{z}}\cdot < E(x_i, y_i) >_R = (\kappa + \frac{q}{T} v^{tot}_{D,i})\frac{\partial < \Phi >_R}{\partial z} \quad \text{(C.7)}$$

However, it doesn't make sense to combine the terms to make a new representation of the flux, since the terms are in orthogonal directions. The previous term for $\delta v^x_{\mathbf{E}\times\mathbf{B}}$ and a new term for the Z-pinch drift should be separately considered. The vertical Z-pinch drift term could be combined with the $\mathbf{E}\times\mathbf{B}$ drift in the vertical direction to compute the vertical flux, such that

$$\Gamma^z_n = \sum_{i=1}^{N} (\delta v^z_{\mathbf{E}\times\mathbf{B},i} + v^{tot}_{D,i})\delta n. \quad \text{(C.8)}$$

Interestingly, the vertical $v^z_{\mathbf{E}\times\mathbf{B}}$ drift doesn't appear in the weight equation. So, as a driver for the weight growth, the curvature/$\nabla\mathbf{B}$ drifts can be combined with the radial $\mathbf{E}\times\mathbf{B}$ drift. However, when making the argument to connect D_{flux} with D_{part}, the vertical drift term must be kept separate since the radial flux is orthogonal to the vertical flux.

The weight equation will end up with a new term $\frac{q}{T} v^{tot}_{D,i}\hat{z}\cdot < \mathbf{E} >_R$, where $\hat{z}$ is the vertical direction in the Z-pinch. As noted above, this term becomes proportional to $\frac{\partial\Phi}{\partial z}$, which is the same derivative that comes from the $\mathbf{E}\times\mathbf{B}$. This will give a new term in the autocorrelation integral when finding $< w_i^2(t) >$, such that:

$$< w_i(t)^2 >= \left\langle \int_0^t \int_0^t dt' dt'' (\kappa + \frac{q v^{tot}_{D,i}}{T})^2 < v^x_{\mathbf{E}\times\mathbf{B},i} >_R (t') < v^x_{\mathbf{E}\times\mathbf{B},i} >_R (t'') \right\rangle \quad \text{(C.9)}$$

This integral can no longer be identified with the correlation function for the radial

$\mathbf{E} \times \mathbf{B}$ drift, except through a redefining of $\kappa \to \kappa + \frac{q v_{D,i}^{tot}}{T}$.

One way to look a this is to see the vertical drift term as an enhancement to the weight growth when comparing the Z-pinch to a slab. The $v_{D,i}^{tot}$ is always positive, so the weights will always grow more quickly with this term added. However, the weight growth still requires a radial (perturbed) electric field.

Bibliography

[1] P. Ricci, B. N. Rogers, and W. Dorland, Phys. Rev. Lett. **97**, 245001 (2006).

[2] A. Clauset, C. R. Shalizi, and M. E. J. Newman, SIAM Review **51**, 661 (2009).

[3] W. Dorland, F. Jenko, M. Kotschenreuther, and B. Rogers, Phys. Rev. Lett. **85**, 5579 (2000).

[4] F. Jenko, W. Dorland, M. Kotschenreuther, and B. Rogers, Phys. Plasmas **7**, 1904 (2000).

[5] F. Jenko and W. Dorland, Phys. Rev. Lett. **89**, 225001 (2002).

[6] B. N. Rogers and W. Dorland, Phys. Plasmas **12**, 062511 (2005).

[7] J. Candy, R. E. Waltz, and W. Dorland, Phys. Plasmas **11**, L25 (2004).

[8] R. E. Waltz, J. M. Candy, and M. N. Rosenbluth, Phys. Plasmas **9**, 1938 (2002).

[9] E. Doyle, W. Houlberg, and Y. Kamada, Nucl Fusion **47**, S18 (2007).

[10] B. A. Carreras *et al.*, Phys. Rev. Lett. **80**, 4438 (1998).

[11] B. van Milligen *et al.*, Nucl Fusion **42**, 787 (2002).

[12] D. del Castillo Negrete, Phys. Plasmas **11**, 3854 (2004).

[13] T. Hauff and F. Jenko, Physics of Plasmas **14**, 092301 (2007).

[14] R. Sánchez *et al.*, Phys. Plasmas **16**, 055905 (2009).

[15] T. M. Antonsen and B. Lane, Phys. Fluids **23**, 1205 (1980).

[16] E. A. Frieman and L. Chen, Phys. Fluids **25**, 502 (1982).

[17] G. G. Howes *et al.*, The Astrophysical Journal **651**, 590 (2006).

[18] A. A. Schekochihin *et al.*, The Astrophysical Journal Supplement **182**, 310 (2009).

[19] M. Beer, Ph.D. thesis, Princeton University, 1995.

[20] A. E. White *et al.*, Phys. Plasmas **15**, 6116 (2008).

[21] C. Holland *et al.*, Physics of Plasmas **16**, 052301 (2009).

[22] P. H. Rutherford, Phys. Fluids **13**, 482 (1970).

[23] U. Frisch, *Turbulence: The Legacy of A. N. Kolmogorov* (Cambridge University Press, Cambridge, 1995).

[24] D. R. Baker, Plasma Phys. Control. Fusion **45**, 251 (2003).

[25] R. Basu, T. Jessen, V. Naulin, and J. Rasmussen, Phys. Plasmas **10**, 2696 (2003).

[26] A. Einstein, *Investigations on the Theory of the Brownian Movement* (Dover, New York, 1956).

[27] A. B. Rechester and M. N. Rosenbluth, Phys. Rev. Lett. **40**, 38 (1978).

[28] G. Y. Antar, P. Devynck, X. Garbet, and S. C. Luckhardt, Phys. Plasmas **8**, 1612 (2001).

[29] P. H. Diamond and T. S. Hahm, Physics of Plasmas **2**, 3640 (1995).

[30] J. A. Krommes, Phys. Plasmas **7**, 1752 (2000).

[31] G. Spizzo, R. B. White, and S. Cappello, Phys. Plasmas **14**, 2310 (2007).

[32] G. Spizzo, R. B. White, S. Cappello, and L. Marrelli, Plasma Physics and Controlled Fusion **51**, 124026 (19pp) (2009).

[33] S. Jones and W. Young, J. Fluid Mech. **280**, 149 (1994).

[34] S. C. Venkataramani, T. M. Antonsen, Jr., and E. Ott, Physical Review Letters **78**, 3864 (1997).

[35] J. D. Meiss and E. Ott, Phys. Rev. Lett. **55**, 2741 (1985).

[36] D. del Castillo Negrete, Phys. Fluids **10**, 576 (1998).

[37] T. M. Antonsen and E. Ott, Phys. Fluids **24**, 1635 (1981).

[38] R. G. Kleva and J. F. Drake, Phys. Fluids **27**, 1686 (1984).

[39] B. Bose, E. Marmar, D. Mikkelsen, and M. Greenwald, in *Bull. Am. Phys. Soc.* (APS, College Park, 2008).

[40] A. Hasegawa and K. Mima, Physics of Fluids **21**, 87 (1978).

[41] A. Hasegawa and M. Wakatani, Phys. Rev. Lett. **50**, 682 (1983).

[42] D. del Castillo Negrete, Phys. Plasmas **7**, 1702 (2000).

[43] S. Annibaldi, G. Manfredi, R. Dendy, and L. Drury, Plasma Phys. Control. Fusion **42**, L13 (2000).

[44] S. V. Annibaldi, G. Manfredi, and R. O. Dendy, Phys. Plasmas **9**, 791 (2002).

[45] G. Manfredi and R. Dendy, Phys. Plasmas **4**, 628 (1997).

[46] V. Naulin, A. Nielsen, and J. Rasmussen, Phys. Plasmas **6**, 4575 (1999).

[47] X. Leoncini, O. Agullo, and S. Benkadda, Phys. Rev. E **72**, 12 (2005).

[48] G. Manfredi and R. Dendy, Phys. Rev. Lett. **76**, 4360 (1996).

[49] T. Hauff and F. Jenko, Phys. Plasmas **13**, 102309 (2006).

[50] T. Hauff, F. Jenko, and S. Eule, Physics of Plasmas **14**, 102316 (2007).

[51] T. Hauff and F. Jenko, Phys. Plasmas **15**, 2307 (2008).

[52] G. S. Burillo, B. P. V. Milligen, and A. Thyagaraja, Phys. Plasmas **16**, 042319 (2009).

[53] J. D. Callen and M. W. Kissick, Plasma Phys. Control. Fusion **39**, 173 (1997).

[54] K. W. Gentle *et al.*, Phys. Plasmas **2**, 2292 (1995).

[55] N. J. L. Cardozo, Plasma Phys. Control. Fusion **37**, 799 (1995).

[56] I. Podlubny, *Fractional Differential Equations* (Academic Press, San Diego, 1999).

[57] B. J. West, M. Bologna, and P. Grigolini, *Physics of Fractal Operators* (Springer-Verlag, New York, 2003).

[58] R. Metzler and J. Klafter, Physics Reports **339**, 1 (2000).

[59] P. Mantica and F. Ryter, Comptes Rendus Physique **7**, 634 (2006).

[60] D. del Castillo-Negrete *et al.*, Nuclear Fusion **48**, 075009 (13pp) (2008).

[61] M. F. Shlesinger, G. M. Zaslavsky, and J. Klafter, Nature **363**, 31 (1993).

[62] R. Balescu, Chaos **34**, 62 (2007).

[63] J.-D. Reuss and J. H. Misguich, Phys. Rev. E **54**, 1857 (1996).

[64] K. H. Burrell, Plasma Physics and Controlled Fusion **48**, A347 (2006).

[65] A. Dimits *et al.*, Phys. Plasmas **7**, 969 (2000).

[66] B. Rogers, W. Dorland, and M. Kotschenreuther, Phys. Rev. Lett. **85**, 5336 (2000).

[67] P. Guzdar, R. Kleva, and L. Chen, Phys. Plasmas **8**, 459 (2001).

[68] J. Krommes, Phys Rep **360**, 1 (2002).

[69] I. Broemstrup, Ph.D. thesis, University of Maryland - College Park, 2008.

[70] M. Barnes, Ph.D. thesis, University of Maryland - College Park, 2008.

[71] G. Plunk, Ph.D. thesis, University of California - Los Angeles, 2009.

[72] R. Numata (unpublished).

[73] R. Hazeltine and F. Waelbroeck, *The Framework of Plasma Physics* (Addison-Wesley, Reading, MA, 1998).

[74] J. G. Charney, Journal of Atmospheric Sciences **4**, 136 (1947).

[75] W. Horton and A. Hasegawa, Chaos **4**, 227 (1994).

[76] D. Dubin, J. Krommes, C. Oberman, and W. Lee, Phys. Fluids **26**, 3524 (1983).

[77] M. Barnes, Hasagawa-Mima Model for Drift Wave Turbulence, private communication, 2006.

[78] W. Dorland and G. Hammett, Physics of Fluids B **5**, 812 (1993).

[79] G. Manfredi, J Plasma Phys **61**, 601 (1999).

[80] M. Kono and E. Miyashita, Physics of Fluids **31**, 326 (1988).

[81] M. Nakata, T. Watanabe, H. Sugama, and W. Horton, in *Bull. Am. Phys. Soc.* (APS, College Park, 2009).

[82] G. I. Taylor, Proc. London Math Soc. A **20**, 196 (1922).

[83] G. Csanady, *Turbulent Diffusion in the Environment* (D. Reidel, Dordrecht, 1973).

[84] M. Shlesinger, G. M. Zaslavsky, and J. Klafter, Nature (London) **31**, 363 (1993).

[85] J. Klafter, A. Blumen, and M. Shlesinger, Physical Review A **35**, 3081 (1987).

[86] G. Zaslavsky, Phys Rep **371**, 461 (2002).

[87] E. W. Montroll and G. H. Weiss, Journal of Mathematical Physics **6**, 167 (1965).

[88] R. Sánchez, B. P. V. Milligen, and B. A. Carreras, Phys. Plasmas **12**, 056105 (2005).

[89] P. Lévy, *Theorie de l'Addition des Variables* (Gauthier-Villiers, Paris, 1937).

[90] R. N. Mantegna and H. E. Stanley, Physical Review Letters **73**, 2946 (1994).

[91] F. Mainardi, Y. Luchko, and G. Pagnini, Fract. Calc. App. Analysis **4**, 153 (2001).

[92] M. Kotschenreuther, G. Rewoldt, and W. M. Tang, Computer Physics Communications **88**, 128 (1995).

[93] J. Candy and R. E. Waltz, J. Comput. Phys. **186**, 545 (2003).

[94] F. Jenko, Computer Physics Communications **125**, 196 (2000).

[95] M. Frigo and S. Johnson, Proceedings of the IEEE **93**, 216 (2005).

[96] I. G. Abel *et al.*, Phys. Plasmas **15**, 122509 (2008).

[97] M. Barnes *et al.*, Phys. Plasmas **16**, 2107 (2009).

[98] A. M. Dimits and W. W. Lee, Journal of Computational Physics **107**, 309 (1993).

[99] R. E. Denton and M. Kotschenreuther, Journal of Computational Physics **119**, 283 (1995).

[100] S. E. Parker *et al.*, Phys. Plasmas **11**, 2594 (2004).

[101] Y. Idomura *et al.*, Computer Physics Communications **179**, 391 (2008).

[102] W. M. Nevins *et al.*, Phys. Plasmas **12**, 122305 (2005).

[103] A. Y. Aydemir, Phys. Plasmas **1**, 822 (1994).

[104] W. W. Lee and W. M. Tang, Phys. Fluids **31**, 612 (1988).

[105] C. Birdsall and A. Langdon, *Plasma Physics Via Computer Simulation* (Taylor and Francis, New York, 1991).

[106] C. Birdsall and A. Langdon, *Computer Simulation Using Particles* (Adam Hilger, Bristol, 1988).

[107] W. W. Lee, Journal of Computational Physics **72**, 243 (1987).

[108] J.-P. Bouchaud and A. Georges, Physics Reports **195**, 127 (1990).

[109] R. Balescu, *Aspects of Anomalous Transport in Plasmas* (IOP Puslishing, Bristol, 2005).

[110] D. del Castillo-Negrete, in *Turbulent transport in fusion plasmas: First ITER International Summer School*, edited by S. Benkadda (AIP, College Park, 2008).

[111] W. Horton, Plasma Physics **23**, 1107 (1981).

[112] S. Benkadda, P. Gabbai, and G. M. Zaslavsky, Phys. Plasmas **4**, 2864 (1997).

[113] S. Kovalyov, Chaos **10**, 153 (2000).

[114] A. Chechkin, V. Gonchar, and M. Szydlowski, Phys. Plasmas **9**, 78 (2002).

[115] D. del Castillo Negrete, Phys. Plasmas **13**, 082308 (2006).

[116] L. Garcia and B. A. Carreras, Physics of Plasmas **13**, 022310 (2006).

[117] I. Calvo *et al.*, Physics of Plasmas **15**, 042302 (2008).

[118] F. Jenko and W. Dorland, Phys. Rev. Lett. **89**, 225001 (2002).

[119] I. Furno *et al.*, Physical Review Letters **100**, 055004 (2008).

[120] H. Aref, Journal of Fluid Mechanics **143**, 1 (1984).

[121] T. Solomon, E. R. Weeks, and H. L. Swinney, Physical Review Letters **71**, 3975 (1993).

[122] J. M. Finn and D. del Castillo Negrete, Chaos **11**, 816 (2001).

[123] A. Mishchenko, A. Könies, and R. Hatzky, Phys. Plasmas **12**, 062305 (2005).

[124] E. W. Montroll and M. F. Shlesinger, in *Nonequilibrium Phenomena II. From Stochastics to Hydrodynamics*, edited by J. L. Lebowitz and E. W. Montroll (Elsevier, Amsterdam, 1984).

[125] I. Koponen, Phys. Rev. E **52**, 1197 (1995).

[126] A. Cartea and D. del Castillo-Negrete, Physical Review E **76**, 041105 (2007).

[127] E. R. Weeks and H. L. Swinney, Phys. Rev. E **57**, 4915 (1998).

[128] F. Dupont, R. I. McLachlan, and V. Zeitlin, Phys. Fluids **10**, 3185 (1998).

[129] T. Benzekri *et al.*, Phys. Rev. Lett. **96**, 124503 (2006).

[130] S. V. Prants, M. V. Budyansky, and M. Y. Uleysky, Chaos **16**, 033117 (2006).

[131] S. G. Samko, A. A. Kilbas, and O. I. Marichev, *Fractional Integrals and Derivatives: Theory and Applications* (Taylor and Francis Books Ltd, London, 1993).

[132] M. A. Fogleman, M. J. Fawcett, and T. H. Solomon, Physical Review E **63**, 020101 (2001).

[133] R. D. Sydora, V. K. Decyk, and J. M. Dawson, Plasma Phys. Control. Fusion **38**, 281 (1996).

[134] W. W. Heidbrink and G. J. Sadler, Nucl Fusion **34**, 535 (1994).

[135] B. Kadomtsev, Sov. Phys. JETP **10**, 780 (1960).

[136] A. N. Simakov, P. J. Catto, and R. J. Hastie, Phys. Plasmas **8**, 4414 (2001).

[137] J. Kesner, Phys. Plasmas **7**, 3837 (2000).

[138] P. Ricci, B. N. Rogers, W. Dorland, and M. Barnes, Phys. Plasmas **13**, 062102 (2006).

[139] F. M. Poli, P. Ricci, A. Fasoli, and M. Podestà, Phys. Plasmas **15**, 032104 (2008).

[140] Z. Lin, S. Ethier, T. S. Hahm, and W. M. Tang, Phys. Rev. Lett. **88**, 195004 (2002).

[141] M. Wilczek, F. Jenko, and R. Friedrich, Phys. Rev. E **77**, 1 (2008).

[142] W. Zhang, Z. Lin, and L. Chen, Phys. Rev. Lett. **101**, 4 (2008).

[143] J. A. Krommes and G. Hu, Phys. Plasmas **1**, 3211 (1994).

[144] C. Estrada-Mila, J. Candy, and R. E. Waltz, Phys. Plasmas **13**, 112303 (2006).

[145] T. Dannert *et al.*, Phys. Plasmas **15**, 062508 (2008).

[146] T. Hauff, M. J. Pueschel, T. Dannert, and F. Jenko, Phys. Rev. Lett. **102**, 75004 (2009).

[147] W. Heidbrink *et al.*, Plasma Phys. Control. Fusion **51**, 125001 (2009).